UNIVERSITY OF SOUTHAMPTON

Faculty of Engineering and Physical Science
Optoelectronics Research Centre

Towards the power-scaling of sub-1 μm cryogenically cooled lasers

by

Silvia Cante

A thesis for the degree of
Doctor of Philosophy

May 2021

University of Southampton

Abstract

Faculty of Engineering and Physical Science
Optoelectronics Research Centre

Doctor of Philosophy

Towards the power-scaling of sub-1 μm **cryogenically cooled lasers**

by Silvia Cante

The general aim of the research presented in this thesis is the power-scaling of Nd-doped cryogenically-cooled solid-state lasers operating on the $9xx\ nm$ quasi-four-level transition. Capitalising on a lower quantum defect compared to the renowned $10xx\ nm$ transition, it has the potential for extremely high optical-to-optical efficiency. Moreover, similar to the well known $1\ \mu m$ transition of Yb-doped crystals, the shorter $0.9\ \mu m$ wavelength is obtained via a 'two-level' energy scheme, which in Nd-doped crystals is the first meta-stable excited to ground state transition, ${}^4F_{3/2} \rightarrow {}^4I_{9/2}$. This relatively low gain $9xx\ nm$ transition competes with the higher gain $10xx\ nm$ transition and must also overcome reabsorption associated with population in the terminal ground-state level. Consequently, and due to the more complex energy level structure, other parasitic energy transfer processes such as Energy Transfer Upconversion and Cross Relaxation, which add to the thermal load, must also be addressed in developing power-scaled $9xx\ nm$ Nd-doped lasers. The cryogenically cooled laser architecture provides an excellent platform for such lasers, though their engineering requires a good knowledge of the parameters that would contribute to, or obstruct, efficient laser operation.

In setting out a treatise for developing these lasers, we first needed to undertake a study of the temperature-dependent spectroscopic properties of key Nd-doped materials. As such, we developed procedures that would be easily applicable to any kind of Nd-doped laser crystal. Firstly, we have characterised the ${}^2H_{9/2} + {}^4F_{5/2}$ absorption cross section at temperatures ranging from Room Temperature to 450 K for Nd:YVO_4 and Nd:$GdVO_4$, and from Room Temperature to 77 K for Nd:YAG. Secondly, we have optimised a z-scan experiment for the characterisation of the macroscopic Energy Transfer Upconversion coefficient. This included a rigorous determination of the parameter dependencies and automation of the data collection. We have employed this setup to probe the dependence of this coefficient on elevated temperatures for Nd:YVO_4 and Nd:$GdVO_4$ over the same range explored with the absorption cross section measurements. Furthermore, we have verified its dependence on the doping-ion concentration of Nd:YAG, and therein characterised the Energy Transfer Upconversion in Nd:YAG at cryogenic temperatures. We have determined that although the ETU coefficient increases with decreasing temperature, the beneficial effects of cryogenic cooling dominate the laser performance, resulting in its overall enhancement.

Utilising previous studies for the absorption cross section dependence on sub-ambient temperatures, for in-banding pumping Nd:YAG around 869 nm, we have engineered a novel Volume-Bragg-Grating-locked at 869 nm diode-laser-array pump. This highly efficient pump-source was used to excite a cryogenically cooled Nd:YAG crystal, enabling record performance for 60 W 946 nm laser, which had a slope, and optical-to-optical, efficiency of 52%. With further improvements to the crystal mounting and pump conditioning, we have demonstrated an even better performance from this laser, with $> 100\ W$ of output power and 82% slope, and 74% optical-to-optical, efficiency. The beam quality of both lasers was found to degrade at high-power, however, these results still stand out as the state-of-the-art in radiance in this wavelength regime.

Through precise determination of the key spectroscopic parameters for cryogenically cooled Nd:YAG, we have gained useful insight into the limiting factors for this architecture and power-scaling of the 946-nm Nd:YAG laser. These findings pave the way for future developments of these sub-micron lasers that will achieve further power-scaling of near-diffraction-limited beams with the excellent efficiency as demonstrated in this thesis.

Contents

List of Figures **xi**

List of Tables **xvii**

Declaration of Authorship **xix**

Acknowledgements **xxi**

Definitions and Abbreviations **xxiii**

1 Introduction **1**
1.1 Overview . . . 1
1.2 Motivation . . . 5
1.3 Background . . . 7
1.4 Thesis layout . . . 8
References . . . 11

2 Theory **15**
2.1 Introduction . . . 15
2.2 Absorption measurements . . . 15
2.3 Energy Transfer Upconversion . . . 17
2.4 Quasi-Four-Level Laser Theory . . . 30
2.4.1 Q4L rate-equation model including ETU . . . 32
References . . . 38

3 Spectroscopy measurements **41**
3.1 Introduction . . . 41
3.1.1 Nd-doped hosts overview . . . 42
3.2 Methodology . . . 44
3.2.1 Experimental setup . . . 44
3.2.2 Doping-ion concentration measurements . . . 48
3.2.3 Absorption cross section measurements . . . 53
3.3 Results and discussion . . . 54
3.3.1 Doping-ion concentration . . . 54
3.3.2 Absorption cross section's temperature dependence . . . 56
3.3.2.1 Nd-vandates at elevated temperatures . . . 56
3.3.2.2 Nd:YAG at sub-ambient temperatures . . . 61
3.4 Conclusions . . . 64

References . . . 65

4 Yb:LuLiF$_4$ spectroscopy at sub-ambient temperatures 67
4.1 Introduction . . . 67
4.2 Absorption cross section . . . 69
4.2.1 Results . . . 71
4.3 Emission cross section . . . 74
4.3.1 Methodology . . . 74
4.3.2 Results . . . 77
4.4 Gain cross section . . . 80
4.4.1 Methodology . . . 81
4.4.2 Results and discussion . . . 83
4.5 Conclusions . . . 88
References . . . 90

5 ETU measurements 93
5.1 Introduction . . . 93
5.2 Methodology and experimental setup . . . 95
5.3 Experimental results . . . 106
5.3.1 ETU at elevated temperatures in Nd-doped Vanadates . . . 106
5.3.2 ETU vs concentration in Nd:YAG . . . 112
5.3.3 ETU at sub-ambient temperatures in Nd:YAG . . . 118
5.4 Discussion: Implications of ETU on laser threshold . . . 123
5.4.1 ETU at elevated temperatures in Nd-doped Vanadates . . . 124
5.4.2 ETU vs concentration in Nd:YAG . . . 126
5.4.3 ETU at sub-ambient temperatures in Nd:YAG . . . 128
5.5 Conclusions . . . 131
References . . . 133

6 Power-scaling 946 *nm* cryogenically cooled Nd:YAG lasers 135
6.1 Introduction . . . 135
6.2 60W 946 *nm* cryogenically cooled laser . . . 136
6.2.1 Pump setup . . . 136
6.2.2 Cavity configuration . . . 141
6.2.3 Results and discussion . . . 142
6.3 110W 946 *nm* cryogenically cooled laser . . . 151
6.3.1 Pump setup . . . 151
6.3.2 Cavity configuration . . . 155
6.3.3 Results and discussion . . . 157
6.4 Conclusions . . . 163
References . . . 165

7 Conclusions 167
7.1 Results' overview . . . 167
7.2 Future work . . . 170

Appendix A General Fitting Procedure 173
Appendix A.1 Overview . . . 173

Appendix A.2 Procedure 174
Appendix A.3 An application 176

Appendix B Laser performance model parameters **179**

Appendix C Publications list **181**
Appendix C.1 Peer-reviewed journals 181
Appendix C.2 Conference papers 181

List of Figures

1.1 Periodic table: common rare earth ions used as doping-impurities are highlighted. . . . 3
1.2 Energy levels of Yb:YAG and Nd:YAG and their most popular pumping schemes and lasing transitions, with their quantum defects. . . . 4
1.3 Absorptivity of several metals, from [33]. . . . 6
1.4 Water's absorption coefficient (left y-axis) and percentage loss (right y-axis) through 1 m of water for wavelengths in the range [300-700] nm, from [35]. . . . 7

2.1 Schematics of the Nd^{3+} Energy levels (not to scale) and possible transitions and energy-transfer processes. Orange arrow: Ground State Absorption (GSA); green: laser transitions; blue: ETU; purple: CR. . . . 18
2.2 3-D plot and respective surface maps of the on-axis time-dependent solution for a 100 mm-long z-scan of a 1 mm-long, 1at.%-doped Nd:YAG crystal probed by a 200 mW pump. . 20
2.3 Comparison between on-axis numerical (solid lines) and steady-state (dashed lines) solutions, at three different locations of a 100 mm-long z-scan, for a 1 mm-long, 1at.%-doped Nd:YAG probed by a 200 mW pump. The coordinates $z = (0, 50, 10)$ mm are indicative of high-intensity, small-signal transmission, and transition between these two regimes, respectively. . . . 21
2.4 Comparison between time-dependent and steady-state solutions for a 100 mm-long z-scan of a 1 mm-long, 1at.%-doped Nd:YAG crystal probed by a 200 mW pump. . . . 22
2.5 Top plot: simulated transmission curves for different W_{ETU} values, and comparison between time-dependent and steady-state solutions for a 1 mm-long, 1at.%-doped Nd:YAG probed by a 200 mW pump. Bottom plot: percentual difference between time-dependent and steady-state solutions for the same values of W_{ETU} as the top plot. . . . 23
2.6 Representation of the ASE intensity model and initialisation of P_{ASE} at the front facet of the crystal . . . 27
2.7 Evolution of the ratios of the rate terms to the pump rate (first term) of Eq. (2.14a) during the propagation through the crystal. Simulation of a 100 mm-long z-scan executed on a 5 mm-long, 0.3at.%-doped, Nd:YAG crystal at LNT. The z-coordinate is fixed to $z = 0$ mm, the point of maximum incident irradiance, and the radial coordinate is on-axis ($r = 0$). . 28
2.8 Ratios of the rate terms of Eq. (2.14a) to the pump rate (first term) vs z-position for a 100 mm-long z-scan executed on a 5 mm-long, 0.3at.%-doped, Nd:YAG crystal at LNT. The crystal-coordinates are fixed to the first facet of the sample for the dashed lines and to the second facet of the sample for the solid lines. The radial coordinate is on-axis ($r = 0$). 29
2.9 Transmitted pump power (blue) and ASE power (red) for a z-scan executed on a 5 mm-long, 0.3at.%-doped, Nd:YAG crystal at LNT. . . . 29
2.10 NdYAG's energy level diagram (not to scale) and possible transitions from the metastable state $^4F_{3/2}$, including ETU and CR. . . . 33

3.1 Absorption measurements setup. . . . 44

3.2 LIMO diode's beam modelling through the absorption setup. 45
3.3 (3x3x1) mm^3 Nd-doped vanadate sample, wrapped in 200 μm-thick Indium and clamped to a heated Copper block. (A) Unshielded. (B) Shielded by a 1 mm-thick Aluminium foil. 45
3.4 (3x3x1) mm^3 Nd:YAG, wrapped in 200 μm-thick Indium and clamped to a Copper block in contact with the cold-head of the cryo-cooler. (A) Front view. (B) Dimetric view. . . . 46
3.5 Operation schematics from the Q-drive 2s132K's manual. 47
3.6 Q-drive 2s132K: cold head and motor pressure wave generator. 47
3.7 Q-drive 2s132K's COP (left axis) and Heat load extraction (right axis), from 2s132K's operational manual. 48
3.8 Top: original $A^*(\lambda)$ (blue) vs corrected $A(\lambda)$ (red) absorption spectra. Bottom: original (blue) and corrected (red) transmitted probe signal. 50
3.9 Linear fit (red) to areas with negligible absorption (top), and and overview on the whole measured spectrum (bottom). 50
3.10 Nd:YAG: reference absorption cross section spectrum and absorption peaks chosen for the analysis. 51
3.11 Details of how peak absorption cross section values for a fixed temperature are retrieved, when the absorption cross section data for the given temperature is not available. 808 nm peak of Nd:YAG. 52
3.12 Nd:YVO_4 absorption cross section, π-pol. 57
3.13 Nd:YVO_4 absorption cross section, σ-pol. 58
3.14 Nd:$GdVO_4$ absorption cross section, π-pol. 58
3.15 Nd:$GdVO_4$ absorption cross section, σ-pol. 59
3.16 Polynomial fits to the dependence of absorption cross section peaks vs temperature in Nd:YVO_4. Secondary y-axis: FWHM ($\Delta\lambda$, bandwidth) for the π-pol peaks vs temperature. 59
3.17 Polynomial fits to the dependence of absorption cross section peaks vs temperature in Nd:$GdVO_4$. Secondary y-axis: FWHM ($\Delta\lambda$, bandwidth) for the π-pol peaks vs temperature. 60
3.18 Nd:YAG absorption cross section for temperatures in the range (RT-LNT). 62
3.19 Nd:YAG absorption cross section for temperatures in the range (RT-LNT), 808 nm peak detail. 62
3.20 Nd:YAG absorption cross section 808 nm peak values (blue circles) for temperatures in the range (RT-LNT), their relative bandwidths (black diamonds), and their respective second degree polynomial fitting curves (dashed blue and black, respectively). 63

4.1 Yb:$LuLiF_4$'s energy level diagram and pumping (orange) and lasing (green) transitions between the ground state $^2F_{7/2}$ to the excited state $^2F_{5/2}$. 69
4.2 Yb:$LuLiF_4$ sample clamped, via two Copper L-shaped brackets, to an Aluminium block in contact with the cold-head of the cryocooler. The contact points between the crystal and the metals are covered with a 100 μm-thick Indium foil. 70
4.3 Yb:$LuLiF_4$'s σ-polarisation absorption cross section for temperatures (63 K-RT). 71
4.4 Yb:$LuLiF_4$'s σ-polarisation absorption cross section peak amplitudes at 960 nm and 972 nm and relative bandwidths for the temperature range (63 K-RT). 72
4.5 Yb:$LuLiF_4$'s π-polarisation absorption cross section for temperatures (63 K-RT). Inset: zoom on the strongest peak around 960 nm. 73
4.6 Yb:$LuLiF_4$'s π-polarisation absorption cross section peaks at 960 nm and relative bandwidths for temperatures (63 K-RT). 73
4.7 Fluorescence spectrum measurement setup. 75

4.8 Comparison between fluorescence spectra without (red line) and with (blue line) Arduino synchronisation of the data collection. . . . 76
4.9 Relative timings of pump pulse (red), fluorescence signal (cyan), Arduino trigger (blue) and OSA measurement (green). Inset: Zoom around the measurement event. . . . 76
4.10 Yb:$LuLiF_4$'s σ-polarisation emission cross section for temperatures (63 *K*-RT). Inset: zoom on the strongest peak around 972 *nm*. . . . 78
4.11 Yb:$LuLiF_4$'s σ-polarisation absorption cross section peaks at 972 *nm* and their bandwidths for temperatures (63 *K*-RT). . . . 79
4.12 Yb:$LuLiF_4$'s π-polarisation emission cross section for temperatures (63 *K*-RT). Inset: zoom on the strongest peak around 995 *nm*. . . . 79
4.13 Yb:$LuLiF_4$'s π-polarisation emission cross section peaks at 993 *nm* and 995 *nm* and their bandwidths for temperatures (63 *K*-RT). . . . 80
4.14 Gain measurement setup. . . . 81
4.15 Gain measurement: data example. . . . 83
4.16 Gain measurement for Yb:$LuLiF_4$ at 183 *K* and population inversion of 20%. Raw and filtered fluorescence spectra with (blue and red) and without (green and yellow) the probe signal. . . . 84
4.17 Gain measurement for Yb:$LuLiF_4$ at 183 *K* and population inversion of 20%. Top subplot: calculated transmitted probe with pumped crystal, raw (black) and smoothed (grey) spectra; bottom subplot: raw measured incident and transmitted probe with unpumped crystal. . . . 84
4.18 Gain measurement for Yb:$LuLiF_4$ at 183 *K* and population inversion of 20%. Gain cross section retrieved from pump-probe measurements: raw (blue) and filtered (red); gain cross section calculated from previously measured absorption and emission cross sections: orange. . . . 85
4.19 Gain measurement for Yb:$LuLiF_4$ at 183 *K*, 153 *K*, 123 *K* and 93 *K*, each at three different population inversion levels. . . . 86
4.20 Gain measurement for Yb:$LuLiF_4$ at 77 *K* and 63 *K*, each at three different population inversion levels. . . . 87

5.1 Automated ETU measurement setup. Lenses: L_1 ($f = 50$ *mm*), L_2 ($f = 300$ *mm* or $f = 100$ *mm*), L_3 ($f = 200$ *mm*), L_4 ($f = 175$ *mm*); flat high reflectivity mirrors at 808 *nm*: M_1 and M_2; M_3 curved mirror (radius or curvature=100 *mm*); glass wedges: W_1 and W_2; Si photodiodes: PD_1, PD_2 and PD_3. . . . 96
5.2 Calibration of reference and transmission PDs: analytical forms of the relations between voltages and powers. . . . 98
5.3 Simulated z-scan transmission curves at different incident powers for a 1 *mm*-long, 0.6at.%-doped Nd:YAG, with $W_{ETU} = 35 \cdot 10^{-18}\ cm^3/s$. . . . 100
5.4 "Experimental" (simulated) data for a 150 *mW* pump (blue circles) and fitted data with a modelled 180 *mW* pump (magenta line). . . . 101
5.5 Typical dataset collected in a z-scan. Green dots: repeated measurements at each fixed z-position; blue line: average P_{in} of the green dots at each z-position; red line: average P_{tran} of the green dots at each z-position. . . . 103
5.6 Typical experimental transmission curve (blue circles) and its fitted theoretical curve (red line). . . . 103
5.7 Typical experimental transmission curve for which the double z-step length option was exploited. Z-step lengths: 0.7 *mm* and 0.2 *mm* outside and inside the dashed gray rectangle, respectively. . . . 104

5.8 Sample of waveforms collected at each z-scan step. Solid lines: PD_1 and PD_2 signals [V], in red and pink respectively; dashed lines: small-signal and high-irradiance regimes fluorescence normalised signals [a.u.], in blue and green respectively. 106
5.9 Experimental 808-nm-pump z-scan curves (circles, color coded) and their respective fitted curves (grey dashed) for 1.1at.%-doped Nd:$GdVO_4$ in the temperature range (RT-453 K). 108
5.10 Experimental 806-nm-pump z-scan curves (circles, color coded) and their respective fitted curves (grey dashed) for 1.1at.%-doped Nd:$GdVO_4$ in the temperature range (RT-453 K). 108
5.11 Experimental 808-nm-pump z-scan curves (circles, color coded) and their respective fitted curves (grey dashed) for 0.5at.%-doped Nd:$GdVO_4$ in the temperature range (RT-453 K). 109
5.12 Experimental 806-nm-pump z-scan curves (circles, color coded) and their respective fitted curves (grey dashed) for 0.5at.%-doped Nd:$GdVO_4$ in the temperature range (RT-453 K). 109
5.13 ETU coefficient for 1at.%- and 0.6at.%- doped Nd:YVO_4 at elevated temperatures. . . . 110
5.14 ETU coefficient for 1at.%- and 0.5at.%- doped Nd:$GdVO_4$ at elevated temperatures. . . 110
5.15 Z-scan experimental data (light coloured circles) and fitted transmission curves when accounting (dashed lines) and not accounting (solid lines) for ASE, for RT and 450 K, for a 1.1at.%-doped, 1 mm-long Nd:$GdVO_4$ crystal. 112
5.16 Z-scan transmission curves, red to blue circles corresponding to highest (1.84at.%) to lowest (0.30at.%) concentrations, and their respective fitted theoretical curves, in gray dashed lines. 113
5.17 W_{ETU} vs Nd^{3+}-doping concentration in Nd:YAG. 114
5.18 Left y-axis (blue): temperature rise over the scan length for a 1.84%-doped Nd:YAG crystal. Right y-axis (black): τ_{heat}, to be compared to the pulse duration and period. . . 116
5.19 Black line: reported dependence $W_{ETU}(T)$ from Yan et. al [1]; red line: estimated dependence $W_{ETU}(T)$ for 1.84at.% doping; blue triangle: measured W_{ETU} for 1.84%-doped Nd:YAG accounting for the estimated temperature rise; red circle: estimated W_{ETU} for 1.84%-doped Nd:YAG at $T = 290$ K employing our measured linear dependence of W_{ETU} vs concentration. 117
5.20 Z-scan transmission curves for a 0.30at.%-doped, 5.10 mm-long, Nd:YAG for temperatures from RT to LNT (red to black circles), and their respective fitted theoretical curves (dashed gray). The curves corresponding to $T = 93$ K and $T = 77$ K have been measured by tuning the pump off-peak. 119
5.21 Z-scan transmission curves for 0.57at.%-doped Nd:YAG for temperatures from RT to LNT (coloured circles), and their respective fitted theoretical curves (dashed gray). 120
5.22 ETU coefficient vs sub-ambient temperatures and quadratic fits for 0.30at.% and 0.57at.% doped Nd:YAG. 120
5.23 Spectral overlap between the emission transition $^4F_{3/2} \rightarrow {}^4I_{11/2}$ (solid lines, from [18]) and the 10x-magnified ESA transition $^4F_{3/2} \rightarrow {}^4G_{9/2}$ (red dashed line, from [19]). . . . 121
5.24 Z-scan experimental data (light coloured circles) and fitted transmission curves when accounting (dashed lines) and not accounting (solid lines) for ASE, for RT and LNT, for a 0.30at.%-doped, 5 mm-long Nd:YAG crystal. 122
5.25 Figure-of-merit F_q as defined in Chapter 2 vs elevated-temperatures for the 0.9 μm and 1 μm transition of 0.5at.%- and 1.0at.%-doped Nd:YVO_4. 124
5.26 P_{th} vs Temperature for 0.9 μm and 1 μm 1.0at.%-doped Nd:YVO_4 laser, with and without including ETU effects. 125
5.27 P_{th} vs Temperature for 0.9 μm and 1 μm 0.5at.%-doped Nd:YVO_4 laser, with and without including ETU effects. 126
5.28 Figure-of-merit F_q as defined in Chapter 2 vs concentration for the 0.9 μm and 1 μm transition of NdYAG. 127

5.29 P_{th} vs Nd^{3+}-doping in Nd:YAG, with and without ETU. Right y-axis: percentual difference between the two. . . . 128
5.30 Calculated laser threshold vs cryo-temperatures, including and not including ETU effects, for 0.3at.%-, 0.6at.%, and 1.07at.%-doped Nd:YAG, according to [6]. . . . 130
5.31 Figure-of-merit F_q as defined in Chapter 2 vs cryo-temperatures for 0.3at.%-, 0.6at.%-, and 1.07at.%-doped Nd:YAG. . . . 130

6.1 Nd:YAG's R-band absorption cross section for temperatures in the range (RT-LNT). Inset: zoom on the strongest peak around 869 nm. . . . 136
6.2 Layout (z-axis not in scale) of the optical components for x- and y- axes. 137
6.3 Central VBG-locked DLA's wavelength chirp for different output powers. Bashed black line: Nd:YAG's 869 nm normalised absorption cross section peak at LNT. . . . 138
6.4 Absorption efficiency of the VBG-locked pump for incident powers from 4 W to 120 W during lasing. . . . 139
6.5 Polarisation combining setup, top view. . . . 140
6.6 Beam quality and spot sizes after the focussing lenses for $P = 120$ W. . . 140
6.7 3x3x15 mm^3 Nd:YAG crystal wrapped in Indium foil and positioned between two Copper blocks, the largest one in contact with the cold head. The two blocks are thermally linked via a Copper braid. (A) Front view. (B) Dimetric view. . . . 141
6.8 Linear plano-concave cavity. . . . 142
6.9 Fundamental laser mode radius in the crystal vs thermal lens. . . . 142
6.10 Emission cross section around 940 nm for several different temperatures in the range (RT-LNT) [3]. Inset: the 946 nm peak's red-shift with decreasing temperature. . . . 143
6.11 Right axis (black diamonds): laser emission wavelength vs absorbed pump power. Left axis (blue dots): slope efficiency vs absorbed pump power for the 60-W, 946 nm, cryogenically cooled Nd:YAG laser developed. 144
6.12 Measured beam qualities for the respective axes for $P_{out} = 1$ W (circles) and $P_{out} = 40$ W (diamonds). . . . 144
6.13 Captured spatial distribution of the laser mode over ~ 10 s: the beam presents a high modal instability. . . . 146
6.14 Spatial distribution of the pump and fundamental laser modes according to measurement and cavity modelling, respectively. . . . 147
6.15 Spatial distribution of $\Delta N(\mathbf{r})$ at the first (top plots) and second (bottom plots) facets of the crystal. . . . 148
6.16 Fraction thermal loading distribution at the first and second facets of the crystal. . . . 149
6.17 Heat loading distribution $Q(\mathbf{r})$, with (top plots) and without (bottom plots) accounting for ETU, at the first and second facets of the crystal. . . . 149
6.18 Ratio of the heat source distributions $Q_{ETU}(\mathbf{r})/Q_{noETU}(\mathbf{r})$ at the first and second facets of the crystal. . . . 150
6.19 Top plot: Representation of the x- and y-axes' pump caustics ($P_{pump} = 120$ W) and the fundamental laser mode according to measurement and modelling (Section 6.3.1), respectively. Bottom plot: mode match $a = W_{0_{x,y}}/w_L$ factor for the x- and y-axes (blue curves) and ellipticity (red curve) of the pump beam over the cavity length. Pink patches: Nd:YAG crystal. . . . 152
6.20 Catastrophic damage of the DLA's emitters. . . . 152

6.21 Top plot: Representation of the x- and y-axes' pump caustics and the fundamental laser mode according to measurement ($P_{pump} = 45\ W$) and modelling, respectively. Fundamental cavity mode modelled (see Section 6.3.2) with a predicted thermal lens of 1000 mm [8]. Bottom plot: mode match $a = W_{0_{x,y}}/w_L$ factor for the x- and y-axes (blue curves) and ellipticity (red curve) of the pump beam over the cavity length. Pink patches: Nd:YAG crystal. 153
6.22 Top plot: Representation of the x- and y-axes' pump caustics and the fundamental laser mode according to measurement ($P_{pump} = 135\ W$) and modelling, respectively. Fundamental cavity mode modelled (see Section 6.3.2) with a predicted thermal lens of 250 mm [8]. Bottom plot: mode match $a = W_{0_{x,y}}/w_L$ factor for the x- and y-axes (blue curves) and ellipticity (red curve) of the pump beam over the cavity length. Pink patches: Nd:YAG crystal. 154
6.23 3x3x15 mm^3 Nd:YAG crystal wrapped in Indium foil and positioned in a 4-quadrant mount. This cylindrical assembly is held in a block in contact with the cold head. (A) Front view. (B) Dimetric view. 155
6.24 Experimental setup for the cryogenically cooled 946 nm Nd:YAG laser developed. 156
6.25 Left y-axis (blue): Absorption efficiency of the 0.3at.%-doped Nd:YAG crystal at 80 K, for the operating laser employing the two tested OCs. Right y-axis (red): pump wavelength variation vs pump power. 157
6.26 Top plot: measured emission wavelength (left y-axis) and estimated temperature of the emitting area of the gain medium (right y-axis). Bottom plot: optical to optical efficiency (red) and output power in function of absorbed pump power (blue) for the two OCs tested. 158
6.27 Spatial distribution of $\Delta N(\mathbf{r})$ at the first (top plots) and second (bottom plots) facets of the crystal. 160
6.28 Fractional thermal loading distribution at several z-coordinates along the crystal length. 161
6.29 Heat-source-density distribution $Q(\mathbf{r})$, with (top plots) and without (bottom plots) accounting for ETU, at the first and second facets of the crystal. 162
6.30 Ratio of the heat source distributions $Q_{ETU}(\mathbf{r})/Q_{noETU}(\mathbf{r})$ at the first and second facets of the crystal. 162

Appendix A.1 Example of raw data for a M^2 measurement. 177
Appendix A.2 Example of raw data vs best fit curve for a M^2 measurement. 177

List of Tables

3.1 Main spectroscopic and thermo-optical properties of Nd:YAG, Nd:YVO_4 and Nd:$GdVO_4$. 42
3.2 Concentration measurements results for different Nd-doped crystals. 55
3.3 Concentration measurement's details for the CLaser 0.6at.% Nd:YAG no. 5. 56
3.4 Doping ion concentration measurements for Nd:YVO_4 and Nd:$GdVO_4$: results and associated uncertainties. 56
3.5 Nd:YVO_4: Second degree polynomial fit coefficients for σ_{abs} vs T dependence. 60
3.6 Nd:$GdVO_4$: Second degree polynomial fit coefficients for σ_{abs} vs T dependence. 60
3.7 Nd:YAG: Second degree polynomial fit coefficients for σ_{abs} vs T dependence. 63

4.1 Main spectroscopic and thermo-optical properties of Yb:$LuLiF_4$, Yb:CaF_4, Yb:YLF, Yb:YAG from [2, 5, 12, 13, 14]. 68
4.2 Details of the Yb:$LuLiF_4$ samples tested. 70

5.1 Details of the Nd-doped samples investigated in the ETU coefficient measurements. . . 96
5.2 Details of the 6 Nd:YAG samples of different doping concentrations employed in the W_{ETU} vs Nd-concentration characterisation. 113
5.3 Nd:YAG: Coefficients for the second degree polynominal fit curves for W_{ETU} vs T in 0.30at.%- and 0.60at.%-doped samples. 122

Declaration of Authorship

I declare that this thesis and the work presented in it is my own and has been generated by me as the result of my own original research.

I confirm that:

1. This work was done wholly or mainly while in candidature for a research degree at this University;
2. Where any part of this thesis has previously been submitted for a degree or any other qualification at this University or any other institution, this has been clearly stated;
3. Where I have consulted the published work of others, this is always clearly attributed;
4. Where I have quoted from the work of others, the source is always given. With the exception of such quotations, this thesis is entirely my own work;
5. I have acknowledged all main sources of help;
6. Where the thesis is based on work done by myself jointly with others, I have made clear exactly what was done by others and what I have contributed myself;
7. None of this work has been published before submission

Signed:..... Date:.....

Acknowledgements

I would like to thank all my colleagues for the help they have given me during these years; thanks to all the support staff for promptly providing me with anything I needed and making the whole process smooth. A special thank you must go to Ed, for the many constructive chats and coffees.

Many thanks to my ”sports” friends (you know who you are!) for the great time shared out of the lab - all the runs, cycles, swims and basketball recharged the battery I needed to carry on working.

A very sincere and huge thank you to my supervisor, Jacob Mackenzie, for providing me with the right tools to face this journey. Thanks for the immense help, support and understanding, all given at the right moments, and for encouraging me to do better when I needed to take an extra step. I feel lucky and honoured to have had your guidance towards becoming a laser scientist.

Un grazie speciale a mia mamma, Enza, e alla mia famiglia Riccarda & Antonello, e Marika & Sara per il loro supporto incondizionato. Grazie per la fiducia che mi avete sempre dato, e per avermi, senza saperlo, fornito la giusta prospettiva sul mondo quando tutto cio' che riuscivo a vedere era il laboratorio.

Finally, the biggest thank you to my partner Claudia, who successfully managed to get through this PhD as well - not as easy task! Thanks for being by my side through it all: the celebrations and accomplishments, but mostly during the numerous challenging times these intense four years have gifted me (and you) with. Thanks for giving me the strength and motivation I needed when I was most tired, and for keeping me all in one piece.

Definitions and Abbreviations

ASE	Amplified Spontaneous Emission
BTS	Beam Transformation System
COP	Coefficient Of Performance
CR	Cross Relaxation
CW	Continuous Wave
DLA	Diode Laser Array
DPSSL	Diode Pumped Solid State Laser
DUV	Deep Ultra Violet
ESA	Excited State Absorption
ETU	Energy Transfer Upconversion
FL	Füchtbauer-Landenburg
FOM	Figure Of Merit
FWHM	Full Width at Half Maximum
HR	Highly Reflective
HT	Highly Transmissive
LIBS	Laser Induced Breakdown Spectroscopy
LIDAR	Light Detection and Ranging
LNT	Liquid Nitrogen Temperature
MOPA	Master Oscillator Power Amplifier
OC	Output Coupler
OSA	Optical Spectrum Analyser
PID	Proportional Integral Derivative
PWG	Pressure Wave Generator
QD	Quantum Defect
Q3L	Quasi Three Level
Q4L	Quasi Four Level
ROC	Radius Of Curvature
RT	Room Temperature
SSL	Solid State Laser
VBG	Volume Bragg Grating
ZPL	Zero Phonon Line

Chapter 1

Introduction

1.1 Overview

From Light Detection and Ranging (LIDAR) systems [1] and materials processing [2], passing through surgery and vision correction [3], underwater communication [4], space exploration [5, 6], and laser intertial confinement fusion [7], the applications of solid state lasers (SSL) are numerous, ranging from everyday life to sophisticated scientific measurements. Since their invention in 1960 [8], solid state lasers have made tremendous progress in both performance and design, making it possible to efficiently employ them in a large variety of fields.

Solid state lasers exploit solid gain media and encompass different geometries - waveguides, thin disks, bulk crystals, i.e. rod or cuboid shaped media with several-mm cross sections - differing from each other by the way the heat deposited by the pump is extracted. In fact, diode lasers, which are solid-state semiconductor waveguide lasers themselves, are commonly employed as pumps for dielectric SSL, leading to the term diode-pumped SSL (DPSSL). Diode lasers have drastically improved in performance in the last years, making them more appealing than flash lamps, traditionally employed to pump SSL. With respect to lamps, diode lasers offer a higher brightness, a narrower bandwidth to better match the absorption spectrum of laser crystals, and a longer lifetime. Furthermore, they provide high-power as well as excellent wall-plug efficiencies as high as 70% [9, 10]. With such powerful and bright pumps in relation to lamps, the heat extraction in DPSSL is a critical aspect for both an efficient operation and a potential power-scaling. Waveguides, comprising ultra-thin slab lasers or optical fibers, and thin disks take advantage of the large cooling-surface to pumped-volume ratio, enablig efficient heat extraction. In waveguide lasers the thermal deposition of the pump is spread over large, face-cooled volumes, allowing a small temperature gradient between the pumped core and the cooled cladding regions. In thin disks, on the other

hand, the active medium is only ~ 200 microns-thick and one face is in contact with the heat sink; suitably engineered coatings are deposited directly onto the cooled surface in order to provide the appropriate reflection features for the laser cavity of choice. These thermal-management, power-scaling, strategies have provided excellent results, with output powers in the order of the hundreds-kW for optical fiber Master Oscillator Power Amplifier (MOPA) systems [11, 12], and tens-kW in thin-disk lasers [13, 14] and crystal waveguide lasers [15].
The heat deposition in rod and slab DPSSL causes high temperature gradients between the pumped region and cooled surface, with potentially strong thermal lensing arising, leading to limited cavity stability, and thermal aberrations that increase losses and worsen the beam quality of the output beam. One successful strategy for power-scaling bulk DPSSL is cryogenic-cooling, that is to aggressively cool the gain medium to cryogenic temperatures ($T < 150\ K$). Exploited since the earliest laser demonstrations [16], cryogenic-cooling of the gain medium has proved to be an effective way of power- and energy-scaling solid-state-lasers [17], mainly due to the enhancement of spectroscopic and thermo-optical properties [18, 19].

Bulk DPSSL can be side- or end-pumped. In the side-pumped architecture the pump source propagates into the gain medium perpendicularly to the laser signal produced inside the cavity. The side-pumped volume can approach the whole volume of the active medium, providing an almost uniform spatial distribution of the population inversion. This configuration is, however, not particularly efficient, due to the large amount of unsaturated gain outside of the lasing mode [20, Chapter 3]. For the end-pumped architecture, instead, the pump laser is conditioned so that its size inside the gain medium is comparable to the laser mode's, providing a much better overlap, and therefore efficiency.

In this thesis we consider crystal gain media doped with a rare earth (RE) impurity ion, typically a trivalent ion of the form A^{3+}. The most commonly employed impurities (highlighted in Fig. 1.1) are the Lanthanides. These have atomic structure $[Xe]4f^n6s^2$, with partially filled 4f shells shielded by the outer 5s and 5p shells. The 4f electrons can be excited to a higher 4f electron state providing a range of potential electronic transitions and energy states for the impurity ion. The outer shell shielding ensures that the surrounding host lattice vibrations (phonons) only weakly affect the electronic states [21, 22, 23], although interaction with the crystal field of the host lattice splits the electronic energy levels into further sub-levels, the Stark levels. Some transition elements are also optically active, for example the Ti^{3+} ion ([Ar]3d), widely employed in Ti:sapphire lasers, exploits the single electron in the 3d shell for electronic transitions. Here the absence of outer shells means strong electron-phonon interaction exist, causing

a broad emission spectrum (650-1100) nm [24], particularly suitable for wavelength tuning and generation of ultrashort pulses.

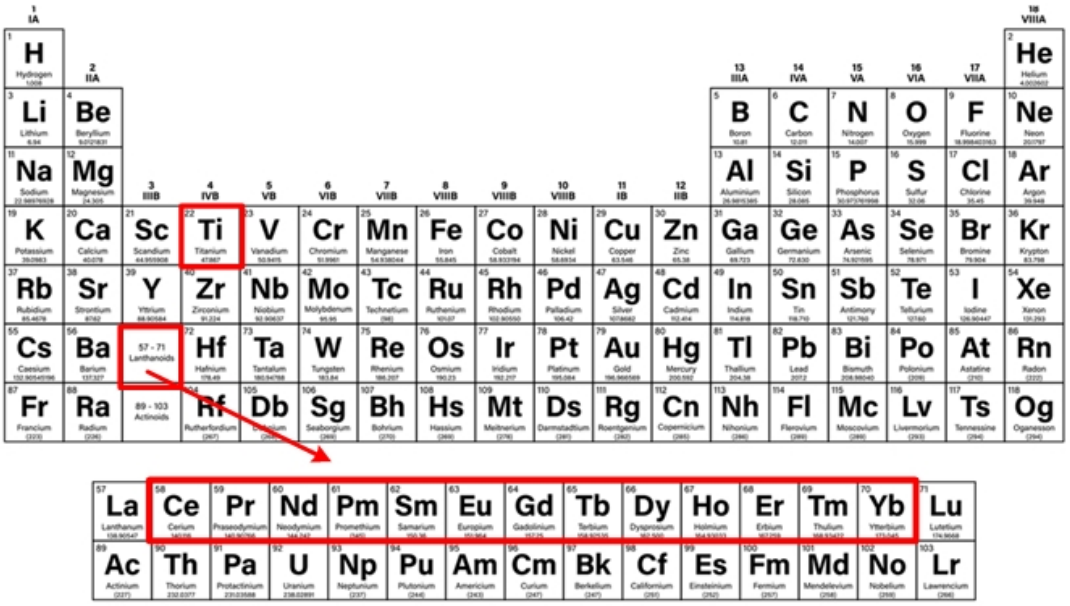

FIGURE 1.1: Periodic table: common rare earth ions used as doping-impurities are highlighted.

In this work, we focus on the Nd^{3+} ion, one of the best known and exploited impurities for DPSSL. The typical pump absorption transition (at 808 nm) takes place from the ground state $^4I_{9/2}$ to the excited state manifold $^5F_{3/2} + {}^2H_{9/2}$; the latter depopulates via phonon-assisted (fast) decay to the metastable manifold $^4F_{3/2}$. The laser transitions take place from this metastable manifold $^4F_{3/2}$, comprising the Stark levels R_1 and R_2, to the ground state manifolds $^4I_{9/2}$, $^4I_{11/2}$, $^4I_{13/2}$, $^4I_{15/2}$, each split into their respective Stark levels when the ion is placed in a host crystal (see Fig. 2.10 for an overview on the energy levels of Nd^{3+}-doped YAG). In the case of in-band pumping, the pump absorption takes place between the manifolds $^4I_{9/2} \rightarrow {}^4F_{3/2}$, for which one transition has a wavelength of around 869 nm (see right-hand side of Fig. 1.2 for details of the in-band pumping exploited in this work).

The most commonly used dopant in the cryogenically-cooled regime is Yb^{3+}, which has been reported at the multi-hundreds-of-Watts in CW bulk systems [19, 25, 26], and up to 2.6 kW of peak power for a MOPA system [27]. Yb-doped crystals present a very simple level structure consisting of only one excited state manifold and one ground-state manifold; this allows a small Quantum Defect (QD) and potentially high efficiency, with very low heat load and deleterious non-radiative effects. However, they only operate close to 1 μm, limiting their use when different lasing frequencies are needed. Nd-doped solid state lasers, on the other hand, although typically employed operating on their 1.06 μm emission line ($^4F_{3/2} \rightarrow {}^4I_{11/2}$), are also capable of working on the 0.9 μm, 1.3 μm and 1.8 μm transitions, $^4F_{3/2} \rightarrow {}^4I_{9/2}$, $^4F_{3/2} \rightarrow {}^4I_{13/2}$, $^4F_{3/2} \rightarrow {}^4I_{15/2}$, respectively. The

energy level scheme of the 0.9 μm transition in Nd^{3+} is comparable to the 1 μm in Yb^{3+}: both terminate in the ground state and therefore exhibit reabsorption losses, the strength of which is temperature dependent, substantially reduced when cryogenically cooled. However, thanks to its shorter wavelength, the 0.9 μm transition of Nd^{3+} has potentially more applications through frequency upconversion.

Fig. 1.2 shows the in-scale energy level scheme of Yb:YAG and Nd:YAG, with the levels' energies in cm^{-1}. The Quantum Defect (QD) for each transition is indicated in the same colour of the respective transition, and the comparable Quasi-Four-Level (Q4L) transitions $^2F_{5/2} \rightarrow {}^2F_{7/2}$ at 1030 nm and $^4F_{3/2} \rightarrow {}^4I_{9/2}$ at 946 nm of Yb:YAG and Nd:YAG's, respectively, are indicated in bold. In fact, considering only the ground and the first meta-stable excited state, akin to the Yb^{3+} energy scheme, the Nd:YAG's $^4F_{3/2} \rightarrow {}^4I_{9/2}$ system if pumped in-band, for example at 869 nm, offers a QD $\sim$ 8%, almost two times smaller than when pumped at 808 nm, traditionally used as the strongest absorption feature.

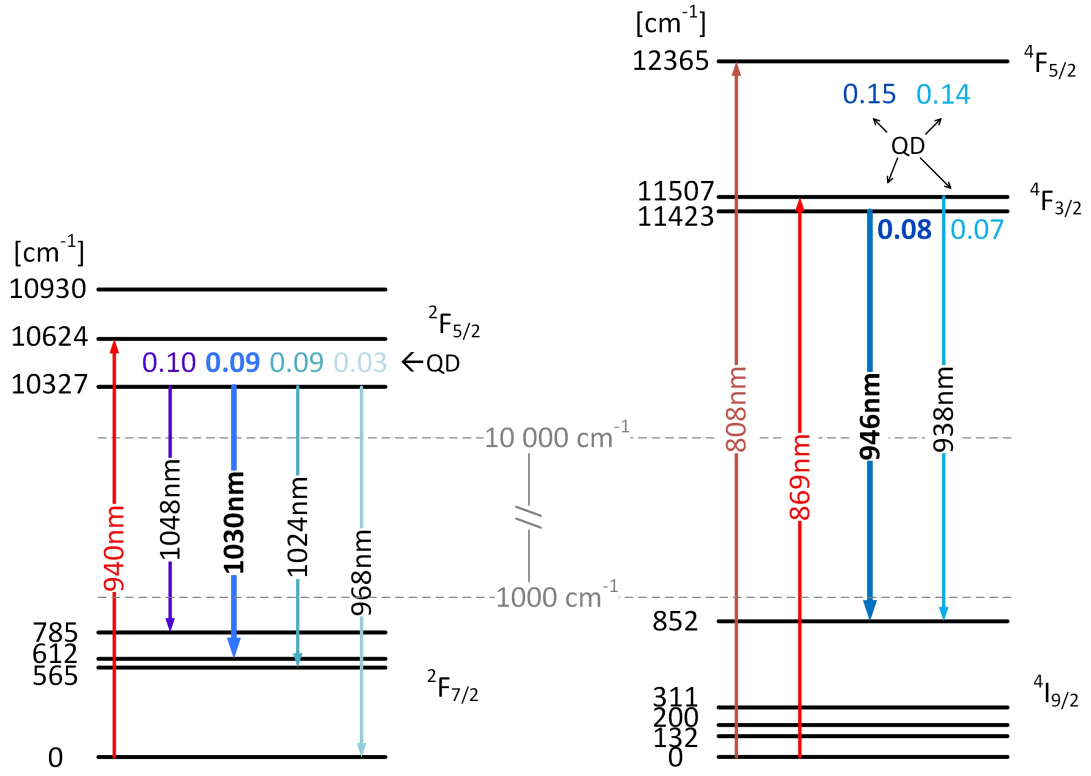

FIGURE 1.2: Energy levels of Yb:YAG and Nd:YAG and their most popular pumping schemes and lasing transitions, with their quantum defects.

Therefore, although the 0.9 μm transition of Nd^{3+} has a relatively low gain, it could potentially be more efficient than the high gain 1 μm due to a lower QD between pump and output wavelengths. Furthermore, the 0.9 μm transition of Nd^{3+} presents a lower Q4L characteristic than the 1030 nm one in Yb^{3+} thanks to the terminating Stark level of the first having a higher energy than the respective one for the second

ion, 852 cm^{-1} as opposed to 612 cm^{-1}, respectively, resulting in a lower reabsorption loss. However, a widely exploited advantage of Yb^{3+} is that, thanks to its simple level structure, it can be used with high doping levels, providing high gain per unit length. Unfortunately, due to its complex level structure, instead, Nd^{3+} is susceptible of harmful effects like concentration quenching, which limit the doping-level achievable for this ion. Additional concentration-dependent parasitic effects like Energy Transfer Upconversion (ETU) and Cross Relaxation (CR) are detrimental for transitions that require high-irradiance pumping, like the Q4L of Nd^{3+} [28, 29, 30], as they further reduce the relatively-low available gain and exacerbate the thermal effects via waste heat deposited during the excitation processes [31]. This heat, on the other hand, worsens the temperature-dependent spectroscopic features for this ion, causing a further decrease in available gain and exacerbating the thermal aberrations already affecting its performance. The negative feedback provided by this dynamics at Room Temperature (RT) can cause a thermal run away, potentially terminating the laser action, or severely limiting it, as we will illustrate in the next section with the state-of-the-art results for this ion. As such, laser performance of Nd-doped lasers operating on the $9xx\ nm$ transition could be improved if key contributors to these effects are well characterised.

1.2 Motivation

Our drive in the pursuit of power-scaling for the Q4L transition of Nd^{3+} is motivated by the advantage that its shorter wavelength, $9xx\ nm$, provides in respect to the longer wavelengths offered by Yb^{3+} or the true four-level transitions of Nd^{3+}. Indeed, it could provide more opportunities for micro-precision material processing in the blue and deeper UV wavelength bands, on top of the biological and underwater applications in the blue spectrum.

In fact, the appealing possibility for these lasers to be frequency-doubled into the blue spectrum has several applications. In material processing blue lasers with wavelengths around 470 nm are the optimal solution to exploiting the higher absorption of several metals, as Fig. 1.3. In fact, with respect to the usually employed IR lasers, the blue wavelength has a 66-times higher absorption in Gold, 13- in Copper, 3- in Aluminium, 1.5- in Nickel and Steel. High-power and high-energy blue lasers would find successful applications in the field of E-mobility, which has substantially developed in the last decade. Electric motors and batteries meant for electric-vehicles require processing of more Copper, Nickel and Lithium with respect to traditional combustion motors, with the Copper materials being foils of only hundreds of microns in size. These are often damaged by the IR sources traditionally employed, as the high energy required to start the welding vaporises the material, which reflects the IR wavelength, leading to spatter and defects. With the blue light, however, the vaporisation process is not initiated, thanks to the higher absorption of Copper in this wavelength, leading to spatter-free

and defect-free welds [32]. Furthermore, the third-harmonic of the 946 *nm* transition of Nd:YAG, at 315 *nm*, corresponds to the absorption peak of Silver, more than 20-times higher with respect to the one in the blue and IR wavelengths. Moreover, it provides almost identical absorption for the other key metals of interest (Au, Cu, Ni) that would provide comparable operating conditions for the laser when processing multi-material products, such different layers in electronic circuits.

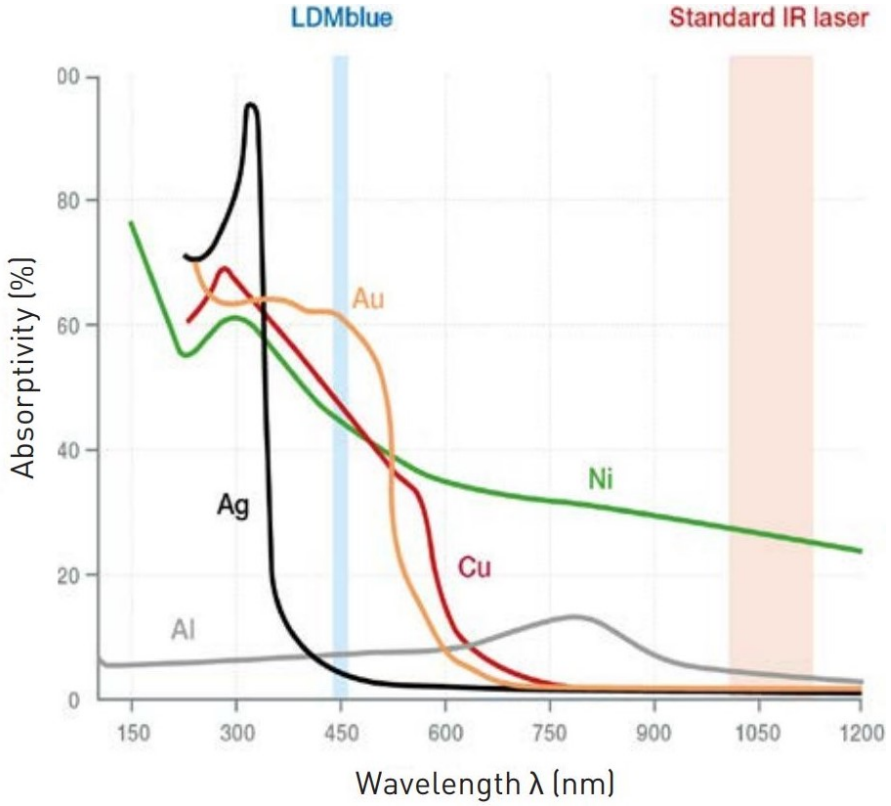

FIGURE 1.3: Absorptivity of several metals, from [33].

A further application benefiting from high-energy blue lasers would be laser shock peening [34], currently employing IR wavelengths and green lasers. This technique has been developed in the last 15 years and uses energetic laser pulses to strengthen and harden the targeted materials, mainly metals. It is exploited especially in the aerospace and nuclear sectors, where it is employed to improve the performance of critical components, such as turbine blades in aircraft and pressurised water reactors. Laser peening is also exploited in the medical field, to strengthen the key parts of prosthetics that are subject to high forces. Adding to the listed advantages of blue over IR, the blue wavelength has a generally higher absorption than the green, the latter also employed in laser peening. For underwater applications, a frequency-doubled 946 *nm* Nd:YAG laser (473 *nm*), would experience a $\sim$ 5% lower loss passing through 1 *m* of water with respect to a frequency doubled 1064 *nm* Nd:YAG laser (532 *nm*) [35], as in Fig. 1.4. This indicates blue lasers as the optimal candidates for the application of laser

peening without coating, where the targeted material is submerged in water, which would minimise the signal loss whilst maximising the absorption into the target metal.

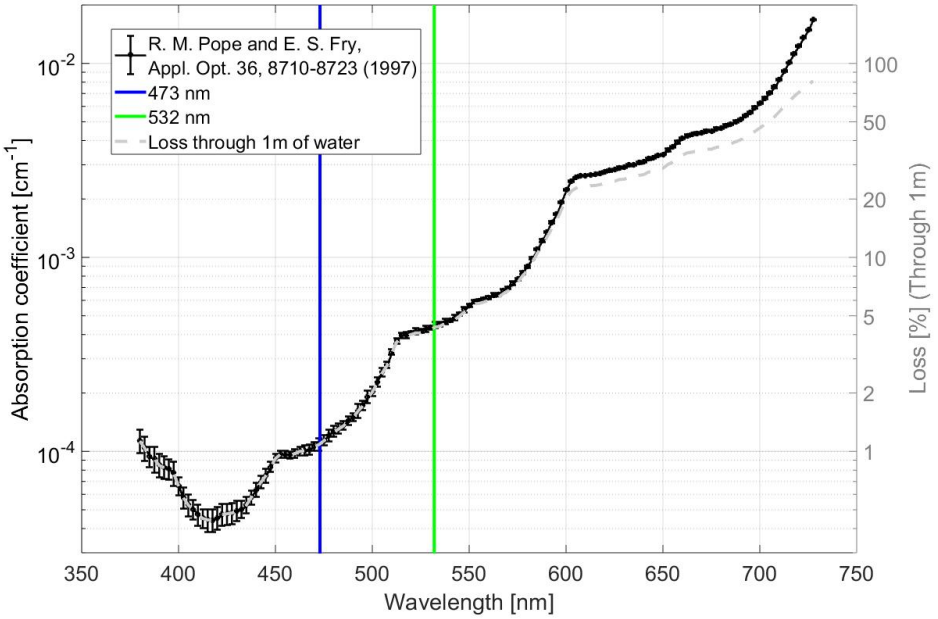

FIGURE 1.4: Water's absorption coefficient (left y-axis) and percentage loss (right y-axis) through 1 m of water for wavelengths in the range [300-700] nm, from [35].

Furthermore, the fourth-harmonic generation of the $9xx$-nm transition into the deep UV would be a wavelength comparable to Excimer lasers', currently employing a potentially harmful element, and used in industrial material processing and eye surgery.
Thanks to cryogenic-cooling of the gain medium, as we will demonstrate in this thesis, the way to the power-scaling of these sub-1 μm lasers is paved, opening new paths towards their numerous applications.

1.3 Background

Over the last 25 years there have been an order of magnitude improvement in the performance of laser-diode pumps, that, together with the development of novel laser architectures, help to mitigate power-scaling limitations, making it possible to reach output powers in the order of the kW [36] with efficiencies as high as 60%. The RT output power of the Q4L Nd^{3+} laser system is primarily constrained by the limits of pump brightness and dynamic thermally-induced losses associated with the crystal and its geometry. Heat generation in the gain medium produces a spatial variation of the temperature that can lead to aberrated thermal lensing and stress-induced birefringence. These affect the beam quality, the threshold pump power and the power of the output

beam, or even cause the fracture of the laser rod [37]. As such, it seems that the performance improvements in recent years for this Q4L laser have saturated. To date, the best demonstrations in laser performance for the ${}^4F_{3/2} \rightarrow {}^4I_{9/2}$ transition of Nd^{3+} in a bulk configuration report 16 W of output power for a rod [38], 34 W for a fiber-rod [39], and 27 W for a fiber-laser [40]. In the thin disk and planar waveguide laser architectures instead, 20 W [41] and 105 W [42] have been achieved, respectively. These demonstrations stand as the room-temperature state-of-the-art for the Q4L sub-1 μm transition of the Nd^{3+} impurity, which as shown in the respective references, is dominantly in the YAG host.
Since the spectroscopic and physical parameters that limit the performance at RT are dramatically improved by cryogenic-cooling, the potential performance enhancement for the aggressively-cooled 946 nm Nd:YAG laser promises to be comparable with that obtained with Yb:YAG lasers, as the first demonstrations suggest [43, 44]. Notwithstanding, there are significant additional technical challenges to address, such as strong gain competition with the dominant ${}^4F_{3/2} \rightarrow {}^4I_{11/2}$ 1 μm transition and a restriction in the Nd^{3+} doping concentration due to enhanced non-radiative decay channels and heating of the host. In power-scaling it became increasingly important to characterise such nonlinear processes, such as ETU and CR, for determining design rule and improved performance models [31, 45]. We will discuss all these aspects in Chapters 3, 5 and 6.

1.4 Thesis layout

This thesis is structured as follows. The next chapter presents the theory underlying the measurements presented in the three subsequent chapters; while the last chapter provides a summary conclusion. Four appendices provide complimentary information to what is presented in the main body of this thesis.

In Chapter 2 we present the basic theory for characterising small-signal absorption, in order to set the scene for the rigorous measurements made on several different active media. The theoretical model for the measurement of ETU is then presented and reviewed. Here, comparison between the previously used time-dependent model and our adopted steady-state approach is given in order to demonstrate the goodness of the latter solution, aimed at decreasing computational time. The definition of quasi-three- and quasi-four-level lasers (respectively, Q3L and Q4L) is introduced, and an analytical formula for the threshold pump power of Q4L including ETU is presented. Here, a Figure-Of-Merit (FOM) for the ETU in Q4L is discussed. Lastly, a laser performance model for Q4L including ETU is reported and discussed.

The following four chapters contain the experimental techniques and results obtained. In Chapter 3 we present the experimental setup employed for small-signal absorption measurements and the general methodology developed to analyse the collected data. We detail how, employing this methodology, we measured the unknown doping-ion concentration of several Nd-doped crystals, the absorption cross section of Nd-doped vanadates at elevated temperatures, and of Nd:YAG at sub-ambient temperatures. These results underpinned the measurement introduced in Chapter 5.
In Chapter 4 we present the characterisation of the spectroscopy of Yb:$LuLiF_4$ in the temperature range (RT-63 K). This crystal, an isomorph of Yb:YLF, though less used, has shown promising performances at RT and could potentially be as successful as Yb:YFL for operation in the cryogenic-cooling regime and on its sub-1 μm wavelength. Firstly, the results for the measurement of the absorption cross section via the same methodology developed in Chapter 3 are presented. Secondly, we introduce and apply the Füchtbauer-Landenburg (F-L) method for measuring the emission cross section in the same temperature regime. Here we introduce a novel methodology for measuring fluorescence spectra free of the pump signal, even when the pump spectrum overlaps the spectrum to be measured. This method works via an ©Arduino-driven synchronisation between the pump pulse and the measurement time. Lastly, we detail the methodology employed for pump-probe gain measurements over the same temperature span and discuss the results, providing possible routes to future improvements for this measurement.
Chapter 5 concerns the ETU coefficient measurements: the automation developed to improve the experimental setup is described, alongside a detailed account of the data collection, uncertainties estimation, and post-processing procedures. The developed automation and data-processing methodology is applicable to any Nd-doped host whose energy level dynamics are suitably described by the theoretical model applied. Results for the ETU coefficient measurements on Nd-doped vanadates and Nd:YAG in the same temperature regimes employed in the absorption cross section characterisation are presented. Finally, we discuss how the measured ETU coefficient would affect the threshold pump power for simple lasers employing the tested crystals in the respective temperature ranges.
Chapter 6 details the power-scaling of the cryogenically cooled 946 nm Nd:YAG laser. To start, we present a novel volume-Bragg-grating (VBG)-locked diode-laser pump that produced a < 0.2 nm linewidth well matched to the cryogenically cooled Nd:YAG's $^4I_{9/2} \rightarrow {}^4F_{3/2}$ 869 nm absorption peak. To follow, two main laser experiments are discussed: the first, resulting in a 60-W laser, and the second, resulting in a >100-W laser, both setting new records at the respective times of demonstration. For each of the lasers introduced, we apply the Q4L laser performance model detailed in Chapter 2 and discuss the respective results, hereby proposing potential improvements.

The last part of the main body of the thesis, Chapter 7, contains the conclusions. We

summarise the results obtained in this work and present potential future paths.

In addition, we complement this work with three appendices. In Appendix A we give an overview on the methodology, employed several times throughout this work, for fitting experimental data to theoretical predictions depending on fitting parameters. To illustrate, we use the fitting of beam caustics to known Gaussian beam propagation formulas to measure the beam quality parameter M^2.
Appendix B provides the modelling parameters employed in Chapter 6 for the application of the laser performance model reported in Chapter 2.
Appendix C lists the publications this thesis is based upon.

References

[1] R. T. H. Collis, "*Lidar,*" Applied Optics **9**, 1782–1788 (1970).

[2] J. Lawrence, *Advances in Laser Materials Processing: Technology, Research and Applications*, Woodhead Publishing Series in Welding and Other Joining Technologies (Elsevier Science, 2017).

[3] https://onlinelibrary.wiley.com/journal/10969101 (2020).

[4] Z. Zeng, S. Fu, H. Zhang, Y. Dong, and J. Cheng, "*A Survey of Underwater Optical Wireless Communications,*" IEEE Communications Surveys Tutorials **19**, 204–238 (2017).

[5] https://www.virgo-gw.eu/ (2020).

[6] https://www.ligo.caltech.edu/ (2020).

[7] R. S. Craxton, K. S. Anderson, T. R. Boehly, V. N. Goncharov, D. R. Harding, J. P. Knauer, R. L. McCrory, P. W. McKenty, D. D. Meyerhofer, J. F. Myatt, A. J. Schmitt, J. D. Sethian, R. W. Short, S. Skupsky, W. Theobald, W. L. Kruer, K. Tanaka, R. Betti, T. J. B. Collins, J. A. Delettrez, S. X. Hu, J. A. Marozas, A. V. Maximov, D. T. Michel, P. B. Radha, S. P. Regan, T. C. Sangster, W. Seka, A. A. Solodov, J. M. Soures, C. Stoeckl, and J. D. Zuegel, "*Direct-drive inertial confinement fusion: A review,*" Physics of Plasmas **22**, 110501 (2015).

[8] T. H. Maiman, "*Stimulated optical radiation in ruby,*" Nature **187**, 493–494 (1960).

[9] P. Crump, J. Wang, T. Crum, S. Das, M. DeVito, W. Dong, J. Farmer, Y. Feng, M. Grimshaw, D. Wise, and S. Zhang, "$>$ 360 *W and* $>$ 70% *efficient GaAs-based diode lasers,*" in *High-Power Diode Laser Technology and Applications III,* vol. 5711 M. S. Zediker, ed., International Society for Optics and Photonics (SPIE, 2005), pp. 21 – 29.

[10] M. Kanskar, T. Earles, T. Goodnough, E. Stiers, D. Botez, and L. J. Mawst, "*High-power conversion efficiency Al-free diode lasers for pumping high-power solid-state laser systems,*" in *Novel In-Plane Semiconductor Lasers IV,* vol. 5738 C. Mermelstein and D. P. Bour, eds., International Society for Optics and Photonics (SPIE, 2005), pp. 47 – 56.

[11] https://www.ipgphotonics.com/en/products/lasers/high-power-cw-fiber-lasers (2020).

[12] M. N. Zervas and C. A. Codemard, "*High Power Fiber Lasers: A Review,*" IEEE Journal of Selected Topics in Quantum Electronics **20**, 219–241 (2014).

[13] https://www.trumpf.com/en_GB/products/laser/disk-lasers/ (2020).

[14] https://www.laserfocusworld.com/lasers-sources/article/16563587/boeing-fires-new-thindisk-laser-at-high-average-power-and-beam-quality.

[15] D. Filgas, T. Clatterbuck, M. Cashen, A. Daniele, S. Hughes, and D. Mordaunt, "*Recent results for the Raytheon RELI program*," in *Laser Technology for Defense and Security VIII*, vol. 8381 (International Society for Optics and Photonics, 2012), p. 83810W.

[16] P. P. Sorokin and M. J. Stevenson, "*Stimulated Infrared Emission from Trivalent Uranium*," Physical Review Letters **5**, 557–559 (1960).

[17] D. C. Brown, "*Ultrahigh-average-power diode-pumped Nd:YAG and Yb:YAG lasers*," IEEE Journal of Selected Topics in Quantum Electronics **33**, 861–873 (1997).

[18] D. C. Brown, "*The promise of cryogenic solid-state lasers*," IEEE Journal of Selected Topics in Quantum Electronics **11**, 587–599 (2005).

[19] T. Y. Fan, D. J. Ripin, R. L. Aggarwal, J. R. Ochoa, B. Chann, M. Tilleman, and J. Spitzberg, "*Cryogenic Yb^{3+}-Doped Solid-State Lasers*," IEEE Journal of Selected Topics in Quantum Electronics **13**, 448–459 (2007).

[20] W. Koechner, *Solid-State Laser Engineering*, Springer Series in Optical Sciences (Springer, 2006).

[21] G. S. Ofelt, "*Intensities of Crystal Spectra of Rare-Earth Ions*," The Journal of Chemical Physics **37**, 511–520 (1962).

[22] B. R. Judd, "*Optical Absorption Intensities of Rare-Earth Ions*," Physical Review **127**, 750–761 (1962).

[23] G. H. Dieke and H. M. Crosswhite, "*The Spectra of the Doubly and Triply Ionized Rare Earths*," Applied Optics **2**, 675–686 (1963).

[24] P. F. Moulton, "*Spectroscopic and laser characteristics of Ti:Al2O3*," Journal of the Optical Society of America B **3**, 125–133 (1986).

[25] D. C. Brown, J. M. Singley, K. Kowalewski, J. Guelzow, and V. Vitali, "*High sustained average power cw and ultrafast Yb:YAG near-diffraction-limited cryogenic solid-state laser*," Optics Express **18**, 24770–24792 (2010).

[26] D. C. Brown, S. Tornegård, J. Kolis, C. McMillen, C. Moore, L. Sanjeewa, and C. Hancock, "*The Application of Cryogenic Laser Physics to the Development of High Average Power Ultra-Short Pulse Lasers*," Applied Sciences **6** (2016).

[27] T. Morioka, K. Hamamoto, S. Nishikata, N. Inoue, Y. Ohtani, H. Ikebuchi, and H. Daigo, "*High power zig-zag active-mirror laser amplifier with jet impingement cooling*," in *Proc. SPIE*, (2019), p. 1089619.

[28] R. J. Beach, "*CW Theory of quasi-three level end-pumped laser oscillators,*" Optics Communications **123**, 385 – 393 (1996).

[29] W. P. Risk, "*Modeling of longitudinally pumped solid-state lasers exhibiting reabsorption losses,*" Journal of the Optical Society of America B **5**, 1412–1423 (1988).

[30] T. Y. Fan and R. L. Byer, "*Modeling and CW operation of a quasi-three-level 946 nm Nd: YAG laser,*" IEEE Journal of Quantum Electronics **23**, 605–612 (1987).

[31] S. Bjurshagen and R. Koch, "*Modeling of energy-transfer upconversion and thermal effects in end-pumped quasi-three-level lasers,*" Applied Optics **43**, 4753–4767 (2004).

[32] M. Hummel, C. SchÃ¶ler, A. HÃusler, A. Gillner, and R. Poprawe, "*New approaches on laser micro welding of copper by using a laser beam source with a wavelength of 450Â nm,*" Journal of Advanced Joining Processes **1**, 100012 (2020).

[33] https://www.osa-opn.org/home/articles/volume_31/october_2020/features/high-powered_diode_lasers%E2%80%94new_bright_and_blue/.

[34] K. Ding and L. Ye, "*2 - Physical and mechanical mechanisms of laser shock peening,*" in *Laser Shock Peening*, K. Ding and L. Ye, eds. (Woodhead Publishing, 2006), Woodhead Publishing Series in Metals and Surface Engineering, pp. 7–46.

[35] R. M. Pope and E. S. Fry, "*Absorption spectrum (380–700 nm) of pure water. II. Integrating cavity measurements,*" Appl. Opt. **36**, 8710–8723 (1997).

[36] G. Huber, C. Kränkel, and K. Petermann, "*Solid-state lasers: status and future,*" (Invited) Journal of the Optical Society of America B **27**, B93–B105 (2010).

[37] W. A. Clarkson, "*Thermal effects and their mitigation in end-pumped solid-state lasers,*" Journal of Physics D: Applied Physics **34**, 2381–2395 (2001).

[38] R. Zhou, E. Li, H. Li, P. Wang, and J. Yao, "*Continuous-wave, 15.2 W diode-end-pumped Nd:YAG laser operating at 946 nm,*" Optics Letters **31**, 1869–1871 (2006).

[39] X. Délen, I. Martial, J. Didierjean, N. Aubry, D. Sangla, F. Balembois, and P. Georges, "*34 W continuous wave Nd:YAG single crystal fiber laser emitting at 946 nm,*" Applied Physics B **104**, 1 (2011).

[40] P. H. Pax, V. V. Khitrov, D. R. Drachenberg, G. S. Allen, B. Ward, M. Dubinskii, M. J. Messerly, and J. W. Dawson, "*Scalable waveguide design for three-level operation in Neodymium doped fiber laser,*" Optics Express **24**, 28633–28647 (2016).

[41] J. Gao, J. Speiser, and A. Giesen, "*25-W diode-pumped continuous-wave quasi-three-level Nd:YAG thin disk laser,*" in *Advanced Solid-State Photonics*, (Optical Society of America, 2005), p. TuB34.

[42] S. P. Ng and J. I. Mackenzie, "*Power and radiance scaling of a 946 nm Nd:YAG planar waveguide laser,*" Laser Physics **22**, 494–498 (2012).

[43] S. J. Yoon and J. I. Mackenzie, "*Cryogenically cooled 946nm Nd:YAG laser,*" Optics Express **22**, 8069–8075 (2014).

[44] C. Y. Cho, T. L. Huang, H. P. Cheng, K. F. Huang, and Y. F. Chen, "*Analysis of the optimal temperature for the cryogenic monolithic Nd:YAG laser at 946-nm,*" Optics Express **24**, 1–8 (2016).

[45] S. J. Yoon, R. P. Yan, S. J. Beecher, and J. I. Mackenzie, "*Concentration dependence of energy transfer upconversion in Nd:YAG,*" Optical Materials Express **5**, 926–931 (2015).

Chapter 2

Theory

2.1 Introduction

In this chapter we present the theoretical background underpinning the experimental methods we will detail in the successive chapters of this thesis. In the next Section we introduce Beer-Lambert law, describing small-signal transmission measurements, upon which the characterisation of spectroscopic properties such as the doping-ion concentration and the absorption cross section of Nd-doped crystals are based. In Section 2.3 we discuss the ETU effect and how to quantify it, in the form of a macroscopic ETU coefficient. We detail the fundamentals of Quasi-Four-Level (Q4L) laser operation in Section 2.4, where we refer to a Figure-of-Merit (FOM) and a simple analytical formula to estimate the threshold pump power for a Q4L laser including the parasitic effect of ETU, developed by Kim et. al. in [1]. Additionally, we also discuss the laser performance model including ETU described by Bjurshagen and Koch in [2], which we employed throughout this work to estimate laser performance and have a deeper insight into the laser operation when cryogenic-cooling the gain element, the main subject of this thesis.

2.2 Absorption measurements

The absorption cross section, $\sigma_{abs}(\lambda)$, and the doping-ion concentration, $C_{\%}$, of laser crystals are key parameters required for simulating the laser performance. They both determine the pump absorption rate, and hence the level of population inversion achieved for a certain pump intensity distribution. A suitable choice of these parameters, and particularly of their product, determines the heat load in the pumped region via the radiation absorbed over the crystal length, and consequently plays an important role in the overall laser efficiency. In light of these observations, it is paramount to determine these quantities with precision. In this section, we present a simple yet efficient way

of characterising the doping-ion concentration of any Nd-doped host, if its absorption cross section spectrum is known. Inversely, the measurement of the absorption cross section is possible, when the doping-ion concentration is known. Both these measurements are based on the application of the Beer-Lambert law to small-signal absorption spectroscopy, as detailed below.
Beer-Lambert law describes how light is absorbed as it propagates inside a material:

$$I_{out}(\lambda) = I_{in}(\lambda)\, e^{-\alpha_{abs}(\lambda) l_r} = I_{in}(\lambda)\, e^{-\sigma_{abs}(\lambda) C_{\%} N_0 l_r} \tag{2.1}$$

where $I_{in}(\lambda)$ is the pump-laser initial intensity, $I_{out}(\lambda)$ is the transmitted intensity, $\alpha_{abs}(\lambda)$ is the absorption coefficient per unit length, $\sigma_{abs}(\lambda)$ is the absorption cross section, l_r is the length of the crystal, $C_{\%}$ the doping-ion concentration, with N_0 the density of doping-ions for 1at.%-doping.
Inverting Eq. (2.1) we have

$$\frac{\alpha_{abs}(\lambda)}{N_0} = \sigma_{abs}(\lambda) C_{\%} = \frac{\ln(\frac{I_{in}(\lambda)}{I_{out}(\lambda)})}{N_0 l_r} = \frac{A(\lambda)}{N_0 l_r} \tag{2.2}$$

In this form, we can easily apply Eq. (2.2) to obtain either the absorption cross section $\sigma_{abs}(\lambda)$ or the doping-ion concentration $C_{\%}$, by measuring the absorption spectrum $A(\lambda)$. We discuss both cases in detail in Chapter 3.
To determine the optical absorption in our sample we recorded the input, $P_{in}(\lambda)$, and the transmitted, $P_{out}(\lambda)$, spectral power distributions of the pump source, with an Optical Spectrum Analyser (OSA). The measured quantities, $P_{in}(\lambda)$ and $P_{out}(\lambda)$ are proportional to, respectively, $I_{in}(\lambda)$ and $I_{out}(\lambda)$ via the irradiated surfaces S_{in} and S_{out}. Given our experimental conditions, detailed in Chapter 3, that the beam size doesn't vary significantly over the crystal length ($l_r < b$, with l_r typically less than 10 mm and $b = 2z_R$ with z_R the Rayleigh range of the pump), $S_{in} = S_{out} = S$, the equivalence (2.3) could be employed.

$$\frac{I_{in}(\lambda)}{I_{out}(\lambda)} = \frac{P_{in}(\lambda)}{P_{out}(\lambda)} \tag{2.3}$$

In our analysis, we distinguished between the intensity $I_{in/out}(\lambda)$ inside the sample facets, and the measured intensity (powers, thanks to Eq. (2.3)) $I_{in/out_{meas}}(\lambda)$ outside the sample facets. These two quantities are related via the transmission (or losses), $T_{in/out}(\lambda)$, at the respective interfaces with air, through the following:

$$I_{in}(\lambda) = I_{in_{meas}}(\lambda) T(\lambda) \tag{2.4a}$$

$$I_{out}(\lambda) = \frac{I_{out_{meas}}(\lambda)}{T(\lambda)} \tag{2.4b}$$

Where we have assumed, for simplicity, that $T_{in}(\lambda) = T_{out}(\lambda) = T(\lambda)$ is the transmission of the facets over the spectral power distribution. This $T(\lambda)$ could be due to Fresnel losses, as well as spectral response of anti-reflection coatings, when they are in place.

For the scope of this analysis, the nature of this loss is not particularly relevant; we will in fact demonstrate below that the broadband losses at the interfaces of the sample can be quantified and corrected for. In Section 3.2 we will detail how we account for these distributed losses in the samples.
The measured absorption spectrum is given by

$$A^*(\lambda) = ln\left(\frac{I_{in_{meas}}(\lambda)}{I_{out_{meas}}(\lambda)}\right) \tag{2.5}$$

If we use Eqs. (2.4) in Eq. (2.5), we obtain

$$A^*(\lambda) = ln\left(\frac{I_{in_{meas}}(\lambda)}{I_{out_{meas}}(\lambda)}\right) = ln\left(\frac{I_{in}(\lambda)T(\lambda)}{I_{out}(\lambda)/T(\lambda)}\right) = \tag{2.6a}$$

$$= ln\left(\frac{I_{in}(\lambda)}{I_{out}(\lambda)}\right) + ln\left(T(\lambda)^2\right) = A(\lambda) + ln\left(T(\lambda)^2\right) = \tag{2.6b}$$

$$= A(\lambda) + L_{BB(\lambda)} \tag{2.6c}$$

Where L_{BB} are the broadband losses discussed above.
In Eq. (2.6) we have shown that any kind of broadband loss, L_{BB}, that doesn't comprise the crystal absorption, i.e. doesn't depend on the absorption cross section, can be detected as an additional term to the absorption spectrum $A(\lambda)$, which we ultimately want to retrieve. A methodology to obtain $A(\lambda)$ from the measured $A^*(\lambda)$ will be presented in Chapter 3.
Once $A(\lambda)$ is known, and recalling Eq. (2.2), we calculate either the absorption cross section or the doping-ion concentration of the sample tested via the methods described in Chapter 3.

2.3 Energy Transfer Upconversion

The energy stored in an excited doping-ion can be transformed into radiation via an optical transition from the excited energy state to a lower one, or, via non-radiative channels, dissipated in the form of a phonon. In the latter case the energy can be transferred from one ion to another identical ion, or, in the cases of samples doped with different impurity species (i.e. different doping-ions), from one species to another.
In some cases, these energy-transfer processes, e.g. Energy Transfer Upconversion (ETU) and Cross Relaxation (CR), can be exploited to improve laser efficiency: this is the case of, for example, the $\sim 3\ \mu m$ operation of Er^+ ions, where the ETU and CR processes occurring on a metastable excited state are exploited to pump a higher energy level that has about double the energy of the pump [3, 4, 5]. Tm-doped media pumped at $\sim 790\ nm$ take advantage of the CR process to increase the excited state population, leading to power-scaling the $2\ \mu m$ transition exploited [6, 7, 8]. Generally, however, ETU and CR are detrimental to laser performance because they constitute an extra source of

heat, and, as detailed below, especially in the cases of low-gain sub-1 μm transition of Nd-doped hosts, treated in this thesis.

For the Nd trivalent impurity in a host medium the ETU process involves the interaction of two neighboring ions, i.e. two Nd^{3+} ions located close enough to interact within the crystal lattice, both in an excited meta-stable energy level (e.g. $^4F_{3/2}$): one of them is de-excited to a lower energy level ($^4I_{15/2}$, $^4I_{13/2}$, $^4I_{11/2}$), while the other is excited to a higher energy level ($^4G_{5/2}$, $^4G_{7/2}$, $^2G_{9/2}$). For most Nd-doped hosts the excited ion then relaxes back to the $^4F_{3/2}$ level, thus reducing the upper laser level population by one [2]. In the CR process two ions, one in a excited state, the other in a lower energy level, exchange energy: the first is de-excited and the second is excited to an intermediate energy level. In both ETU and CR waste heat is produced via the non-radiative decay channels of both the ions. Fig. 2.1 shows various energy transfer processes, including ETU, CR and non-radiative processes occurring in the Nd^{3+} energy system that generate heat (indicated by arrows with a red background).

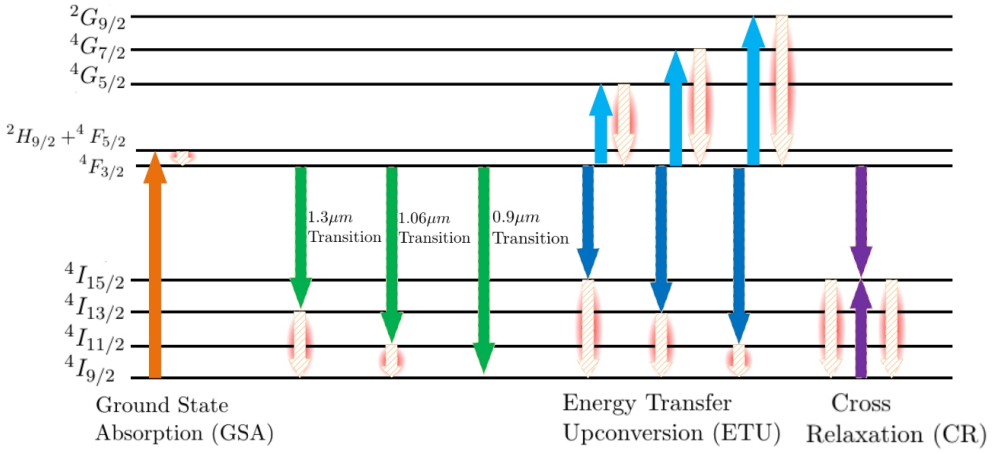

FIGURE 2.1: Schematics of the Nd^{3+} Energy levels (not to scale) and possible transitions and energy-transfer processes. Orange arrow: Ground State Absorption (GSA); green: laser transitions; blue: ETU; purple: CR.

ETU and CR are particularly deleterious for transitions that require high-intensity pumping to reach threshold, as they reduce the already relatively low achievable gain and add to the heat generated by the QD, which is usually the main source of heat in a generic laser system. They are ultimately undesirable effects that are necessary to account for when designing and optimising low-gain systems.

The strength of ETU is driven by several factors like the ion-density, i.e. the intra-ion distance, spectroscopic properties and structure of the doped gain medium. The literature is populated by various models that account for the microscopic interactions between neighbouring ions, and distinguish between different kinds of donor-acceptor energy-trasfer dynamics [9, 10, 11]. On a macroscopic-scale, however, ETU can be conveniently described by a single macro-parameter: W_{ETU}. The latter is the coefficient we measure via a simple z-scan technique.

The z-scan technique has been previously employed to determine the magnitude of the ETU coefficient for various rare-earth ions in different host media [12, 13, 14, 15]. It consists in scanning the sample through the waist of a converging/diverging pump beam, thus enabling the control of the input intensity, from values significantly lower than (small-signal transmission regime) to ones comparable to, or higher than, the saturation intensity. The transmission through the sample with respect to each z-scan position (intensity) is compared to the predictions of the spatially dependent two-level rate-equation model (2.7).

$$\frac{dN_1(r,z)}{dt} = -\frac{I_p(r,z)}{h\nu_p}\sigma_{abs}N_1(r,z) + \frac{N_2(r,z)}{\tau_0} + W_{ETU}N_2(r,z)^2 + W_{CR}N_1(r,z)N_2(r,z) \tag{2.7a}$$

$$\frac{dN_2(r,z)}{dt} = \frac{I_p(r,z)}{h\nu_p}\sigma_{abs}N_1(r,z) - \frac{N_2(r,z)}{\tau_0} - W_{ETU}N_2(r,z)^2 - W_{CR}N_1(r,z)N_2(r,z) \tag{2.7b}$$

$$\frac{dI_p(r,z)}{dz} = -\sigma_{abs}N_1(r,z)I_p(r,z) \tag{2.7c}$$

Where, with reference to Fig. 2.1, for the neodymium-doped host $N_1(r,z)$ is the population density of the ground state ${}^4I_{9/2}$, $N_2(r,z)$ is the population density of the excited state ${}^4F_{3/2}$, σ_{abs} is the measured effective absorption cross section at the pump photon energy $h\nu_p$, W_{CR} is the CR macroparameter, τ_0 is the intrinsic lifetime of the excited state, and W_{ETU} is the macroscopic ETU coefficient to be determined. The CR coefficient can be determined via the measurement of the fluorescence lifetime (τ_f) at weak excitation densities compared to the known intrinsic lifetime (τ_0) of the crystal being probed, as per the method previously used by Yoon in [14]. Where the parameter τ_0 is not known, the term $\frac{N_2(r,z)}{\tau_f}$ can be employed in place of the terms proportional to τ_0 and W_{CR}, accounting for both the intrinsic lifetime of the sample in question and the cross relaxation rate [16]. $I_p(r,z)$ is the spatial distribution of the pump intensity that changes according to (2.7c). To illustrate, we present in Fig. 2.2 the on-axis ($r = 0$) solution of model (2.7) for $N_1(r = 0, z, t)$ calculated at the first facet of a 1 mm-long, 1at.%-doped Nd:YAG crystal probed by a 200 mW pump with a waist of 20 μm. The solution was computed for each step of a 100 mm-long z-scan with, $z = -50$ mm the (arbitrary) starting coordinate and $z = 50$ mm the end coordinate. As Fig. 2.2 shows, the ground state population N_1 has an initial value of N_{tot}, which is increasingly depleted as the incident intensity becomes higher, i.e. the z-scan coordinate approaches $z = 0$ mm (high-irradiance regime). The transient time between the start of the pump pulse $t = 0$ s and the N_1 population reaching steady-state also becomes faster, compared to the 1 ms pulse length, as the pump intensity increases.

Model (2.7), as presented, emphasises the ETU process and the temporal dependence of the latter, however several papers from our group [17, 14, 15] have confirmed the

goodness of this description through the comparison of the temporal simulated waveforms to the measured ones. Therefore, we chose to optimise the computational time of the simulation by removing the temporal dependence of Eqs. (2.7) and, instead, increasing the density of the grid used for the iterative calculation (300 radial and 1000 longitudinal steps) by assuming steady-state conditions for the population densities, $dN_i/dt = 0 \;\; (i = 1, 2)$. With these updates, the execution time of the code decreased from $\sim$ 4 minutes to under 2 seconds, a $>$ 100x improvement.

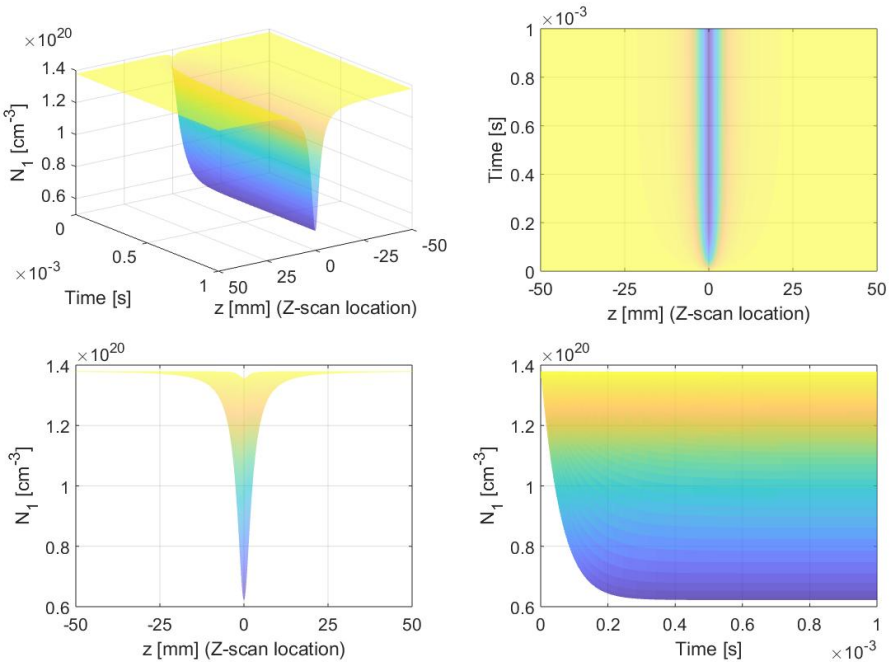

FIGURE 2.2: 3-D plot and respective surface maps of the on-axis time-dependent solution for a 100 mm-long z-scan of a 1 mm-long, 1at.%-doped Nd:YAG crystal probed by a 200 mW pump.

The steady-state conditions are satisfied if the duration of the light pulse is long enough for the populations to reach steady-state and short enough to avoid a localised temperature increase due to the non-radiative decay of the absorbed power transferring to the host lattice: these requirements were met by the $\sim$ 1 ms pulse we employed. This potential temperature increase depends upon the thermal and spectroscopic properties of the host medium: we estimated that the above conditions were satisfied for all the samples investigated, except for one case presented in Section 5.4.2. Using the steady-state conditions and (2.8a), N_1 is obtained from the simple analytical solution of (2.7), presented in (2.8b).

At the end of the iteration steps the transmitted intensity $I_t(r, z)$ is integrated over the effective beam area in order to obtain the theoretical transmitted pump power P_t, to compare the simulated transmittance, $T_{th} = P_t/P_{in}$, with the measured one. The automated data collection, described in detail in Chapter 5, enabled the minimisation of the uncertainty associated with the fixed parameters of model (2.7). In order to verify the

goodness of the steady-state assumption, we compared the solutions obtained by solving system (2.7) for steady-state conditions, employing (2.8), and the time-dependent (2.7), where we set the pulse length to $\tau_{pulse} = 1\ ms$.

$$N_2(r,z) = N_{tot} - N_1(r,z) \tag{2.8a}$$

$$N_1(r,z) = \frac{-b \pm \sqrt{b^2 - 4ac}}{2a} \tag{2.8b}$$

$$a = W_{ETU} - W_{CR}$$

$$b = \frac{I_p(r,z)}{h\nu_p}\sigma_{abs} - \frac{1}{\tau_0} - 2W_{ETU}N_{tot}$$

$$c = \frac{N_{tot}}{\tau_0} + W_{ETU}N_{tot}^2 + W_{CR}N_{tot}$$

To demonstrate how we verified that the steady-state solution to Eqs. (2.7) produced results in agreements with the time-dependent ones, we computed both solutions and compared as follows. Fig. 2.3 shows the comparison between the two different approaches for the same z-scan as detailed above. Here, too, the solutions were calculated on-axis at the first facet of the sample. The z-scan locations chosen are $z = (0, 10, 50)\ mm$ because these are representative of high(est)- and low(est)-intensity regimes ($z = (0, 50)\ mm$) and transition between the two ($z = 10\ mm$). Note that in our modelling and choice of reference system the solutions are symmetrical around $z = 0\ mm$.

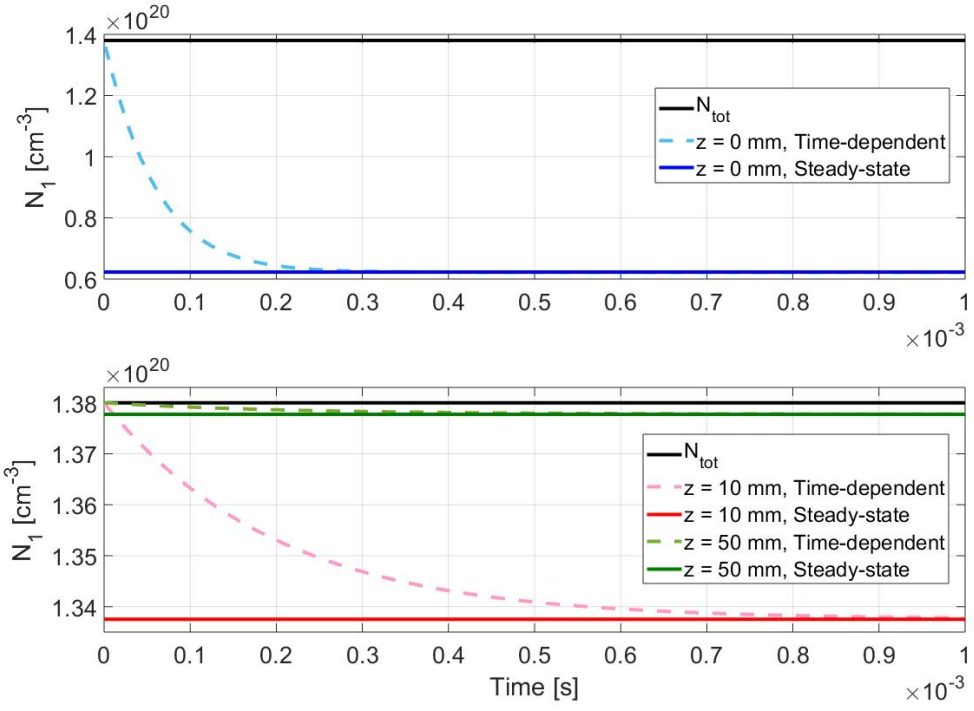

FIGURE 2.3: Comparison between on-axis numerical (solid lines) and steady-state (dashed lines) solutions, at three different locations of a 100 mm-long z-scan, for a 1 mm-long, 1at.%-doped Nd:YAG probed by a 200 mW pump. The coordinates $z = (0, 50, 10)\ mm$ are indicative of high-intensity, small-signal transmission, and transition between these two regimes, respectively.

In the case of highest irradiance, corresponding to $z = 0\ mm$, the time-dependent approaches the steady-state solution within 0.3 s (top plot, blue curves). In the low-irradiance regime (bottom plot, green curves) the populuation inversion in negligible by definition, hence even if our approximation didn't exactly match the time-dependent solution, this discrepancy would be negligible. In the transition regime, $\sim z = 10\ mm$, the time-dependent takes as long as $\sim 0.9\ ms$, nearly the pump pulse length, to match the steady-state solution: in this situation, the approximation needs to be carefully evaluated. In order to gauge the exact discrepancy between the two solutions, we computed the percentual difference between them, shown in Fig. 2.4, where we compared the N_1 value calculated at the end of the pump-pulse to the steady-state solution for N_1.

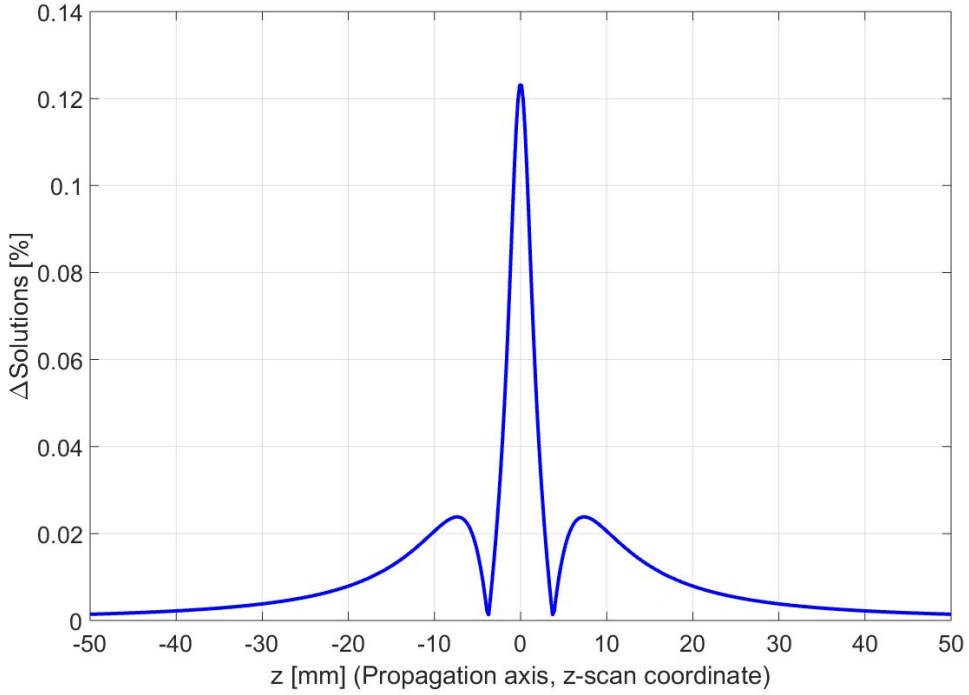

FIGURE 2.4: Comparison between time-dependent and steady-state solutions for a 100 mm-long z-scan of a 1 mm-long, 1at.%-doped Nd:YAG crystal probed by a 200 mW pump.

This calculation reveals two key facts. Firstly, and most importantly, the absolute percentual difference between the steady-state and the time-dependent solutions is overall within 0.002% and 0.12%, which is negligible with respect to the experimental uncertainty associated to the measurement, as we will detail in Chapter 5; this result by itself is enough to conclude that our approximation is valid. Secondly, as opposed to what Fig. 2.3 suggests, the area of maximum (still negligible!) discrepancy between the two solutions is around the maximum transmission, i.e. high-irradiance regime. Furthermore, having the calculation been executed on-axis, $z = 0\ mm$ also corresponds to the maximum irradiance value employed within the entire simulation, hence, in this case, the worst case scenario, still well within the experimental uncertainty. The

quantity reported in Fig. 2.4, the percentual difference between the two approaches, was computed employing different values of time-steps in order to make sure that the time resolution of the time-dependent simulation was not spoiling the final population inversion value; however the same result were obtained regardless of the time resolution employed.
Additionally, we found negligible difference in the transmission curves simulated by solving model (2.7) in the time-dependent compared to the steady-state regime: the percentual difference between the two solutions over the entire length of a 100 *mm*-long z-scan was between 0.006% and 0.2%, as shown in Fig. 2.5. We obtained equivalent results for simulations involving the other Nd-doped crystals. This result provided further proof of the applicability of Eqs. (2.8) under the conditions stipulated.

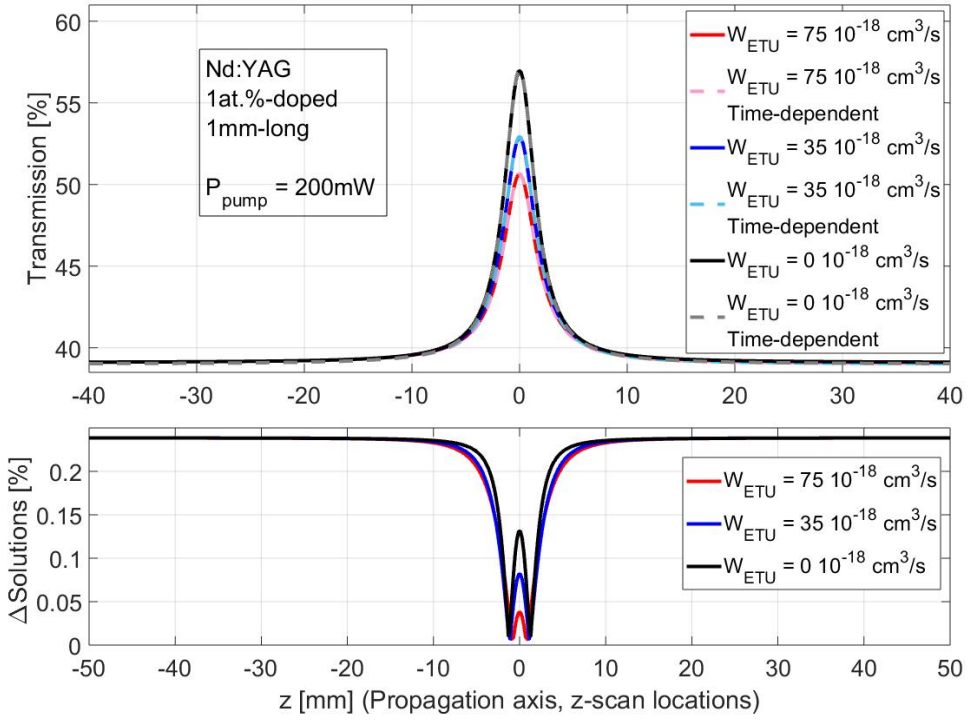

FIGURE 2.5: Top plot: simulated transmission curves for different W_{ETU} values, and comparison between time-dependent and steady-state solutions for a 1 *mm*-long, 1at.%-doped Nd:YAG probed by a 200 *mW* pump. Bottom plot: percentual difference between time-dependent and steady-state solutions for the same values of W_{ETU} as the top plot.

Automated measurements of the pump laser's M^2-parameter were employed to characterise the beam size at each position of the scan, and to infer the pump's beam size's variation through the setup. Once the multi-mode beam waist W_0 at the crystal position and the M^2 are known, the beam size $W(z)$ with respect to the waist position is given by

$$W(z) = W_0 \sqrt{1 + \frac{z^2}{z_R^2}} \tag{2.9}$$

where z_R is the Rayleigh range of the beam, $z_R = \frac{\pi W_0^2}{M^2 \lambda}$.
The pump intensity distribution is then defined as

$$I_p(r,z) = T_{facet_1} \frac{P_{in}}{\pi W(z)^2} e^{-\frac{2r^2}{W(z)^2}} \tag{2.10}$$

where r is the radial position with respect to the propagation axis, $W(z)$ is the beam size at the particular step (z-position) of the z-scan given by Eq. (2.9), T_{facet_1} is the transmittance of the first facet of the sample, and P_{in} is the incident power on the first facet of the sample.
An important assumption of the model is that the pump's beam size $W(z)$ doesn't vary significantly through the sample, which translates into the condition that $l_r < 2z_R$, always verified in the measurements executed, and described in Chapter 5. Despite this condition being satisfied, to be accurate we define an effective beam area averaged over the crystal length, whilst accounting for the z-scan position z:

$$A_{eff}(z) = \frac{\pi}{l_r} \int_z^{z+l_r} W^2(\zeta) d\zeta \tag{2.11}$$

At each step of the z-scan a radial grid of radii in the range from $r = \left(0 - 4\sqrt{A_{eff}(z)/\pi}\right)$ was defined. The pump intensity propagation was calculated by numerically solving the system of equations (2.7) for a fixed power P_{in}, measured beam dimensions, and by iteratively calculating the variation of $I_p(r,z)$, accounting for the intensity distribution and its dependence upon $N_1(r,z)$.
At the point of highest pump intensity, corresponding to the smallest beam radius as per Eq. (2.10), the pump transmission is lower than it would be in the case with $W_{ETU} = 0$, i.e. accounting solely for the saturation of the ground state (see Fig. 2.5): this is due to ETU countering ground state bleaching.
An additional energy-level process that depopulates the upper laser level is the amplification through stimulated emission of spontaneously generated photons, or more commonly referred to as Amplified Spontaneous Emission. Therefore, photons generated by spontaneous emission via the channels ${}^4F_{3/2} \rightarrow {}^4I_{15/2}$, ${}^4F_{3/2} \rightarrow {}^4I_{13/2}$, ${}^4F_{3/2} \rightarrow {}^4I_{11/2}$, ${}^4F_{3/2} \rightarrow {}^4I_{9/2}$, that can propagate through the excited region of the crystal, potentially stimulate the de-excitation of neighbouring excited ions. Consequently, depopulating the upper laser level and therein amplifying the spontaneously emitted photon number according to the available gain at the respective wavelengths corresponding to each transition.
For a spatial intensity distribution of the spontaneous emission, $I_{ASE}(r,z,\lambda_j)$ at a photon energy $h\nu_{j,ASE}$, the wavelength-dependent ASE rate, $\frac{I_{ASE}(r,z,\lambda_j)}{h\nu_{j,ASE}} \sigma_e(\lambda_j) N_2(r,z)$, is proportional to the effective emission cross section $\sigma_e(\lambda_j)$ at the emission wavelength λ_j, and population inversion $N_2(r,z)$. The total ASE rate is the sum of each wavelength-dependent term associated with the respective transitions.

$I_{ASE}(r,z)$ could potentially become of comparable magnitude to $I_p(r,z)$ if the appropriate conditions exist, i.e. a long enough crystal length with sufficient population inversion distribution (gain). In order to gauge the magnitude of the ASE intensity with respect to the saturation intensity, a "worst-case-scenario" case for the end-pumped configuration employed in the ETU coefficient measurement can be employed. We can suppose the population inversion distribution $N_2(r,z)$ does not depend on the spatial coordinate (r,z) and hence has a constant value throughout the crystal length and across the pumped region. This population inversion can be fixed to the maximum value it will assume throughout a single z-scan, according the different experimental conditions (i.e. crystals probed and respective temperature regimes) described in the following sections. Accordingly, the crystal length, l_r is fixed to either 1 mm or 5 mm, and the emission cross section to the appropriate value at 1.06 μm, the dominant emission transition. Therefore, we obtain

$$I_{ASE} = I_{ASE,0}\, e^{\sigma_e N_2 l_r} \tag{2.12}$$

and using this we have that

$$\frac{I_{ASE}}{I_{ASE,0}} = e^{\sigma_e N_2 l_r} = G_0 \tag{2.13}$$

which is the well-known equation for the small-signal gain (in linear units) of a probe passing through a l_r-long medium with stimulated emission cross section σ_e and population inversion N_2, as given in [18]. A spontaneously emitted photon at the center of the pump beam at one facet would see a solid angle defined by the pumped volume of $\Omega = A_{cr}/l_r^2$ [19, Chapter 4], where A_{cr} is the pumped area at the first facet of the crystal, equal to $A_{eff}(z)$ calculated above. This would result in the ratio between the intensity of the ASE, I_{ASE}, and the saturation intensity at the wavelength of the ASE, I_{Sat}, of $I_{ASE}/I_{Sat} = (\Omega/4)\, G_0/\sqrt{(\ln G_0)}$ [19, Chapter 4].
By executing this calculation for the different kinds of crystals tested under the respective conditions, we obtained ratios of I_{ASE}/I_{Sat} between 0.04 and 0.10, i.e. the intensity of the ASE is between 4% and 10% the saturation intensity. Because these percentages could potentially be significant, we have computed full z-scan simulations including the effects of the ASE at 1 μm for the respective cases (discussed in the relevant sections), to completely rule out the potential significant role of this effect in depopulating the upper laser level and hence compromising the measurement of the ETU macroparameter, where ETU and CR are assumed to be the dominant upper-state-depopulation mechanisms.
In order to account for the evolution of the intensity distribution $I_{ASE}(r,z,\lambda_j)$, the set of

equations (2.7) are augmented, obtaining the following:

$$\frac{dN_1(r,z)}{dt} = -\frac{I_p(r,z)}{h\nu_p}\sigma_{abs}N_1(r,z) + \frac{N_2(r,z)}{\tau_0} + W_{ETU}N_2(r,z)^2 + \\ + W_{CR}N_1(r,z)N_2(r,z) + \sum_4^{j=1}\frac{I_{ASE}(r,z,\lambda_j)}{h\nu_{j,ASE}}\sigma_e(\lambda_j)N_2(r,z) \tag{2.14a}$$

$$\frac{dN_2(r,z)}{dt} = \frac{I_p(r,z)}{h\nu_p}\sigma_{abs}N_1(r,z) - \frac{N_2(r,z)}{\tau_0} - W_{ETU}N_2(r,z)^2 + \\ - W_{CR}N_1(r,z)N_2(r,z) - \sum_4^{j=1}\frac{I_{ASE}(r,z,\lambda_j)}{h\nu_{j,ASE}}\sigma_e(\lambda_j)N_2(r,z) \tag{2.14b}$$

$$\frac{dI_p(r,z)}{dz} = -\sigma_{abs}N_1(r,z)I_p(r,z) \tag{2.14c}$$

$$\frac{dI_{ASE}(r,z,\lambda_j)}{dz} = \sigma_e(\lambda_j)N_2(r,z)I_{ASE}(r,z,\lambda_j) + \frac{N_2(r,z)BR_{ASE_j}h\nu_{j,ASE}\Delta\Omega}{\tau_f} \tag{2.14d}$$

Where the term $\sum_4^{j=1}\frac{I_{ASE}(r,z,\lambda_j)}{h\nu_{j,ASE}}\sigma_e(\lambda_j)N_2(r,z)$ was added to Eq. (2.7a) and subtracted from Eq. (2.7b), and Eq. (2.14d) indicates that the wavelength-dependent intensity of the ASE builds up along the crystal length, via the proportionality with the emission cross section and the population inversion distribution, and is increased by the spontaneous emission term moderated by the solid angle into which spontaneously emitted photons may be emitted. This solid angle is given by $\Delta\Omega = 1/(4\pi)2\pi(1-(l_r-l)/\sqrt{(l_r-l)^2+r^2})$ where l and r are the coordinate along the crystal and the radial coordinate, respectively. Although the ASE rate is the sum over all the possible ASE transitions, j, in this analysis we consider the dominant emission peak of the transition ${}^4F_{3/2} \rightarrow {}^4I_{11/2}$ at 1.06 μm, as it has the highest cross section with respect to the other decay channels. In Sec. 5.4 we demonstrate that, considering the geometry of the ETU setup, ASE has a negligible effect on the ETU coefficient measurement we performed; therefore, we conclude that extending the discussion to include the additional, weaker, transitions would not be significant. In this case, the dependence on the particular transition j can be eliminated from system of Eqs. (2.14), and $\lambda = 1.06\ \mu m$, i.e. the wavelength of the dominant ASE transition ${}^4F_{3/2} \rightarrow {}^4I_{11/2}$.

In this analysis it is essential to consider the initial value for I_{ASE}, i.e. the boundary condition at the front facet of the crystal assuming a trajectory along the pump propagation axis, at each step of the z-scan. In order to estimate this value, we have executed a simple z-dependent calculation, also illustrated in Fig. 2.6. The initial power of the ASE is given by the photon flux, Φ, multiplied by the photon energy $E_{ASE} = h\nu$. We have estimated the photon flux to be $\Phi = N_{2,max}(z)A_{eff}(z)\Delta l \cdot BR_{ASE}\Delta\Omega/\tau_f$, where $N_{2,max}(z)$ is the maximum inversion achieved at the z-step evaluated, i.e. at the first facet of the sample, before accounting for ASE. As such, this initial value is therefore an overestimation of the inversion reached when ASE takes place; however a lower inversion would make the ASE less significant, and hence this approximation does not compromise the subsequent discussion. $A_{eff}(z)$ is the effective area defined above,

BR_{ASE} is the branching ratio of the dominant ${}^4F_{3/2} \rightarrow {}^4I_{11/2}$ transition at 1 μm [20], τ_f is the fluorescence lifetime, Δl is the z-step distance (i.e. a slice of the crystal on the order of microns), according to the parameters set up in the simulation code, and $\Delta\Omega$ is the solid angle into which spontaneously emitted photons may be emitted, as defined above. Furthermore, it is important to highlight that employing the branching ratio of the manifold-to-manifold ${}^4F_{3/2} \rightarrow {}^4I_{11/2}$ transition is again an overestimation, due to the fact that we do not account for the actual bandwidth of said transition, but we only consider a single wavelength, 1.06 μm, which is only a small part of the $\sim$ 100-nm-broad spectral line ${}^4F_{3/2} \rightarrow {}^4I_{11/2}$. This estimation, which following the arguments above represents an overestimation of the initial power of the ASE, was executed for the respective samples and measurements conditions, provided values in the order of (0.06-20) nW, which we have employed in the respective simulations as initial P_{ASE} parameters. Fig. 2.6 shows our assumption of how the ASE signal (green) is initiated, via initial spontaneous emission with the photon flux estimated above, at the front facet of the crystal (blue), over the same pumped area (red), and propagates in the same direction as the pump signal, along the crystal, a typical assumption to estimate the ASE signal build [21].

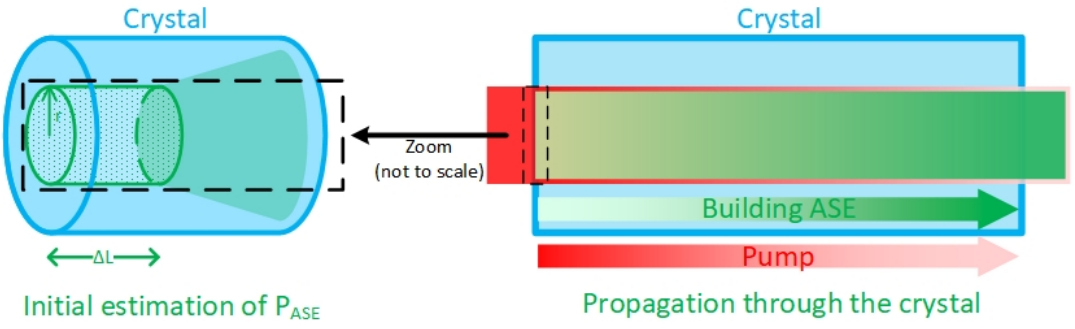

FIGURE 2.6: Representation of the ASE intensity model and initialisation of P_{ASE} at the front facet of the crystal

In Figs. 2.7 and 2.8 we have plotted each term of rate equation (2.14a) in order to gauge the relative magnitude with respect to the pump rate for a 100 mm-long z-scan executed on a 5 mm-long, 0.3at.%-doped, Nd:YAG crystal at LNT, one of the key cases for the ETU coefficient measurement detailed in Chap. 5. Fig. 2.7 shows the on-axis ($r = 0$) relative magnitude of the terms of Eq. (2.14a) along the crystal length when the z-coordinate of the z-scan corresponds $z = 0$ mm referenced to Fig. 2.8, i.e. to the maximum incident irradiance within a scan, when the ETU has the most relevance. As expected, the ASE rate builds up, throughout the propagation, by almost 3 orders of magnitude, however remaining 4- and generally at least 3-orders of magnitude smaller than all the other rates, to indicate its practically negligible effect on the overall rate equation (2.14a).

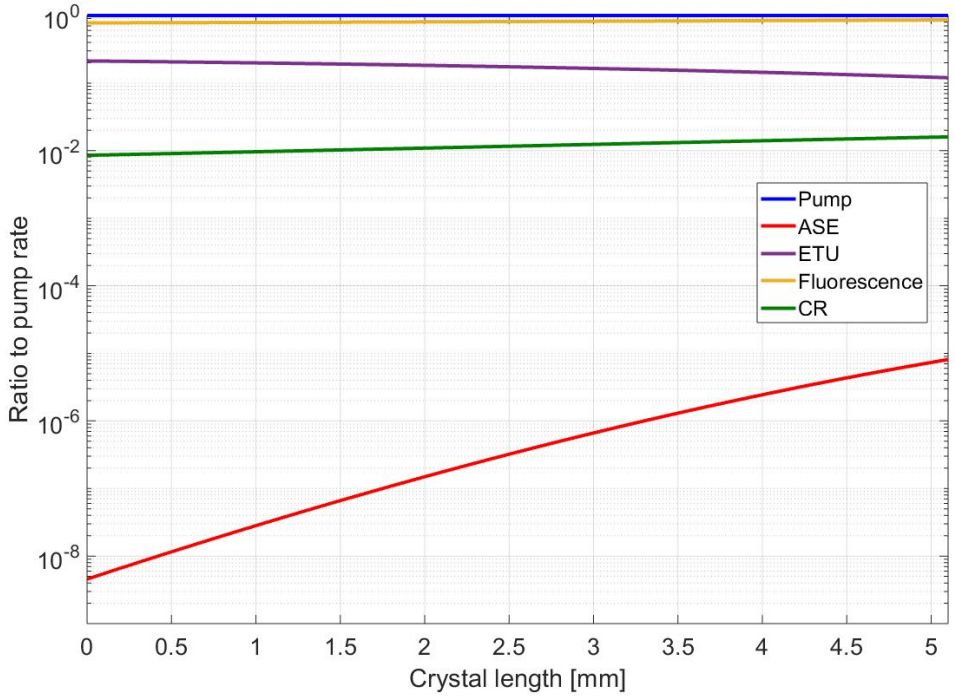

FIGURE 2.7: Evolution of the ratios of the rate terms to the pump rate (first term) of Eq. (2.14a) during the propagation through the crystal. Simulation of a 100 mm-long z-scan executed on a 5 mm-long, 0.3at.%-doped, Nd:YAG crystal at LNT. The z-coordinate is fixed to $z = 0$ mm, the point of maximum incident irradiance, and the radial coordinate is on-axis ($r = 0$).

To highlight that the case reported in Fig. 2.7 is the most extreme case throughout the entire simulated z-scan, 2.8 shows the on-axis ($r = 0$) relative magnitude of the terms of Eq. (2.14a) through the same 100 mm-long z-scan when the crystal-coordinates are fixed to the first (dashed lines) and second facet of the sample (solid lines). As expected, the ASE rate has the highest contribution when the irradiance is maximum, i.e. at $z = 0$ mm, the case analysed in detail in Fig. 2.7. It is worth observing that the ETU and the ASE rates both increase as the incident irradiance increases, while their relative magnitude with respect to each other remains roughly constant within the small-signal regime area, reaching its minimum as the z-scan proceeds in the high-irradiance area, approaching the maximum irradiance at $z = 0$ mm.
Similar results were obtained for the other crystals in the respective temperature regimes investigated, the details of which are presented in the corresponding sections.
Finally, it is worth comparing the simulated transmitted pump power with the ASE power, both calculated as solutions of the revised system of equations (2.14). Fig. 2.9 shows that the transmitted pump power (blue) is at least 2 orders of magnitude higher than the ASE power (red) throughout the entire z-scan, becoming more than 3 orders of magnitude smaller around the maximum irradiance value. Therefore, given our measurement methodology and experimental conditions detailed in Sec. 5.2, the contribution from the ASE is not only well within the experimental uncertainty associated

with the measured transmission curve, but also overall negligible with respect to the transmitted pump power.

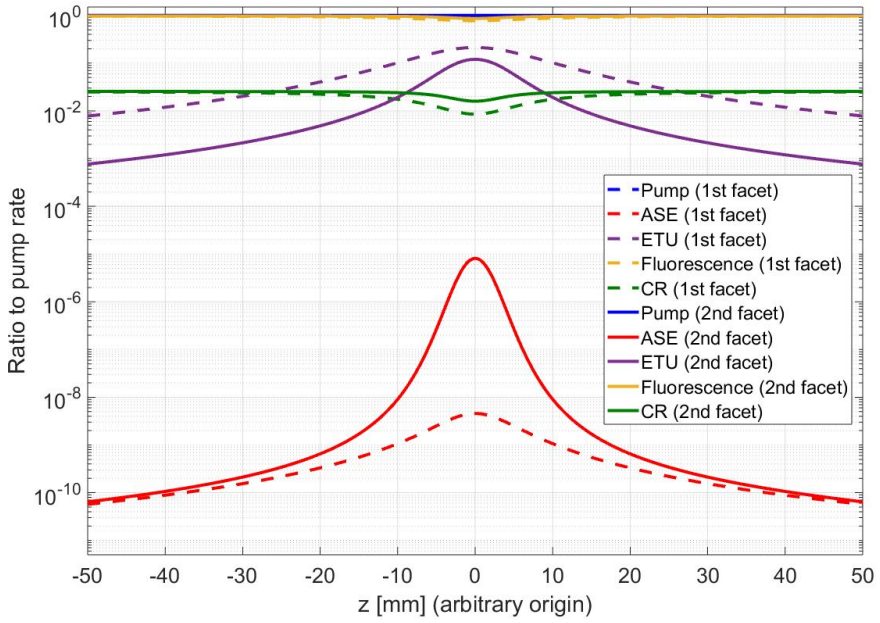

FIGURE 2.8: Ratios of the rate terms of Eq. (2.14a) to the pump rate (first term) vs z-position for a 100 *mm*-long z-scan executed on a 5 *mm*-long, 0.3at.%-doped, Nd:YAG crystal at LNT. The crystal-coordinates are fixed to the first facet of the sample for the dashed lines and to the second facet of the sample for the solid lines. The radial coordinate is on-axis ($r = 0$).

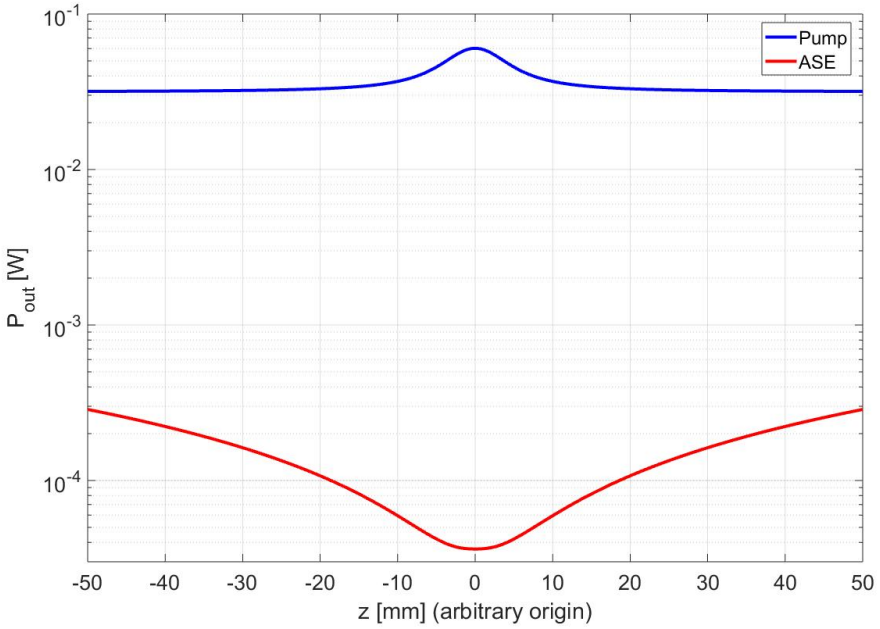

FIGURE 2.9: Transmitted pump power (blue) and ASE power (red) for a z-scan executed on a 5 *mm*-long, 0.3at.%-doped, Nd:YAG crystal at LNT.

Considering this, the previous, and the results we will show in the relevant experimental sections, we can consider the ASE a negligible effect in the measurement of the ETU coefficient described in this thesis.

2.4 Quasi-Four-Level Laser Theory

The distinction between "Quasi-four-level" (Q4L) and "Quasi-three-level" (Q3L) laser was introduced by Barnes and Walsh [22], and re-visited by White in a later paper [23]. The quasi-four- or quasi-three-levelness of a laser is determined by the lasing transition, and specifically by the relative fractional Boltzmann populations, f_2 and f_1, of the upper and lower laser Stark levels, respectively.
A simple expression for small signal gain g_0 [22] is given by

$$g_0 = \sigma \left[\gamma N_2 - (\gamma - 1) N_{tot}\right] \tag{2.15}$$

where σ is the Start-to-Stark level transition cross section, N_2 is the upper laser level (manifold) population density, N_{tot} is the total doping ion density. γ is the inversion reduction factor, related to the fractional Boltzmann populations f_1 and f_2 via $\gamma = 1 + \frac{f_1}{f_2}$. Given the upper and lower laser manifolds, the fractional Boltzmann populations of each Stark level i within each manifold are given by

$$f_i(T) = \frac{N_i(T)}{N_{tot}} = \frac{g_i}{Z(T)} e^{-\frac{E_i}{k_B T}} = \frac{g_i}{Z(T)} e^{-\frac{hc\nu_i}{k_B T}} \tag{2.16}$$

where N_i and g_i are respectively the population density and the degeneracy of the Stark level i, and E_i its energy, k_B is the Boltzmann's constant, T is the temperature of the crystal, h is the Plank's constant and c is the speed of light. $Z(T)$ is the partition function, given by $Z(T) = \sum_{j=1}^{n} g_j \exp\left(-\frac{E_j}{k_B T}\right)$, where n is the number of Stark levels within the manifold considered.
Given the above definitions, it is straightforward to associate the three-level or four-level nature to a laser system having respectively $\gamma = 2$ and $\gamma = 1$:

$$\gamma = 2 \longrightarrow g_0 = \sigma \left[2N_2 - N_{tot}\right] \tag{2.17a}$$

$$\gamma = 1 \longrightarrow g_0 = \sigma N_2 \tag{2.17b}$$

In (2.17a) there's gain only when the upper state population is more than half of the total population, which is the case of a pure three-level transition; whereas in (2.17b) the gain is proportional to the upper state population only, implying zero population in the lower state, i.e. a pure four-level transition. For laser transitions the operation of which is neither true-four- nor true-three-level, γ factors between 1 and 2 are possible: $\gamma > 1.5$ indicates a quasi-three-level laser and $\gamma < 1.5$ indicates a quasi-four-level laser.
Typically the strongest $9xx\ nm$ transition of the Nd^{3+} system originates from the R_1

Stark level (and the secondary, weaker $9xx\ nm$ transition originates from the R_2 Stark level), according to the nomenclature of [24], of the ${}^4F_{3/2}$ manifold, and terminates in the Z_5 Stark level of the ground ${}^4I_{9/2}$ manifold. In Nd:YAG, for instance, the respective fractional thermal populations at RT are $f_2 = 0.60$ and $f_1 = 0.0077$, which according to the definition above gives $\gamma = 1.013$, describing a Q4L transition. A similar situation is observed in several Nd-doped crystals. Furthermore, at Liquid Nitrogen Temperature (LNT) $f_1 = 1.07\ 10^{-7}$, 3 orders of magnitude less than at RT: as a consequence f_1/f_2 is in the order of 10^{-7} and therefore $\gamma \sim 1$, i.e. the laser transition becomes practically four-level, with the equivalent reduction in reabsorption losses. Additionally, besides what we may call a "spectroscopic classification" of the $9xx\ nm$ transition, and the quasi-levelness, we should consider how this characteristic affects laser operation: as opposed to a true-four-level, this transition at RT is characterised by a small residual lower level population, that can be regarded as a saturable (reabsorption) loss, added to the intrinsic cavity losses and the output coupling [2, 25, 26, 27, 28]. Being a saturable loss proportional to the length of the gain media, the quasi-four-level nature of this transition can be overcome by employing a very short crystal, i.e. the thin disk architecture. However, efficient operation is not so easy: if on one side the thin disk architecture reduces the reabsorption losses, on the other it requires the use of high doping levels (or multi-pass pumping schemes, or both) to achieve a suitable fraction of excited ions to overcome the cavity losses. This causes dynamics such as ETU and CR to worsen the laser performance and increase the threshold pump power [29, 2, 1]: the mitigation of these effects would require longer laser rods with low doping levels. Moreover, the high irradiance required to reach threshold produces thermal aberrations and thermal lens, that need to be properly managed [29].

The arguments made above can be quantitatively expressed via a simple formula for the threshold pump power P_{th} of a quasi-four-level system that includes ETU, reported in [1], and that will be of frequent use in successive parts of this report. Note that the following is only valid for relatively low doping-ion concentration values: when this condition does not hold, we employ the model presented in the next section, and developed in [2], to estimate the threshold pump power of Q4L lasers including ETU.

$$\begin{aligned} P_{th} \simeq & \frac{h\nu_p \pi w_p^2}{2(f_1+f_2)\sigma\tau_f\eta_q\eta_{LP}\eta_a}\left(L_T + 2\sigma\eta_{LP}f_1N_{tot}l_r\right) \\ & \left[1 + W_{ETU}\frac{\tau_f\alpha_{abs}}{4(f_1+f_2)\sigma\eta_{LP}}\left(L_T + 2\sigma\eta_{LP}f_1N_{tot}l_r\right)\right] = \\ & = P_{th}(without\ ETU)\left[1 + W_{ETU}\frac{\tau_f\alpha_{abs}}{4(f_1+f_2)\sigma\eta_{LP}}\left(L_T + 2\sigma\eta_{LP}f_1N_{tot}l_r\right)\right] = \\ & = P_{th}(without\ ETU)\left[1 + \frac{L_T + 2\sigma\eta_{LP}f_1N_{tot}l_r}{F_q\eta_{LP}}\right] \end{aligned} \tag{2.18}$$

Where $h\nu_p$ is the pump energy, w_p is the pump spot radius, f_1 and f_2 are the fractional populations of ground and excited laser levels respectively, σ is the Start-to-Stark transition cross section at the laser wavelength, τ_f is the fluorescence lifetime of the excited

state, η_q is the pump quantum efficiency, $\eta_{LP} = 1 - exp(-2w_p^2/w_l^2)$ is the spatial overlap factor between pump and laser mode spot sizes, η_a is the pump absorption efficiency, L_T is the cavity loss factor that includes intrinsic cavity losses and output coupling, N_{tot} is the unpumped population density, l_r is the crystal length, W_{ETU} is the ETU coefficient, α_{abs} is the absorption coefficient at the pump wavelength. The factor F_q

$$F_q = \frac{4(f_1 + f_2)\sigma}{W_{ETU}\tau_f \alpha_{abs}} \tag{2.19}$$

is a Figure-Of-Merit (FOM) for the laser. By its definition, this quantity, independent of the particular laser design employed, is defined by the gain material properties, and, as argued in [1], a high F_q is essential for keeping a low threshold with minimal additional thermal load.
From Eq. (2.18) it can be seen that the residual lower level population $f_1 N_{tot}$ represents a saturable reabsorption loss, proportional to the crystal length l_r, that adds to the cavity losses L_T. Furthermore, Eq. (2.18) highlights that one of the effects of ETU is the increase in the threshold pump power, as we will also discuss in Section 5.4.
It is clear, at this point, that there must be a trade-off of the factors that affect the efficient operation of the Q4L transition of the Nd^{3+} system. Although the ETU process has the effect of increasing the threshold, as in Eq. (2.18), it will be demonstrated (in Section 5.4.3) to be less significant at cryogenic temperatures thanks to an overall improvement of spectroscopic properties. A quantitative analysis of what has been stated above is presented in Chapter 5. Furthermore, in cryogenically cooled laser crystals, the thermal conductivity and thermal diffusivity increase, and the thermo-optic, thermal expansion and dn/dT (variation of refractive index with temperature) coefficients decrease [30], defining a reduction in thermal lens and aberrations [31].

2.4.1 Q4L rate-equation model including ETU

As detailed in the previous section, the Q4L transition of Nd:YAG, although potentially very efficient, presents some difficulties such as parasitic effects like ETU and CR that reduce the upper laser level population and produce extra waste heat, a lower gain with respect to the competing 1 μm transition, and reabsorption losses. These problems require high irradiance pumping, favouring a high-brightness diode-laser end-pumping configuration. In this situation, the overlap between the pump and the laser mode becomes a critical value in both optimising the efficiency of the laser and minimising the detrimental effects given by ETU in the unsaturated pumped regions. This requires the knowledge of the spatial distribution of the population inversion, given by the photon distribution with respect to the pump and signal beams in the cavity. Next, we summarise the rate-equation model developed by Bjurshagen and Koch and reported in [2], describing the output performance of CW Q4L lasers, including the influence of ETU, for generalised pump and laser mode distributions, i.e. other than Gaussian.

Furthermore, we highlight how ETU diminishes the population inversion and ultimately is the source of additional heating in the active volume of the crystal.
To illustrate, we consider the Nd:YAG's system in Fig. 2.10. The upper laser level is ${}^4F_{3/2}$ (R) and the lower laser level is ${}^4I_{9/2}$ (Z), with lasing occurring from the R_1 to the Z_5 Stark levels, according to the nomenclature of [24]. The Stark levels R_1 and Z_5 have respective population densities $N_b = f_b N_2$ and $N_a = f_a N_0$, where f_b and f_a are the fractional populations of the populations densities N_2 and N_0 in the upper, ${}^4F_{3/2}$, and lower, ${}^4I_{9/2}$, laser levels, respectively.
Neglecting the depletion of the ground-state, the steady-state rate equation for the upper laser-level population density, N_2, can be written as [25]

$$\begin{aligned}\frac{dN_2(\mathbf{r})}{dt} =& Rr_P(\mathbf{r}) - \frac{N_2(\mathbf{r}) - N_2^0}{\tau} + \\ &- \frac{c\sigma_e}{n}[N_b(\mathbf{r}) - N_a(\mathbf{r})]\Phi\phi_0(\mathbf{r}) - W_{ETU}[N_2(\mathbf{r}) - N_2^0]^2 = 0\end{aligned} \tag{2.20}$$

where we have indicated with $(\mathbf{r})$ the spatial-dependence in the coordinate system of choice. N_2^0 is the unpumped population density of the upper level, τ_0 is the upper level's lifetime, c is the speed of light in vacuum, σ_e is the emission cross section for the Q4L laser transition, n is the refractive index of the gain medium, and W_{ETU} is the macroscopic ETU coefficient introduced in Section 2.3.

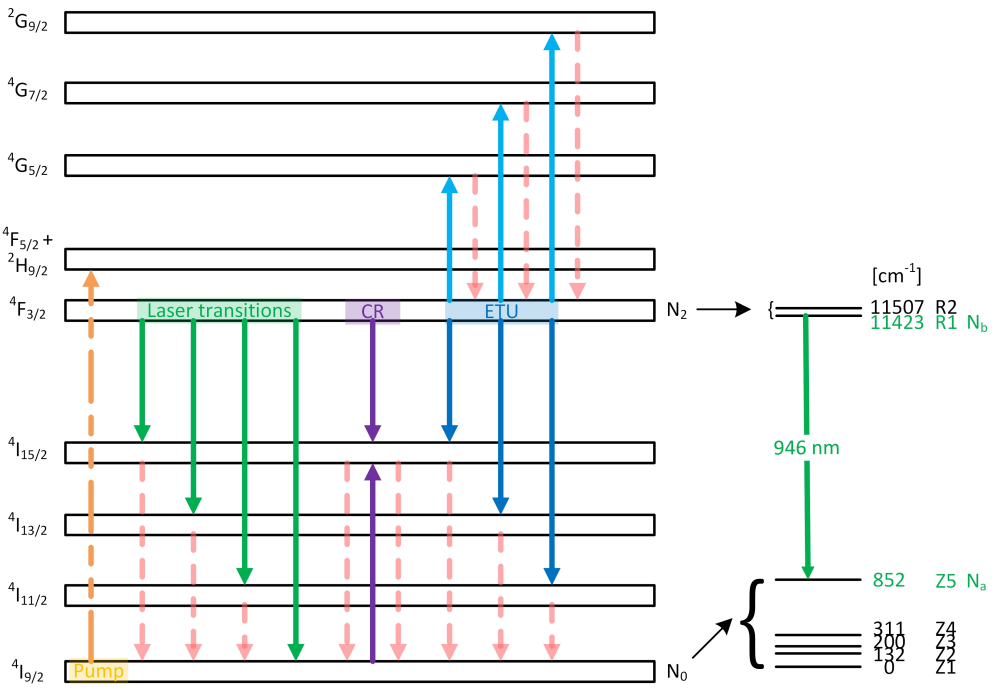

FIGURE 2.10: NdYAG's energy level diagram (not to scale) and possible transitions from the metastable state ${}^4F_{3/2}$, including ETU and CR.

The rate equation for the population density, N_b, for the upper Stark level is obtained by multiplying Eq. (2.20) by f_b:

$$\frac{dN_b(\mathbf{r})}{dt} = f_b R r_P(\mathbf{r}) - \frac{N_b(\mathbf{r}) - N_b^0}{\tau_0} + \\ - \frac{c\sigma_e}{n} f_b [N_b(\mathbf{r}) - N_a(\mathbf{r})] \Phi \phi_0(\mathbf{r}) - \frac{W_{ETU}}{f_b} [N_b(\mathbf{r}) - N_b^0]^2 = 0 \tag{2.21}$$

where N_a^0 and N_b^0 are the unpumped population densities of the laser Stark levels. The pumping rate R is given by

$$R = \frac{P_p \eta_a}{h\nu_P} \tag{2.22}$$

with P_P the incident pump power, $h\nu_P$ the pump photon energy, and $\eta_a = 1 - e^{-\alpha l_r}$ is the pump absorption efficiency for a rod of length l_r and absorption coefficient α. The total number of laser photons in the cavity, Φ, is given by

$$\Phi = \frac{2 l_c^* P_{out}}{ch\nu_L T} \tag{2.23}$$

with $l_c^* = l_c + (n-1) l_r$ optical path length of the l_c-long cavity, P_{out} laser output power, $h\nu_L$ laser photon energy, T output coupler transmission.
The spatial distributions of the pump and laser modes are described by the functions $r_P(\mathbf{r})$ and $\phi_0(\mathbf{r})$, respectively. $r_P(\mathbf{r})$ is normalised over the crystal:

$$\iiint_{crystal} r_P(\mathbf{r})\, dV = 1 \tag{2.24}$$

and $\phi_0(\mathbf{r})$ over the entire cavity:

$$\iiint_{cavity} \phi_0(\mathbf{r})\, dV = 1 \tag{2.25}$$

For brevity of notation, we define the pumping rate's and total number of generated laser photons' spatial distributions as follows:

$$R_P(\mathbf{r}) = R r_P(\mathbf{r}) = \frac{P_P \eta_a}{h\nu_P} r_P(\mathbf{r}) \tag{2.26}$$

$$\Phi_L(\mathbf{r}) = \Phi \phi_0(\mathbf{r}) = \frac{2 l_c^* P_{out}}{ch\nu_L T} \phi_0(\mathbf{r}) \tag{2.27}$$

The population inversion density is $\Delta N = N_b - N_a$. Noting that the total number of doping ions $N_{tot} = N_0 + N_2 = N_0^0 + N_2^0$, and $N_a = f_a N_0$ and $N_b = f_b N_2$, we have

$$\Delta N = \frac{N_b}{f_b}(f_a + f_b) - f_a N_{tot} \tag{2.28}$$

Furthermore, in thermal equilibrium $N_a^0 \gg N_b^0$ as the thermal population in the upper

manifold is negligible, hence the unpumped population inversion can be written as $\Delta N^0 \simeq -N_a^0 \simeq -f_a N_{tot}$. The steady-state rate equation for the population inversion density can then be written as

$$\begin{aligned}\frac{d\Delta N(\mathbf{r})}{dt} =& fR_P(\mathbf{r}) - \frac{\Delta N(\mathbf{r}) - \Delta N^0}{\tau_0} + \\ &- \sigma_e \frac{c}{n} f \Delta N(\mathbf{r}) \Phi \phi_0(\mathbf{r}) - \frac{W_{ETU}}{f} [\Delta N(\mathbf{r}) - \Delta N^0]^2 = 0\end{aligned} \tag{2.29}$$

where $f = f_a + f_b$.
The rate equation for the cavity photon number is written as

$$\frac{d\Phi}{dt} = \frac{c\sigma_e}{n} \iiint\limits_{crystal} \Delta N(\mathbf{r}) \Phi \phi_0(\mathbf{r})\, dV - \frac{\Phi}{\tau_c} = 0 \tag{2.30}$$

where $\tau_c = 2l_c^*/c\delta$ is the cavity photon lifetime, $\delta = L + T$ is the round-trip loss, and L is the intrinsic cavity loss.
From Eq. (2.29), expanding the last bracket and solving the resultant quadratic equation with a general solution, we can calculate the population-inversion at steady-state as

$$\begin{aligned}\Delta N(\mathbf{r}) = \frac{2\tau_0 f R_P(\mathbf{r}) + 2\frac{c\sigma_e\tau_0}{n} f N_a^0 \Phi_L(\mathbf{r})}{1 + \frac{c\sigma_e\tau_0}{n} f \Phi_L(\mathbf{r}) + \big[(1 + \frac{c\sigma_e\tau_0}{n} f \Phi_L(\mathbf{r}))^2 + \\ + 4W_{ETU}\tau_0^2 R_P(\mathbf{r}) + 4W_{ETU}\tau_0^2 \frac{c\sigma_e}{n} N_a^0 \Phi_L(\mathbf{r})\big]^{1/2}} - N_a^0\end{aligned} \tag{2.31}$$

Inserting Eq. (2.31) into Eq. (2.30) we obtain an implicit relation between the pump rate R and the cavity photon number Φ:

$$\frac{2\sigma_e l_c^*}{n} \iiint\limits_{crystal} \Delta N(\mathbf{r}) \phi_0(\mathbf{r})\, dV = \delta \tag{2.32}$$

This equation suggests that the total gain integrated over the laser cavity-mode distribution within the active crystal, including upconversion and reabsorption losses, is equal to the total loss, including cavity loss and output coupling. Substituting $\Delta N(\mathbf{r})$ with Eq. (2.31), Eq. (2.32) becomes

$$\begin{aligned}&\frac{2\sigma_e l_c^*}{n} \iiint\limits_{crystal} \frac{2\tau_0 f R_P(\mathbf{r})\phi_0(\mathbf{r}) + 2\frac{c\sigma_e\tau_0}{n} f N_a^0 \Phi \phi_0(\mathbf{r})^2}{1 + \frac{c\sigma_e\tau_0}{n} f \Phi_L(\mathbf{r}) + \big[(1 + \frac{c\sigma_e\tau_0}{n} f \Phi_L(\mathbf{r}))^2 + \\ &\qquad + 4W_{ETU}\tau_0^2 R_P(\mathbf{r}) + 4W_{ETU}\tau_0^2 \frac{c\sigma_e}{n} N_a^0 \Phi_L(\mathbf{r})\big]^{1/2}} dV = \\ &= \delta + \frac{2\sigma_e l_c^* N_a^0}{n} \iiint\limits_{crystal} \phi_0(\mathbf{r})\, dV = \delta + \delta_l\end{aligned} \tag{2.33}$$

where we have indicated with δ_l the reabsorption loss due to the residual population in the lower Stark level. When solving Eq. (2.33) we can retrieve the output power of the laser.
By applying the threshold condition that $\Phi = 0$, we obtain an equation for the the pump

rate at threshold, i.e. for the threshold pump power:

$$R_{th} = \frac{\delta + \delta_l}{2\sigma_e \tau_0 f l_c^*} \left[\iiint_{crystal} \frac{2 r_P(\mathbf{r}) \phi_0(\mathbf{r})}{1 + \sqrt{1 + 4 W_{ETU} \tau_0^2 R_{th} r_P(\mathbf{r})}} \right]^{-1} \tag{2.34}$$

As explained in Section 2.3, ETU produces additional waste heat that adds to the other sources of heat, i.e. quantum defect and other non-radiative decay channels, e.g. multi-phonon relaxation from higher excited levels ($^4G_{5/2}$, $^4G_{7/2}$, $^2G_{9/2}$) back to the upper laser level ($^4F_{3/2}$) or ground level ($^4I_{9/2}$). In order to quantify the thermal load due to ETU, we calculate the fraction of excited ions, F_{ETU}, involved in the ETU process, given by the ratio between the last term in Eq. (2.29), proportional to W_{ETU}, and the total absorption rate. To illustrate, we distinguish between three parts of Eq. (2.29): the total absorption rate R_{abs}, the total emission rate R_{em}, and the upconversion rate R_{ETU}.

$$\begin{aligned} R_{abs} &= f R_P(\mathbf{r}) - \sigma_e \frac{c}{n} f \Delta N^0(\mathbf{r}) \Phi \phi_0(\mathbf{r}) \\ R_{em} &= -\frac{\Delta N(\mathbf{r}) - \Delta N^0}{\tau_0} - \sigma_e \frac{c}{n} f [\Delta N(\mathbf{r}) - \Delta N^0] \Phi \phi_0(\mathbf{r}) \\ R_{ETU} &= -\frac{W_{ETU}}{f} [\Delta N(\mathbf{r}) - \Delta N^0]^2 \end{aligned} \tag{2.35}$$

where R_{abs} includes both the pumping rate and the reabsorption of ions from the ground state to the upper state, R_{em} includes spontaneous and stimulated emission. Therefore we can express F_{ETU} as

$$F_{ETU} = \left| \frac{R_{ETU}}{R_{abs}} \right| = 1 - \left| \frac{R_{em}}{R_{abs}} \right| \tag{2.36}$$

where $|R_{em}/R_{abs}|$ is the fraction of excited ions that decay by emission. Substituting R_{em} and R_{abs} as defined in Eq. (2.35), we obtain

$$F_{ETU}(\mathbf{r}) = 1 - \frac{\Delta N(\mathbf{r}) + N_a^0}{\Delta N_{noETU}(\mathbf{r}) + N_a^0} \tag{2.37}$$

where $\Delta N(\mathbf{r})$ is given by Eq. (2.31) and $\Delta N_{noETU}(\mathbf{r})$ is the population inversion distribution without including ETU effects, given by

$$\Delta N_{noETU}(\mathbf{r}) = \frac{\tau_0 f R_P(\mathbf{r}) + \frac{c\sigma_e \tau_0}{n} f N_a^0 \Phi_L(\mathbf{r})}{1 + \frac{c\sigma_e \tau_0}{n} f \Phi_L(\mathbf{r})} - N_a^0 \tag{2.38}$$

Substituting Eq. (2.38) into Eq. (2.37) we obtain

$$F_{ETU}(\mathbf{r}) = 1 - \frac{2}{1 + \sqrt{1 + \frac{4 W_{ETU} \tau_0^2 R_P(\mathbf{r}) + 4 W_{ETU} \tau_0^2 \frac{c\sigma_e}{n} N_a^0 \Phi_L(\mathbf{r})}{[1 + \frac{c\sigma_e \tau_0}{n} f \Phi_L(\mathbf{r})]^2}}} \tag{2.39}$$

and we can employ this equation to write $\Delta N(\mathbf{r})$ as

$$\Delta N(\mathbf{r}) = (\Delta N_{noETU}(\mathbf{r}) + N_a^0)(1 - F_{ETU}(r)) - N_a^0 \tag{2.40}$$

which clearly shows that the fraction of ions involved in the ETU process reduces the positive part of the population inversion.
The fractional thermal loading distribution can be written as

$$\xi(\mathbf{r}) = \xi_0[1 - F_{ETU}(\mathbf{r})] + F_{ETU}(\mathbf{r}) \tag{2.41}$$

where ξ_0 represents the thermal loading without ETU, i.e. the quantum defect $1 - \lambda_P/z\lambda_L$ with λ_P and λ_L the pump and laser wavelengths, respectively. Finally, the heat source density in the crystal can be expressed as

$$Q(\mathbf{r}) = \xi(\mathbf{r}) P_P \eta_a r_P(\mathbf{r}) \tag{2.42}$$

where we have assumed that $Q(\mathbf{r})$ has the shape of the absorbed pump radiation weighted by the thermal loading distribution.
In Chapter 6 we will apply this model to show how ETU affected the thermal load for the case of the lasers discussed.

References

[1] J. W. Kim, J. I. Mackenzie, and W. A. Clarkson, "*Influence of energy-transfer-upconversion on threshold pump power in quasi-three-level solid-state lasers*," Optics Express **17**, 11935–11943 (2009).

[2] S. Bjurshagen and R. Koch, "*Modeling of energy-transfer upconversion and thermal effects in end-pumped quasi-three-level lasers*," Applied Optics **43**, 4753–4767 (2004).

[3] S. A. Pollack, D. B. Chang, and N. L. Moise, "*Upconversion-pumped infrared erbium laser*," Journal of Applied Physics **60**, 4077–4086 (1986).

[4] S. A. Pollack and D. B. Chang, "*Ion-pair upconversion pumped laser emission in Er^{3+} ions in YAG, YLF, SrF_2, and CaF_2 crystals*," Journal of Applied Physics **64**, 2885–2893 (1988).

[5] R. Scheps, "*Upconversion laser processes*," Progress in Quantum Electronics **20**, 271 – 358 (1996).

[6] S. D. Jackson, "*Cross relaxation and energy transfer upconversion processes relevant to the functioning of 2 μm Tm^{3+}-doped silica fibre lasers*," Optics Communications **230**, 197 – 203 (2004).

[7] E. C. Honea, R. J. Beach, S. B. Sutton, J. A. Speth, S. C. Mitchell, J. A. Skidmore, M. A. Emanuel, and S. A. Payne, "*115-W Tm:YAG diode-pumped solid-state laser*," IEEE Journal of Quantum Electronics **33**, 1592–1600 (1997).

[8] R. Hayward, W. Clarkson, P. Turner, J. Nilsson, A. Grudinin, and D. Hanna, "*Efficient cladding-pumped Tm-doped silica fibre laser with high power singlemode output at 2 μm*," Electronics Letters **36**, 711–712 (2000).

[9] L. Agazzi, K. Worhoff, and M. Pollnau, "*Energy-Transfer-Upconversion Models, Their Applicability and Breakdown in the Presence of Spectroscopically Distinct Ion Classes: A Case Study in Amorphous Al_2O_3:Er^{3+}*," The Journal of Physical Chemistry C **117**, 6759–6776 (2013).

[10] P. Loiko and M. Pollnau, "*Stochastic model of energy transfer processes among rare earth ions*," in *Fiber Lasers and Glass Photonics: Materials through Applications*, vol. 10683 S. Taccheo, J. I. Mackenzie, and M. Ferrari, eds., International Society for Optics and Photonics (SPIE, 2018), pp. 241 – 248.

[11] M. Eichhorn, "*Quasi-three-level solid-state lasers in the near and mid infrared based on trivalent rare earth ions*," Applied Physics B **93**, 269–316 (2008).

[12] J. O. White and C. E. Mungan, "*Measurement of upconversion in Er:YAG via z-scan*," Journal of the Optical Society of America B **28**, 2358–2361 (2011).

[13] W. Lima, V. Martins, A. Monte, D. Messias, N. Dantas, M. Bell, and T. Catunda, "*Energy transfer upconversion on neodymium doped phosphate glasses investigated by Z-scan technique*," Optical Materials **35**, 1724 – 1727 (2013).

[14] S. J. Yoon, R. P. Yan, S. J. Beecher, and J. I. Mackenzie, "*Concentration dependence of energy transfer upconversion in Nd:YAG*," Optical Materials Express **5**, 926–931 (2015).

[15] R. Yan, S. J. Yoon, S. J. Beecher, and J. I. Mackenzie, "*Measuring the Elevated Temperature Dependence of Up-Conversion in Nd:YAG*," IEEE Journal of Selected Topics in Quantum Electronics **21**, 329–336 (2015).

[16] S. Goldring, R. Lavi, and V. Lupei, "*Decay Dynamics of Excited Nd Ions in Nd:YVO Following Weak Excitation*," IEEE Journal of Quantum Electronics **46**, 169–181 (2010).

[17] R. Yan, X. Yu, X. Li, D. Chen, and J. Yu, "*Theoretical and experimental investigation of actively Q-switched Nd:YAG 946 nm laser with considering ETU effects*," Applied Physics B **108**, 591–596 (2012).

[18] G. J. Linford, E. R. Peressini, W. R. Sooy, and M. L. Spaeth, "*Very Long Lasers*," Applied Optics **13**, 379–390 (1974).

[19] W. Koechner, *Solid-State Laser Engineering*, Springer Series in Optical Sciences (Springer, 2006).

[20] S. J. Yoon, "*Cryogenically-cooled neodymium-doped solid-state lasers*," Ph.D. thesis, University of Southampton (2016).

[21] L. Casperson and A. Yariv, "*Spectral narrowing in high-gain lasers*," IEEE Journal of Quantum Electronics **8**, 80–85 (1972).

[22] N. P. Barnes, B. M. Walsh, R. L. Hutcheson, and R. W. Equall, "*Pulsed* $^4F_{3/2}$ *to* $^4I_{9/2}$ *operation of Nd lasers*," Journal of the Optical Society of America B **16**, 2169–2177 (1999).

[23] J. O. White, "*Parameters for Quantitative Comparison of Two-, Three-, and Four-Level Laser Media, Operating Wavelengths, and Temperatures*," IEEE Journal of Quantum Electronics **45**, 1213–1220 (2009).

[24] E. H. Carlson and G. H. Dieke, "*The State of the* Nd^{3+} *Ion as Derived from the Absorption and Fluorescence Spectra of* $NdCl_3$ *and Their Zeeman Effects*," The Journal of Chemical Physics **34**, 1602–1609 (1961).

[25] W. P. Risk, "*Modeling of longitudinally pumped solid-state lasers exhibiting reabsorption losses*," Journal of the Optical Society of America B **5**, 1412–1423 (1988).

[26] T. Y. Fan and R. L. Byer, "*Modeling and CW operation of a quasi-three-level 946 nm Nd: YAG laser*," IEEE Journal of Quantum Electronics **23**, 605–612 (1987).

[27] T. Y. Fan and R. L. Byer, "*Diode laser-pumped solid-state lasers*," IEEE Journal of Quantum Electronics **24**, 895–912 (1988).

[28] T. Taira, W. M. Tulloch, and R. L. Byer, "*Modeling of quasi-three-level lasers and operation of CW Yb:YAG lasers*," Applied Optics **36**, 1867–1874 (1997).

[29] W. A. Clarkson, "*Thermal effects and their mitigation in end-pumped solid-state lasers*," Journal of Physics D: Applied Physics **34**, 2381–2395 (2001).

[30] D. C. Brown, "*The promise of cryogenic solid-state lasers*," IEEE Journal of Selected Topics in Quantum Electronics **11**, 587–599 (2005).

[31] H. Glur, R. Lavi, and T. Graf, "*Reduction of thermally induced lenses in Nd:YAG with low temperatures*," IEEE Journal of Quantum Electronics **40**, 499–504 (2004).

Chapter 3

Spectroscopy measurements

3.1 Introduction

Spectroscopic properties of laser crystals are fundamental parameters required to design lasers: they need to be known with certainty in order to allow the designer to suitably engineer the targeted device. In this chapter we report on the methodology and the results of the spectroscopic measurements performed for various neodymium-doped crystals, over a range of temperatures, e.g. elevated and sub-ambient temperatures.
The active impurity concentration is an important parameter for tailoring the laser gain and thermal characteristics. Coupled with pump brightness, the product of the active-ion density and transition cross section, defines the population inversion density, hence gain in that laser crsytal. While a nominal value for the doping-ion concentration is usually supplied by crystal manufacturers, its accuracy can vary greatly. When employing the Czochralski growth method, the most popular technique utilised to grow crystals, the doping-ion concentration varies across the length of the boule [1], with variations up to 30% for boules of 10 *cm* diameter and 25 *cm* length in Nd:YAG growths [2]. It is therefore necessary to quantify the doping-ion concentration of a given sample prior to utilising it in a laser, in order to establish whether this key parameter is within design tolerances. The most reliable methods to measure the doping-ion concentration, like laser induced breakdown spectroscopy (LIBS), are destructive, that renders the crystal unusable. A spatially-resolved non-destructive method proposed in [3], although successful, is not relevant for our aim to measure a general feature of the sample, and not a localised one.
Here, we first present a method to determine the doping level of Nd-doped samples, starting from absorbance measurements and well accepted absorption cross section data, and employing the Beer-Lambert law introduced in Chapter 2. This methodology, applicable to any laser crystal once its absorption cross section spectrum is known, has been employed to determine the doping-ion concentration of several Nd-doped crystals. Subsequently, we present the characterisation of the ground absorption cross section

into the ${}^2H_{9/2} + {}^4F_{5/2}$ energy levels for Nd-doped Vanadates (YVO_4 and $GdVO_4$) in the elevated temperatures regime, (RT-450 K), underpinned by the previous doping-level measurements.
Lastly, we detail the thorough characterisation of the same absorption cross section for Nd:YAG under cryogenic-cooling, in the temperature range (LNT-RT).

3.1.1 Nd-doped hosts overview

The crystals investigated in this chapter are Nd:YAG, Nd:YVO_4 and Nd:$GdVO_4$: Table 3.1 shows their main thermo-optical and spectroscopic properties. Nd:YAG is possibly the best known and most exploited crystal in solid-state lasers, thanks to its excellent spectroscopic and thermo-optical properties [2]. Nd-doped orthovanadate crystals, e.g. Nd:YVO_4 and Nd:$GdVO_4$, however, have gained much popularity in the last few decades, thanks to their superior spectroscopic properties (for the π-polarised light), and comparable thermo-optical properties to Nd:YAG's.

	Nd:YAG	Nd:YVO_4	Nd:$GdVO_4$	
Lattice symmetry	Cubic	Tetragonal	Tetragonal	
Ion density @ 1at.% [10^{20} cm^{-3}]	1.39	1.25	1.25	[4]
Refractive index @ 1 μm	1.82	$n_0 = 1.96$ $n_e = 2.17$	$n_0 = 1.97$ $n_e = 2.17$	[5]
Thermal conductivity @ 300 K [$Wm^{-1}K^{-1}$]	11	9(a) 12(c)	8.6(a) 5.1(c)	[6]
Thermal expansion coefficient @ 300 K [10^{-6} K^{-1}]	7.5	1.7(a) 8.2(c)	1.1(a) 8.0(c)	[5]
dn/dt @ 1 μm @ 300 K [10^{-6} K^{-1}]	7.3	7.9(c)	13.8(a) 10.1(c)	[5]
σ_{abs} @ 808 nm @ 300 K [pm^2]	6.9	12(a) 60(c)	11(a) 55(c)	[6]
σ_{em} @ 1 μm @ 300 K [pm^2]	26	2.9(a) 141(c)	2.1(a) 103(c)	[7, 8]
σ_{em} @ 0.9 μm @ 300 K [pm^2]	2.4	3.1	2.4	[8]

TABLE 3.1: Main spectroscopic and thermo-optical properties of Nd:YAG, Nd:YVO_4 and Nd:$GdVO_4$.

Very similar crystals overall, Nd:YVO_4 and Nd:$GdVO_4$ present subtle differences in their thermo-optical properties. Several papers have demonstrated the superiority of Nd:$GdVO_4$ as a laser crystal [9, 10, 11, 12], although nominally Nd:YVO_4 presents higher absorption and emission cross sections (see Table 3.1). These crystals present an absorption cross section above 55 pm^2 for π-, and above 11 pm^2 for σ-polarised light, respectively [5, 13]. Their relatively broad absorption cross section ($\sim$ 2 nm) allows diode-pumping without stringent control of the pump spectrum; at the same time, the high absorption cross section permits the use of short crystals and the development of very short cavities, e.g. monolithical micro-chip lasers [6, 7, 14, 15, 16, 17]. In fact, their ground absorption cross section into the $^2H_{9/2} + {}^4F_{5/2}$ energy levels (around 808 nm) is $\sim$ 8 times higher than in Nd:YAG, while the emission cross section $^4F_{3/2} \rightarrow {}^4I_{11/2}$ (around 1 μm) is $\sim$ 6 times higher than Nd:YAG's (see Table 3.1). Such a strong absorption, however, causes an extreme increase in temperature in the pumped region, potentially over 100 ^oC [18]. Moreover, this leads to the subsequent change to the spectroscopic parameters, as they are temperature-dependent. While the papers referenced above present an extensive characterisation of spectroscopic and optical properties such as the emission cross section and the thermal conductivity at elevated temperatures, especially for Nd:YVO_4 and Nd:$GdVO_4$, there is no record of an equivalent characterisation of the absorption cross section. The latter is as important as the former parameters for enabling reliable laser performance modelling.

The choice of the hosts in the respective temperature regimes investigated in this thesis, adding to the motivations depicted above, was also driven by the equipment availability at the time of the experiments. Characterising Nd-doped vanadates at elevated temperatures, in fact, provided not only useful additional data to the lack thereof in the literature, but also the chance to optimise the experimental setup in an absorption regime similar to the one experienced later, for the equivalent measurements on the cryogenically cooled Nd:YAG. The latter experiments could only be executed once the cryocooler employed was available and functional, which wasn't the case at the time of the measurements on the vanadates. Measuring the absorption cross section of the available vanadate crystals at cryogenic temperatures was not possible due to the very high absorption of these crystals, as explained above and demonstrated later even at high-temperatures, which would have been only exacerbated at sub-ambient temperatures. A solution to the problem of a negligible transmission signal would have been to slice the crystals into thinner pieces, an operation that was not straightforward with the available means. Therefore, the choice was made to focus on the cryogenic-cooling regime only for our crystal of choice, Nd:YAG.

3.2 Methodology

3.2.1 Experimental setup

The setup employed for the small signal absorption measurements comprises a symmetric optical system, shown in Fig. 3.1, with two equivalent telescopes, the first to couple the probe source into the crystal, the second to collected the transmitted light. Broadband amplified spontaneous emission (ASE) of a sub-threshold fibre-coupled (200 μm core, 0.22 NA) diode-laser (LIMO60-F200-DL808) was used as the probe source. The $\sim 6\ mW$ of ASE exiting the patch cable had a bandwidth of $\sim 40\ nm$ centred around 808 nm, and was collimated by lens L_1 ($f = 30\ mm$) and focused by lens L_2 ($f = 150\ mm$) onto the sample under test. The incident light was polarised with a cube polariser. The estimation of the beam quality parameter of the LIMO diode laser from its fibre's specifications resulted in $M^2 \simeq 54$. Then using Gaussian beam propagation theory and the appropriate transfer matrices for our experimental setup depicted in Fig. 3.1, we calculated the multi-mode waist radius produced on the crystal to be $W_0 \simeq 500\ \mu m$, giving a confocal parameter of $b = \frac{2\pi W_0^2}{M^2 \lambda} \simeq 36\ mm$. The transmitted light was re-collimated by lens L_3 ($f = 150\ mm$) and finally re-imaged by lens L_4 ($f = 30\ mm$) into the (200 μm core, 0.22 NA) optical fibre connected to an Optical Spectrum Analyser (OSA) (ANDO AQ6317B). When probing different polarisations, the setup was kept fixed, and the crystal rotated so that the optical axis of the uni-axial crystals tested was aligned parallel (π) or perpendicular (σ) to the polarisation axis of the cube polariser.

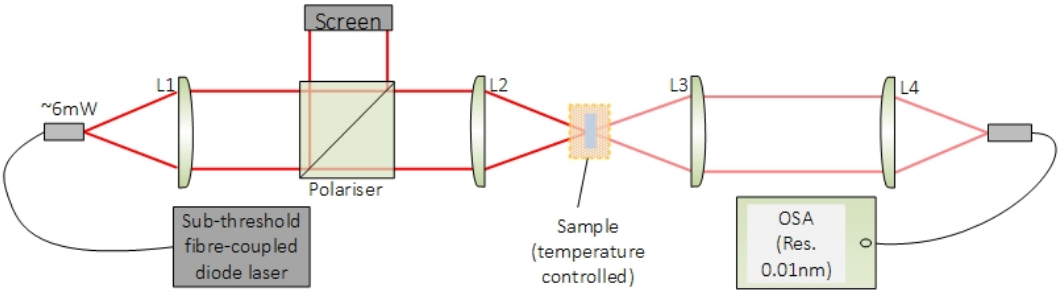

FIGURE 3.1: Absorption measurements setup.

The input, $P_{in}(\lambda)$, and the transmitted, $P_{out}(\lambda)$, spectral power distributions were recorded with a resolution of 0.01 nm, without and with the sample in place, respectively. Finally Eq. (2.2) was applied to retrieve either the doping-ion concentration or the absorption cross section.

Fig. 3.2 shows the modelled beam size through the setup illustrated in Fig. 3.1. The pump's low irradiance ($\sim 0.6\ W/cm^2$) ensured that the experiment was in the small-signal transmission regime, i.e. negligible inversion levels, as required by the applicability of the Beer-Lambert law (2.1), presented in Section 2.2.

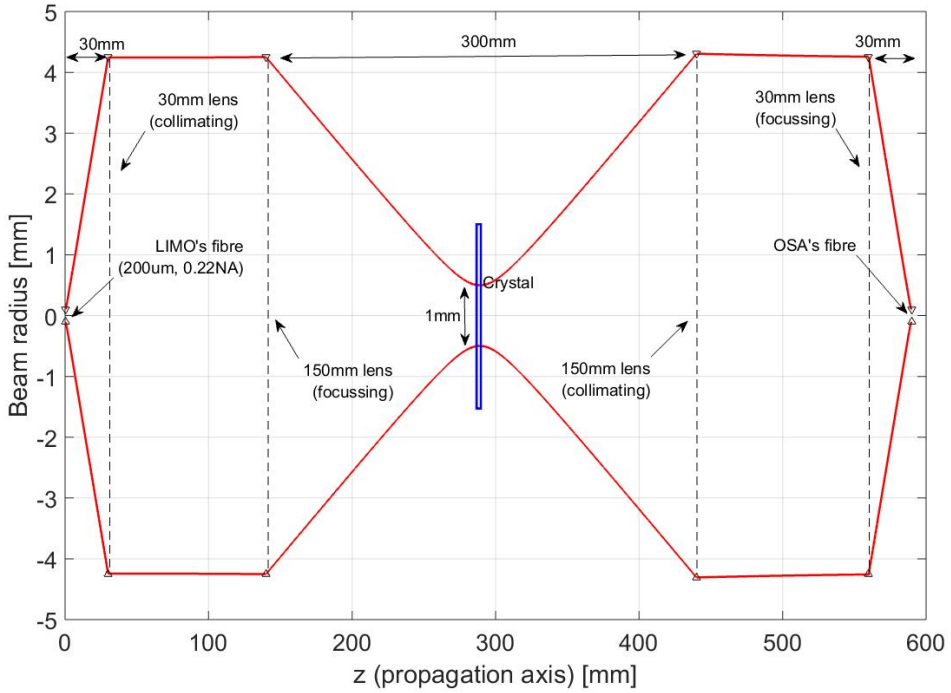

FIGURE 3.2: LIMO diode's beam modelling through the absorption setup.

The mounting of the sample was chosen according to the temperature range investigated. For the elevated temperature regime, explored for the Nd-doped vanadates, the samples were clamped to a Copper block, which was heated to the desired temperature by a resistor, as shown in Fig. 3.3. A 1 mm-thick Aluminium shield, with suitably positioned holes to maintain optical access to the sample, as in Fig. 3.3b, provided the insulation necessary to minimise convective heat flow.

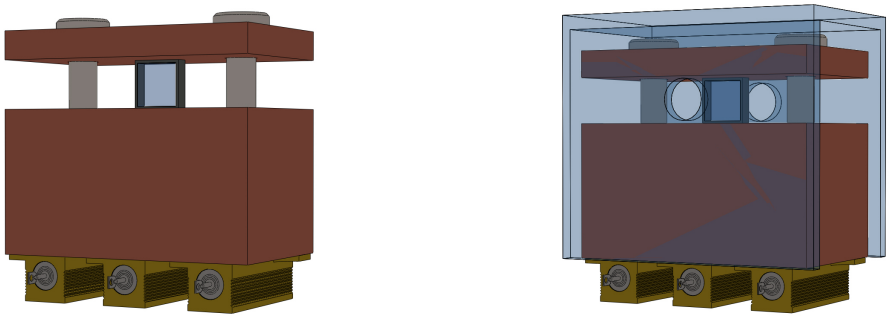

(A) (B)

FIGURE 3.3: (3x3x1) mm^3 Nd-doped vanadate sample, wrapped in 200 μm-thick Indium and clamped to a heated Copper block. (A) Unshielded. (B) Shielded by a 1 mm-thick Aluminium foil.

The temperature was monitored by a thermocouple fixed in close proximity to the sample under test, and a DC power supply was used to provide a constant power level,

set manually, with regard to the target temperature. A suitably long time was left, in order for the entire system to stabilise at the desired temperature.
In the case of cryogenically cooled Nd:YAG, the crystal was wrapped in 200 μm-thick Indium foil, and clamped between a Copper plate and a thin Copper foil strip (5 mm wide and 500 μm thick) to ensure thermal contact with the remaining three free sides of the crystal, as in Fig. 3.4.

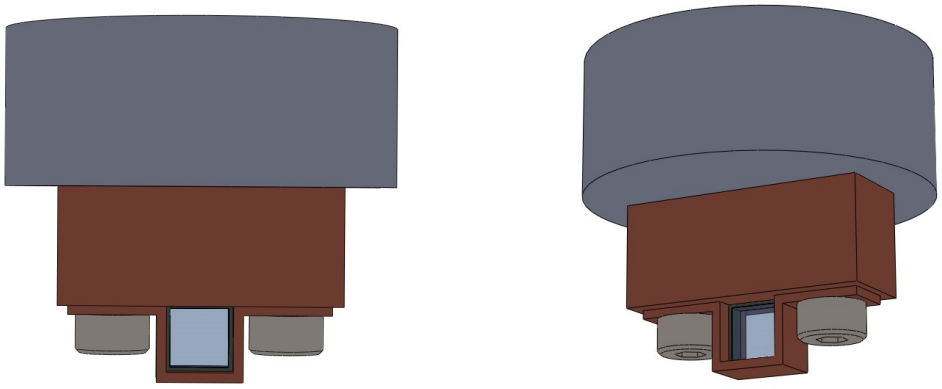

(A) (B)

FIGURE 3.4: (3x3x1) mm^3 Nd:YAG, wrapped in 200 μm-thick Indium and clamped to a Copper block in contact with the cold-head of the cryo-cooler. (A) Front view. (B) Dimetric view.

The plate was bolted directly to the cold-head of the closed-loop Q-drive 1s132K cryocooler, described in more detail below, thus providing cooling through all side faces of the crystal. The assembly was isolated from the surrounding environment via a $\sim 10^{-7}$ $mbar$ vacuum, and the vacuum chamber was equipped with 6-mm-thick windows that allowed optical access to the crystal while acting as sealing plates. The temperature of the system was monitored by two temperature sensors positioned on the side of the cold head and on the Copper base, as close as physically possible to the crystal.
The operation of the commercial closed-loop cryostat Q-drive 2s132K was based on a pressure wave generator (PWG, in Fig. 3.5) driven by STAR© linear reciprocating motors and a coaxial Stirling pulse-tube coldhead. The operation schematics, as well as the physical appearance of the cryocooler are displayed in Figs. 3.5 and 3.6 (both images were taken from the user manual), respectively.
In each cycle, the pressurised Helium contained in the system is driven, by the forward stroke of pistons in the pressure wave generator (PWG), through the first heat exchanger (left-hand side "Warm HX" in Fig. 3.5), where heat is removed. The gas then passes through the regenerator, where it is precooled before reaching the cold heat exchanger ("Cold HX"); at the same time the gas contained in the acoustic network ("Thermal buffer, "Inertance Tube", "Compliance tank") is propelled forward too, even when the pistons reach their compression limit, due to the initial inertia provided by the pressure

wave generator. This way, gas is driven away from the cold heat exchanger, and the remaining expanded, gathering heat from the cold head and its surroundings, i.e. the Copper mounting in contact with the crystal. When the pistons withdraw, the Helium is pulled back, followed by the gas in the acoustic network, and the compression in the heat exchanger area begins again. Finally, the pistons initiate another cycle.

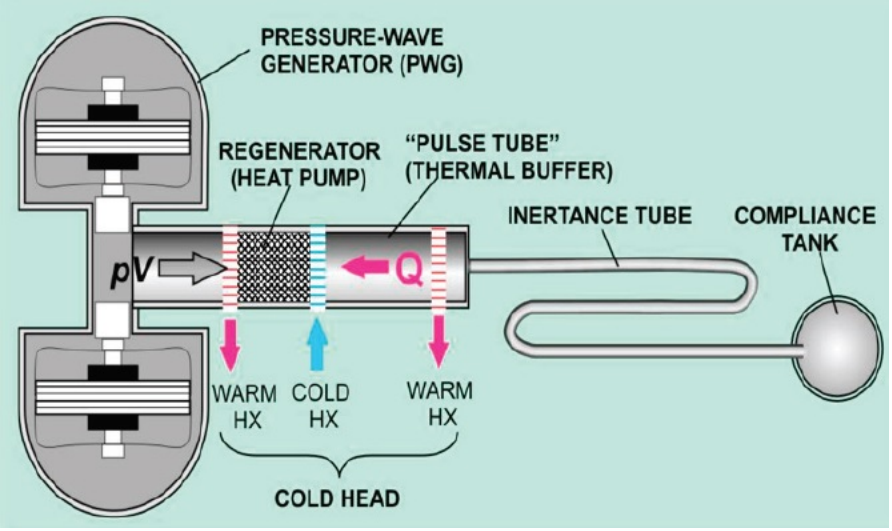

FIGURE 3.5: Operation schematics from the Q-drive 2s132K's manual.

For the cryocooler model we employed, the inertance tube was positioned after the pressure wave generator and before the cold head; the latter was positioned underneath the compliance tank, as Fig. 3.6 shows. Furthermore, the heat exchangers were water-cooled through an external water loop, although in other models these are air-cooled.

FIGURE 3.6: Q-drive 2s132K: cold head and motor pressure wave generator.

Requiring 600 W of electrical power, the unit had a Coefficient of Performance (COP = electrical power, W_e, over heat load extraction power, W_h) shown on the left y-axis of Fig. 3.7, where the linear dependence of the heat load extraction capacity (Q_c, right y-axis) on temperature was taken from the 2s132K's datasheet.

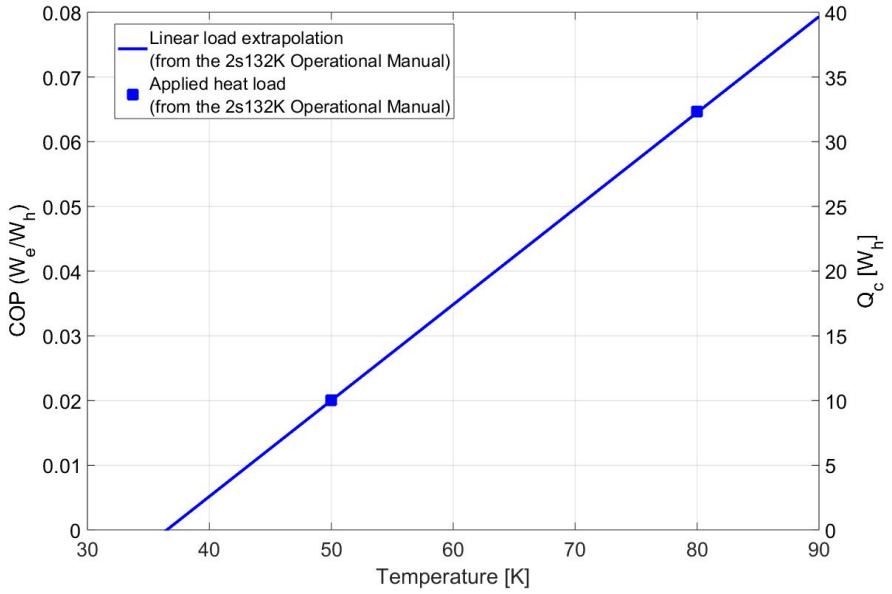

FIGURE 3.7: Q-drive 2s132K's COP (left axis) and Heat load extraction (right axis), from 2s132K's operational manual.

With a heat extraction capacity of $\sim 30\ W$ at $77\ K$, this unit provided a good cooling system not only for the small-signal absorption measurements, which required nearly no heat extraction given the low power density deposited in the crystal, but also for the high power Nd:YAG laser we will present in Chapter 6.
The typical operating voltage and frequency of the unit were $(90 - 105)\ V$, and 60 Hz, respectively. Thanks to the electronics driving the cryocooler, the user could choose a set temperature, which the unit would maintain, adjusting its operating voltage (effectively changing the cool-down rate) by performing a in-built PID (Proportional Integral Derivative) algorithm. This way, we could perform small-signal absorption measurements for several fixed temperatures in the range (LNT-RT).

3.2.2 Doping-ion concentration measurements

The exact doping-ion concentration for a crystal can be sometimes unknown due to fabrication tolerances or lack of traceability. Here, we present a novel methodology where we employ the measured absorbance and a reference absorption cross section spectrum to identify more precisely the doping-ion concentration.
Eq. (2.2) can be used to calculate either $\sigma_{abs}(\lambda)$ or $C_{\%}$. To determine $C_{\%}$, the usual

practice is to measure $\alpha_{abs}(\lambda)$ for a fixed wavelength λ^*, usually one corresponding to the strongest absorption line, and applying Eq. (2.2), with $\sigma_{abs}(\lambda^*)$ known from trusted sources. In order to minimise the error on the doping-ion concentration determination, or rather, increase the confidence in its value, we employed Eq. (2.2) in the form of Eq. (3.1) using several different values, λ_i, corresponding to different absorption peaks, i, of known $\sigma_{abs}(\lambda_i)$, and averaged, the (ideally identical, but in reality not) results.

$$C_{\%}(\lambda^*) = \frac{\alpha_{abs}(\lambda^*)}{\sigma_{abs}(\lambda^*)N_0} = \frac{\ln(\frac{I_{in}(\lambda^*)}{I_{out}(\lambda^*)})}{\sigma_{abs}(\lambda^*)N_0 L} \tag{3.1}$$

We minimised the calculation times by developing an algorithm that could be employed for virtually all rare earth-doped crystals, if the absorption cross section spectrum of the sample tested is available. As an example, we illustrate how we measured the doping-ion concentration of a Nd:YAG crystal.

The applicability of this methodology is limited by the smallest bandwidth between the available absorption cross section data's and the probe spectrum's; provided that they both extend over more than one absorption peak, the algorithm can be employed. In our experiment, the known absorption cross section data was rather extensive, in the range (750-950) nm [5, 13], however the probe's bandwidth was in the range of (760-850) nm, effectively restricting our analysis to the latter wavelength interval. A wider overall wavelength range would possibly provide more absorption lines to be employed, resulting in a more accurate doping-concentration value; however this accuracy could also be affected by the crystal structure, i.e. the quality of the crystal, and the homogeneity of the doping and the active ions sites.

Fig. 3.8 shows an example of the measured probe's input ($P_{in}(\lambda)$) and output ($P_{out}(\lambda)$) spectra, in dashed-black and blue lines, respectively. The fact that our source's spectrum extended not only over the absorption features of the crystal, but also over no-absorption areas, allowed the removal of the broadband background losses. The latter could be due to Fresnel reflections or the wavelength-response of the anti-reflection coatings, and, as detailed in Section 2.2 and Eq. (2.6), can be regarded as an additional term to the absorption spectrum $A(\lambda)$ we are interested in. This additional term was estimated by choosing two areas (if possible on opposite limits of the spectrum) where the absorption was negligible and performing a linear fit to the experimental points in the chosen ranges, as in Fig. 3.9. The fitted line was then subtracted from the absorption spectrum, obtaining the corrected absorption spectrum, the red lines in Fig. 3.8. The proof that this correction worked optimally was given by the fact that the ground of the corrected absorption spectrum $A(\lambda)$ was zero within the noise level of the measurement, as the red line in the top plot of Fig. 3.8 shows.

Once the absorption spectrum was corrected for broadband losses, the algorithm chose the wavelengths λ_i corresponding to the strongest peaks $\sigma_{abs}(\lambda_i)$ of the known cross section spectrum (in this case from [5]), as in Fig. 3.10. As it is known that the absorption cross section spectrum changes with temperature [19], we also took into account the

temperature of the crystal, monitored throughout the whole measurement.

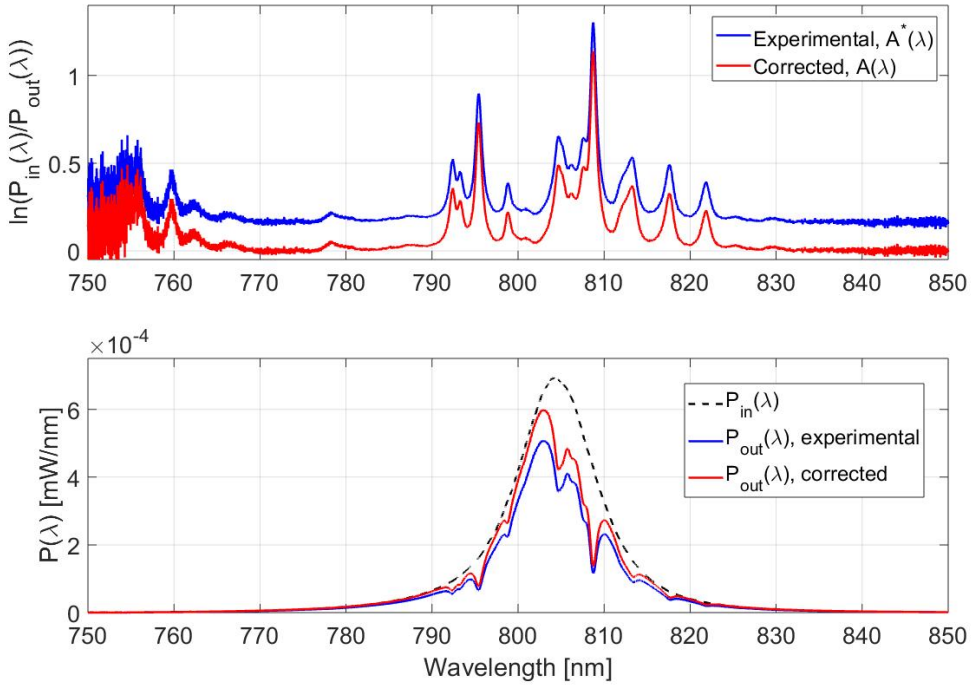

FIGURE 3.8: Top: original $A^*(\lambda)$ (blue) vs corrected $A(\lambda)$ (red) absorption spectra. Bottom: original (blue) and corrected (red) transmitted probe signal.

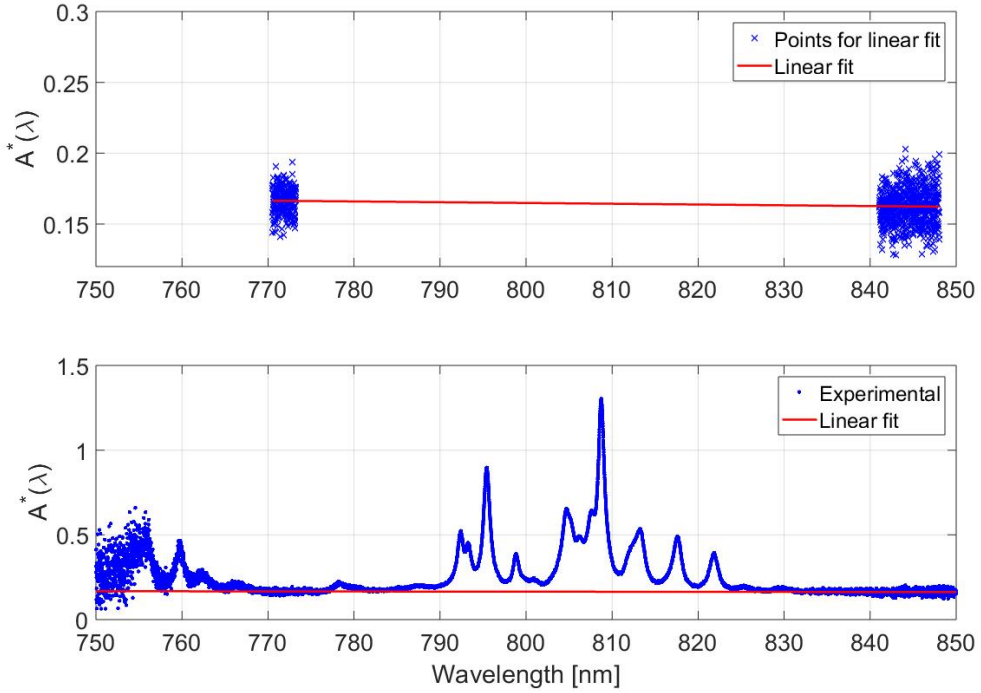

FIGURE 3.9: Linear fit (red) to areas with negligible absorption (top), and and overview on the whole measured spectrum (bottom).

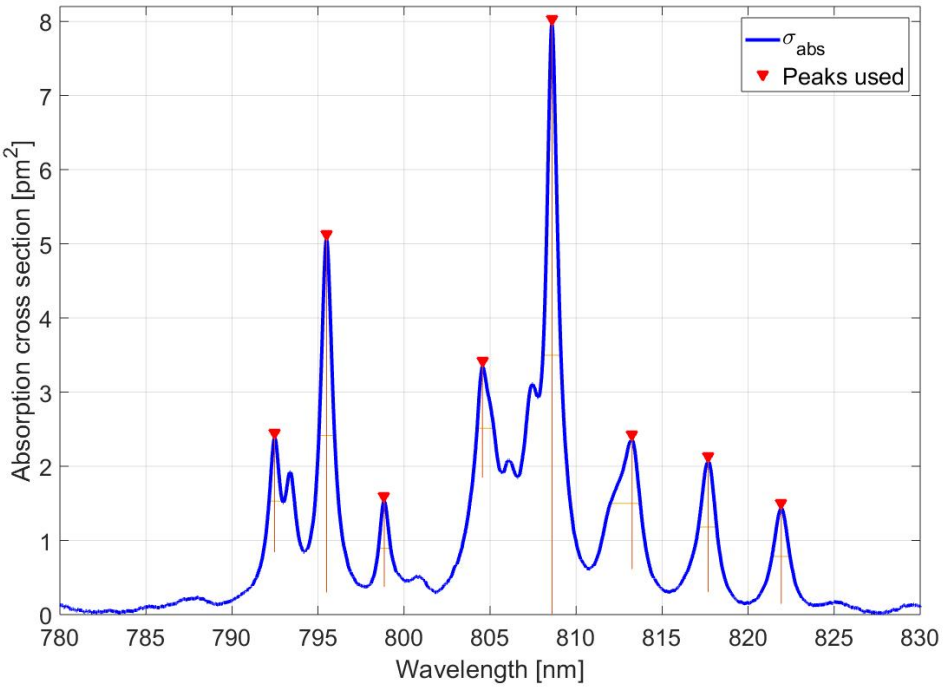

FIGURE 3.10: Nd:YAG: reference absorption cross section spectrum and absorption peaks chosen for the analysis.

When the cross section data for the crystal's exact temperature was not available, we used two other data sets, one collected at a higher temperature and one at a lower, and a linear approximation for the absorption cross section variation vs temperature, valid for very small temperature changes, whilst also accounting for the peaks' spectral-shift. This way, we could retrieve peak absorption cross section values at the desired temperature. Fig. 3.11 shows an example of this procedure, employed for a Nd:YAG sample being measured at an experimental temperature of $T = 293\ K$, where absorption cross section spectra were only available for temperatures of $T = 273\ K$ and $T = 296\ K$. To illustrate, Fig. 3.11 only shows the 808 nm peak, however the same procedure was applied to all the other peaks $\sigma_{abs}(\lambda_i)$ chosen in Fig. 3.10. Therefore, the peak absorption cross section values retrieved from known absorption data for the right temperature, $\sigma_{abs}(\lambda_i)$, and the measured absorption data peak values at the same wavelengths, $A(\lambda_i)$, were ready to be used. Eq. (3.1) was employed for each absorption peak $\sigma_{abs}(\lambda_i)$ at the respective wavelength λ_i, for which the doping-ion concentrations $c_{\%,i}$ were calculated. Ideally, all the $c_{\%,i}$ would be the same, but in reality they were not; hence, their average value was calculated and regarded as the doping-ion concentration for the crystal tested. The standard deviation from the average was associated to this measurement as its

uncertainty, as in Eqs. (3.2a) and (3.2b).

$$C_{\%} = \frac{1}{N}\sum_{i=1}^{N} c_{\%,i} = \frac{1}{N}\sum_{i=1}^{N} \frac{\alpha_{abs}(\lambda_i)}{\sigma_{abs}(\lambda_i) N_0} \tag{3.2a}$$

$$\Delta C_{\%} = \sqrt{\frac{1}{N-1}\sum_{i=1}^{N} |c_{\%,i} - C_{\%}|^2} \tag{3.2b}$$

with N the total number of available peaks. The analysis stopped here when measuring cubic crystals, like the Nd:YAG in the example, whereas it had to be taken one step further when employing uni-(or bi-)axial crystals, like Nd-doped vanadates or fluorides.

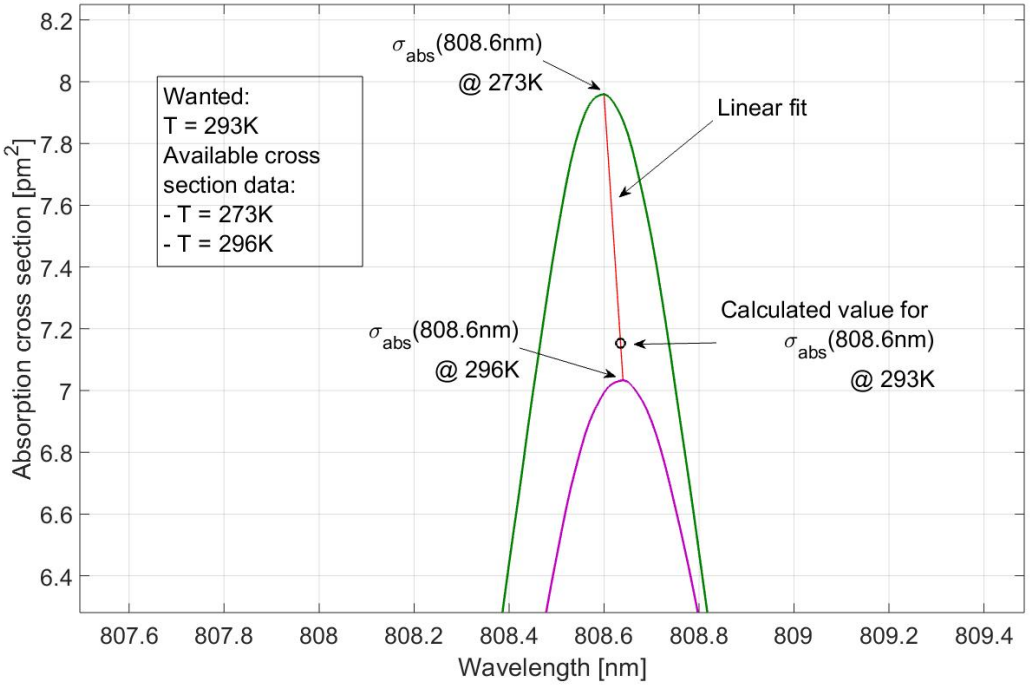

FIGURE 3.11: Details of how peak absorption cross section values for a fixed temperature are retrieved, when the absorption cross section data for the given temperature is not available. 808 *nm* peak of Nd:YAG.

In the case of non-cubic crystals (e.g. Nd:YVO_4, Nd:$GdVO_4$ and Nd:YLF), we kept the polarised pump fixed, and repeated the measurement after rotating the crystal, in order to access the different polarisation axes. Then re-applied the procedure detailed above using the appropriate polarisation-dependent absorption cross section spectrum. For the majority of the measurements, as expected, we found that the polarisation-dependent average concentrations, $C_{\%,j}$, were compatible within uncertainty, when accessing the different polarisation axes j. In this case, the final concentration of the crystal was the weighted average of the $C_{\%,j}$ with their respective standard deviations $\Delta C_{\%,j}$, and the uncertainty associated to it was chosen to be the standard error of the weighted mean;

in formulae:

$$C^*_{\%} = \frac{\sum_{j=1}^{2(3)} \Delta C_{\%,j} C_{\%,j}}{\sum_{j=1}^{2(3)} \Delta C_{\%,j}} \tag{3.3a}$$

$$\Delta C^*_{\%} = \sqrt{\frac{1}{\sum 1/\Delta C^2_{\%,j}}} \tag{3.3b}$$

It's worth mentioning that, even in the case of non-cubic samples, the last passage was in most cases unnecessary as the majority of our applications and according modelling are polarisation-dependent. For these applications and modelling we simply used the appropriate $C_{\%,j}$. Furthermore, the further averaging of the $C_{\%,j}$ for different polarisations usually results in the increase in the error associated to the final concentration $C_{\%}$, as the dispersion of the single $c_{\%,i,j}$ around the final average increases. As the only change in our experimental conditions between the measurements for the different polarisations is the orientation of the crystal, the increase in dispersion might be due to the different relative precisions of the reference polarised spectra employed. This is however not disruptive, because the typical error on the doping-concentration for the cubic YAG crystals was less than 1%, as discussed in Section 3.3.1 and detailed in Table 3.2. This error increased to $< 5\%$ in the case of the uniaxial Nd-doped orthovanadates (see Table 3.4). Overall still a rather small uncertainty on this key parameter for modelling laser performance.
This methodology provides the doping-ion concentration, $C_{\%}$, and its uncertainty, $\Delta C_{\%}$, as a general property of the crystal tested: this parameter is key when performing measurements that are not strictly related to a particular wavelength, like the absorption cross section measurements that we will present in the next section.

3.2.3 Absorption cross section measurements

In this section we present the thorough characterisation of the $^2H_{9/2} + {}^4F_{5/2}$ absorption cross section and its dependence upon temperature for two Nd-doped vanadate crystals, Nd:YVO_4 and Nd:$GdVO_4$, in the range from RT to 450K. During these measurements the crystal was positioned on a heated Copper mount, the temperature of which could be controlled in the mentioned range.
We measured the absorption coefficient for two different concentrations (nominally 0.5at.% and 1.0at.%, see Table 3.4) of the two available type of crystals in the range from RT to 450K and, using the parameters $C_{\%}$ from Table 3.4 in Eq. (2.2), we retrieved the absorption cross section spectra $\sigma_{abs}(\lambda)$. From the excellent agreement between the spectra of the different concentrations of the same kind of samples (Nd:YVO_4 and Nd:$GdVO_4$) we also confirmed the validity of the previous doping-ion concentration measurements.
Consistent with the theme of this thesis, cryogenically cooled lasers, we characterised

the absorption cross section around 808 nm for Nd:YAG in the sub-ambient temperature range (LNT-RT). Here we employed the setup presented in Chapter 3 and shown in Fig. 3.1, with the 1 mm-long, 0.6at.%-doped, Nd:YAG crystal mounted as in Fig. 3.4, in the cryocooler Q-drive 1s132K described above.

3.3 Results and discussion

3.3.1 Doping-ion concentration

Once developed the measurement procedure, we measured the concentration of several different Nd-doped samples and compared it to the nominal value provided by the suppliers. Tables 3.2 and 3.4 summarise our results; we have dedicated a separate table to the Nd-doped vanadate samples because those results will be of particular interest for successive analysis.

The discrepancy between the nominal and measured values of doping-ion concentration was found to be up to 30%, as in the case of the higher doping Nd:YAG samples provided by Altechna. The Nd:YLF samples, grown in-house at Pisa University for spectroscopy measurement purposes, present a very high discrepancy with the measured $(0.888 \pm 0.002)\ at.\%$ value for the highest nominal doping level, 2.5at.%. This is likely due to a mistaken labelling.

The results reported in Table 3.2 show that the precision of the measurement is rather high, with a typical standard deviation below 1%. The accuracy of the technique, however, needs to be discussed further. To illustrate how the standard deviation from the average is also a legitimate accuracy indicator, we reported, in Table 3.3, the details of two different measurements performed on the same, nominally 0.6at.%-doped Nd:YAG sample (CLaser no. 5).

Both Measurement 1 and 2 were executed employing the methodology detailed in Section 3.2.2 and the results obtained via Eq. (3.2a). The difference between the two were as follows: Measurement 1 was executed with a resolution of 0.2 nm and sensitivity setting "Medium" (OSA ANDO AQ6317B), whereas Measurement 2 with a higher resolution of 0.01 nm and sensitivity setting "High 2". It is appreciable that the dispersion of Measurement 1's values around their average was nearly 3 times larger than the respective Measurement 2's. Furthermore, the fact that the calculated concentration corresponding to the highest cross section peak at 808.6 nm was the lowest of the data set suggests that the peak was not optimally resolved. Measurement 2, on the other hand, appears overall more consistent, resulting in a lower standard deviation from the average doping-ion concentration value. Given the low dispersion of Measurement 2's values, it is arguable that this measurement also provided the highest accuracy. We can draw this conclusion because all the single doping values, $c_{\%,i}$, are obtained within one measurement, and therefore the exact same experimental conditions, systematic

and human errors apply to all the data points. A factor of 3 difference in the standard deviation from the average value can only be attributed to the lower quality of the data set, hence less accurate measurement.

Vendor	Sample, no.	Dimensions [mm]	Nom. $C_{\%}$ [at.%]	Meas. $C_{\%}$ [at.%]
CLaser	Nd:YAG, 1	3x3x15	0.3	0.366 ± 0.002
	Nd:YAG, 2			0.369 ± 0.002
	Nd:YAG, 3			0.365 ± 0.002
	Nd:YAG, 4			0.371 ± 0.002
	Nd:YAG, 5			0.367 ± 0.002
CLaser	Nd:YAG, 1	3x3x7.5	0.6	0.733 ± 0.004
	Nd:YAG, 2			0.734 ± 0.003
	Nd:YAG, 3			0.735 ± 0.003
	Nd:YAG, 4			0.734 ± 0.004
	Nd:YAG, 5			0.734 ± 0.009
Altechna	Nd:YAG	$d = 5, L = 1.05$	0.1	0.110 ± 0.004
	Nd:YAG	$d = 5, L = 1.05$	0.4	0.633 ± 0.005
	Nd:YAG	$d = 5, L = 1.10$	0.7	0.740 ± 0.007
	Nd:YAG	$d = 5, L = 1.08$	1.0	1.333 ± 0.008
	Nd:YAG	$d = 5, L = 1.10$	1.3	1.841 ± 0.008
Castech	Nd:YAG, 1	3x3x1.09	1.1	1.038 ± 0.007
	Nd:YAG, 2	3x3x1.09	1.1	1.069 ± 0.008
	Nd:YAG, 3	3x3x1.09	1.1	1.035 ± 0.006
	Nd:YAG, 4	3x3x1.08	0.6	0.570 ± 0.006
Pisa Univ.	Nd:YLF	4.5x4x1.06	1.0	1.052 ± 0.006
	Nd:YLF	4x3x1.15	1.5	1.840 ± 0.030
	Nd:YLF	4.3x3x1.06	2.5	0.888 ± 0.002

TABLE 3.2: Concentration measurements results for different Nd-doped crystals.

Ultimately, although the procedure we have developed is very reliable and self-consistent, we have to remember that it strongly depends on employing both an appropriate instrument resolution and reliable absorption cross section data to reference the peaks to. It is therefore paramount that its source is reliable in order for the doping-ion concentration measurement to be accurate.

The results for the doping-ion concentration measurement executed on the Nd:YVO_4 and Nd:$GdVO_4$ samples are summarised in Table 3.4. With small signal absorption measurements performed in the band (780-830) *nm* around the peak absorption at 808 *nm*,

for both polarisations σ-pol and π-pol, there were on the order of 7 peaks available (N). For this measurement, we assumed reference peaks from [5, 13].

Wavelength λ_i [nm]	$\sigma_{abs}(\lambda_i)$ [pm^2]	$c_{\%,i}$ [at.%] Measurement 1	$c_{\%,i}$ [at.%] Measurement 2
792.53	2.22	0.6810	0.7311
795.53	4.59	0.6881	0.7297
798.88	1.41	0.6718	0.7246
804.59	3.15	0.7117	0.7255
808.64	7.15	0.6626	0.7308
813.27	2.31	0.7258	0.7412
817.69	2.02	0.7147	0.7427
821.93	1.39	0.7171	0.7485
		0.697 ± 0.024	0.734 ± 0.009

TABLE 3.3: Concentration measurement's details for the CLaser 0.6at.% Nd:YAG no. 5.

Sample	Dimensions [mm]	Nominal $C_{\%}$ [at.%]	Measured $C_{\%}$ [at.%]
Nd:YVO_4	3x3x1.09	0.5	0.60 ± 0.02
Nd:YVO_4	3x3x1.03	1.0	0.97 ± 0.02
Nd:$GdVO_4$	3x3x1.03	0.5	0.54 ± 0.03
Nd:$GdVO_4$	3x3x1.03	1.0	1.15 ± 0.03

TABLE 3.4: Doping ion concentration measurements for Nd:YVO_4 and Nd:$GdVO_4$: results and associated uncertainties.

3.3.2 Absorption cross section's temperature dependence

3.3.2.1 Nd-vandates at elevated temperatures

The results for the measurement of the ${}^2H_{9/2} + {}^4F_{5/2}$ absorption cross section and its dependence upon elevated temperatures in the range from RT to 430 K, for Nd:YVO_4 and Nd:$GdVO_4$, are shown in Figs. 3.12 to 3.14.

The highest peak for the π-polarisation absorption cross section of Nd:YVO_4, centred at (808.90 ± 0.05) nm, decreased from (58.6 ± 0.2) pm^2 at 291 K to (30.9 ± 0.6) pm^2 at 430 K, the bandwidth (FWHM) broadened from (1.25 ± 0.02) nm to (2.29 ± 0.02) nm, and red-shifted (0.20 ± 0.05) nm between the lowest and the highest temperature. The maximum value for the σ-polarised spectrum, centred at (808.80 ± 0.05) nm, reduced from (12.4 ± 0.2) pm^2 to (6.6 ± 0.2) pm^2, also red-shifting by (0.20 ± 0.05) nm over the whole temperature range.

Similarly, for Nd:$GdVO_4$ the strongest peak is for the π-polarisation absorption cross

section, centred at (808.60 ± 0.05) nm, decreasing from (54.0 ± 0.3) pm^2 at 293 K to (25.7 ± 0.5) pm^2 at 453 K and broadening from (1.51 ± 0.02) nm to (2.74 ± 0.02) nm. The σ-polarisation strongest peak, centred at (808.80 ± 0.05) nm, decreases from (11.9 ± 0.2) pm^2 at 293 K to (6.6 ± 0.1) pm^2 at 453 K. Both peaks show a (0.10 ± 0.05) nm redshift from RT to the highest temperature.

Furthermore, we retrieved the maximum amplitude of the strongest absorption cross section peaks for the spectra associated with the two polarisation axes and fit the data sets to second degree polynominal functions, dependent upon the crystal's temperature. The results are displayed in Figs. 3.16 and 3.17 and summarised in Tables 3.5 and 3.6. These results show that generally the absorption cross section decreases, while its bandwidth increases, with increasing temperature. With an equivalent behaviour of the emission cross section [15, 16], the overall gain of Nd-doped vanadate lasers decreases with increasing temperature, and hence their performance could be severely affected by the strong temperature gradients created within the pumped region. This dependence may be crucial for efficient diode-pumped Nd-doped orthovanadate lasers.

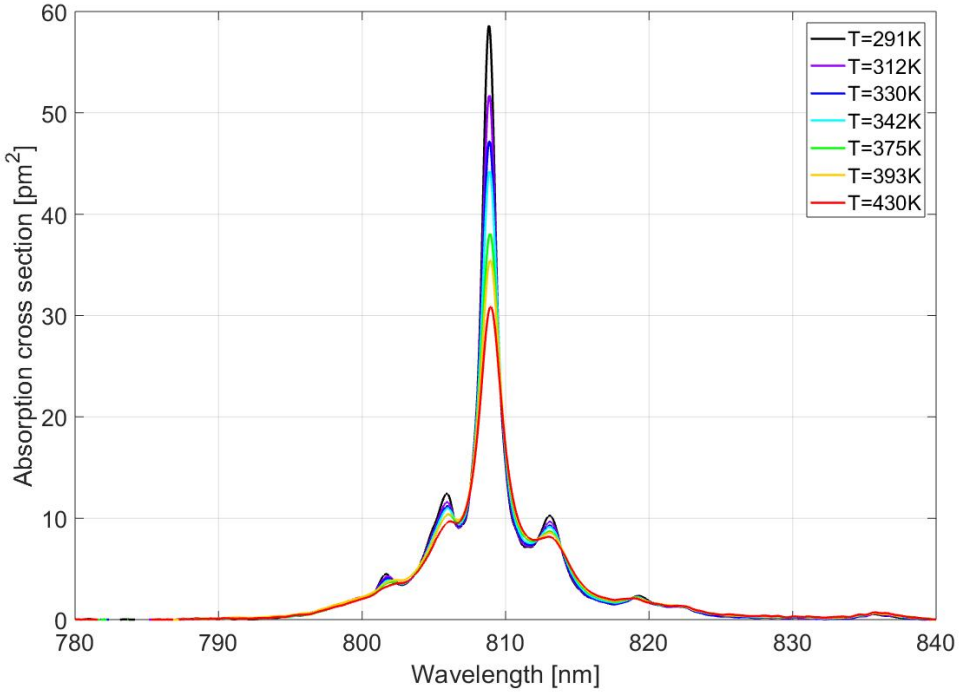

FIGURE 3.12: Nd:YVO_4 absorption cross section, π-pol.

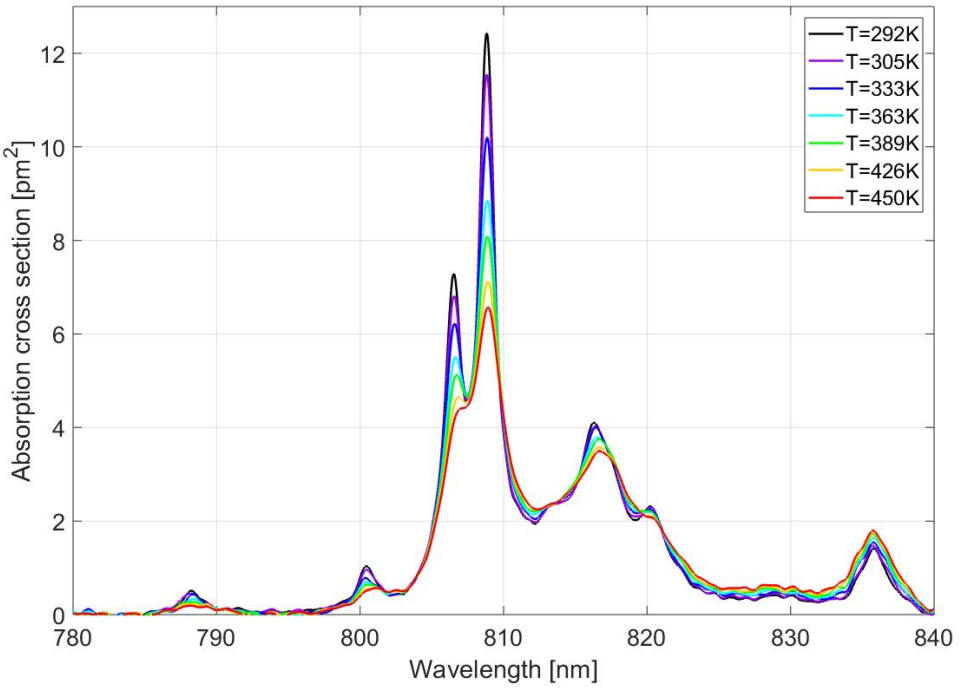

FIGURE 3.13: Nd:YVO_4 absorption cross section, σ-pol.

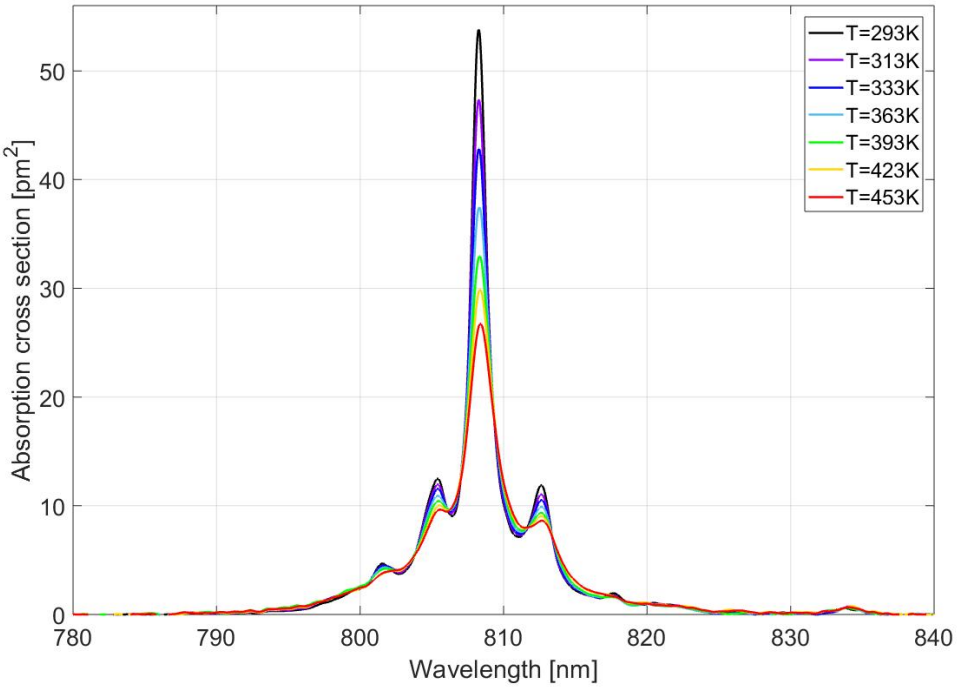

FIGURE 3.14: Nd:$GdVO_4$ absorption cross section, π-pol.

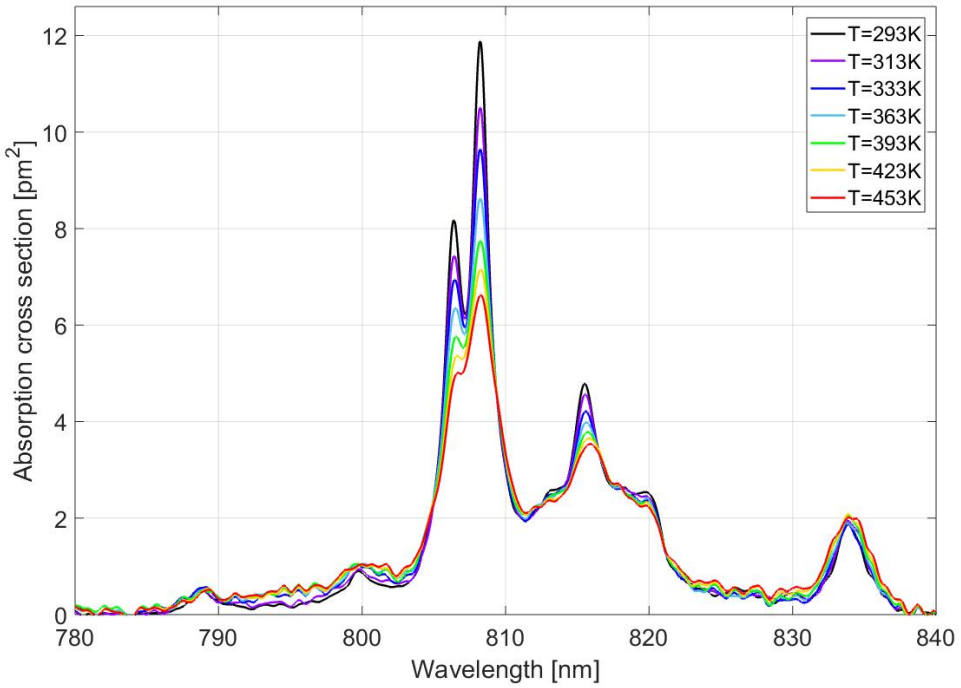

FIGURE 3.15: Nd:$GdVO_4$ absorption cross section, σ-pol.

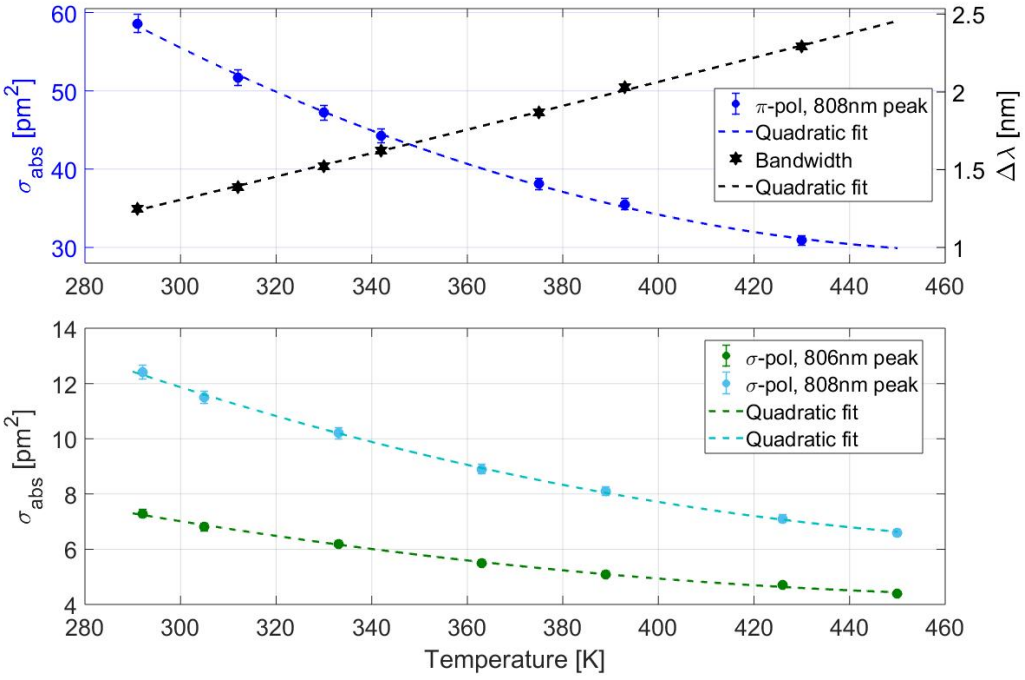

FIGURE 3.16: Polynomial fits to the dependence of absorption cross section peaks vs temperature in Nd:YVO_4. Secondary y-axis: FWHM ($\Delta\lambda$, bandwidth) for the π-pol peaks vs temperature.

Model: $p_1 + p_2T + p_3T^2$			
	p_1	p_2	p_3
$\sigma_{abs,\pi}(808)\ [pm^2]$	221.56	-0.809	8.5e-4
$\Delta\sigma_{abs,\pi}(808)\ [nm]$	-0.767	0.006	1.7e-6
$\sigma_{abs,\sigma}(808)\ [pm^2]$	40.28	-0.135	1.3e-4
$\sigma_{abs,\sigma}(806)\ [pm^2]$	21.91	-0.071	7.2e-5

TABLE 3.5: Nd:YVO_4: Second degree polynomial fit coefficients for σ_{abs} vs T dependence.

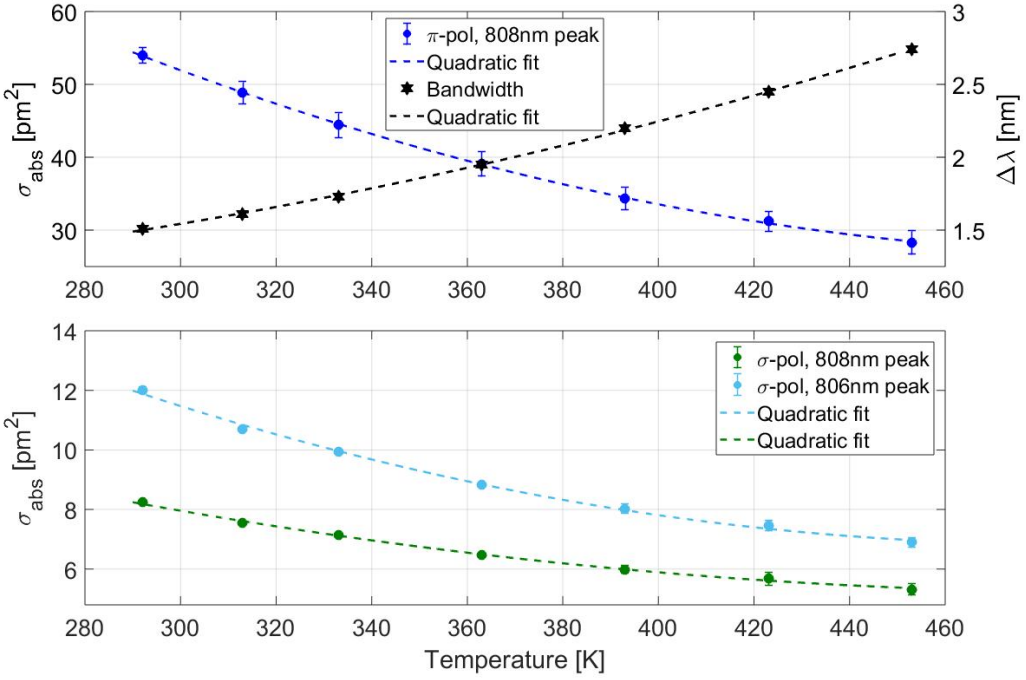

FIGURE 3.17: Polynomial fits to the dependence of absorption cross section peaks vs temperature in Nd:$GdVO_4$. Secondary y-axis: FWHM ($\Delta\lambda$, bandwidth) for the π-pol peaks vs temperature.

Model: $p_1 + p_2T + p_3T^2$			
	p_1	p_2	p_3
$\sigma_{abs,\pi}(808)\ [pm^2]$	176.04	-0.586	5.7e-4
$\Delta\sigma_{abs,\pi}(808)\ [nm]$	1.285	-0.004	1.5e-05
$\sigma_{abs,\sigma}(808)\ [pm^2]$	38.82	-0.132	1.4e-4
$\sigma_{abs,\sigma}(806)\ [pm^2]$	22.53	-0.069	7.0e-5

TABLE 3.6: Nd:$GdVO_4$: Second degree polynomial fit coefficients for σ_{abs} vs T dependence.

The values of the peak absorption cross section for Nd:YVO_4 and Nd:$GdVO_4$ presented in the literature vary across a wide range. Sato et. al. [7] report an absorption cross section for Nd:YVO_4 and Nd:$GdVO_4$ of $\sim 50\ pm^2$ and $\sim 25\ pm^2$, respectively; while the spectroscopy database in Czeranowsky's Ph.D. thesis [13] reports $\sim 60\ pm^2$ for Nd:YVO_4 and $\sim 54\ pm^2$ for Nd:$GdVO_4$, as does one of his publications [6]; Lupei also reports a peak value for Nd:$GdVO_4$ of $\sim 55\ pm^2$ [17]. Furthermore, other values published by our group [5] are around $60\ pm^2$, in agreement with the results from this work. It is not unlikely that, as emphasised earlier in this chapter, the absorption cross section measurements can be spoilt by an incorrect assumption for the value of the doping-ion concentration of the sample investigated.
Finally, these measurements underpinned the ETU coefficient characterisation on the same crystals and over the same temperature range, presented in Chapter 5.

3.3.2.2 Nd:YAG at sub-ambient temperatures

In this section we report the thorough characaterisation of the ground absorption cross section into the ${}^2H_{9/2} + {}^4F_{5/2}$ energy levels in Nd:YAG, for temperatures spanning from RT to Liquid Nitrogen Temperature (LNT).
Cryogenically cooled Nd:YAG is the focus for this study in power-scaling the sub-1 μm transition at 946 nm, ${}^4F_{3/2} \rightarrow {}^4I_{9/2}$. Moreover, although we exploit in-band pumping at 869 nm, to demonstrate this, as we discuss in Chapter 6, it was necessary to accurately study the ground state absorption characteristics that would underpin the subsequent and important measurement of the ETU coefficient over the same range of temperatures, as reported in Section 5.3.3. Besides providing a solid base to build the ETU coefficient measurement upon, this detailed characterisation represents a valuable set of information for the engineering of 808-nm-pumped cryogenically cooled Nd:YAG lasers. Furthermore, these results at cryogenic temperatures have a better resolution than previously published values [20, 21, 22].
The characterisation of the Nd:YAG's absorption cross section around 808 nm was performed via small-signal absorption measurements, as detailed in Section 3.2.3, employing a 1.08 mm-long, 0.57at.%-doped Nd:YAG crystal (Castech n.4 in Table 3.2). The spectra were measured with a resolution of 0.01 nm in order to suitably resolve the sharp features of the low-temperature spectra that we present below. The temperature-dependent spectra are shown in Fig. 3.18: the absorption peaks' intensity increase while their bandwidths reduce, with decreasing temperature, as reported in other works [19, 20]. The strongest absorption peak, at $\sim 808\ nm$ (Fig. 3.19), exploited in the ETU coefficient measurements presented in Chapter 5, increased from $(6.9 \pm 0.3)\ pm^2$ at RT to $(42.3 \pm 2.1)\ pm^2$ at LNT, it blueshifted by $(0.21 \pm 0.02)\ nm$ while its bandwidth decreased from $(0.93 \pm 0.02)\ nm$ to $(0.21 \pm 0.02)\ nm$ over the same temperature range, as shown in Fig. 3.20. This four-fold decrease in bandwidth provides a challenge for

diode-pumping, introducing the requirement of wavelength stabilisation in order to maximise absorption.

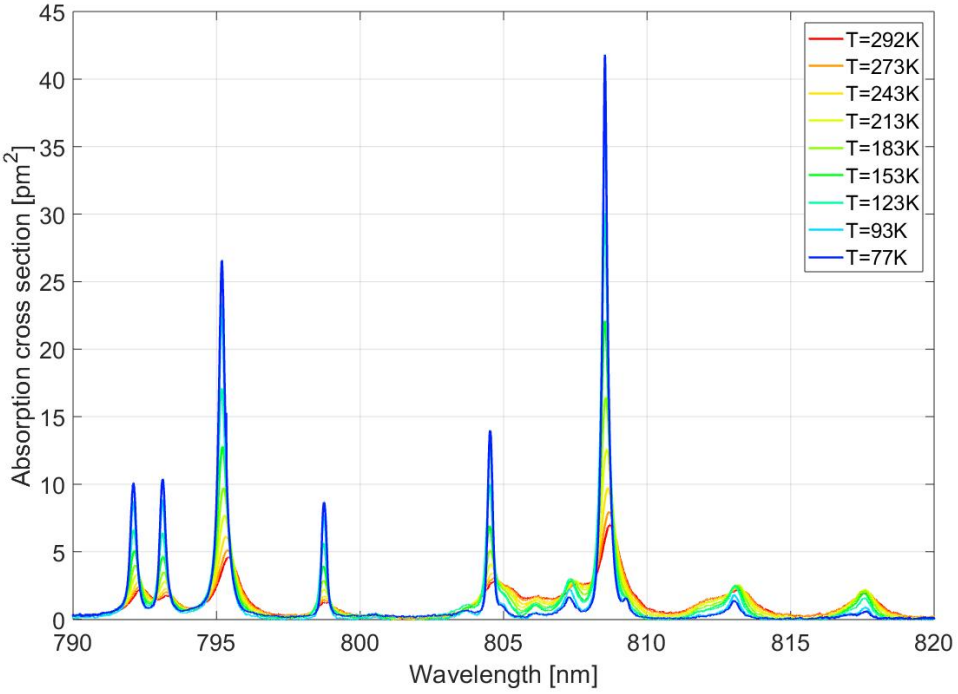

FIGURE 3.18: Nd:YAG absorption cross section for temperatures in the range (RT-LNT).

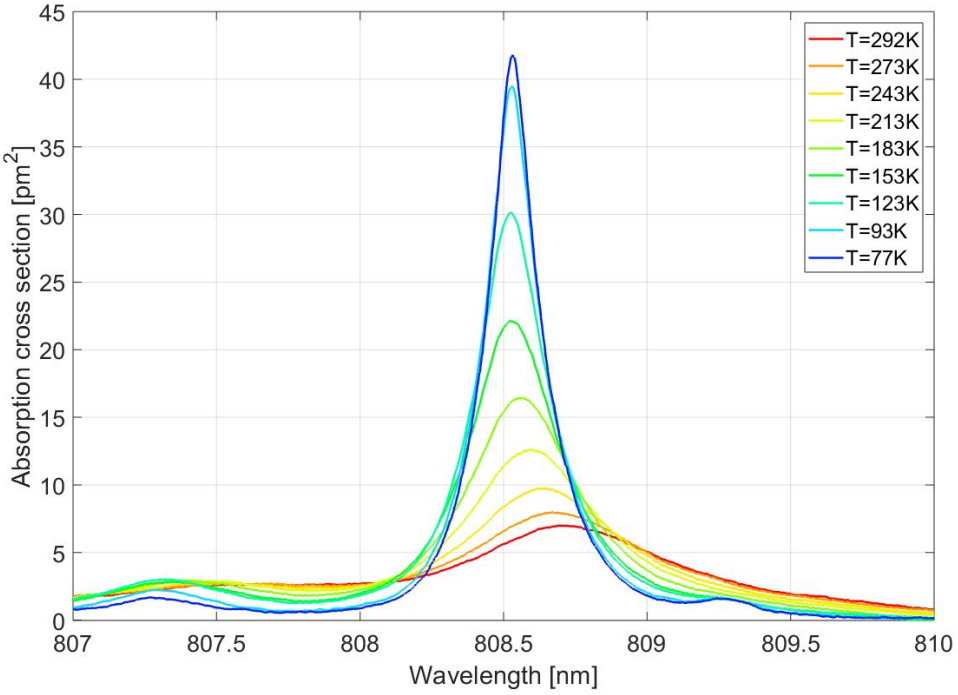

FIGURE 3.19: Nd:YAG absorption cross section for temperatures in the range (RT-LNT), 808 *nm* peak detail.

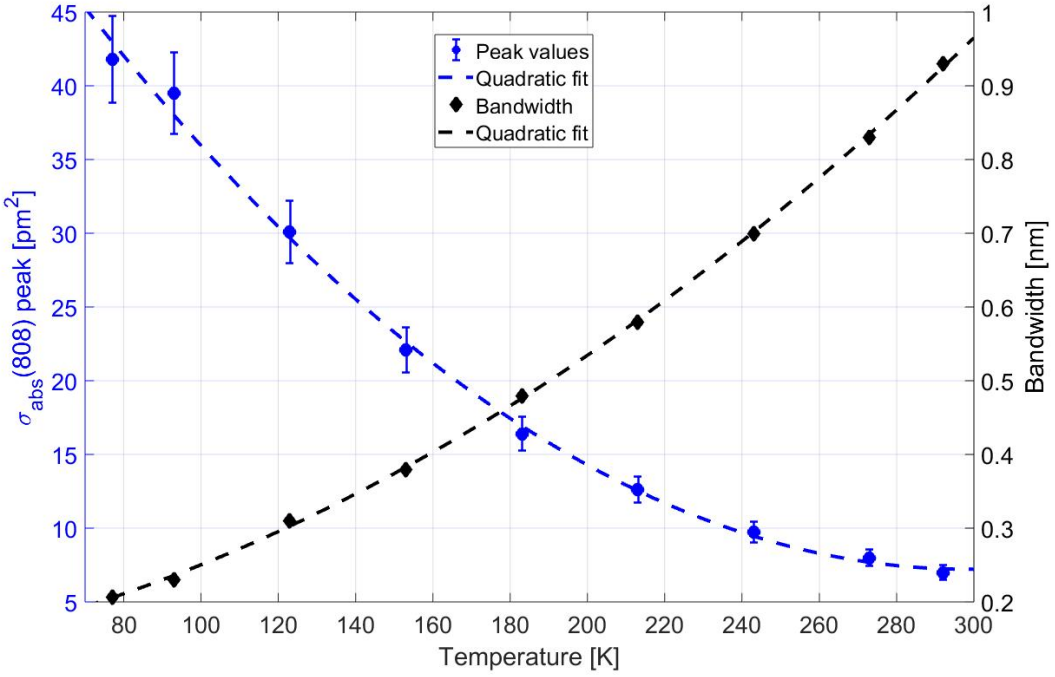

FIGURE 3.20: Nd:YAG absorption cross section 808 nm peak values (blue circles) for temperatures in the range (RT-LNT), their relative bandwidths (black diamonds), and their respective second degree polynomial fitting curves (dashed blue and black, respectively).

Notwithstanding, we were able to utilise this peak for the ETU coefficient measurements presented in Section 5.3.3, as the bandwidth decrease didn't affect the effectiveness of Ti:sapphire-pumping, thanks to its narrow linewidth ($< 0.2\ nm$). A similar decrease in bandwidth has been demonstrated for the 869 nm absorption peak too, well characterised and reported in [5, 21]. We exploited this absorption peak for in-band pumping via an in-house built Volume Bragg Grating (VBG)-locked diode-bar, presented in Chapter 6. The temperature dependence of both the amplitude of the 808-nm peak and its bandwidth are well described by a second degree polynomial. The fitting coefficients are displayed in Table 3.7.

Model: $p_1 + p_2T + p_3T^2$			
	p_1	p_2	p_3
$\sigma_{abs}\ [pm^2]$	72.21	-0.44	4.35e-4
$\Delta\sigma_{abs}\ [nm]$	0.11	6.45e-4	7.32e-6

TABLE 3.7: Nd:YAG: Second degree polynomial fit coefficients for σ_{abs} vs T dependence.

3.4 Conclusions

In conclusion, in this chapter we have reported a general methodology for calculating with high precision and accuracy the doping-ion concentration of Nd-doped crystals. After classic small-signal absorption measurements, the broadband losses can be removed via automated fitting of the out-of-band ground and the collected data corrected, in order to obtain the absorption spectrum. Consequently, the effective doping-ion concentration could be calculated by averaging the calculated concentrations obtained at several absorption peaks, assuming a commons reference absorption cross section data-set. Exploiting this method, we have measured the doping-ion concentration of several different Nd-doped crystals, highlighting the useful insight that the dispersion of the calculated concentration values is linked to the precision and accuracy of the measurement.
Conversely, once the doping-ion concentration is known, the absorption cross section dependence upon other influencing parameters can be explored. As such, we characterised the elevated-temperatures absorption cross section in the ${}^4I_{9/2} \rightarrow {}^2H_{9/2} + {}^4F_{5/2}$ band for Nd:YVO_4 and Nd:$GdVO_4$ crystals, presenting values that will provide added knowledge for the operation of diode-pumped vanadate lasers under high thermal load and/or operational temperatures. Our results were within the range of values provided in the literature for these crystals.
Furthermore, we characterised the absorption cross section for the ${}^4I_{9/2} \rightarrow {}^2H_{9/2} + {}^4F_{5/2}$ transition in Nd:YAG in the low-temperature regime, providing improved precision with respect to what has been previously published for this important absorption transition. The absorption cross section characterisation of Nd-doped Vanadates and Nd:YAG in their respective temperatures ranges underpinned the measurement of the ETU coefficient for the same samples and temperature regimes, to be presented in the following chapter.
These simple yet powerful methods provide general tools that can be employed for several crystals.

References

[1] M. Saleh, S. Kakkireni, J. McCloy, and K. G. Lynn, "*Improved Nd distribution in Czochralski grown YAG crystals by implementation of the accelerated crucible rotation technique*," Optical Materials Express **10**, 632–644 (2020).

[2] V. Lupei and A. Lupei, "*Nd:YAG at its 50th anniversary: Still to learn*," Journal of Luminescence **169**, 426 – 439 (2016).

[3] J. L'huillier, G. Bitz, V. Wesemann, A. Borsutzky, and R. Wallenstein, "*A sensitive non-destructive method for measuring the Nd doping concentration in Nd:YAG with high spatial resolution*," Applied Physics B **77**, 601 – 606 (2003).

[4] A. A. Kaminskii, *Laser Crystals, Their Physics and Properties*, Springer Series in Optical Sciences (Springer, 1981).

[5] S. J. Yoon, "*Cryogenically-cooled neodymium-doped solid-state lasers*," Ph.D. thesis, University of Southampton (2016).

[6] C. Czeranowsky, M. Schmidt, E. Heumann, G. Huber, S. Kutovoi, and Y. Zavartsev, "*Continuous wave diode pumped intracavity doubled Nd:$GdVO_4$ laser with 840 mW output power at 456 nm*," Optics Communications **205**, 361 – 365 (2002).

[7] Y. Sato and T. Taira, "*Comparative study on the spectroscopic properties of Nd:$GdVO_4$ and Nd:YVO_4 with hybrid process*," IEEE Journal of Selected Topics in Quantum Electronics **11**, 613–620 (2005).

[8] T. Taira, "*RE^{3+}-Ion-Doped YAG Ceramic Lasers*," IEEE Journal of Selected Topics in Quantum Electronics **13**, 798–809 (2007).

[9] C. Wang, Y. Chow, L. Reekie, W. Gambling, H. Zhang, L. Zhu, and X. Meng, "*A comparative study of the laser performance of diode-laser-pumped Nd:$GdVO_4$ and Nd:YVO_4 crystals*," Applied Physics B **70**, 769–772 (2000).

[10] T. Jensen, V. C. Ostroumov, J. P. Meyn, G. Huber, A. I. Zagumennyi, and I. A. Shcherbkov, "*Spectroscopic characterization and laser performance of diode-laser-pumped Nd:$GdVO_4$*," Applied Physics B Photophysics Laser Chemistry **58**, 373–379 (1994).

[11] K. Shimamura, S. Uda, V. V. Kochurikhin, T. Taniuchi, and T. Fukuda, "*Growth and Characterization of Gadolinium Vanadate $GdVO_4$ Single Crystals for Laser Applications*," Japanese Journal of Applied Physics **35**, 1832–1835 (1996).

[12] H. Zhang, X. Meng, L. Zhu, J. Liu, C. Wang, and Z. Shao, "*Laser Properties at* 1.06 *μm for Nd:$GdVO_4$ Single Crystal Pumped by a High Power Laser Diode*," Japanese Journal of Applied Physics **38**, L1231–L1233 (1999).

[13] C. Czeranowsky, *Resonatorinterne Frequenzverdopplung von diodengepumpten Neodym-Lasern mit hohen Ausgangsleistungen im blauen Spektralbereich*, Berichte aus der Physik (Shaker, 2002).

[14] Y. Sato and T. Taira, "*Spectroscopic Properties of Neodymium-Doped Yttrium Orthovanadate Single Crystals with High-Resolution Measurement,*" Japanese Journal of Applied Physics Part 1 **41**, 5999–6002 (2002).

[15] Y. Sato and T. Taira, "*Temperature dependencies of stimulated emission cross section for Nd-doped solid-state laser materials,*" Optical Materials Express **2**, 1076–1087 (2012).

[16] G. Turri, H. P. Jenssen, F. Cornacchia, M. Tonelli, and M. Bass, "*Temperature-dependent stimulated emission cross section in Nd^{3+}:YVO_4 crystals,*" Journal of the Optical Society of America B **26**, 2084–2088 (2009).

[17] V. Lupei, N. Pavel, Y. Sato, and T. Taira, "*Highly efficient 1063-nm continuous-wave laser emission in Nd:$GdVO_4$,*" Optics Letters **28**, 2366–2368 (2003).

[18] J. Didierjean, E. Herault, F. Balembois, and P. Georges, "*Thermal conductivity measurements of laser crystals by infrared thermography. Application to Nd:doped crystals,*" Optics Express **16**, 8995–9010 (2008).

[19] T. Kushida, "*Linewidths and Thermal Shifts of Spectral Lines in Neodymium-Doped Yttrium Aluminum Garnet and Calcium Fluorophosphate,*" Physical Review **185**, 500–508 (1969).

[20] H. Glur, R. Lavi, and T. Graf, "*Reduction of thermally induced lenses in Nd:YAG with low temperatures,*" IEEE Journal of Quantum Electronics **40**, 499–504 (2004).

[21] S. J. Yoon and J. I. Mackenzie, "*Implications of the temperature dependence of Nd:YAG spectroscopic values for low temperature laser operation at 946 nm,*" Proc. SPIE 9135, Laser Sources and Applications II **913503** (2014).

[22] C. Y. Cho, T. L. Huang, H. P. Cheng, K. F. Huang, and Y. F. Chen, "*Analysis of the optimal temperature for the cryogenic monolithic Nd:YAG laser at 946-nm,*" Optics Express **24**, 1–8 (2016).

Chapter 4

Yb:$LuLiF_4$ spectroscopy at sub-ambient temperatures

4.1 Introduction

The advantages of Yb^{3+} over Nd^{3+} systems have already been introduced in Chapter 1: the energy-level structure of the first, i.e. with only a single excited-state due to its almost full 4f electron orbital [1], precludes parasitic energy-transfer effects like ETU, CR and ESA [2], allowing higher doping-levels than crystals with more complex level structures like Nd:YAG [3]. Furthermore, the low quantum defect between pump and lasing wavelengths ($\sim$ 8%) allows an accordingly low thermal load. The most exploited Yb-doped host, especially in the cryogenic-cooling regime, is Yb:YAG [4], however fluoride hosts have been widely employed thanks to their promising thermo-optical properties, e.g. a weak and negative thermo-optic coefficient and a low refractive index [5].

Although Yb:$LuLiF_4$ is a rather different crystal than the Nd:YAG exploited in the remaining part of this work, and a relatively new laser material [6], it has been recognised as a good candidate for operation under cryogenic-cooling, with the possibility of lasing on the sub-1 μm, 995 nm wavelength, and the generation of high energy pulses, thanks to its long upper-state lifetime (> 2 ms) [5]. Moreover, Yb:$LuLiF_4$ has been shown to have a slightly better laser performance at Room Temperature [7] than its more common isomorph Yb:YLF; the latter has in fact already been successfully exploited in the cryogenic-cooling regime [8, 9, 10, 11]. Table 4.1 summarises the key spectroscopic and thermo-optical properties of Yb:$LuLiF_4$ and two other widely employed Yb-doped fluoride hosts [2, 5, 12, 13, 14].

Fig. 4.1 shows the possible electronic transitions between the ground $^2F_{7/2}$ and the excited $^2F_{5/2}$ manifolds. The energy levels were indicated with numbers 1-7 in order of

increasing energy, for simplicity in successive referencing. In Fig. 4.1 we have indicated in orange the typical pumping- and in green the lasing-transitions.

	Yb:$LuLiF_4$	Yb:CaF_2	Yb:YLF	Yb:YAG
Lattice symmetry	Tetragonal	Cubic	Tetragonal	Cubic
Ion density (1at.%) $[cm^{-3}]$	1.44 10^{20}	2.45 10^{20}	1.44 10^{20}	1.38 10^{20}
τ_f $[ms]$	2.0	2.4	2.1	1.2
λ_p $[nm]$	960(a,c), 940(a)	980	960, 940	968, 941
σ_{ab}^{peak} $[10^{-20}\ cm^2]$	0.99(c), 0.30(a)	0.54	1.1	0.82
$\Delta\lambda_p$ $[nm]$	12, 20	8	12, 20	3, 18
σ_{em}^{peak} $[10^{-20}\ cm^2]$	1.00(c), 0.40(a)	0.90	1.10(c), 0.41(a)	2.20
Thermal conductivity @ 300 K $[Wm^{-1}K^{-1}]$	5(a) 6.3(c)	9.7 7.2(c)	4.4(a)	8.2
$\frac{dn}{dT}$ @ 300 K $[10^{-6}\ K^{-1}]$	-3.6(a) -6(c)	-11.3	-4.6(a) -6.6(c)	7.8
Thermal expansion coeff. @ 300 K $[10^{-6}\ K^{-1}]$	13.6(a) 10.1(c)	19.4	14.3(a) 10.1(c)	6.14
Thermal conductivity @ 77 K $[Wm^{-1}K^{-1}]$	23.6(a) 31.3(c)	68	11.3(a, 100 K) 33.7(c, 100 k)	25(100 K)
$\frac{dn}{dT}$ @ 77 K $[10^{-6}\ K^{-1}]$	-7.2(a, 140 K) -7.5(c, 140 K)	-3	-0.5(a) -1.8(c)	0.9
Thermal expansion coeff. @ 77 K $[10^{-6}\ K^{-1}]$	3.0(a, 100 K) 3.9(c, 100 K)	10.7	2.4(a, 100 K) 3.2(c, 100 K)	1.9

TABLE 4.1: Main spectroscopic and thermo-optical properties of Yb:$LuLiF_4$, Yb:CaF_4, Yb:YLF, Yb:YAG from [2, 5, 12, 13, 14].

It is well known that in both Yb:YLF and Yb:$LuLiF_4$ there is a strong electron-phonon interaction [6, 15] that introduces additional absorption and emission peaks and results in the widening of the spectra around the peaks associated with electronic transitions, as we will discuss in the following sections.

In this appendix we present the characterisation of the absorption cross section of Yb:$LuLiF_4$ in the sub-ambient temperature range (RT-63 K). Furthermore we also present emission cross section measurements over the same temperature range, while introducing a novel method for collecting pump-signal-free fluorescence spectra via appropriate synchorinsation between the pump pulse and the fluorescence data collection. Lastly, we present preliminary gain measurements executed via pump-probe experiments in the same sub-ambient temperatures.

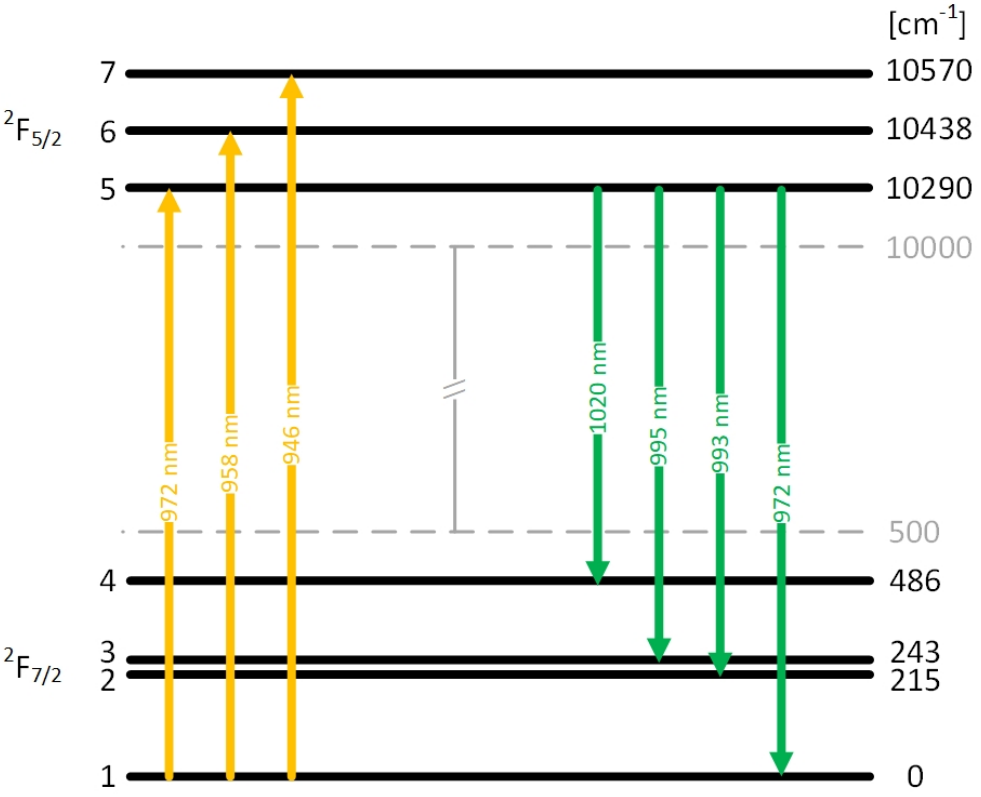

FIGURE 4.1: Yb:LuLiF$_4$'s energy level diagram and pumping (orange) and lasing (green) transitions between the ground state $^2F_{7/2}$ to the excited state $^2F_{5/2}$.

4.2 Absorption cross section

In this section we present the characterisation of the absorption cross section of Yb:LuLiF$_4$ in the cryogenic-temperature range (63 *K*-RT).
The methodology employed to execute these measurements is the same as detailed in Section 3.2; in this case, however, we couldn't employ the same LIMO diode, as its spectral distribution wasn't in the absorption band of the crystals to be tested. Additionally, as diode ASE sources would have insufficient bandwidth to cover the entire the wavelength range required (900-1100) nm. As such, we built a white light source, using a 50 W halogen bulb [16] with a spectral range extending across the wavelength interval (600-1400) nm. This source provided an excellent power stability until end of life, i.e. damage of the filaments. A small portion of the light emitted from the bulb, $\sim$ 0.5 W, was captured by a $f = 11$ mm aspheric lens and coupled into a 200 μm, 0.22 NA patch fibre (F1 in Fig. 3.1). The output of the patch fibre was measured to be $\sim$ 3.5 mW, a strong enough signal for the absorption measurements of the thin samples we studied to be well resolved. We were provided with two Yb:LuLiF$_4$ samples, the details of which are summarised in Table 4.2, grown in-house by Pisa University. The two samples were cut from the same boule and were grown with a nominal doping-concentration of 5 $at.\%$.

Surface [mm^2]	Length [mm]	Nominal $C_{\%}$ [$at.\%$]	Measured $C_{\%}$ [$at.\%$]
10x10	1.10	5.00	5.03 ± 0.13
10x10	0.44	5.00	3.96 ± 0.04

TABLE 4.2: Details of the Yb:$LuLiF_4$ samples tested.

Upon measuring the respective doping concentrations employing the methodology depicted in Section 3.2.2 and with referenced peaks from [17], the two crystals were found to have slightly different values, as detailed in Table 4.2; this difference was probably due to the two samples having been cut from different areas of the boule, across the length of which the variation in doping concentrations can be significant, as explained in Section 3.1. To verify the consistency of the doping-level measurements and the independence of the absorption cross section on the ion-concentration, we measured the absorption cross sections for several different temperatures in both the samples, finding that the spectra were in excellent agreement for the respective temperatures. Therefore here we only present the absorption data obtained employing the 0.44 mm-long crystal, with $(3.96 \pm 0.04) at.\%$ doping, as it provided the best resolution at the lower temperatures.

As for the other measurements executed at sub-ambient temperatures and described in Section 3.2.1, the Q-drive 1s132K cryocooler was employed to control the sample's temperature. The crystal's mounting configuration is displayed in Fig. 4.2: the sample was held in contact with an Aluminium block via two L-shaped Copper brackets; the surfaces of contact between the crystal and the metal clamps were covered with a 100 μm-thick Indium foil (not visible in the sketches). The Al-Cu-Crystal compound was bolted to the cold-head of the cryocooler.

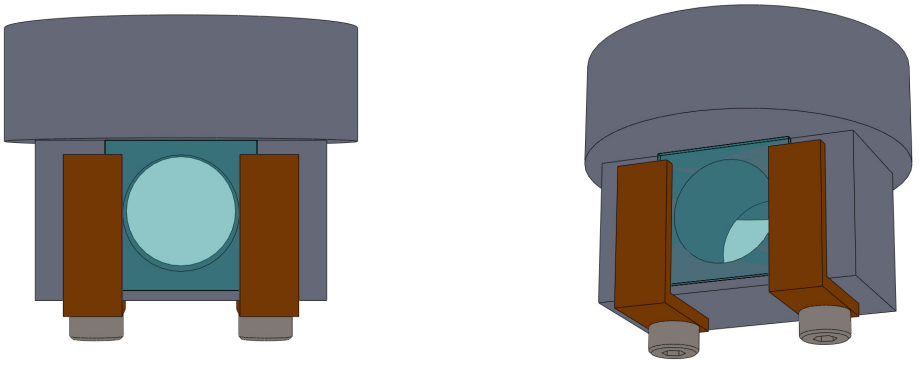

(A) Front view. (B) Dimetric view.

FIGURE 4.2: Yb:$LuLiF_4$ sample clamped, via two Copper L-shaped brackets, to an Aluminium block in contact with the cold-head of the cryocooler. The contact points between the crystal and the metals are covered with a 100 μm-thick Indium foil.

4.2.1 Results

The results of the absorption cross section characterisation for both σ- and π-polarisations in the cryogenic temperature range (63 K-RT) are reported in Figs. 4.3-4.6.

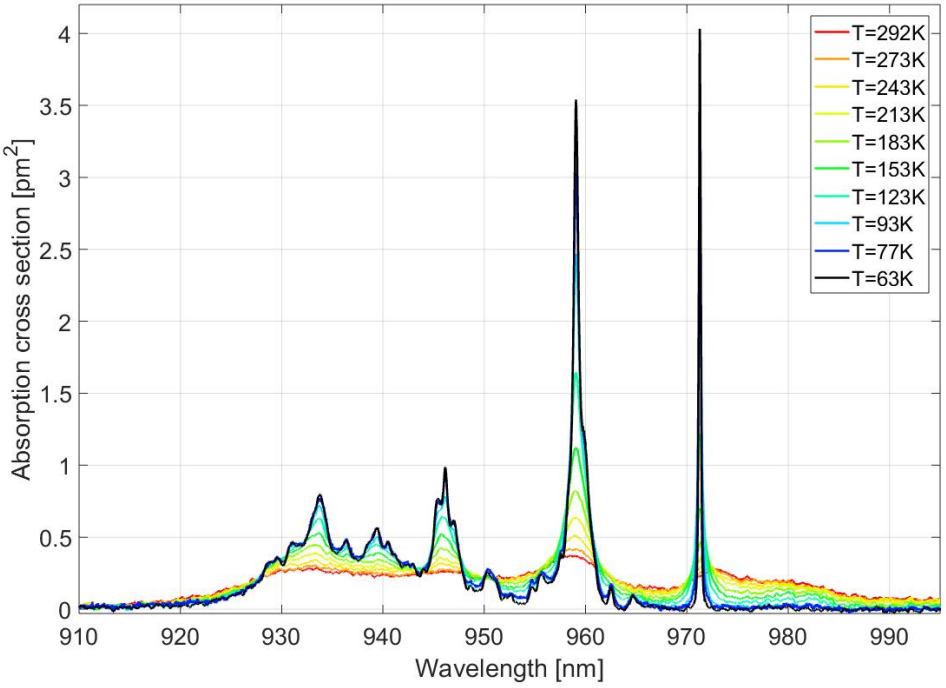

FIGURE 4.3: Yb:LuLiF$_4$'s σ-polarisation absorption cross section for temperatures (63 K-RT).

The σ-polarised spectra of the absorption cross section present two main peaks: one around 960 nm, corresponding to the transition $1 \rightarrow 6$ and the other one corresponding to the Zero-Phonon Line (ZPL), the $1 \rightarrow 5$ transition. As observed for the sub-ambient temperatures spectra of Nd:YAG, detailed in Section 3.3.2.2, the two main absorption peaks become stronger and sharper as the temperature lowers. The 960 nm peak's strength increases from (0.37 ± 0.04) pm^2 to (3.50 ± 0.04) pm^2, a $\sim$ 9.4x increase, its bandwidth narrows from (5.60 ± 0.02) nm to (0.68 ± 0.02) nm, and it redshifts from (958.4 ± 0.1) nm to (959.1 ± 0.1) nm over the temperature range from RT to 63 K. The ZPL increases from (0.27 ± 0.03) pm^2 to (4.03 ± 0.04) pm^2, a $\sim$ 15x increase, and it blueshifts from (972.9 ± 0.1) nm to (971.3 ± 0.1) nm over the same temperature range. This peak narrows from a combined bandwidth of ~ 15 nm with the adjacent peak at RT to (0.25 ± 0.02) nm at 63 K. Fig. 4.4 summarises these results. Note that the bandwidth of the ZPL is only reported when the peak becomes clearly distinguishable.
The σ-polarisation spectra also present a broad band extending in the spectral range $(925 - 950)$ nm and due to the electron-phonon interaction. At RT, the absorption cross section value is approximately constant around 0.4 pm^2 throughout the whole band, while at 63 K some peaks become distinguishable around $935, 940, 946$ nm with values

$\sim 1\ pm^2$. Although the cross section value of this band is not as high as the peak around 960 nm, its extended bandwidth makes it particularly suitable for diode pumping in the cryogenic-cooling regime, where usually one of the biggest challenges is to efficiently exploit the narrow absorption peaks, making the use of wavelength stabilisation devices necessary, as we have done and detailed in Chapter 6.

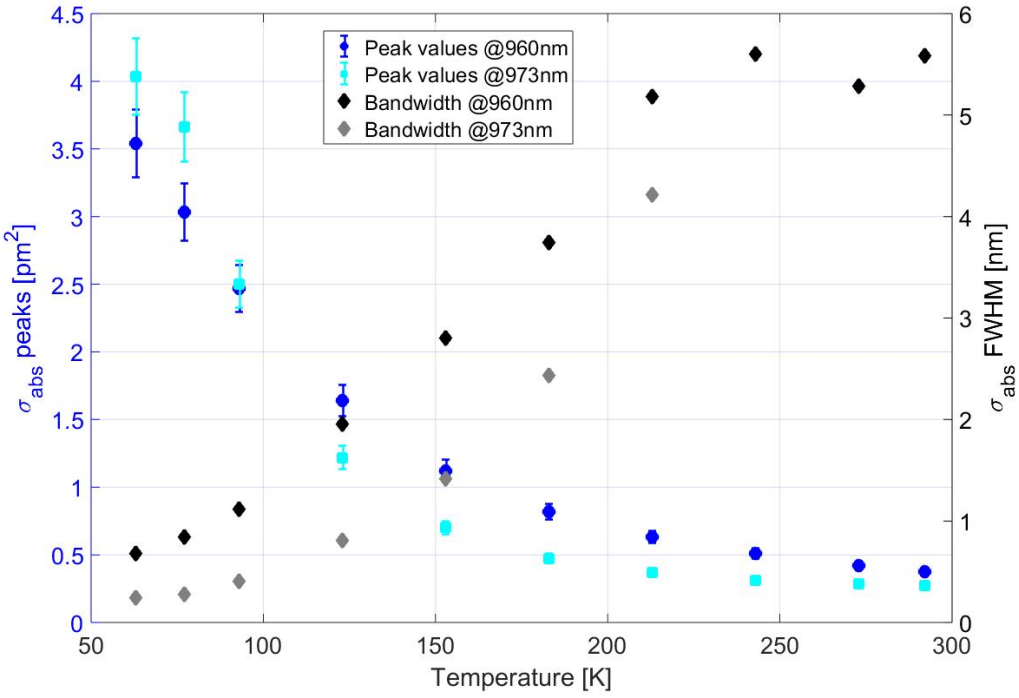

FIGURE 4.4: Yb:LuLiF$_4$'s σ-polarisation absorption cross section peak amplitudes at 960 nm and 972 nm and relative bandwidths for the temperature range (63 K-RT).

The π-polarised absorption spectra present one main peak around 960 nm. This peak increases from $(1.02\ pm0.02)\ pm^2$ to $(9.65 \pm 0.08)\ pm^2$, a $\sim$ 9.5x increase, its bandwidth narrows from $(9.50 \pm 0.02)\ nm$ to $(0.70 \pm 0.02)\ nm$, and it redshifts from $(958.97 \pm 0.02)\ nm$ to $(959.07 \pm 0.02)\ nm$ over the temperature range from RT to 63 K. Compared to peaks of similar strength at cryogenic temperature, e.g. Nd:YAG's 869 nm [18] and Yb:YAG's 970 nm peak [1] at LNT, the $\sim$ 960 nm absorption line of Yb:LuLiF$_4$ is up to 5x wider, hence much more suitable for diode pumping even at cryogenic temperatures.

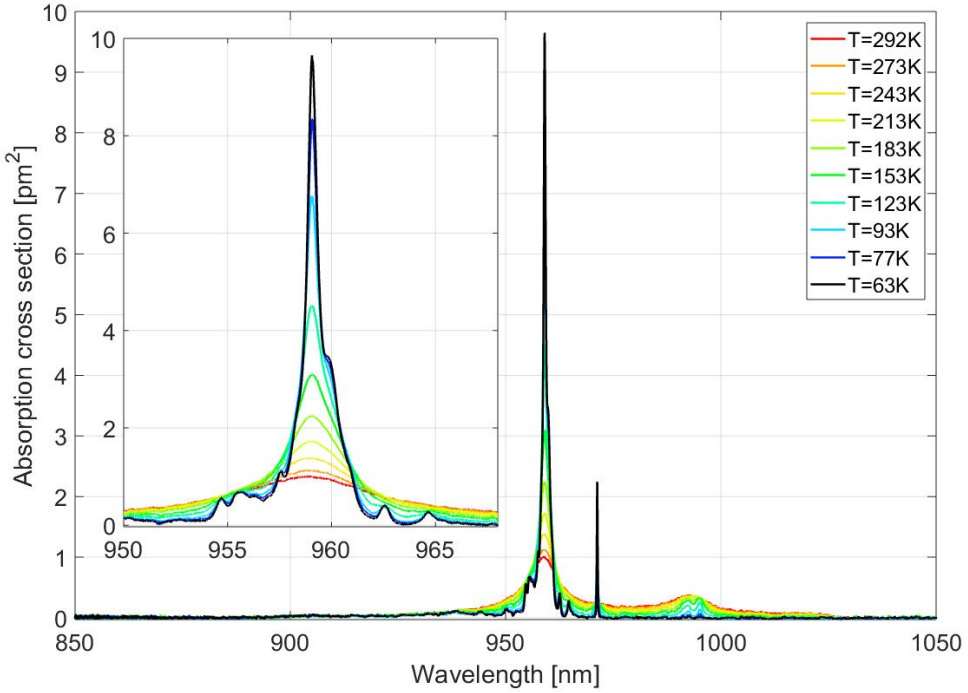

FIGURE 4.5: Yb:LuLiF$_4$'s π-polarisation absorption cross section for temperatures (63 *K*-RT). Inset: zoom on the strongest peak around 960 *nm*.

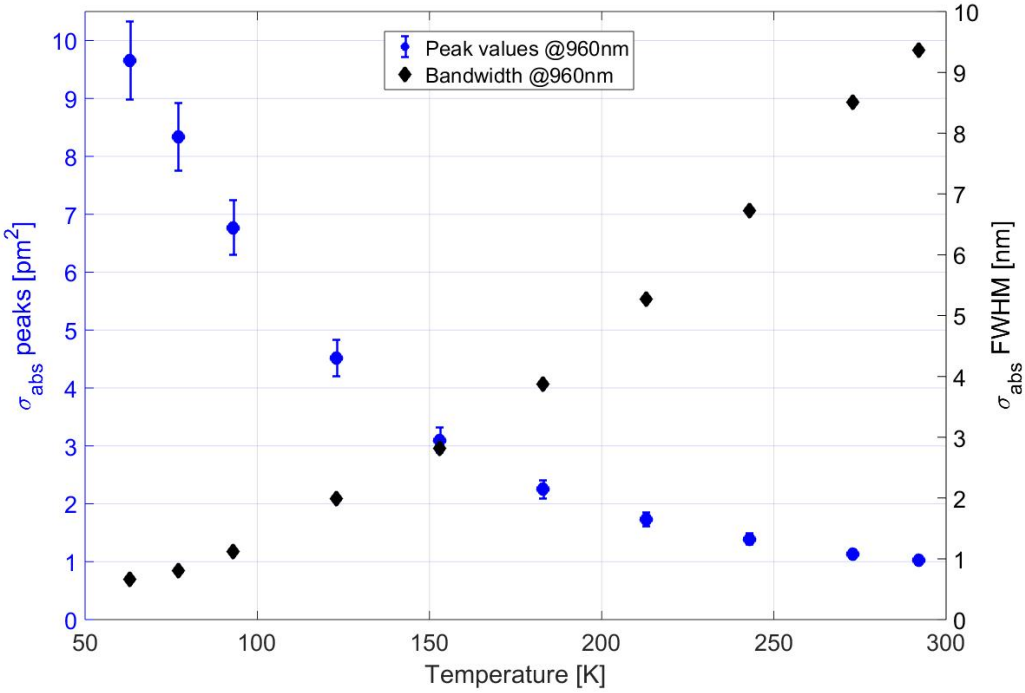

FIGURE 4.6: Yb:LuLiF$_4$'s π-polarisation absorption cross section peaks at 960 *nm* and relative bandwidths for temperatures (63 *K*-RT).

4.3 Emission cross section

The emission cross section is a fundamental parameter underpinning laser performance, as it determines, combined with the absorption cross section, the amount of gain produced in a pumped laser medium. There are several different ways to determine the emission cross section spectrum of active media: the McCumber, or Reciprocity, method [19] and the Füchtbauer-Landenburg (F-L) method [20, 21, 22] being the most common. The integral F-L method [22] is based on fluorescence spectrum and lifetime measurements, and it is generally more accurate for wavelengths longer than the ZPL's, particularly for spectral areas that present a strong reabsorption, i.e. with a strong overlap of emission and absorption spectra, and high doping-levels [2]. The Reciprocity method starts from measured absorption spectra and Stark level energy values, and it is more accurate for wavelengths shorter than the ZPL's and in spectral regions where there is a strong reabsorption, as it is not affected by distortion in the fluorescence spectrum due to the latter. This method is however not valid when eletron-phonon interaction take place in the crystal, as demonstrated in [22].
The formula for the calculation of the emission cross section following the integral F-L method [22] is reported in Eq. (4.1):

$$\sigma_{em}(\lambda) = \frac{1}{8\pi} \frac{\eta \lambda^5}{\tau_f f_j n_j^2 c} \frac{I_j(\lambda)}{\sum_{j=1}^{3} \int \lambda I_j(\lambda)\, d\lambda} \tag{4.1}$$

where $I_j(\lambda)$ is the j-polarised measured fluorescence spectrum and j represents the polarisation axis, τ_f the fluorescence lifetime of the excited state, λ is the wavelength, η is the quantum efficiency, n_j is the refractive index for the j-polarisation state, and c is the speed of light.

4.3.1 Methodology

Fluorescence spectrum measurements were executed with the 0.44 mm-long, 3.96$at.\%$-doped Yb:LuLiF$_4$ crystal in the temperature range (RT-63 K). We chose this sample in order to minimise the reabsorption effects in the fluorescence spectrum. The experiemntal setup employed is shown in Fig. 4.7. A fibre-coupled (105 μm, 0.22 NA) IPG pump-laser extending in the spectral range (952-959) nm, ideal for pumping the absorption band of Yb:LuLiF$_4$ around 960 nm, was collimated by lens L$_1$ ($f = 11$ mm) to a beam the size which covered most of the available 5x5-mm^2 crystal surface. Two crossed polarisers, the first positioned after lens L$_1$ and the second after the crystal, effectively attenuating the transmitted pump directing it into a beam dump (screen). This configuration also provided polarisation discrimination for the collected fluorescence, passing only the σ-polarised fluorescence. In order to collect π-polarised fluorescence both polarisers were rotated 90^o. The sample under test was mounted as described

in Section 4.2 and depicted in Fig. 4.2. An aperture was positioned after the second polariser in order to block the residual pump let through due to the finite extinction ratio of the polarisers. Lenses L_5 ($f = 60\ mm$) and L_3 ($f = 8\ mm$) provided an off-axis imaging system of the crystal's second facet on to the collecting-fibre (105 μm, 0.22 NA), coupled to the OSA (ANDO AQ6317B). Despite the setup providing a nearly complete extinction of the residual pump signal, a portion was still collected by the OSA and it dominated the fluorescence spectrum signal of only a few nW/nm. Furthermore, its spectral overlap with the fluorescence meant a loss of spectral information around the $\sim 960\ nm$ emission line (see the red line in Fig. 4.8).

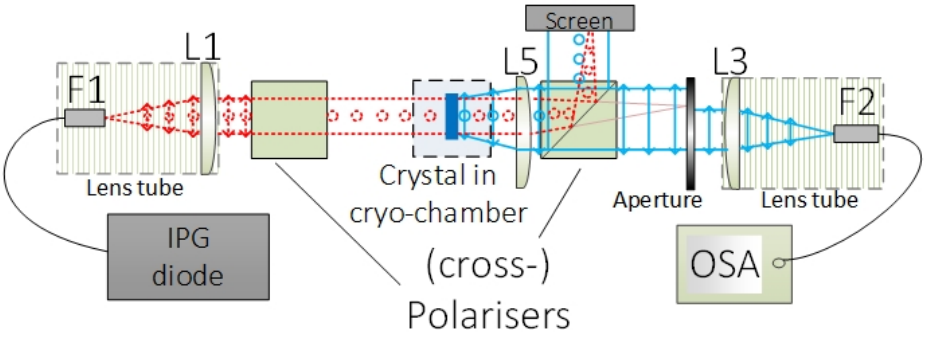

FIGURE 4.7: Fluorescence spectrum measurement setup.

To mitigate the residual pump contamination of the signal, the pump was modulated with 9 ms-long pulses at a frequency of 2.5 Hz, and the OSA was triggered to collect a single data point with a 1 ms-delay with respect to the end of the pump pulse. The synchronisation was executed by an Arduino Uno [23], which detected the end of the pump pulse and triggered the OSA measurement after the set delay. The rather long $\sim 2\ ms$ fluorescence lifetime of Yb:$LuLiF_4$ provided a sufficient signal even 1 ms into the decay, with $\sim 60\%$ of the emitted photons being collected with respect to that obtained at the zero-delay signal, as Fig. 4.9 shows. Fig. 4.8 shows the comparison between the signals acquired without (red line) and with (blue line) the Arduino synchronisation, where we have applied a Matlab built-in Savitzky-Golay filter [24] to the blue curve. The excellent agreement between the two spectra and the clear improvement given by the avoided loss of information around 960 nm in the blue curve confirmed the efficacy of this novel combination of Arduino and the OSA , which allowed us to employ it in all the successive fluorescence spectrum measurements.
Furthermore, due to a delay of less than 20 μs between the trigger signal sent to the OSA by the Arduino and the actual data-point collection (see inset of Fig. 4.9), we could optimise the delay between the end of the pump pulse and the measurement execution to obtain the maximum signal-to-noise ratio and ensure that the pump signal was totally extinguished. Employing this methodology, fluorescence spectra for both polarisations states, at several crystal temperatures in the range (RT-63 K) were obtained.

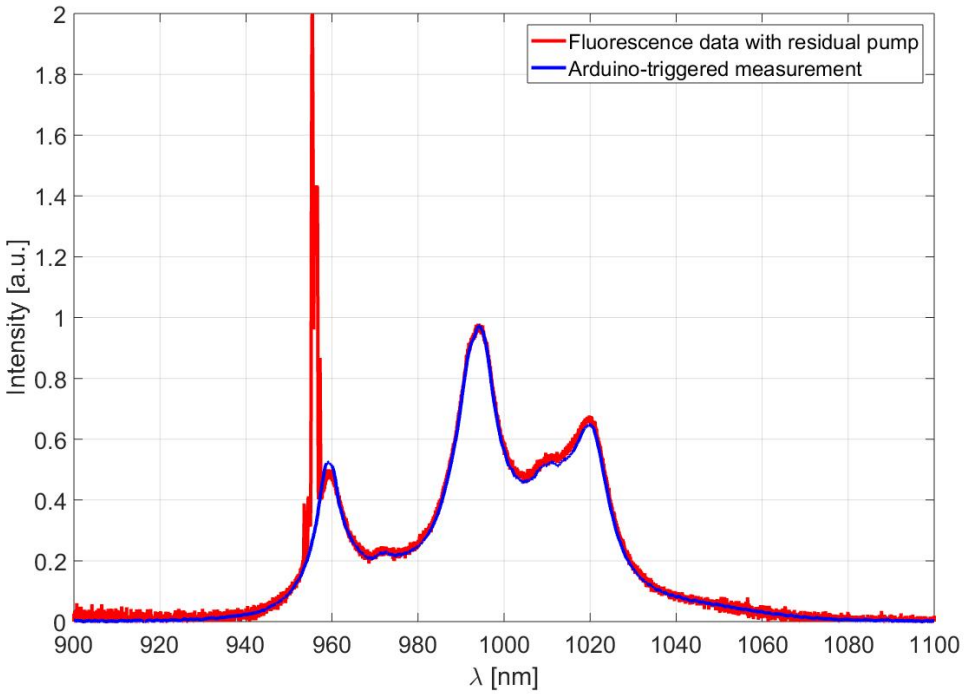

FIGURE 4.8: Comparison between fluorescence spectra without (red line) and with (blue line) Arduino synchronisation of the data collection.

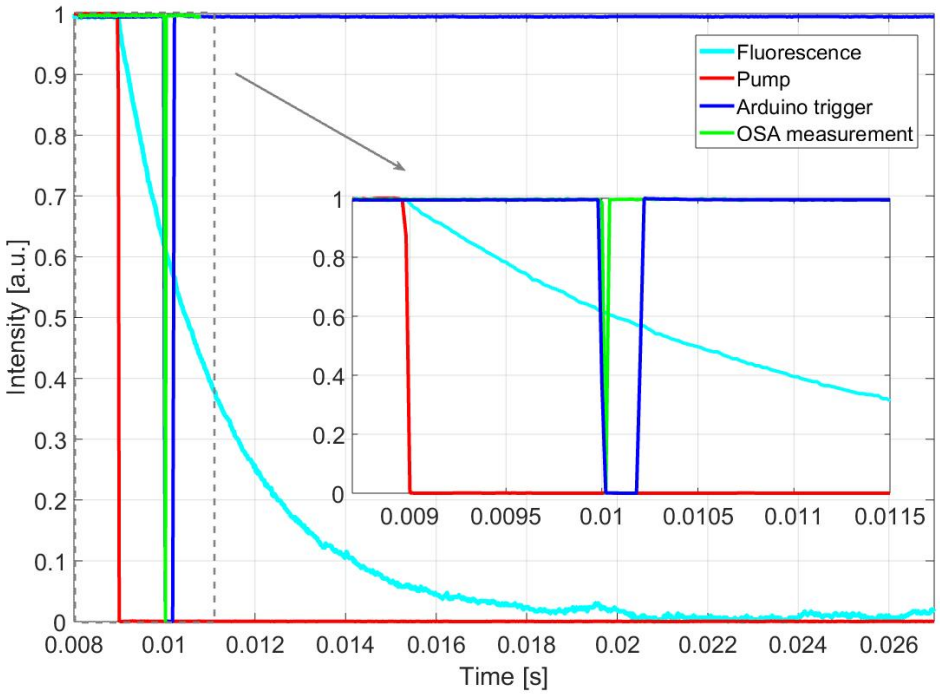

FIGURE 4.9: Relative timings of pump pulse (red), fluorescence signal (cyan), Arduino trigger (blue) and OSA measurement (green). Inset: Zoom around the measurement event.

The other key measurement for the calculation of the emission cross section is the fluorescence lifetime. In order to measure this temperature-dependent parameter, we positioned a long-pass filter in place of the aperture in Fig. 4.7 and a fast photodiode after it. This provided a strong enough signal in a spectral range above 1 μm, as the wavelengths below it, including the residual pump, were cut by the long-pass filter. For these measurements, the pump was modulated to a frequency of 20 Hz with a duty cycle of 50%: this allowed enough time both for the populations to reach steady state and for the fluorescence decay to end.

4.3.2 Results

In order to characterise the emission cross section of Yb:$LuLiF_4$, we firstly measured the temperature-dependent fluorescence lifetime, τ_f at RT and 63 K. This measurement was executed by positioning a long-pass filter followed by a fast photodiode in place of the screen in Fig. 4.7; this provided the complete extinction of light in the spectral range $\lambda < 1\ \mu m$, thus including the pump, and still an adequate fluorescence signal to result in a well resolved decay waveform. At RT the fluorescence lifetime was measured to be $(2.23 \pm 0.03)\ ms$, which lowered to $(1.85 \pm 0.03)\ ms$ at 63 K. ~ 330 individual waveforms were captured and analysed, fitting a single-exponential decay to the data. An average of the resulting lifetime parameters along with the standard deviation provided a more precise measurement of the crystal's lifetime with the associated uncertainty. These results for the 3.96at.%-doped sample fit well with the values reported in [6]: 2.61 ms and 2.03 ms at RT, and 1.88 ms and 1.80 ms at 12 K, for 5at.%- and 0.5at.%-doped Yb:$LuLiF_4$, respectively. This suggests that our measured value for the fluorescence lifetime at 63$\boldsymbol{K}$ is in fact compatible with the radiative lifetime values obtained for similarly doped Yb:$LuLiF_4$.
Employing the value of τ_f at 63 K in Eq. (4.1) we converted the measured fluorescence into emission cross section spectra for several different temperatures in the range (RT-63 K), presented in Figs. 4.10 and 4.12. The RT value of both σ- and π-polarised emission cross sections are in agreement with the ones provided in [2].
Yb:$LuLiF_4$'s σ-polarised emission cross section presents one main peak corresponding to the ZPL around 972 nm and a $\sim$ 20-nm-wide band extending over the wavelength range $(990 - 1020)\ nm$ due to electron-phonon interactions. The ZPL peak is not distinguishable at RT, at which the spectrum appears to be constant at around 0.3 pm^2 from 970 nm to 1020 nm. As the temperature gets colder the spectroscopic features become sharper, and three lines can be distinguished at 960 nm, 972 nm and 995 nm, and a $\sim$ 10-nm-wide band around 1010 nm. At 63 K their respective peak values are $(0.20 \pm 0.02)\ pm^2$, $(1.79 \pm 0.02)\ pm^2$ and $(0.62 \pm 0.04)\ pm^2$, and $\sim 0.6\ pm^2$ for the latter. Fig. 4.11 shows the σ-polarised peak values of the 972 nm emission line and its bandwidth for temperatures in the range (63 K-RT), over which its strength increases from $(0.28 \pm 0.02)\ pm^2$ to $(1.82 \pm 0.13)\ pm^3$ and its bandwidth narrows from $\sim 7.4\ nm$ to

(0.48 ± 0.04) nm. As shown in Fig. 4.10, in the temperature range (RT-213 K) the peak is not clearly discernible, hence the Full Width at Half Maximum (FWHL), or bandwidth, is not definite. As the peak becomes visible and sharper, below 213 K, the bandwidth is well defined.

The π-polarised emission cross section is generally stronger than the σ-polarised, with two main broad peaks distinguishable at RT, around 995 nm and 1020 nm, with values (1.06 ± 0.07) pm^2 and (0.80 ± 0.01) pm^2, respectively. As the temperature reduces, the peak around 995 nm splits in two sharp peaks centered on 992.5 nm and 995.5 nm, the latter being dominant, as shown in the inset of Fig. 4.12 and in Fig. 4.13. These two were measured to have peak values of (3.86 ± 0.27) pm^2 and (9.46 ± 0.66) pm^2 at 63 K, almost a 10-fold increase for the strongest peak. Their respective bandwidths have the same value up to $\sim$ 183 K, as the two peaks are overlapped, forming one $\sim$ 18 nm-broad peak; below $\sim$ 183 K they split, with the stronger peak narrowing to (0.96 ± 0.02) nm and the weaker to (1.92 ± 0.02) nm at 63 K. At the same temperature, the peak value for the transition around 1020 nm becomes (2.87 ± 0.30) m^2, while its bandwidth doesn't significantly reduce due to the electron-phonon interaction broadening it.

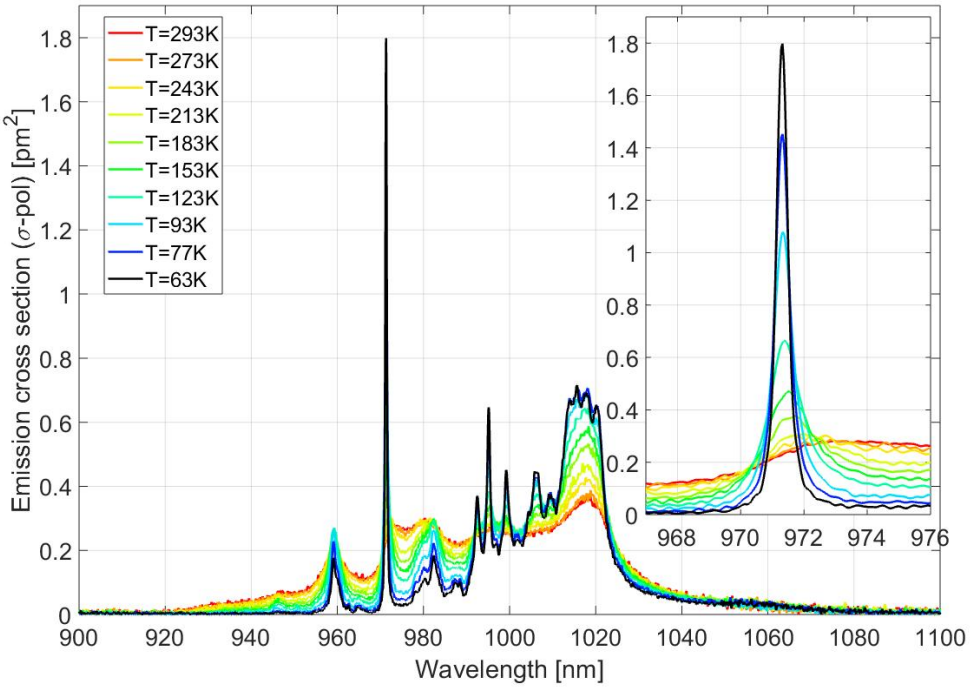

FIGURE 4.10: Yb:$LuLiF_4$'s σ-polarisation emission cross section for temperatures (63 K-RT). Inset: zoom on the strongest peak around 972 nm.

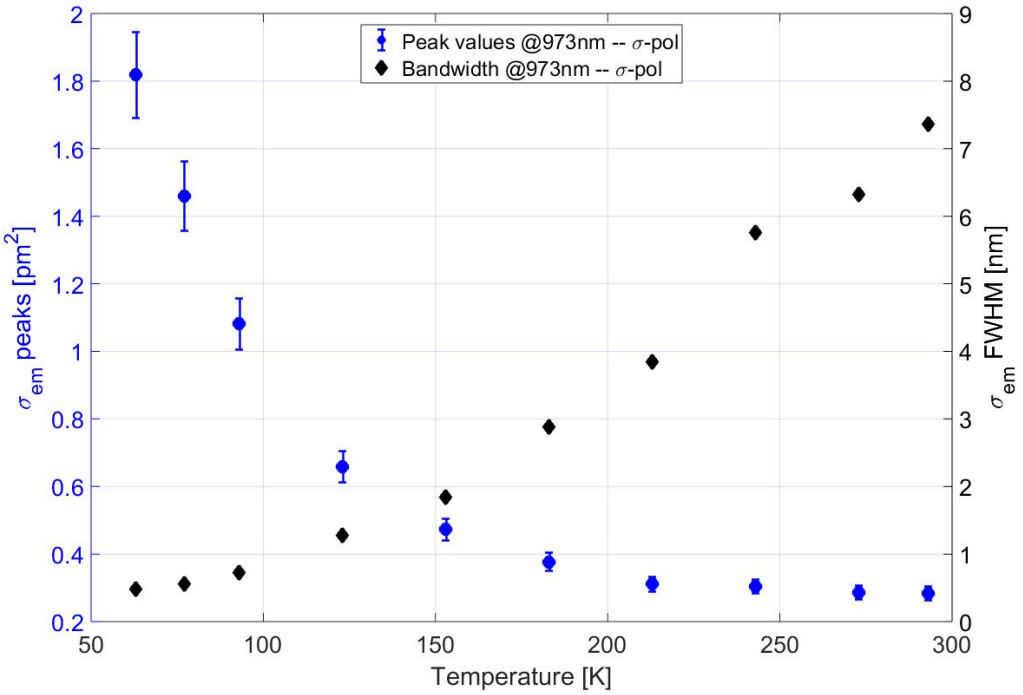

FIGURE 4.11: Yb:$LuLiF_4$'s σ-polarisation absorption cross section peaks at 972 nm and their bandwidths for temperatures (63 K-RT).

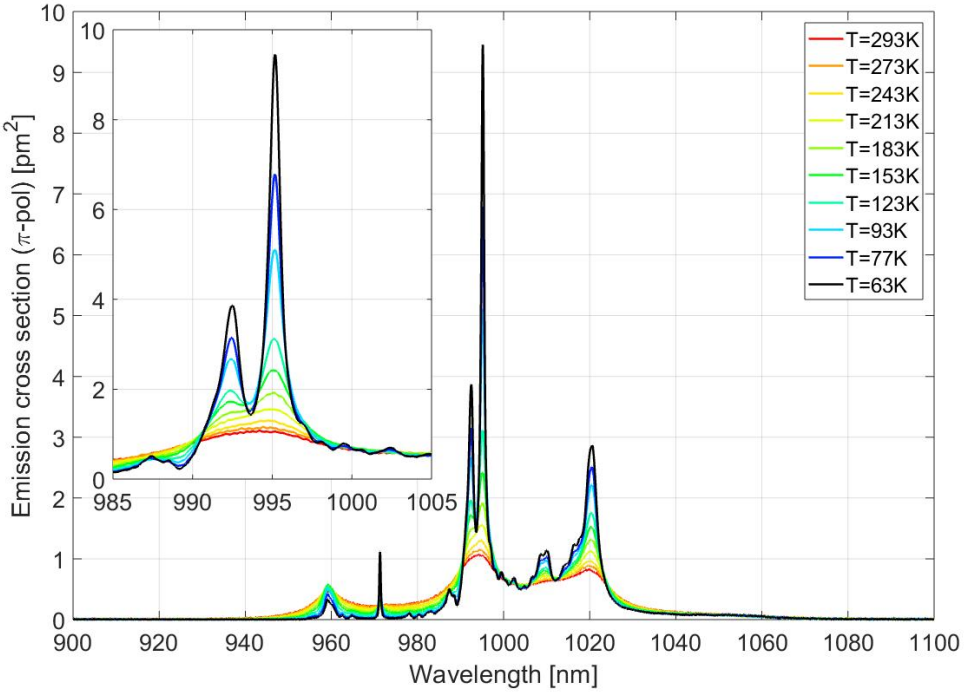

FIGURE 4.12: Yb:$LuLiF_4$'s π-polarisation emission cross section for temperatures (63 K-RT). Inset: zoom on the strongest peak around 995 nm.

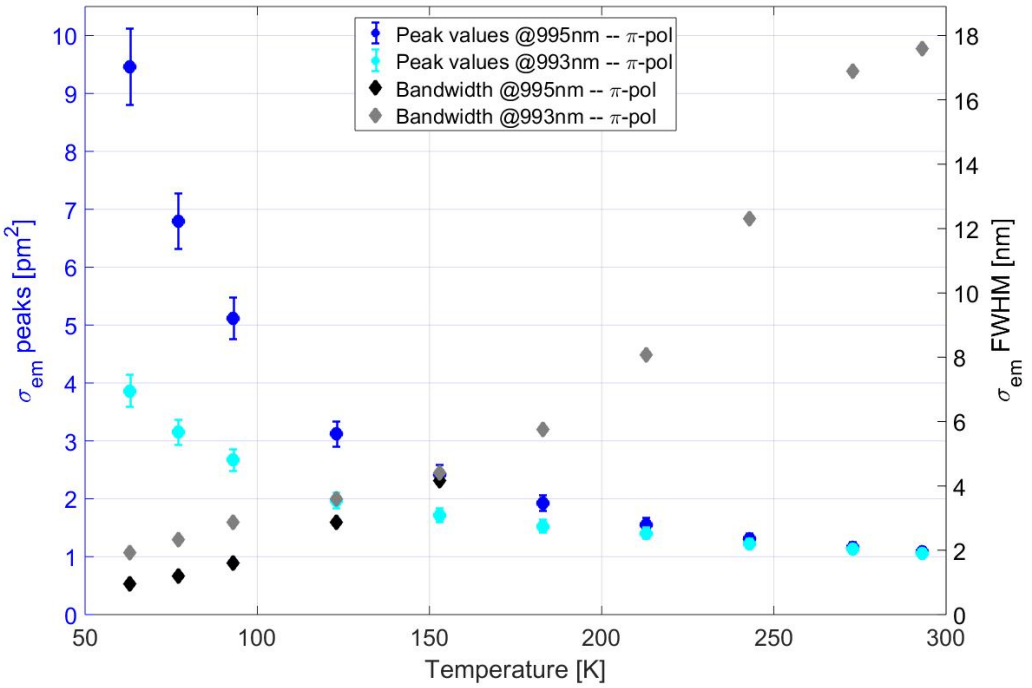

FIGURE 4.13: Yb:LuLiF$_4$'s π-polarisation emission cross section peaks at 993 nm and 995 nm and their bandwidths for temperatures (63 K-RT).

4.4 Gain cross section

It is known [2, 6] that the laser crystal Yb:LuLiF$_4$ presents a strong electron-phonon interaction, which causes both the absorption and the emission cross section spectra to broaden around what can be identified with electronic transition lines. As we have seen in the results presented in Section 4.2.1 and 4.3.2, this happens primarily in the σ-polarised absorption and emission cross sections. As this strong interaction results in the non-reciprocity between absorption and emission cross sections [22], the Reciprocity method cannot legitimately be applied to retrieve one from the other. Furthermore, it is also known [2] that the F-L method leads to a possibly imprecise estimation of the emission cross section when there is an overlap between the absorption and emission spectra, i.e. reabsorption effects, like in Yb:LuLiF$_4$. Utimately, the relevant parameter for a correct estimation of the laser performance, is the gain cross section σ_g, which links the absorption, σ_{abs}, and emission, σ_{em}, cross sections via the following:

$$\sigma_g(\lambda) = \beta\sigma_{em}(\lambda) - (1-\beta)\sigma_{abs}(\lambda) \tag{4.2}$$

where β is the fractional population inversion given by $\beta = N_2/N_{tot}$.
The sample we employed to collect fluorescence spectra was relatively thin, only 0.44 mm, to minimise the effects of reabsorption leading to incorrect estimation of the emission

cross section. However, the measurement of the gain cross section would allow an independent calculation of the emission cross section via Eq. (4.2), and thus enable the comparison with the results provided by the direct measurement detailed in Section 4.3.1 to gauge, if any, the discrepancies between the two results. Furthermore, measuring the gain cross section would provide the added knowledge of this important spectroscopic parameter.

4.4.1 Methodology

Experimentally, the gain cross section spectrum can be measured via developing a laser system and applying a laser laser-performance model with the gain as the fitting parameter; however this methodology requires a precise knowledge of all the other parameters involved in the model, most of which are not straightforward to measure, like the cavity losses. Another way of measuring the gain cross section is pump-probe spectroscopy, coupled to the following equation [25]

$$\sigma_g(\lambda,\beta) = \frac{\ln\left(\frac{I_{pumped}(\lambda,\beta)}{I_{in}(\lambda)}\right)}{N_{tot} l_r} \tag{4.3}$$

where $I_{in}(\lambda)$ is the incident probe intensity (as in Section 3.2), $I_{pupmed}(\lambda,\beta)$ is the probe's transmitted intensity when the crystal is pumped, N_0 is the total ion-density of the crystal, and l_r is the sample's length. The dependence upon the inversion population is emphasised through registration of the terms with dependency on β.

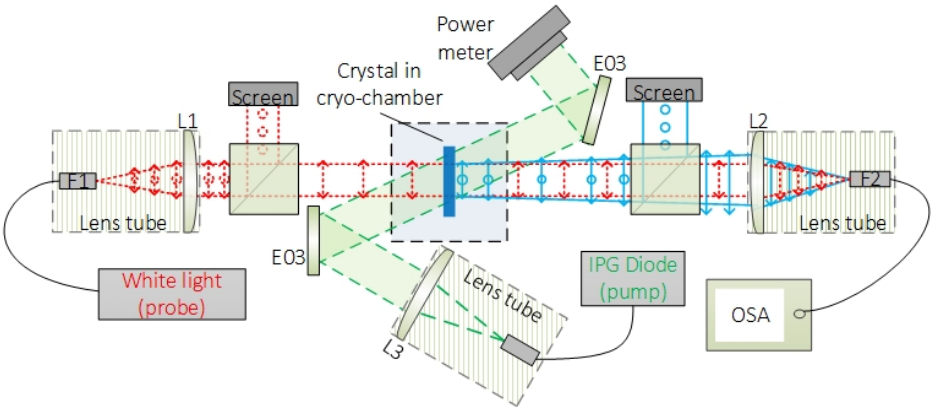

FIGURE 4.14: Gain measurement setup.

Fig. 4.14 shows a schematic of the setup employed for the gain measurements. The output of the in-house built white light source (detailed in Section 4.2) was collimated by lens L_1 and polarised by the cube polariser to the chosen probe polarisation, incident on the tested sample. The probe beam passed through the crystal and a second cube polariser, with its axis transmission axis parallel to the first, and focussed into the OSA's fibre using lens L_2. For the pump laser, we employed the same modulated IPG diode

mentioned previously for the absorption measurements (Section 4.2), though operated at peak power levels in the range (10-12) W. The pump beamline (indicated in green Fig. 4.14) was not co-linear to the probe's, however the two overlapped in the crystal so that the pumped area was always slightly bigger than the probed area. A portion of the fluorescence signal produced by the pumping and emitted over the whole solid angle 4π, was collected after the second polariser before being coupled into the OSA's fibre (collected portion of the fluorescence signal in blue). For each experimental run, we executed four spectral intensity measurements: the incident probe's (with no crystal in the setup) $I_{in}(\lambda)$, the transmitted probe's (unpumped crystal) $I_{out}(\lambda)$, the fluorescence (pumped crystal, but blocked probe) $I_f(\lambda)$, and the probe+fluorescence (pumped crystal with unblocked probe) $I_{f,pumped}(\lambda)$. Upon assessing that the signal level recorded by the OSA was independent of the pump modulation, the spectral measurements that didn't involve the pump laser were executed in the CW regime, as the execution time was up to 10x quicker than in the pulsed regime. Furthermore, in the first regime the signal-to-noise ratio was better than in the second case, as we will illustrate in the discussion Section 4.4.2. The measured spectra relate to Eq. (4.3) via the following:

$$I_{pumped}(\lambda, \beta) = I_{f,pumped}(\lambda, \beta) - I_f(\lambda) \tag{4.4}$$

Eq. (4.4) states that the transmitted probe signal when the crystal is pumped is equal to the probe+fluorescence signal minus the fluorescence signal. To illustrate, Fig. 4.15 shows the four collected spectra and the $I_{pumped}(\lambda, \beta)$ spectrum obtained for a temperature of 183 K and estimated inversion level of $\beta = 0.20$; the details of this estimation are discussed below. It can be observed that the calculated $I_{pumped}(\lambda, \beta)$ spectrum matches the incident probe's spectrum $I_{in}(\lambda)$ in the out-of-band wavelengths, indicating a good stability of the probe's signal between different spectra measurements. The spectra were measured with a resolution of 0.04 nm.

From the constant measurement of the transmitted (absorbed) pump via a power meter positioned to collect the transmitted signal, and having previously measured the pump radius in the crystal to be $\sim 450\mu m$, we could estimate the ion inversion in the crystal by employing the Eqs. (2.7) with $W_{ETU} = 0$, thus accounting for the ground state bleaching at the same time. In order to probe different levels of population inversion we didn't change the pump power, but rather the delay at which the measurement was executed with respect to the end of the pump pulse, as explained in Section 4.3.1. Hence, a zero delay corresponded to the the maximum level of estimated population inversion, $N_{2,max}$ and this value re-scaled according to the measured fluorescence decay curve. For example, the measurement illustrated in Fig. 4.9 would correspond to an inversion level of 0.6 $N_{2,max}$ where $N_{2,max}$ was estimated as depicted above. Note that in the measurements described in Section 4.3.1, however, the ion inversion level was negligible, as required for a correct fluorescence spectrum collection aimed to measure the emission cross section, and as opposed to the requirements for the measurement of the gain cross section.

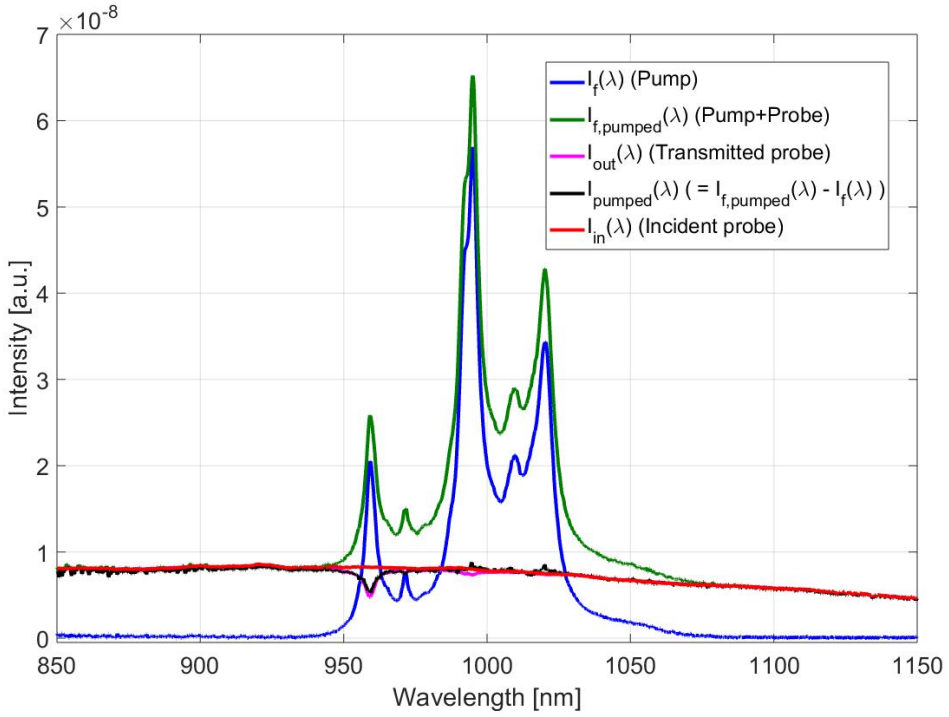

FIGURE 4.15: Gain measurement: data example.

4.4.2 Results and discussion

We executed the pump-probe gain measurements for temperatures in the range $(183 - 63)\ K$. The runs executed for higher temperatures provided data that was dominated by noise, and thus not analysable. In the case of lower temperatures, further discussion is needed regarding the validity of the collected data. To illustrate in further detail, we consider the same data set as in Fig. 4.15, as this represents the best case of all the collected ones.

Fig. 4.16 shows the raw and filtered fluorescence spectra $I_{f,pumped}()$ (blue and red) and $I_f(\lambda)$ (green and yellow): they present a good signal-to-noise ratio and the (almost superfluous) filtering, executed via ©Matlab build-in filters, is smoothing the data providing a clean signal with no loss of information. This is the case for all the fluorescence spectra, as for lower temperatures the signal strength increases, hence so does the signal-to-noise ratio.

Recalling Eq. (4.3), the key quantity for the calculation of the gain cross section $\sigma_g(\lambda)$ is $I_{pumped}(\lambda)$, the difference between $I_{f,pumped}()$ and $I_f(\lambda)$. This difference, however, results in a signal that has a relatively low signal-to-noise ratio, as the top subplot of Fig. 4.17 shows. It is relevant that the measurements of $I_{f,pumped}(\lambda)$ and $I_f(\lambda)$ were executed in the pulsed regime, i.e. as detailed in Section 4.4, as this provided noisier data with respect to the measurements of $I_{in}(\lambda)$ and $I_{out}(\lambda)$, executed in the CW regime (bottom subplot of Fig. 4.17). In the latter case, in fact, no smoothing was necessary.

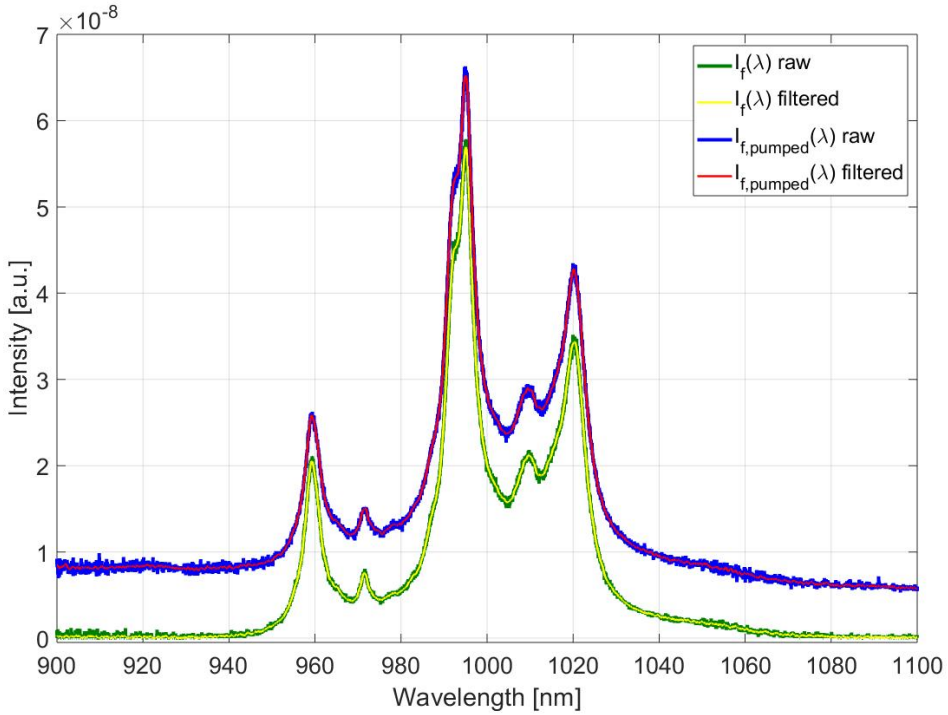

FIGURE 4.16: Gain measurement for Yb:LuLiF$_4$ at 183 K and population inversion of 20%. Raw and filtered fluorescence spectra with (blue and red) and without (green and yellow) the probe signal.

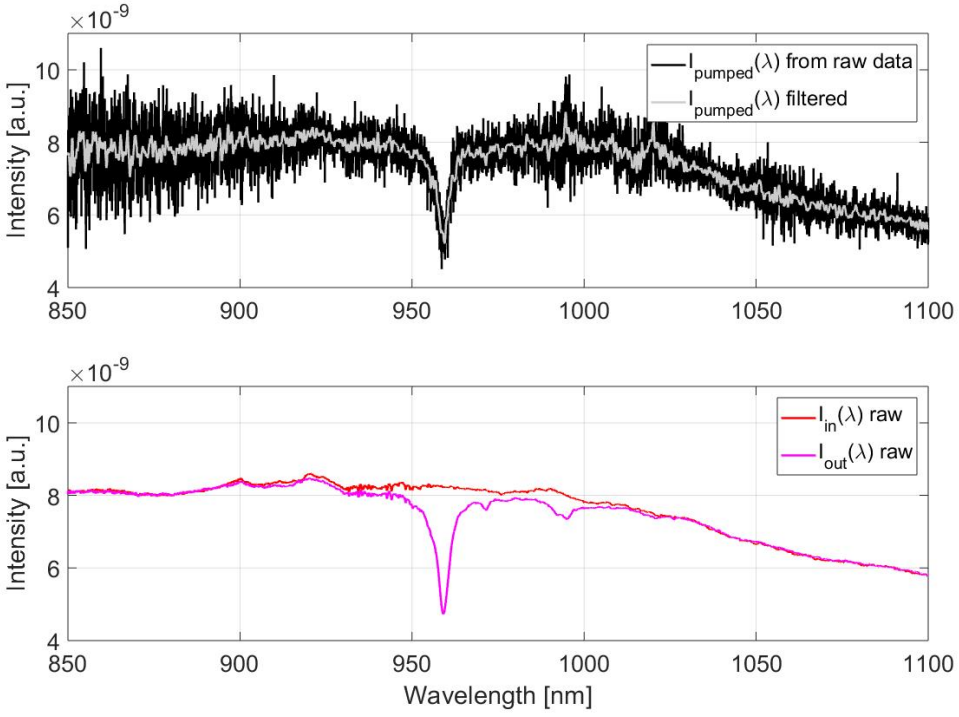

FIGURE 4.17: Gain measurement for Yb:LuLiF$_4$ at 183 K and population inversion of 20%. Top subplot: calculated transmitted probe with pumped crystal, raw (black) and smoothed (grey) spectra; bottom subplot: raw measured incident and transmitted probe with unpumped crystal.

Despite adjusting the OSA's measurement settings in the pulsed regime, the data could not be resolved as it was in the CW regime, thus spoiling the measurements. The situation was further exacerbated by the fact that the gain cross section spectrum is proportional to the logarithm of the ratio between $I_{pumped}(\lambda)$ and $I_{in}(\lambda)$, resulting in the cyan signal in Fig. 4.18. Although the filtered signal removed some noise, the peaks around 995 nm and 1020 nm were not clearly resolved and appeared to be within the noise level. A comparison with the gain cross section calculated employing the measured absorption and emission cross sections (presented in Section 4.2.1 and 4.3.2), corresponding to the orange line in Fig. 4.18 revealed that the strongest (negative) peak around 972 nm was reasonably resolved and seemed to match well the one obtained from the pump-probe experiments, however the signals around the other two peaks weren't in as good agreement.

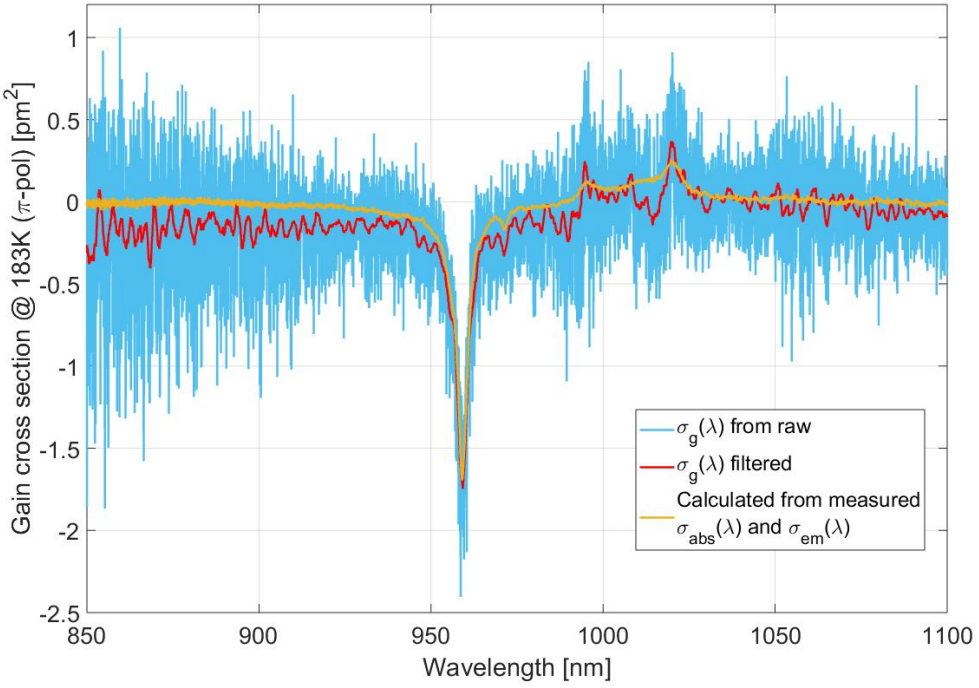

FIGURE 4.18: Gain measurement for Yb:LuLiF$_4$ at 183 K and population inversion of 20%. Gain cross section retrieved from pump-probe measurements: raw (blue) and filtered (red); gain cross section calculated from previously measured absorption and emission cross sections: orange.

In order to give an overview on all the other measurements, we also present a full data set for the gain measurement of the π-polarisation in the temperature range $(183 - 63)$ K (similar results were obtained for the σ-polarisation). Each plot presents four spectra: the dotted black line is the gain cross section estimated using the measured absorption and emission cross sections and assuming a population inversion level of $\beta = 0.20$; the three solid lines are obtained from pump-probe measurements with a set measurement delay of 1.0 ms, 1.5 ms, and 2.0 ms with respect to the end of the pump pulse, corresponding to the blue, red, and orange lines, respectively. Note that these three curves were all filtered

to eliminate the excessive noise produced by the raw data processing. The legends report the inversion level estimated by monitoring the average transmitted pump power and accounting for the set measurement delay, as detailed in Section 4.4.
Noticeably, in most cases the trend of increased gain in the band $(990 - 1020)$ nm with higher population inversion is not respected: at the temperature of 153 K there appears to be more gain for 13.7% inversion (red line) than for 17.6% inversion (blue line); for the temperature of 93 K the gain spectrum for 11.7% inversion is significantly stronger than the one for 19.4% inversion, as opposed to expectations. A similar situation occurs in the gain around 960 nm for 77 K and 63 K. In the cases of 123 K and 63 K, as the blue spectrum appears to be much stronger than the the red one, it is possible that the population inversion was underestimated. Generally, with the increased signal-to-noise ratio due to the temperature-dependent increase in the magnitude of the gain cross section peaks, the noise becomes a secondary problem, however there doesn't seem to be consistency between measurements that permits extrapolation of any significant result.

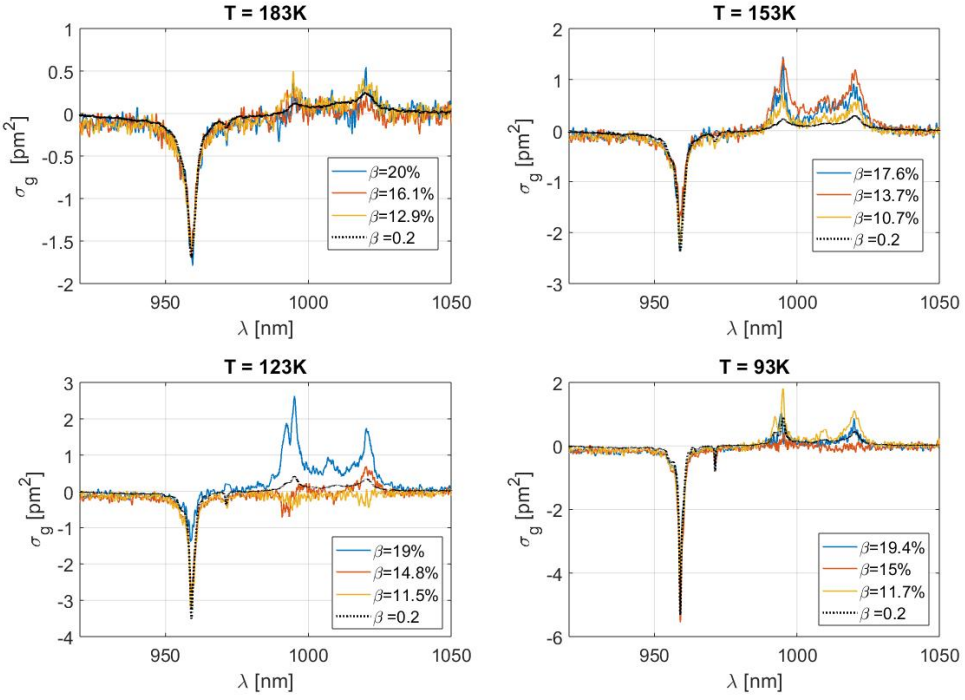

FIGURE 4.19: Gain measurement for Yb:LuLiF$_4$ at 183 K, 153 K, 123 K and 93 K, each at three different population inversion levels.

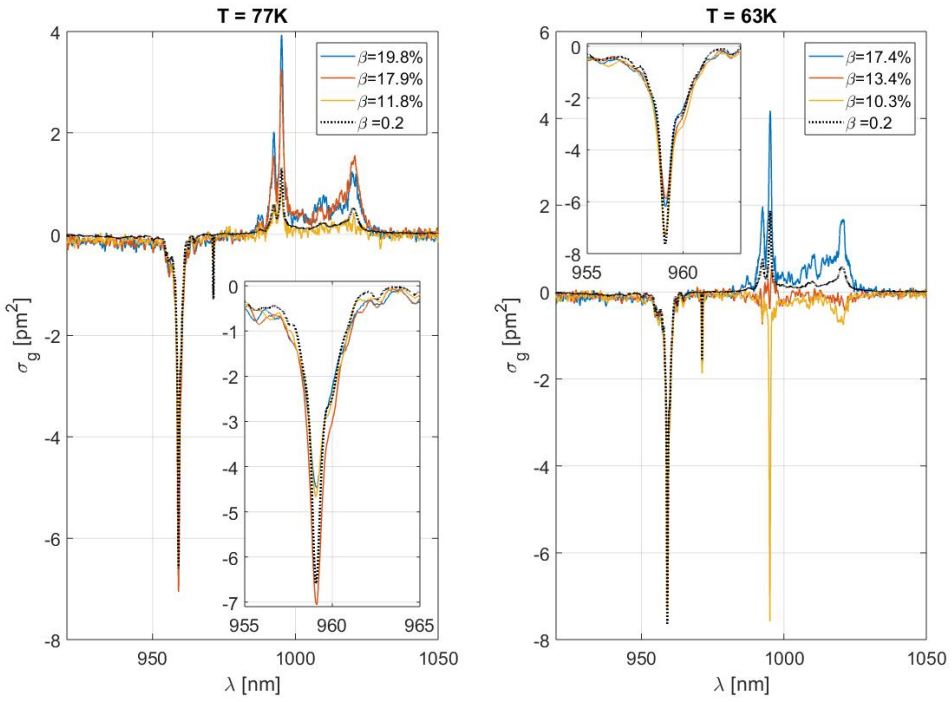

FIGURE 4.20: Gain measurement for Yb:$LuLiF_4$ at 77 K and 63 K, each at three different population inversion levels.

Furthermore, apart from the $T = 183\ K$ case, there is no good match between the simulated gain cross section (black dotted lines) and the respective calculated from pump-probe measurements (solid lines).

Given the success of the fluorescence spectra measurements for the estimation of the emission cross section, and the reasonable results obtained, presented in Section 4.3.2, we are not able, at this stage, to establish with certainty where the discrepancy with the pump-probe measurements lay. Although part of the methodologies of these two characterisations was shared, it is likely that the further data processing required for the pump-probe measurements didn't allow to reach a satisfying resolution. An added source of error, which might have to be more thoroughly characterised in future experiments, is the pump source. In our calculations it is assumed this had a flat intensity distribution over the probed area; this is reasonable as it is derived from imaging the output facet of the fibre coupled to the diode laser, but should in fact have been checked with more caution. The requirement of the probe's diameter being smaller than the pump's over the entire crystal length was relatively difficult to verify with certainty given the restrictions introduced by the angle of the pump beam with respect to the propagation axis of the probe and the need for the first to fully enter and exit the vacuum chamber through the 1-inch optical windows. In hindsight, a more precise monitoring of the input and output pump power would reflect in a better estimation of the population inversion. Particularly challenging was excessive noise in the collected spectra, for which employing another technique woudl have possibly provided a less noisy

measurement, although it would have substantially increased the long measurement execution time, already in the order of 30 *min* for each collected spectrum.
These results, unfortunately, didn't provide the information we were seeking, i.e. another way of determining the emission cross section, and characterising the gain cross section. However, with an increased level of understanding of the equipment employed and a more careful characterisation of the pump laser, we are confident that the presented is a solid methodology for measuring the gain cross section of not only the tested Yb:$LiLuF_4$ crystal, but any laser crystal, especially thanks to the synchronisation between the pump pulse and the spectral measurement, which provides pump-signal-free spectral measurements regardless of the pump wavelength.

4.5 Conclusions

In conclusion, we have investigated Yb:$LiLuF_4$ a promising candidate for pulsed laser operation in the cryogenic-cooling regime, potentially more efficient than the isomorph Yb:YLF crystal. Due to the lack of spectroscopic data at low temperatures in the literature, we characterised its σ- and π-polarised absorption and emission cross sections in the temperature range (RT-63 *K*).
The absorption cross section measurement methodology was the same employed for the Nd-doped crystals, and was well established throughout this work. In order to make up for the lack of an adequate probe, we developed a white light source extending in over the wavelength range (600-1400) *nm*, which can be employed to probe other laser crystals with absorption features in this range. We found that the σ-polarised absorption cross section presents two main peaks, corresponding to the $1 \rightarrow 5$ transition around 960 *nm* and to the ZPL around 972 *nm*, and they respectively present a 9.4- and 15-fold increase in peak value, from (0.37 ± 0.04) pm^2 and (0.27 ± 0.03) pm^2 to (3.50 ± 0.04) pm^2 and (4.03 ± 0.04) pm^2, respectively, while narrowing and slightly redshifting over the temperature range explored. We also measured a ~ 25 *nm*-wide band extending in the wavelength range $(925 - 950)$ *nm*, due to the electron-phonon interaction typical for this crystal. This band, with an average value around 0.5 pm^2 at 63 *K*, is particularly suitable for diode-pumping with commercial high-power diodes operating at 940 *nm*, which would not require any wavelength stabilisation, as opposed to when pumping narrow absorption lines. The π-polarised absorption cross section presented one main peak around 960 *nm*, the strength of which increased by 9.5-times, from (1.02 ± 0.02) pm^2 to (9.65 ± 0.08) pm^2, over the same temperature range explored for the σ-polarisation.
Furthermore, we developed a novel methodology that provided pump-signal-free spectra when measuring the fluorescence spectral distribution. For this measurement, we employed a 960 *nm* diode pump, the signal of which would have determined a loss of spectral information in the wavelength region of its bandwidth. Hence we modulated the pump, and developed an Arduino-driven synchronisation that timed the

OSA measurement with respect to the end of the pump's pulse; this way the pump signal was completely extinguished and the collected spectral data was purely due to the fluorescence signal. At the same time, we characterised the temperature-dependent fluorescence lifetime, obtaining results in good agreement with the literature. By applying the integral F-L method, we calculated the emission cross section for several temperatures in the range (RT-63 K). The *sigma*-polarised emission cross section exihibited one main peak corresponding to the ZPL, and a ~ 20 nm-broad band extending over the range $(990 - 1020)$ nm. The main peak presented a 4x strength increase, from ~ 0.3 pm^2 to (1.79 ± 0.02) pm^2 over the temperature range explored. The π-polarised emission cross section presents one main peak around 994 nm that splits into two peaks below ~ 150 K: one peak is centred in 993 nm and the other, stronger one, centred in 995 nm. Their peak values increase from a common value of (1.06 ± 0.07) pm^2 at RT to (3.86 ± 0.27) pm^2 and (9.46 ± 0.66) pm^2, respectively, at 63 K.

It is known that Yb:$LuLiF_4$'s emission cross section is affected by reabsorption due to the overlap between absorption and emission spectra. In our experiment, we employed the thinnest available sample, however had no other means of verifying how precise the obtained emission cross section was. This was also due to the known non-reciprocity between absorption and emission cross sections in presence of electron-phonon interaction, thus compromising the reciprocity method. An alternative way of measuring the emission cross section was to undertake pump-probe measurements of the gain cross section, and retrieving the emission cross section from the first. For these measurements, we employed a slightly modified setup than the one used for fluorescence spectra measurements, to include a non-colinear pump to the probe laser. Moreover, we employed the same Arduino synchronisation to obtain pump-signal-free spectra. Unfortunately, the collected data wasn't resolved well enough to provide consistent information and produced trends for the different tested temperatures in the range $(183 - 63)$ K that didn't match our expectations. At this stage, we are unable to pin down with certainty what the cause, or the mixture of causes were. We are confident that with improvements and appropriate measurement settings, this methodology, comprehensive of a novel way of providing pump-signal-free fluorescence data, will provide the sought results in the near future.

References

[1] T. Y. Fan, D. J. Ripin, R. L. Aggarwal, J. R. Ochoa, B. Chann, M. Tilleman, and J. Spitzberg, "*Cryogenic Yb^{3+}-Doped Solid-State Lasers*," IEEE Journal of Selected Topics in Quantum Electronics **13**, 448–459 (2007).

[2] H. Lin, F. Pirzio, A. Volpi, G. Cittadino, A. D. Lieto, M. Tonelli, and A. Agnesi, "*Crystal growth, spectroscopic characterization, and sub-100 femtosecond mode-locked operation of a Yb:LiLuF4 laser,*" Journal of the Optical Society of America B **33**, 2350–2356 (2016).

[3] J. Kawanaka, K. Yamakawa, H. Nishioka, and K. Ueda, "*Improved high-field laser characteristics of a diode-pumped Yb:$LiYF_4$ crystal at low temperature,*" Optics Express **10**, 455–460 (2002).

[4] D. C. Brown, S. Tornegård, J. Kolis, C. McMillen, C. Moore, L. Sanjeewa, and C. Hancock, "*The Application of Cryogenic Laser Physics to the Development of High Average Power Ultra-Short Pulse Lasers,*" Applied Sciences **6** (2016).

[5] R. L. Aggarwal, D. J. Ripin, J. R. Ochoa, and T. Y. Fan, "*Measurement of thermo-optic properties of $Y_3Al_5O_12$, $Lu_3Al_5O_12$, $YAIO_3$, $LiYF_4$, $LiLuF_4$, BaY_2F_8, $KGd(WO_4)_2$, and $KY(WO_4)_2$ laser crystals in the 80–300K temperature range,*" Journal of Applied Physics **98**, 103514 (2005).

[6] A. Bensalah, Y. Guyot, A. Brenier, H. Sato, T. Fukuda, and G. Boulon, "*Spectroscopic properties of Yb3+: LuLiF4 crystal grown by the Czochralski method for laser applications and evaluation of quenching processes: a comparison with Yb3+: YLiF4,*" Journal of Alloys and Compounds **380**, 15 – 26 (2004). Proceedings of the 4th International Spring Workshop on Spectroscopy, Structure and Synthesis of Rare Earth Systems.

[7] J. Yin, Y. Hang, X. He, L. Zhang, C. Zhao, J. Gong, and P. Zhang, "*Direct comparison of Yb3-doped LiYF4 and LiLuF4 as laser media at room-temperature,*" Laser Physics Letters **9**, 126–130 (2011).

[8] L. E. Zapata, D. J. Ripin, and T. Y. Fan, "*Power scaling of cryogenic Yb:LiYF4 lasers,*" Optics Letters **35**, 1854–1856 (2010).

[9] D. E. Miller, J. R. Ochoa, and T. Y. Fan, "*Cryogenically cooled, 149 W, Q-switched, Yb:LiYF4 laser,*" Optics Letters **38**, 4260–4261 (2013).

[10] N. Ter-Gabrielan, V. Fromzel, T. Sanamyan, and M. Dubinskii, "*Highly-efficient Q-switched Yb:YLF laser at 995 nm with a second harmonic conversion,*" Optical Materials Express **7**, 2396–2403 (2017).

[11] U. Demirbas, H. Cankaya, J. Thesinga, F. X. Kärtner, and M. Pergament, "*Efficient, diode-pumped, high-power (>300W) cryogenic Yb:YLF laser with broad-tunability*

(995-1020.5 nm): investigation of E//a-axis for lasing," Optics Express **27**, 36562–36579 (2019).

[12] N. Coluccelli, G. Galzerano, L. Bonelli, A. D. Lieto, M. Tonelli, and P. Laporta, "*Diode-pumped passively mode-locked Yb:YLF laser,*" Optics Express **16**, 2922–2927 (2008).

[13] F. Druon, S. Ricaud, D. N. Papadopoulos, A. Pellegrina, P. Camy, J. L. Doualan, R. Moncorgé, A. Courjaud, E. Mottay, and P. Georges, "*On Yb:CaF_2 and Yb:SrF_2: review of spectroscopic and thermal properties and their impact on femtosecond and high power laser performance (invited).*" Optical Materials Express **1**, 489–502 (2011).

[14] V. Cardinali, E. Marmois, B. Le Garrec, and G. Bourdet, "*Determination of the thermo-optic coefficient dn/dT of ytterbium doped ceramics (Sc2O3, Y2O3, Lu2O3, YAG), crystals (YAG, CaF2) and neodymium doped phosphate glass at cryogenic temperature,*" Optical Materials **34**, 990–994 (2012). 6th Laser Ceramics Symposium.

[15] A. Lupei, V. Lupei, C. Presura, V. N. Enaki, and A. Petraru, "*Electron-phonon coupling effects on Yb3spectra in several laser crystals,*" Journal of Physics: Condensed Matter **11**, 3769–3778 (1999).

[16] https://https://uk.rs-online.com/web/p/halogen-capsule-bulbs/0250413/.

[17] A. Volpi, G. Cittadino, A. D. Lieto, A. Cassanho, H. P. Jenssen, and M. Tonelli, "*Investigation of Yb-doped LiLuF4 single crystals for optical cooling,*" Optical Engineering **56**, 1 – 5 (2016).

[18] S. J. Yoon and J. I. Mackenzie, "*Implications of the temperature dependence of Nd:YAG spectroscopic values for low temperature laser operation at 946 nm,*" Proc. SPIE 9135, Laser Sources and Applications II **913503** (2014).

[19] D. E. McCumber, "*Einstein Relations Connecting Broadband Emission and Absorption Spectra,*" Physical Review **136**, A954–A957 (1964).

[20] W. B. Fowler and D. L. Dexter, "*Relation between Absorption and Emission Probabilities in Luminescent Centers in Ionic Solids,*" Physical Review **128**, 2154–2165 (1962).

[21] W. Krupke, "*Induced-emission cross sections in neodymium laser glasses,*" IEEE Journal of Quantum Electronics **10**, 450–457 (1974).

[22] B. Aull and H. Jenssen, "*Vibronic interactions in Nd:YAG resulting in nonreciprocity of absorption and stimulated emission cross sections,*" IEEE Journal of Quantum Electronics **18**, 925–930 (1982).

[23] https://www.arduino.cc/.

[24] https://uk.mathworks.com/help/signal/ref/sgolayfilt.html.

[25] S. A. Payne, J. A. Caird, L. L. Chase, L. K. Smith, N. D. Nielsen, and W. F. Krupke, "*Spectroscopy and gain measurements of Nd3+ in SrF2 and other fluorite-structure hosts*," Journal of the Optical Society of America B **8**, 726–740 (1991).

Chapter 5

ETU measurements

5.1 Introduction

Energy Transfer Upconversion (ETU), as detailed in Section 2.3, is a detrimental effect that, added to other heat-generating processes, like Cross Relaxation (CR), worsens the laser performance and can potentially lead to catastrophic failure of laser operation. ETU is a mechanism that depopulates the upper laser level via the exchange of energy between two neighbouring ions, of which one is excited to a higher energy level, and the other is de-excited to a lower energy level. These two ions produce waste heat via their respective decay channels. In the CR process, two ions, one in a higher energy level, one in a lower, exchange energy so that the first decays, and the other is promoted, to a common intermediate energy level. They both finally relax to the ground level, generating extra heat. Furthermore, also this process depopulates the upper laser level. Figure 2.1 shows the possible ETU and CR channels in the Nd^{3+} doping-ion, the main dopant investigated in this thesis.
The quadratic dependence of the strength of ETU on the upper laser level population N_2, as detailed in Section 2.3, coupled with the need to achieve sufficient gain to efficient laser operation, makes the ETU a key factor affecting the laser operation, therefore its knowledge is key for a correct modelling of the laser performance. This is especially true for the low-gain sub-1 μm laser transitions that require a relatively high population inversion to overcome the cavity loss, like the Nd^{3+} systems we have investigated in this thesis. Currently there is little literature providing data on the ETU coefficient in Nd-doped hosts across different temperature regimes, hence here we provide new useful data.
In this chapter, we present the methodology employed, and its improvements with respect to the previously reported techniques, for the measurement of the ETU coefficient in Nd-doped crystals. The newly developed automated setup provides higher precision, i.e. a smaller uncertainty, in the collected data and subsequent determination of the ETU coefficient. Furthermore, judicious choice in the experimental parameters allowed

the system of equations (2.7) to be solved in the steady-state regime, as opposed to the time-dependent solution employed previously [1, 2]. This provides a 60 to 100 times shorter computation time and enables the use of an iterative fitting algorithm based on the minimisation of the variance, where the ETU coefficient, W_{ETU}, is the only fitting parameter.

In order to test the consistency of this upgraded methodology, we measured the dependence of the ETU coefficient on the Nd^{3+} concentration in YAG; this characterisation had previously been executed using an earlier configuration and method, as reported in [2]. The new results are in good agreement with others in the literature for relatively low concentrations, while the data for high doping-concentrations deviated from the trend measured for lower values. Here we give a possible explanation as to why.

Stimulated by the knowledge that the ETU coefficient has a dependence on temperature for different rare-earth impurities in the YAG host [1, 3], we probed the elevated-temperature-dependence of the W_{ETU} macro-parameter in Nd-doped Vanadates with the aim of expanding the knowledge around their spectroscopy. The latter has indeed been widely investigated at both RT and the high-temperature regime [4, 5], however the temperature dependence of some key paramters, e.g. the ETU coefficient, had not been reported at all. These materials, because of their short absorption lengths, operate at relatively high temperatures, due to the high thermal load density produced in the pumped region. In addition, this temperature increase reduces the gain cross section and exacerbates thermal-induced lensing, aberrations, and losses, meaning higher inversion levels are required. In this case, the contribution from ETU may have a strong effect, and it is therefore important to characterise it. As a limiting factor to laser performance, especially when operating on the lower-gain ${}^4F_{3/2} \rightarrow {}^4I_{9/2}$ 9xx-nm transition (914 *nm* for Nd:YVO_4, 912 *nm* for Nd:$GdVO_4$, the two crystals tested), characterising the elevated-temperature dependence of ETU has provided a deeper knowledge of the laser dynamics of these crystals. We tested YVO_4 and $GdVO_4$ hosts, for two different doping levels each, thus again verifying, at the same time, the dependence of this energy transfer process on the dopant concentration. We observed, as for Nd:YAG [1], that the ETU coefficient in Nd-doped Vanadates is inversely proportional to rising temperature, and directly proportional to the doping level.

It is known that, if countermeasures are not taken, as we will discuss in Section 5.4.2, ETU is a limiting parasitic process for efficient laser performance of the 946 *nm* Nd:YAG laser at RT. Driven by the lack of data for ETU coefficient at cryogenic-temperatures in Nd:YAG, we finally characterised the ETU coefficient's dependence on sub-ambient temperatures, from RT to 77 *K*, in 0.3at.%- and 0.57at.%-doped Nd:YAG. We found that the ETU coefficient increases with decreasing temperature, and, consistent with the RT case, is directly proportional to the Nd^{3+}-concentration.

Employing existing laser-performance models including the effect of ETU [6], and accounting for the temperature-dependent spectroscopy results presented in Chapter 3, we calculated, and then demonstrated by developing a cryogenically-cooled laser as

detailed in Chapter 6, that despite an increase in the ETU coefficient with decreasing temperature, the net effect of cryogenic-cooling on the overall laser performance is overwhelmingly positive.

5.2 Methodology and experimental setup

In Section 2.3 we showed that the z-scan technique is the method of choice for a sensitive measurement of the ETU coefficient [1]. This technique entails moving a sample through the focus of a pump laser beam, thus controlling the incident irradiance. In order to obtain suitable data, the range of the incident irradiance values needs to go from the small-signal regime, to values comparable, if not higher than, the saturation irradiance, I_{sat}, of the crystal being investigated, as argued in Chapter 2.
Figure 5.1 depicts a schematic of the setup that was first employed to perform M^2 measurements of the Ti:sapphire pump-laser, used in our experiment, and subsequent z-scan measurements. Appropriate modifications, that will be highlighted throughout this chapter, to the setup, were made according to the needs of specific samples and the regime in which they were tested. As shown in Fig. 5.1, the output beam a lineary-polarised CW Ti:sapphire laser (Spectra-Physics, 3900S) passes through a $\lambda/2$ waveplate, defining the polarisation direction, and a polariser, with its transmission axis aligned to the table top. The combined action of these two components was used to control the incident power, and therefore the irradiance, on the samples. When testing uniaxial crystals, such as the orthovanadates, we turned the sample by 90^o according to the crystal axis we required access to.
The Ti:sapphire was tuned to the desired wavelength in the band (800-820) nm, according to the absorption peak to be probed. While measuring the ETU coefficient of Nd-doped Vanadates, we demonstrated that this measurement is independent of the absorption peak employed, as we detail in Section 5.4.1. This important result allowed us to tune the pump's wavelength slightly off peak during the measurement of the ETU coefficient for Nd:YAG at cryogenic-temperatures, when the peak absorption was too high (Chapter 3) for the transmitted signal to be detected. The thorough characterisation of the absorption cross section prior to the ETU coefficient measurement of all the samples listed in Table 5.1 meant that the small-signal transmission value could be calculated a-priori, regardless of the particular pump wavelength employed. Its experimental value obtained during a z-scan, i.e. the value in the wings of the transmission curve (see, for example, Fig. 5.3), was then a further confirmation of the quality of the setup calibration, which we detail later in this section.

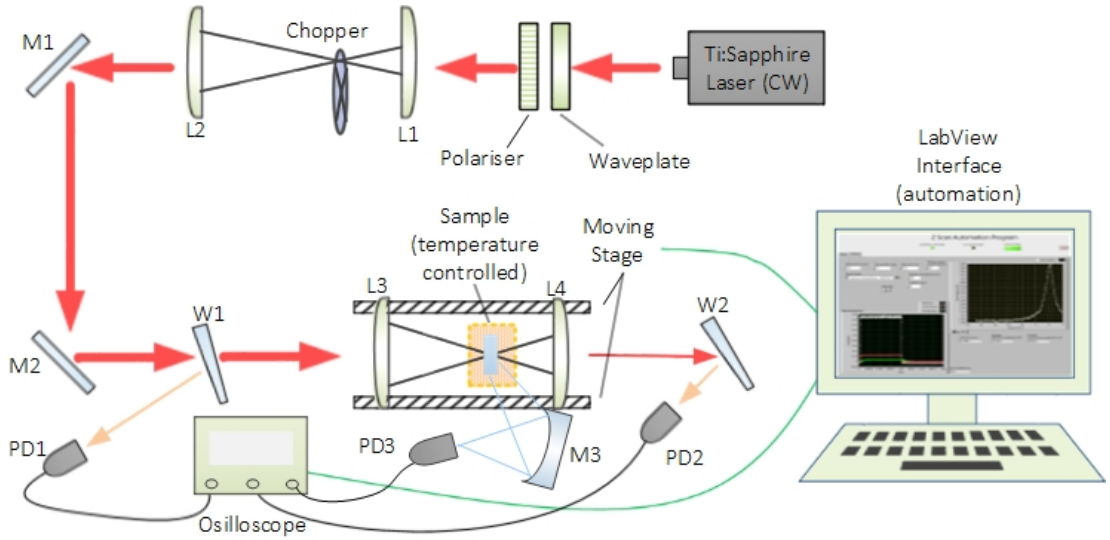

FIGURE 5.1: Automated ETU measurement setup. Lenses: L_1 ($f = 50\ mm$), L_2 ($f = 300\ mm$ or $f = 100\ mm$), L_3 ($f = 200\ mm$), L_4 ($f = 175\ mm$); flat high reflectivity mirrors at 808 nm: M_1 and M_2; M_3 curved mirror (radius or curvature=100 mm); glass wedges: W_1 and W_2; Si photodiodes: PD_1, PD_2 and PD_3.

A list of the samples tested, their lengths and doping-ion concentrations is reported in Table 5.1.

Sample	Doping [at.%]	Length [mm]	Temp. regime [^oK]	Manufacturer
Nd:YAG	0.301 ± 0.003	5.10	RT	Castech
Nd:YAG	0.584 ± 0.005	1.10	RT	Altechna
Nd:YAG	0.740 ± 0.007	1.10	RT	Altechna
Nd:YAG	1.068 ± 0.007	1.10	RT	Altechna
Nd:YAG	1.333 ± 0.008	1.08	RT	Altechna
Nd:YAG	1.841 ± 0.008	1.10	RT	Altechna
Nd:YVO_4	0.60 ± 0.02	1.00	RT-450	Castech
Nd:YVO_4	0.97 ± 0.02	1.00	RT-450	Castech
Nd:$GdVO_4$	0.54 ± 0.03	1.00	RT-450	Castech
Nd:$GdVO_4$	1.15 ± 0.03	1.00	RT-450	Castech
Nd:YAG	0.301 ± 0.003	5.10	77-RT	Castech
Nd:YAG	0.570 ± 0.005	1.08	77-RT	Castech

TABLE 5.1: Details of the Nd-doped samples investigated in the ETU coefficient measurements.

In order to always satisfy the assumption that the beam doesn't change significantly through the sample, as detailed in Section 2.3, we employed different focal lengths for lens L_2, after lens L_1 (f=50 mm), providing different magnifications and thus second moment beam radii $w_{x,y}$ after the the moving lens L_3 (f=200 mm). For the $\sim 1\ mm$-thick samples a lens $L_2 = 300\ mm$ provided a 6x magnification that expanded the beam

to a size suitable to obtain, after lens L_3, beam waist radii $w_x = (19.7 \pm 0.2)\ \mu m$ and $(w_y = 19.9 \pm 0.2)\ \mu m$ with an average confocal parameter in air of $(3.05 \pm 0.15)\ mm$. A lens $L_2 = 100\ mm$ was employed to provide a 2x magnification, and ultimately $w_x = (37.0 \pm 0.2)\ \mu m$ and $(w_y = 36.2 \pm 0.2)\ \mu m$ with an average confocal parameter in air of $(9.5 \pm 0.1)\ mm$, for the 5.1 mm-long Nd:YAG sample tested.
A mechanical chopper modulated the Ti:sapphire beam to get a pulse width of (0.75-1) ms, a long enough time for the crystal's population to reach steady state, while short enough to avoid significant localised heating of the sample during the duration of the pump-pulse. A duty cycle of 5% was employed in order to allow enough time for the complete diffusion of heat away from the excited volume of the sample between successive pulses. A quantitative estimation of the restrictions introduced by these assumptions, and a case where these possibly weren't fulfilled is presented in Section 5.3.2.
An uncoated glass wedge, W_1, directed $\sim 4\%$ of the incident collimated beam to the photodiode PD_1: this provided a reference signal to the oscilloscope. The second wedge W_2, after the lens L_4, which recollimated the pump beam, reflected $\sim 4\%$ of the transmitted light to the photodiode PD_2, providing quantification of the transmitted power with respect to the incident power, captured on the same oscilloscope. The curved mirror M_3 (Radius Of Curvature, $ROC = 100\ mm$) imaged the resulting fluorescence from the pumped region onto the fast photodiode PD_3, which was employed to characterise the fluorescence lifetime of the samples tested.
As in Chapter 3, the sample was placed on a controlled heating stage when characterising ETU at elevated-temperature for Nd-doped Vanadates, and in a cryostat, when probing the sub-ambient temperature-dependence in Nd:YAG.
Automation of the experiment was coordinated through ©LabView and comprised a linear translation stage (Stackshot) for the lenses L_3 and L_4. At each (adjustable-length) step of the scan, communication between the oscilloscope (Agilent MSO6104A) and the LabView interface allowed the collection of the incident and transmitted waveforms (sample in Fig. 5.8), which could be repeated for as many times as required.
Prior to a z-scan measurement run, the pump's beam quality parameter, M^2, was measured with a wedge positioned after the L_3 focusing lens. A CCD beam profiling camera (Spiricon BGP-USB-SP503U), was used to measure the beam distribution and caustic around the beam waist, obtaining $M^2_{x,y} = (1.06 \pm 0.01)$ when testing the 1 mm-long samples, and $M^2_x = (1.05 \pm 0.01)$ when probing the 5.1 mm-long sample. This measurement was periodically repeated in order to verify its consistency. We also verified that it was independent of power of the Ti:sapphire.
The z-scan setup was calibrated in order to retrieve a quantitative relationship between the voltages read by the reference and transmission photodiodes, PD_1 and PD_2, and the power after the 200 mm moving lens (L_3), i.e. incident power P_{in}, and before the 175 mm moving collection lens (L_4), i.e. transmitted power P_{tran}, respectively. Fig. 5.2 shows a typical calibration dataset.

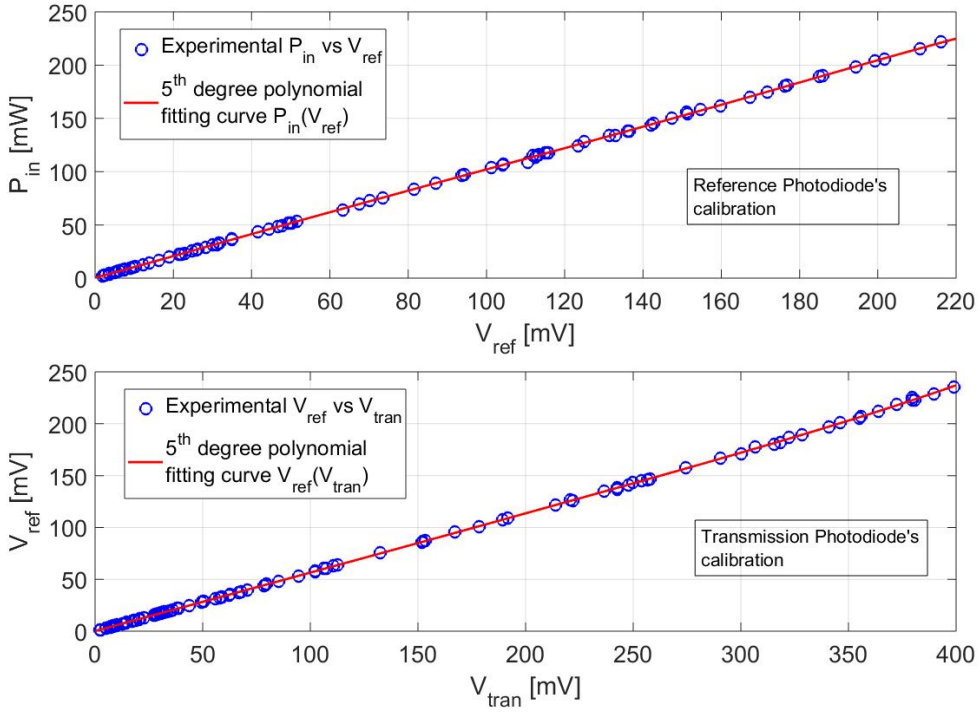

FIGURE 5.2: Calibration of reference and transmission PDs: analytical forms of the relations between voltages and powers.

The upper plot of Fig. 5.2 shows the calibration of the reference PD (PD_1). This was carried out by positioning a power meter after the focusing lens L_3, and collecting power, as read by the power meter, and voltage values, as read by PD_1, while increasing the Ti:sapphire's power via rotating the waveplate. The calibration of the transmission PD (PD_2), shown in the bottom plot, was carried out by collecting voltage values as read by PD_1 and PD_2 simultaneously, with increasing pump power (again, by rotating the waveplate). The analytical forms of the relations were obtained by fitting polynomial curves to the calibration data. In the first case $P_{in} = f(V_{PD_1})$, while in the second case $V_{PD_1} = g(V_{PD_2})$, which could be converted into power via the first relation, hence $P_{tran} = f(g(V_{PD_2}))$. Both f and g were 5^{th}-degree polynomial functions, which optimally fitted the experimental data and hence provided a high level of precision when converting voltages into powers, so that we could always precisely quantify P_{in} and P_{tran} from PD_1 and PD_2's voltage readings. The goodness of the calibration was firstly verified by making sure that z-scan measurements performed with no sample in the setup always returned, after the conversion of voltages into powers, a transmittance of $(100 \pm 1)\%$. Secondly, a further confirmation of a successful calibration of the setup was given by the small-signal transmission through the sample matching, within experimental uncertainty, the ones calculated employing the previously collected absorption data, i.e. absorption cross section characterisation of the tested samples (Chapter 3). In the case of the ETU coefficient measurement for the cryogenically-cooled Nd:YAG the calibration of the setup was performed accounting for the chamber's windows' presence

by positioning them after lens L_3 and before lens L_4 in common lens mounts. This way, the calibration already accounted for the windows' losses (measured to be $\sim$ 1% at the pump wavelength), and the incident and transmitted powers calculated from the voltage measurements didn't need any further correction.
While this calibration methodology worked flawlessly for the ETU coefficient measurements of Nd-doped Vanadates at elevated temperatures and Nd:YAG at RT, it didn't always work in the case of the cryogenically-cooled Nd:YAG, as explained below. The challenge, in this case, was that the transmitted signal in the small-signal regime was the order of a few mV, given the high absorption cross section of Nd:YAG at sub-ambient temperatures (Chapter 3), while in the high-irradiance regime it became as high as $\sim 350\ mV$, determining a $\sim 13\ dB$ increase to be detected within the same measurement. While this value was well within the dynamic range of the transmission PD, the calibration of the setup was not always within our self-imposed tolerance of 1% over the entire voltage range, especially in the range from zero up to $\sim 10\ mV$. This discrepancy meant that the conversion to transmitted power was affected by a systematic error which we were not able to quantify with sufficient precision that we could correct for it. This error was particularly appreciable in a, randomly, too high or too low, value of for the small-signal transmission at temperatures lower than 150 K, when the transmittance was below 10%. In these cases, the pump was tuned off-peak to increase the signal-to-noise ratio and operate in optimal-calibration zones. Off-peak tuning of the pump has already been employed in [3] for equivalent measurements on Er:YAG samples, furthermore we verified, in our measurements on Nd-doped Vanadates, which will be presented later, that the ETU coefficient measurement is independent on the absorption peak employed.
A possible way to avoid collecting data in the low-end region of the transmission range, would be to employ a lock-in amplifier to boost the value in a range where the calibration of the setup was optimal. This, however, would have meant an added level of complexity for the automation, and in evaluating this possibility we concluded that off-peak tuning was a solution optimal to our case because it worked well, had already been employed by other authors [3], and didn't require any further adjustment.
Other possible sources of uncertainty in the measurements were evaluated by propagating the uncertainties associated to the other fixed parameters through the numerical model (2.7). Here we established that the power instability of the pump beam, measured to be (10-20)%, dominated. In order to explain how this instability affected the measurement and why it had to be addressed with caution, we present some examples of simulated transmission curves, differing only by the incident pump power P_{in}. As an example, we model a 0.6at.%-doped, 1 mm-long Nd:YAG crystal at RT, of typical length and doping-level as the ones investigated herein, and an ETU coefficient value of $W_{ETU} = 35 \cdot 10^{-18}\ cm^3/s$, consistent with the results presented in Section 5.3.2.
Figure 5.3 shows the simulated z-scan transmission curves for incident Ti:sapphire powers of 150 mW (blue), 180 mW (green) and 200 mW (red): here it is interesting to appreciate how the transmission curves' height changes with the incident power.

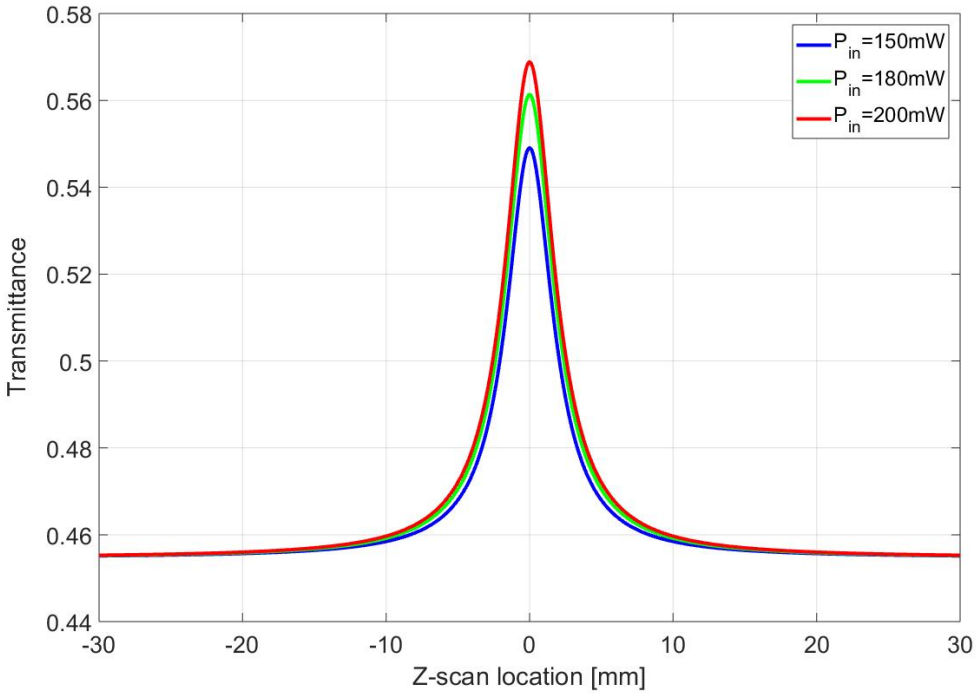

FIGURE 5.3: Simulated z-scan transmission curves at different incident powers for a 1 mm-long, 0.6at.%-doped Nd:YAG, with $W_{ETU} = 35 \cdot 10^{-18}\ cm^3/s$.

For the wings, with the arbitrary z-scan coordinate $|z| \gtrapprox 20\ mm$), the pump size in the crystal is big enough for this area to correspond to the small-signal transmission regime, the same exploited in Chapter 3 to characterise the spectroscopy of the samples. In this regime the population inversion is negligible, and the transmission is governed by the Beer-Lambert law (2.1), independent of the incident power (or irradiance). As the scan moves away from the wings, and hence from the small-signal regime, the pump size in the crystal becomes smaller, and the incident power (irradiance) is big enough to create a substantial level of population inversion so that the ground state starts bleaching, and the transmission increases, reaching its maximum around $z = 0\ mm$, the position of the beam waist. In this high-irradiance regime the transmission is dependent on the incident power, hence the three different curves for the distinct Ti:sapphire powers. It is important to mention that the ETU coefficient measurement itself is independent of the incident pump power, as demonstrated in [7], however Fig. 5.3 shows that the transmission level isn't. Having the ETU coefficient as the only fitting parameter meant that our fitting algorithm adjusted this coefficient to make the theoretical curve's height match the experimental data while minimising the variance, as the value of the wings' transmission was fixed by the absorption cross section characterised in Chapter 3. With this in mind, one can understand the challenge to estimate the ETU coefficient precisely with a strongly fluctuating pump power.
An example of the worst case scenario follows, and is shown in Fig. 5.4.

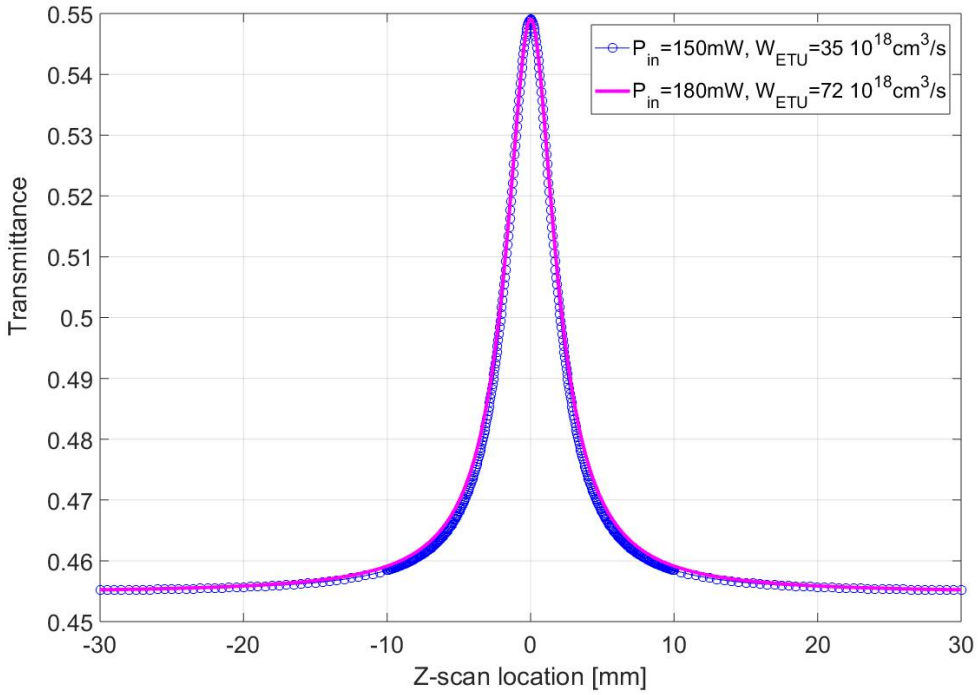

FIGURE 5.4: "Experimental" (simulated) data for a 150 mW pump (blue circles) and fitted data with a modelled 180 mW pump (magenta line).

We hypothesise we measure an average pump power of 180 mW, and we collect experimental data corresponding to the blue-circles transmission curve in Fig. 5.4. Due to the pump's $\sim 15\%$ fluctuation, the power could be low as ~ 150 mW. In the worst case scenario, if the "experimental" (blue circles) data points within the z-scan coordinate range $|z| \lesssim 10$ corresponded to $P_{in} = 150$ mW, and we tried to fit the ETU model with a fixed $P_{in} = 180$ mW as per our initial measurement, we would calculate an W_{ETU} value of $72 \cdot 10^{-18}$ cm^3/s, as per the magenta solid line in Fig. 5.4. The magenta fitted curve and the "experimental" blue circles present a good overlap, however the fitted W_{ETU} value is almost two times larger than the first, real, value ($W_{ETU} = 35 \cdot 10^{-18}$ cm^3/s)! This gives a good indication of how the pump's instability could negatively affect the measurement.

In order to address this problem, and hence minimise this source of uncertainty, we put three mitigation measures in place, employing a LabView-driven interface. Firstly, thanks to constant and precise monitoring of the incident and transmitted powers (voltages), we fixed a suitable tolerance window for the input power: the measurements corresponding to incident powers outside the allowed band were discarded. Secondly, we measured P_{in} and P_{tran} (voltages) simultaneously, so that each transmission value could be tied to its corresponding P_{in}. Lastly, the transmittance measurement was repeated multiple times at each z-scan position, in order to increase the confidence in the measured value and at the same time determine an uncertainty on each data point given by the standard deviation from the mean as defined in Eq. (3.2b). These mitigation

strategies provided a substantial improvement in the collected data, as Fig. 5.6 shows. The fitting procedure we employed was based on the minimisation of the variance defined as

$$S^2(W_{ETU}) = \sum_z \left[(T_z - T_{th}(z, W_{ETU}))^2 \right] \tag{5.1}$$

where the dependence of the theoretical transmission value $T_{th}(z)$ (calculated numerically from model (2.7)) on the ETU coefficient, W_{ETU}, is emphasised, because the latter is the minimising parameter being sought.

Following the previous discussion on the effects that the Ti:sapphire's power instability had on the measurements, we further upgraded our fitting procedure in order to account for said fluctuations. By monitoring the input and transmitted powers (voltages), P_{in} could be measured and associated to each step of the z-scan. The calculated theoretical transmission T_{th} from model (2.7) was therefore $T_{th}(z, P_{in,z}, W_{ETU})$, dependent on the measured parameters z, the z-scan coordinate (and associated pump radius), and $P_{in,z}$, the average incident power corresponding to the z, and the fitting parameter W_{ETU}. To illustrate, we present in Fig. 5.5 a typical dataset collected during a z-scan. The green dots for each z correspond to single measurements, and are a good representation of the pump power dispersion, already mitigated by a set collection-window, as detailed above. The blue and red crosses are the z-dependent averages of the single measurements, for each z. As one can observe, despite the averaging over multiple measurements, noise is still present, although the signal-to-noise ratio is dramatically improved by the averaging. The average P_{in} values were employed in the fitting procedure as z-dependent incident powers when calculating $T_{th}(z, P_{in,z}, W_{ETU})$. Finally, the transmission P_{tran}/P_{in} was calculated, and this curve fitted to the model (2.7) through the procedure explained above. To illustrate, we present in Fig. 5.6 the measured transmission curve (blue circles) and its fitted W_{ETU}-dependent theoretical curve (red line).

Only for the measurement of the ETU in Nd:YAG at cryogenic temperatures, we further improved the z-scan data collection by introducing the possibility to select two arbitrary z-step lengths, effectively giving a double resolution within the same scan, corresponding to the two different irradiance regimes – low irradiance, i.e. small-signal transmission, and high-irradiance, i.e. bleaching of the ground state, around which the transmission increased up to its maximum. In the case of Fig. 5.6, for which this feature was not exploited, these would correspond to the coordinates $|z| \gtrsim 10\ mm$ and $|z| \lesssim 10\ mm$, respectively. As it is evident, with constant step length the sampling rate in the $|z| \gtrsim 10\ mm$ region is good, but it could however be increased in the $|z| \lesssim 10\ mm$ area, given the sharp variation of the curve within a relatively small z-scan distance ($\sim 5\ mm$).

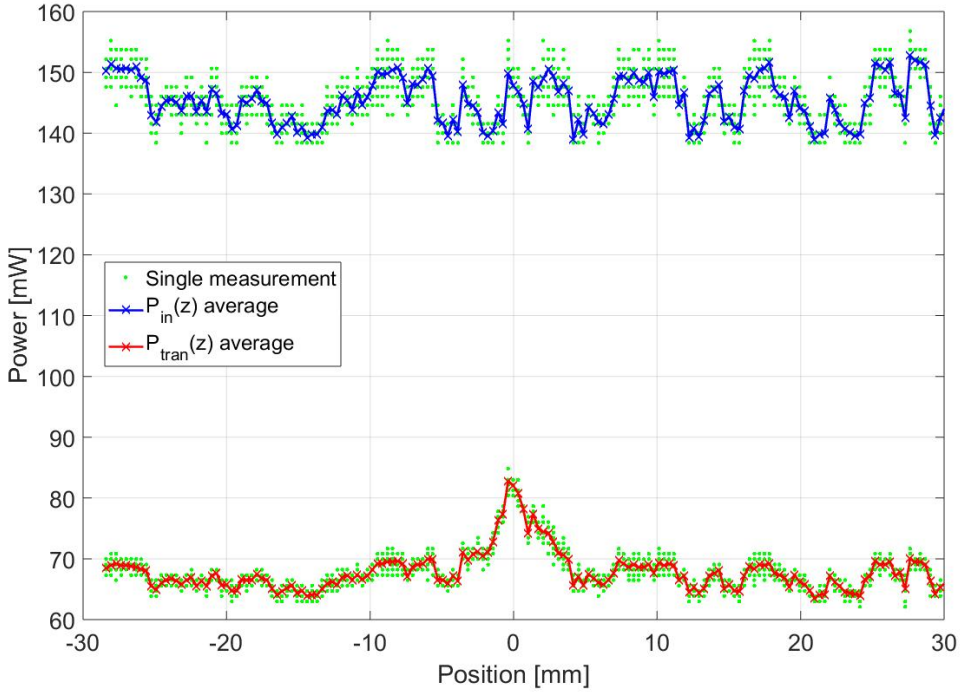

FIGURE 5.5: Typical dataset collected in a z-scan. Green dots: repeated measurements at each fixed z-position; blue line: average P_{in} of the green dots at each z-position; red line: average P_{tran} of the green dots at each z-position.

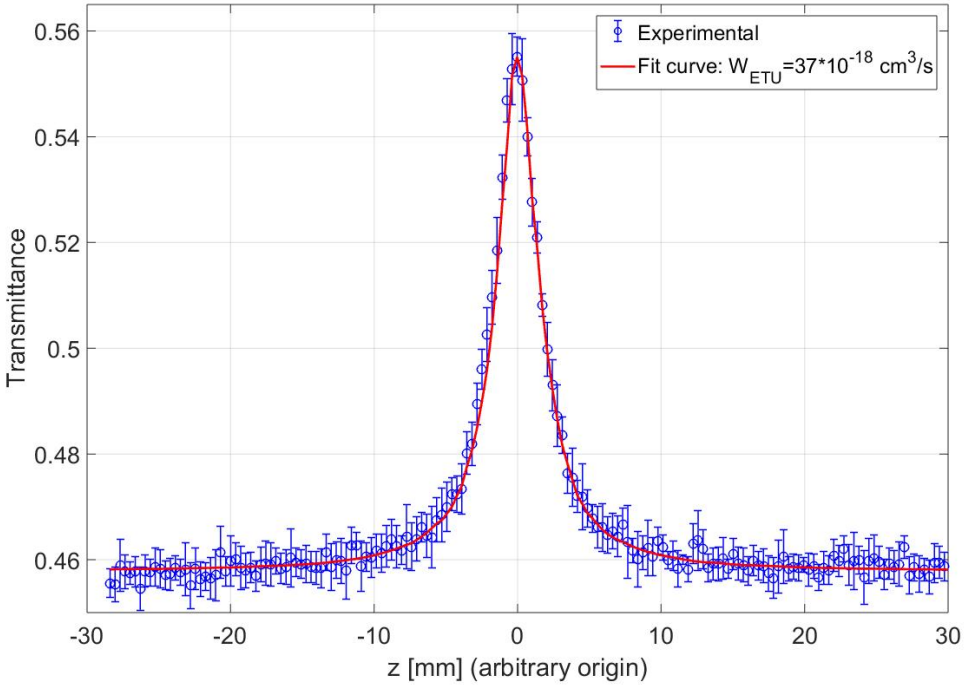

FIGURE 5.6: Typical experimental transmission curve (blue circles) and its fitted theoretical curve (red line).

A typical collected dataset for which this feature was exploited is presented in Fig. 5.7. We often observed experimental data exceeding the theoretically modelled data in the region around $z \sim 10\ mm$. This is possibly due to the actual beam size deviating the most from the calculated one used in the model around the Rayleigh range distance from the arbitrary $z = 0$.

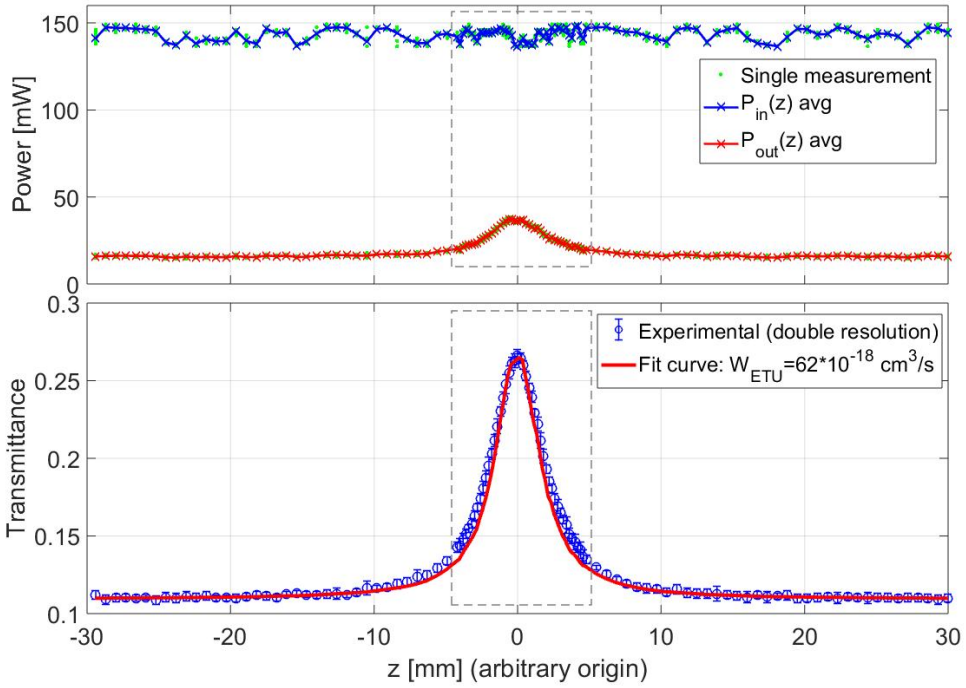

FIGURE 5.7: Typical experimental transmission curve for which the double z-step length option was exploited. Z-step lengths: 0.7 *mm* and 0.2 *mm* outside and inside the dashed gray rectangle, respectively.

In the figure we have highlighted, with a dashed rectangle, the area where a smaller step length was used. In this case, the double z-step-length feature was set to 0.7 *mm*-long, and 0.2 *mm*-long z-steps in the small-signal transmission wings and high-irradiance areas, respectively. This resulted in a higher density of points collected in the high-irradiance regime, effectively providing better data to fit the theoretical model (2.7) to, without however over-sampling the small-signal transmission wings, where a higher density of datapoints would not have been more useful. This particular feature was only developed for the ETU coefficient measurement of the cryogenically-cooled Nd:YAG, where the difference in transmission within the same z-scan was higher than the other cases, namely Nd-doped Vanadates at elevated temperatures and Nd:YAG at RT.
Noticeably, the signal-to-noise ratio of the data shown in Fig. 5.7 is lower than the one in Fig. 5.6: this is because the acceptance window for the P_{in} values was reduced with respect to the previous case, as the lower dispersion of the average $P_{in}(z)$ values shows. Furthermore, because the data collected outside the acceptance window was discarded and the number of data points to be collected at each z-position was fixed, having a

smaller window meant a much longer execution time, which could vary from $\sim 15\ min$ to an hour, according to how severe the pump instability was. At times, the pump's fluctuation required a previous evaluation in order to establish what was the average value, and hence where the central value of the acceptance window should be. Instances where this value was chosen too far from the pump's average meant an even longer execution time. Finally, the parameters chosen for each z-scan, namely step length(s), number of measurements to execute at each z-position, acceptance window's width and scan length, had to be a trade-off between the quality (signal-to-noise ratio, density of data points) of the data collected and the time employed to execute the z-scan.
During the measurements executed on Nd:YAG at RT, we characterised the small-signal fluorescence lifetime. In order to do so, we employed the same fitting procedure based on the minimisation of the variance presented in (5.1): the theoretical model

$$V(t) = V_0\, e^{-\frac{t}{\tau_f}} + V_s \tag{5.2}$$

was fitted to the fluorescence waveform collected at each step of the z-scan by using V_0, τ_f and V_s as fitting parameters. A sample dataset is presented in Fig. 5.8. We only accounted for the data collected in the small-signal transmission regime, obtaining a number of usable waveforms in the order of 100 and a typical dispersion around the average result of $\sim 1\%$, which gave us good confidence in the resulting value for the fluorescence lifetime, moderated by the cross relaxation process (see Section 2.3). The fluorescence signal was also monitored throughout the z-scan: the effect of ETU in shortening the lifetime in the high-irradiance regime can be observed in Fig. 5.8. This shortened lifetime effect was exploited in [8] to determine the ETU coefficient; however the pump distribution employed both experimentally and in the reported model was a simple top-hat, as opposed to our more complex Gaussian distribution. Implementing the latter into the model reported in [8] would have been more time-consuming than conducting our reported experiments, hence our choice to make qualitative observation of a shortened lifetime, without quantitative conclusions drawn from it.
This upgraded setup provided a relatively low uncertainty on the single W_{ETU} measurement, in the order of $\sim 5\%$. However, the dispersion of these measurements around their average, i.e. how repeatable they were, dominated the uncertainty associated with each single one. The errors associated to every W_{ETU} coefficient we will present herein is therefore the standard deviation from the average, with the number of ETU coefficient measurements executed for each case in the order of ~ 7. The typical associated uncertainty was in the order of 15%, comparable to other uncertainties reported for similar ETU coefficient measurements [1, 2, 9, 3]. Although this is a rather substantial value, we think it truthfully reflects the sensitivity of this measurement coupled with the limitation of the setup, e.g. pump instability.

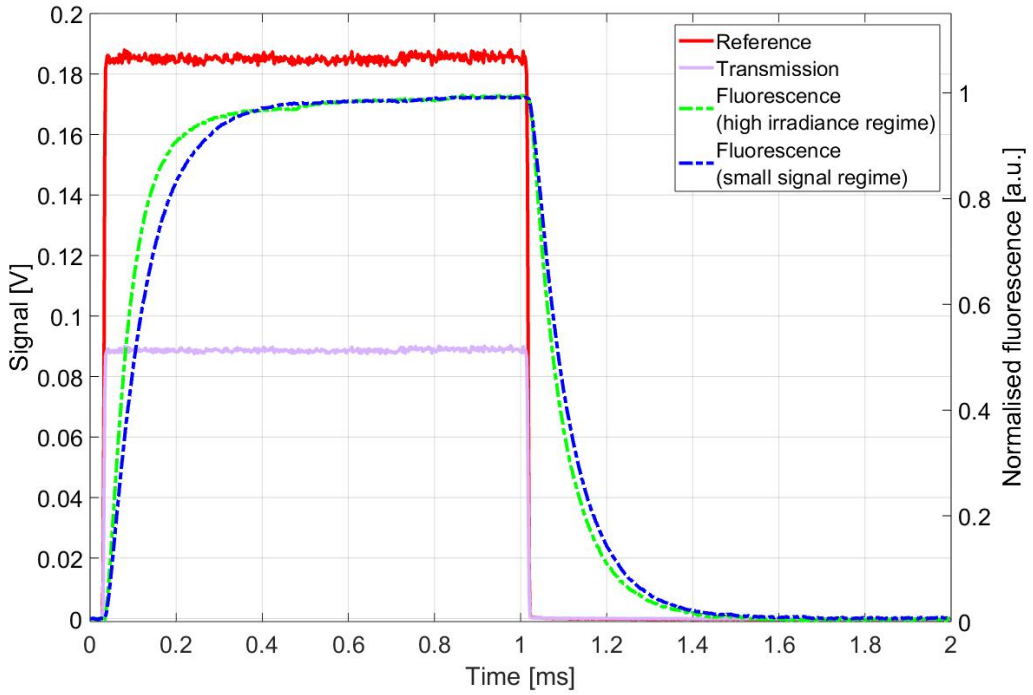

FIGURE 5.8: Sample of waveforms collected at each z-scan step. Solid lines: PD_1 and PD_2 signals [V], in red and pink respectively; dashed lines: small-signal and high-irradiance regimes fluorescence normalised signals [a.u.], in blue and green respectively.

Finally, we have developed a general procedure to measure the ETU coefficient of Nd-doped crystals, once all the required parameters are known and provided that the energy level dynamics is well described by the model (2.7).

5.3 Experimental results

In this section we present the experimental results for three separate cases of the measurement of the ETU coefficient for neodymium ions. Firstly, for Nd-doped orthovanadate, important host materials for compact laser applications. Secondly, the ETU dependence on the Nd^{3+}-doping concentration in the workhorse host material (YAG). Lastly, the temperature dependence for ETU in Nd:YAG, with the primary focus to evaluate its potential effect on laser performance of cryogenically cooled lasers with this active material.

5.3.1 ETU at elevated temperatures in Nd-doped Vanadates

Although some values are reported in literature for the ETU coefficient for Nd-doped Vanadates [10, 11], the temperature dependence of these parameters has not been investigated so far. However, characterising this dependence is beneficial for understanding

how vanadate lasers that operate in the high-temperature regime would be affected by ETU, e.g. laser spark plugs [5, 12, 13]. Hence the knowledge of these parameters provides valuable information for laser engineers.
In previous work, a strong temperature-dependence was demonstrated for the ETU coefficient in Nd:YAG [1]. Underpinned by a comprehensive study of the ${}^2H_{9/2} + {}^4F_{5/2}$ energy level absorption cross section over the range from RT to 450 K, presented in Chapter 3, here we use the same z-scan technique to probe the analogous dependence of the ETU coefficient in Nd:YVO_4 and Nd:$GdVO_4$. In doing so, we prove that the ETU measurement is independent of the absorption peak the pump is tuned to. In fact, we executed the measurements with the Ti:sapphire tuned first on the 808 nm-peak and then on the 806 nm-peak, having characterised their strength in the range (RT-450 K), as presented in Chapter 3. As already detailed in the Methodology Section 5.2, this previous characterisation provided values for the small-signal transmission that were matched by the wings of the z-scan transmission curves for the respective peaks and temperatures. This, provided that the absorption cross section is well characterised within the band employed, paved the road to utilising absorption peaks other than the strongest one. Furthermore, this technique was employed when probing the strongest peak meant that there was close to no transmitted power, as in the case of the ETU coefficient measurement for cryogenically cooled Nd:YAG, presented in Section 5.3.3.
The experimental z-scan transmission curves and their respective fitted theoretical curves, obtained via model (2.7) are presented, for an 808 nm or 806 nm pump, in Figs. 5.9 and 5.10, and Figs. 5.11 and 5.12, for 1.1at.%- and 0.5at.%-doped Nd:$GdVO_4$, respectively. Due to the comparable spectroscopic properties between Nd:$GdVO_4$ and Nd:YVO_4, similar curves and fittings were obtained for the latter. For brevity we have only included examples for Nd:$GdVO_4$. The decrease in the absorption cross section, as predicted by the results presented in Chapter 3 is appreciable, noting the increase in the small-signal transmission with increasing temperature.

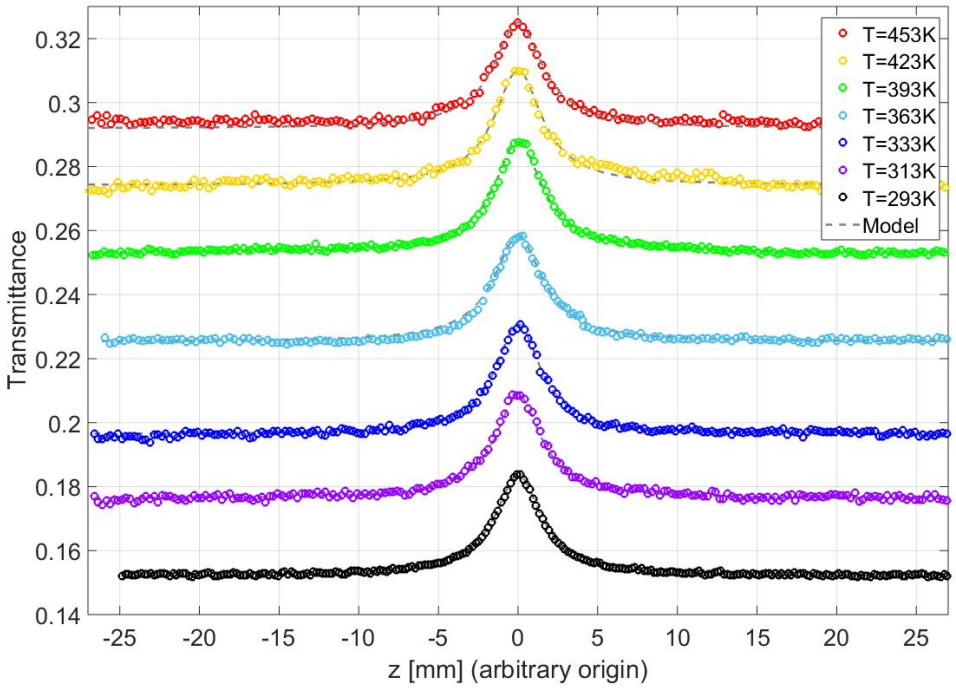

FIGURE 5.9: Experimental 808-nm-pump z-scan curves (circles, color coded) and their respective fitted curves (grey dashed) for 1.1at.%-doped Nd:$GdVO_4$ in the temperature range (RT-453 *K*).

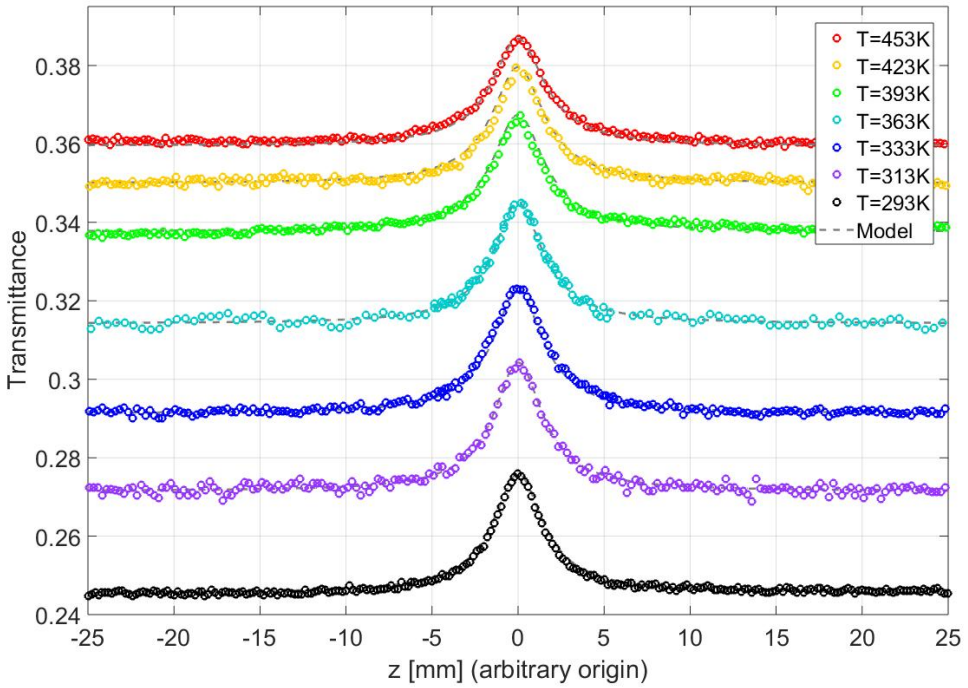

FIGURE 5.10: Experimental 806-nm-pump z-scan curves (circles, color coded) and their respective fitted curves (grey dashed) for 1.1at.%-doped Nd:$GdVO_4$ in the temperature range (RT-453 *K*).

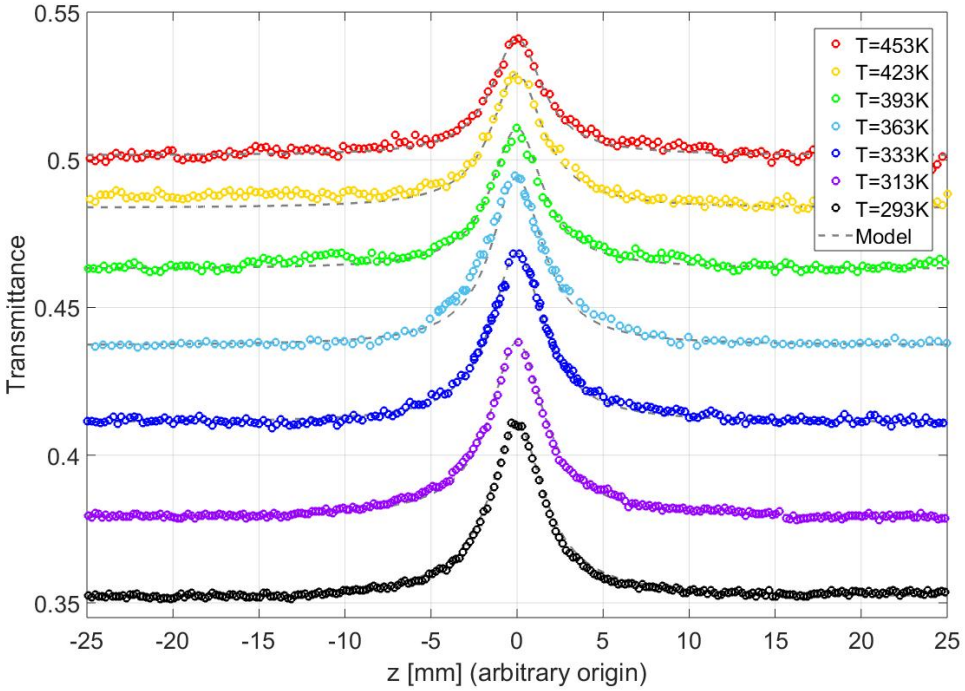

FIGURE 5.11: Experimental 808-nm-pump z-scan curves (circles, color coded) and their respective fitted curves (grey dashed) for 0.5at.%-doped Nd:$GdVO_4$ in the temperature range (RT-453 *K*).

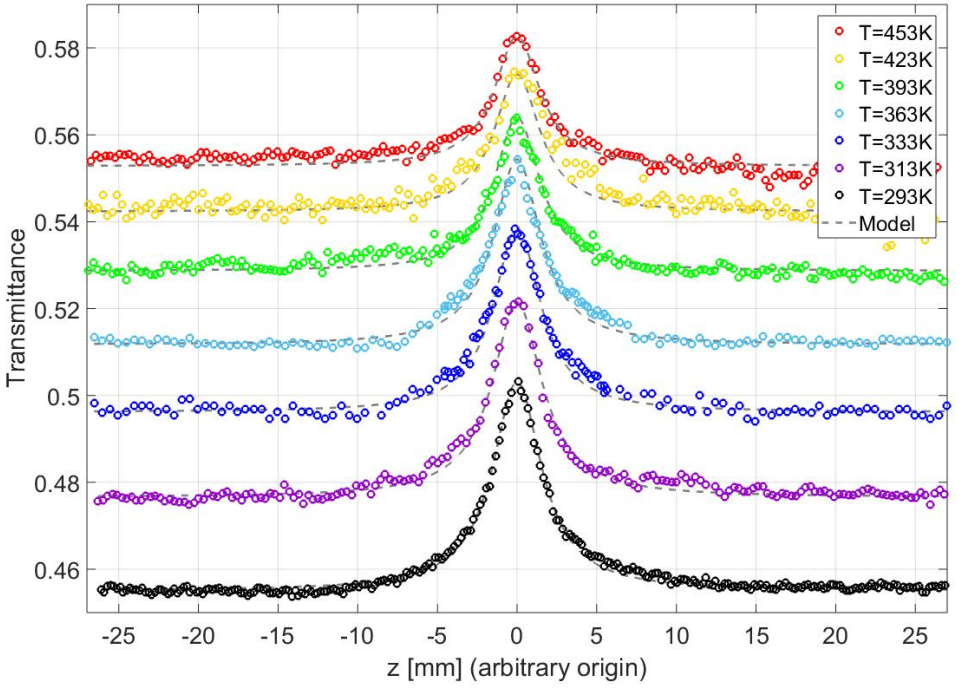

FIGURE 5.12: Experimental 806-nm-pump z-scan curves (circles, color coded) and their respective fitted curves (grey dashed) for 0.5at.%-doped Nd:$GdVO_4$ in the temperature range (RT-453 *K*).

Figures 5.13 and 5.14 show the results of the ETU coefficient measurements for the investigated Nd:YVO_4 and Nd:$GdVO_4$ samples. The ETU coefficient's magnitude decreases with temperature and concentration, showing two distinct dependencies for the two concentrations tested.

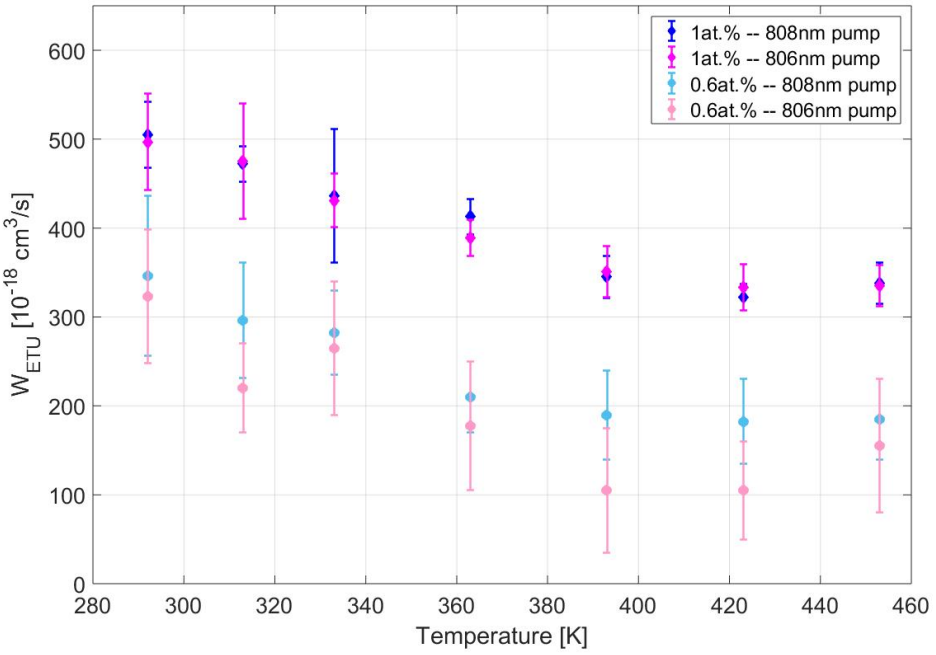

FIGURE 5.13: ETU coefficient for 1at.%- and 0.6at.%- doped Nd:YVO_4 at elevated temperatures.

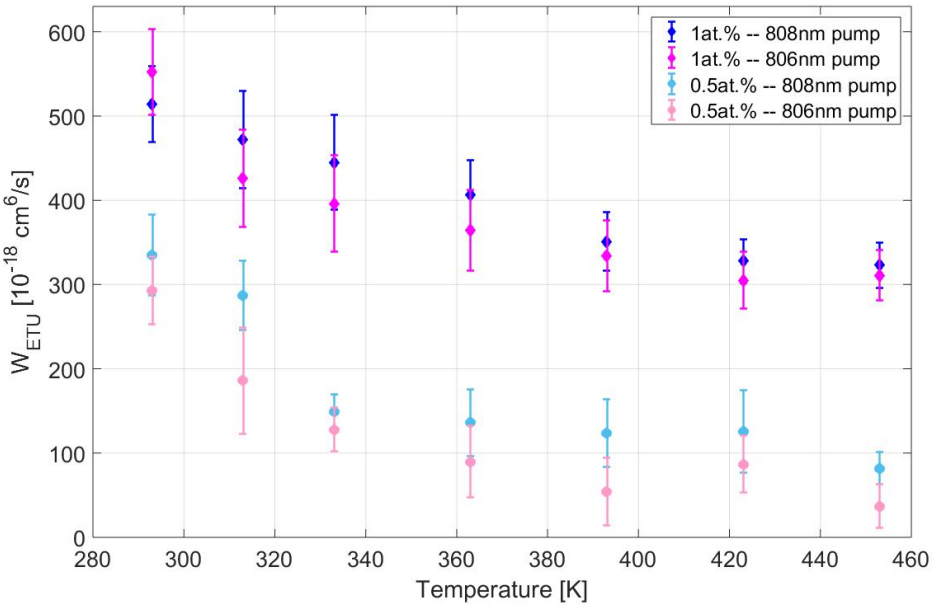

FIGURE 5.14: ETU coefficient for 1at.%- and 0.5at.%- doped Nd:$GdVO_4$ at elevated temperatures.

W_{ETU} decreases from $(320 \pm 70)\ 10^{-18}\ cm^3/s$ to $(180 \pm 40)\ 10^{-18}\ cm^3/s$ for 0.6at.%-, and $(500 \pm 50)\ 10^{-18}\ cm^3/s$ to $(340 \pm 20)\ 10^{-18}\ cm^3/s$ for 1at.%-doped Nd:YVO_4 respectively. Furthermore, for 0.5at.% and 1.1at.% Nd:$GdVO_4$, ETU decreases from $(330 \pm 50)\ 10^{-18}\ cm^3/s$ to $(80 \pm 20)\ 10^{-18}\ cm^3/s$ and $(550 \pm 50)\ 10^{-18}\ cm^3/s$ to $(310 \pm 30)\ 10^{-18}\ cm^3/s$, respectively.

The two crystal types show similar values and overall trends. Note any additional temperature rise in the gain medium due to the pumping cycle has been checked to meet the assumptions detailed in Section 2.3 and Subsection 5.4.2 for this analysis.

The fluorescence lifetime of the $^4F_{3/2}$ level in the small-signal regime was constantly monitored throughout the whole temperature range for the $1.0at.\%$-doped Nd:YVO_4 and the values were compatible with each other within uncertainty, the average being $(93 \pm 2)\ \mu s$, also compatible with the value reported in [14]. The lifetime values for the other concentrations and host were taken from [14].

In Sec. 2.3 we have highlighted the possibility of ASE as a further potential mechanism of excited state depopulation and executed calculations to estimate the magnitude of the ASE intensity compared to the saturation intensity. The results suggested that, in the case of the vanadates, due to the high gain at 1 μm, $\sim 100\ pm^2$ [14], this ratio is around 10%, a non-negligible value. In order to verify that the results presented above were not spoilt by neglecting ASE dynamics in the model employed (system of equations (2.7)), we have compared the simulated transmission curves with and without accounting for ASE, i.e. compared the results provided by system of equations (2.7) to the ones provided by system of equations (2.14). We consider the highest doping-ion concentration and highest and lowest temperature values among the ones explored, RT and 450 K for Nd:$GdVO_4$. Fig. 5.15 shows that there is negligible difference between the simulated z-scan curves when accounting (dashed lines) and not accounting (solid lines) for ASE for a 1.1at.%-doped Nd:$GdVO_4$ crystal. Given that, as detailed in Sec. 3.3.2.1, the $GdVO_4$ host has stronger spectroscopic features than YVO_4, we reasonably expect similar, if not better, results for the latter, i.e. a negligible difference when including and not including ASE effects. Furthermore, for the lower ion-percentage investigated on crystals of the same 1 mm-length, the 1 μm gain is expected to be even lower, therefore implying the same conclusion as above.

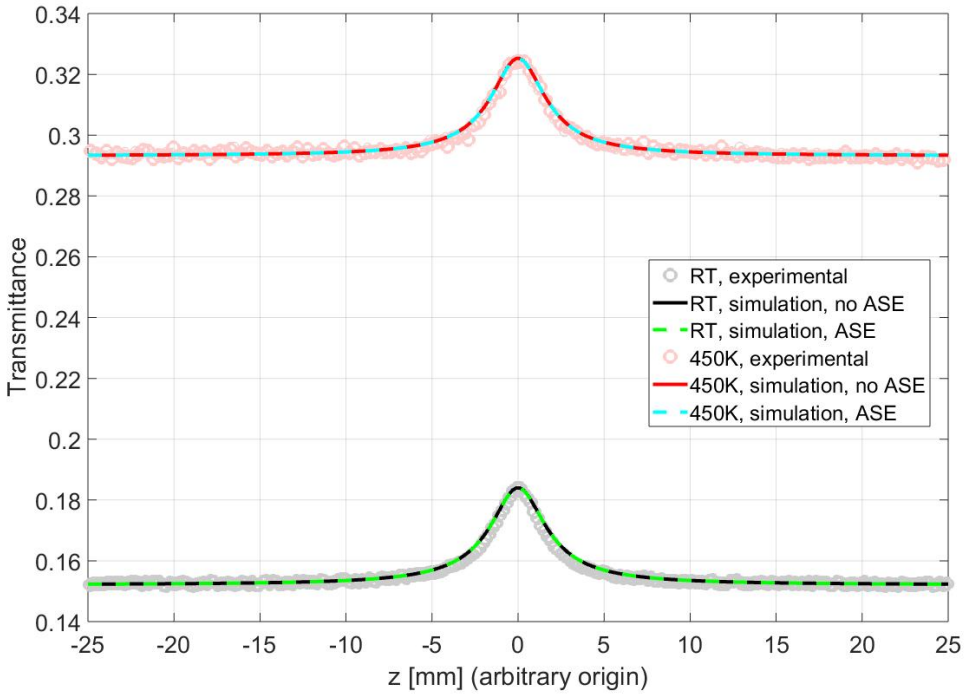

FIGURE 5.15: Z-scan experimental data (light coloured circles) and fitted transmission curves when accounting (dashed lines) and not accounting (solid lines) for ASE, for RT and 450 K, for a 1.1at.%-doped, 1 mm-long Nd:$GdVO_4$ crystal.

5.3.2 ETU vs concentration in Nd:YAG

It is well known that there is a dependence in ETU coefficient on the Nd^{3+} active ion concentration (see Section 2.3): the literature is populated with measurements for different hosts executed employing different techniques, and the results show a consistent trend of increasing ETU with increasing concentration [2, 3, 8, 9]. This is due to the inter-ion separation decreasing with increasing concentration, and hence the likelihood of ion-ion interaction increasing.

With available published data to compare to, and requiring a test that would legitimise the upgraded methodology detailed above, we characterised the ETU coefficient dependence on the Nd^{3+}-doping level in Nd:YAG. The measurements were executed on 6 samples of measured doping levels, the details of which are shown in Table 5.2. The pump was tuned to the strongest ${}^4I_{9/2} \rightarrow {}^2H_{9/2} + {}^4F_{5/2}$ (808 nm) peak.

Throughout the execution of the z-scans, we characterised the concentration-dependent fluorescence lifetime in the small-signal regime of each sample, collecting a number of waveforms to fit to model (5.2) in the order of 70 for several z-scans. The fitted lifetimes were averaged and the standard deviation from the average was taken as the error associated with the measurements, providing the results shown in Table 5.2. Using these, we also retrieved the value of the CR coefficient (W_{CR}) by employing the method described in [2].

The z-scan raw data (circles) and the relative fitted theoretical curves (gray, dashed) are displayed in Fig. 5.16. The raw data presents an excellent signal-to-noise ratio, and the fit with the theoretical curves is excellent for all measurements, which gave us good confidence in the results obtained. The small-signal transmission of each curve is consistent with the RT absorption cross section at 808 nm measured in Chapter 3: $(6.9 \pm 0.3)\ pm^2$.

Doping [at.%]	Length [mm]	τ_f [μs]	W_{CR} [$10^{-18}\ cm^3/s$]
0.301 ± 0.003	5.10	252 ± 5	2.95 ± 1.93
0.584 ± 0.005	1.10	250 ± 5	1.92 ± 1.02
0.740 ± 0.007	1.10	238 ± 3	3.48 ± 0.55
1.068 ± 0.007	1.10	232 ± 5	3.14 ± 0.65
1.333 ± 0.008	1.08	216 ± 3	4.27 ± 0.38
1.841 ± 0.008	1.10	192 ± 5	5.36 ± 0.56

TABLE 5.2: Details of the 6 Nd:YAG samples of different doping concentrations employed in the W_{ETU} vs Nd-concentration characterisation.

It can indeed be observed that for the crystals of comparable length $\sim 1\ mm$, all except for the 0.30at.%-doped, 5.1 mm-long one, there is the expected trend of decreasing small-signal transmission with increasing concentration.

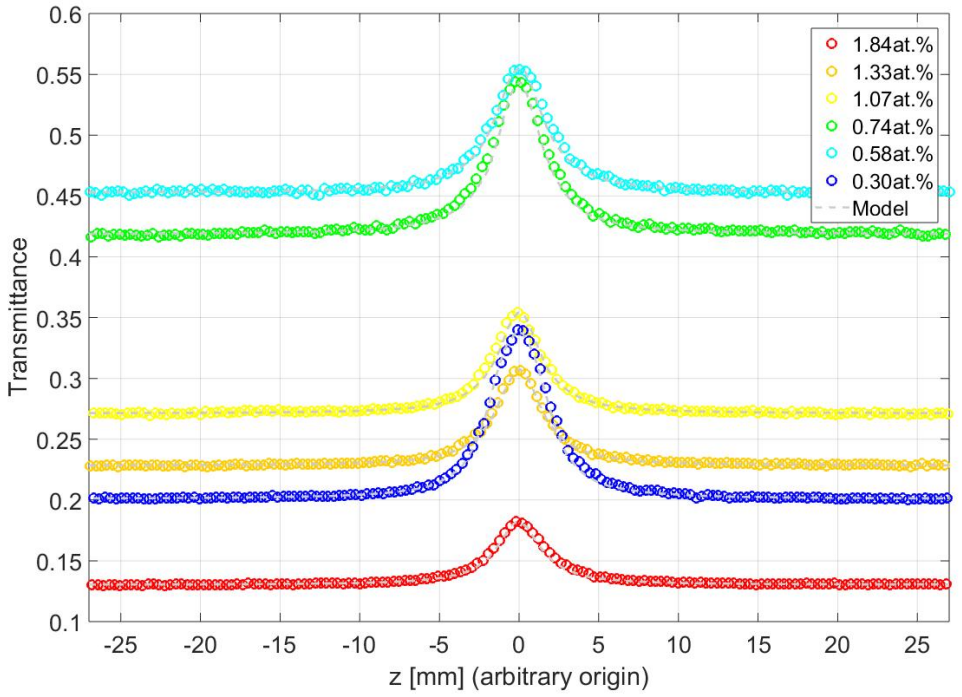

FIGURE 5.16: Z-scan transmission curves, red to blue circles corresponding to highest (1.84at.%) to lowest (0.30at.%) concentrations, and their respective fitted theoretical curves, in gray dashed lines.

The calculated W_{ETU} coefficients for the different doping-levels in Nd:YAG crystals are displayed in Fig. 5.17, in blue diamonds. On the same figure, in green circles, we plotted the data from [2] for direct comparison. The error bars, ΔY_i, for each data point represent the standard deviation from the average over ~ 6 measurements. This dispersion was greater than the uncertainty associated to the single W_{ETU} values obtained.
The ETU coefficient was found to increase from $(21.5 \pm 2.0)\ 10^{-18}\ cm^3/s$ to $(81.9 \pm 12.3)\ 10^{-18}\ cm^3/s$ when the doping-level ranges from 0.30at.% to 1.84at.%. The analytical dependence on the ETU coefficient on the doping-ion concentration is a disputed matter in the literature: both linear [9, 15] and quadratic [8] relations have been reported. As in [2], we chose the simplest function capable of describing our results, a linear dependence. Furthermore, the thorough analysis presented in [15] demonstrated the linear dependence of ETU on doping-ion concentration. The fitting line was obtained by the minimisation of the variance, employing the model $W_{ETU}(c_{\%}) = p \cdot c_{\%}$. In this analysis the fitting function is a line with a 0 intercept, to indicate that there is no ETU process occurring when the distance between neighbouring ions tends to infinity; hence the only fitting parameter p is the slope of the line. Accounting for the errors associated to each data point, the fitted slope resulted $p = (52 \pm 5)\ 10^{-18}\ \frac{cm^3}{s\ at.\%}$. Fig. 5.17 reports the confidence interval associated with the fitted slope, p, in dashed pink lines, showing that our results are mostly compatible within uncertainty with the ones reported in [2].

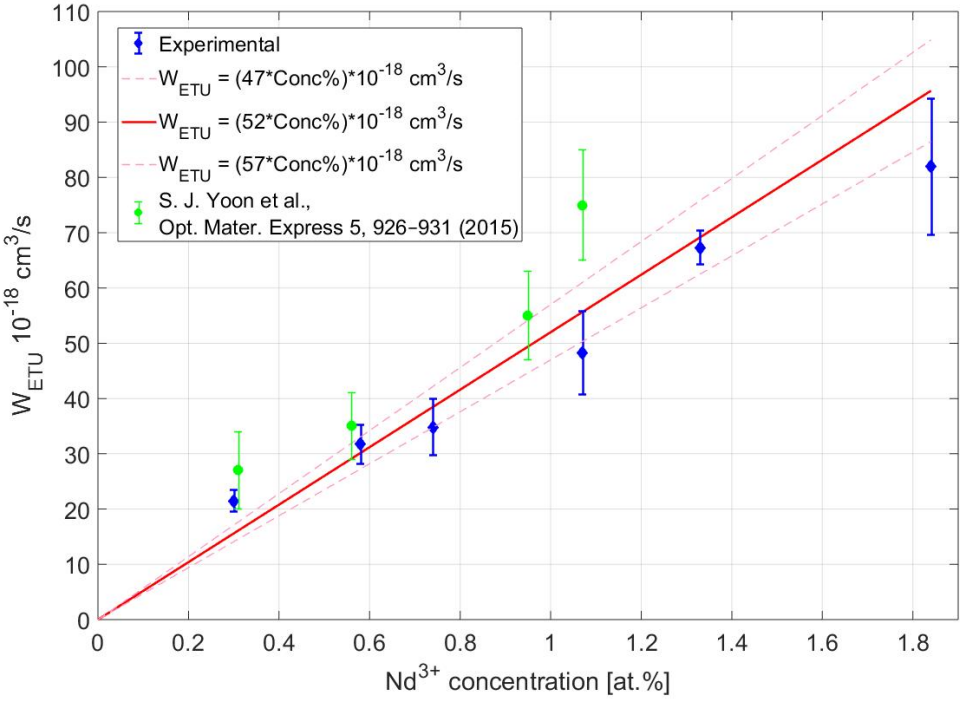

FIGURE 5.17: W_{ETU} vs Nd^{3+}-doping concentration in Nd:YAG.

The point corresponding to 1.84at.%, although compatible within uncertainty to the fitted linear trend, seems to deviate from it more than the other points: we have attributed

the discrepancy of this result from the trend shown by the other doping-levels to an excessive thermal load caused by the strong absorption over the 1 mm-thick sample. Furthermore, considering the results shown below, we have also ignored this point when estimating the linear trend of W_{ETU} vs Nd^{3+}-doping concentration.
Our model is based on the following assumptions concerning the thermal management of the pumped sample:

- The pump pulse is fast compared to the time constant associated with heat flow in the sample, i.e. there is no time for the sample to settle to a different temperature than the initial one, so all the temperature-dependent spectroscopic and thermo-optical variables remain at the initial temperature.
- If the above is not satisfied, then we assume that the localised temperature rise is negligible, so that the above mentioned assumptions are still satisfied.

In order for us to quantify the experimental conditions required, we have executed rough calculations that would provide sufficient guidelines for the adjustment of pump parameters.
The heat flow is generally described by the equation

$$\frac{\partial T}{\partial t} = \kappa \nabla^2 T \tag{5.3}$$

where κ is the thermal diffusivity of the material, measured in cm^2/s and given by

$$\kappa = \frac{K}{C_v d} \tag{5.4}$$

where K is the thermal conductivity, C_v is the specific heat capacity, d is the density of the material. From Eq. (5.3), the thermal diffusivity κ gives a time-scale over which the heat flows through a certain distance within the material: it is thus necessary to choose a reference length. For our analysis, we have used the beam radii $w(z)$ of the pump produced at each step of the z-scan. This would produce different z-dependent time-scales $\tau_{heat}(z) = w(z)^2/\kappa$, associated to the different positions (pump radii) of the z-scan. Given that the typical time-scale for the $^4F_{3/2}$ energy level's populations to reach steady state is $\sim 500\ \mu s$, we have used a pulse duration of $\tau_{pulse} \simeq 750\ \mu s$. The three time-constants to be compared are τ_{heat}, τ_{pulse} and T_{pulse} (the pulse period). In an ideal situation, one would have $\tau_{pulse} < \tau_{heat} < T_{pulse}$: a short enough pulse for the heat not to diffuse through the irradiated area and a long enough time between pulses so that the heat diffuses away from the irradiated area before the next pulse.
We have also estimated the localised temperature rise ΔT inside the crystal at each step of the z-scan, given by

$$\Delta T = \frac{E}{C_v m} \tag{5.5}$$

Where E is the energy of the pulse given by $E = P_{abs}\tau_{pulse}$ with P_{abs} absorbed power, m is the mass of the irradiated volume in the crystal ($m = \pi w^2 L d$, with L crystal length) and C_v is the specific heat capacity. In this calculation we have assumed no other thermal load than the one given by the pump beam and we have averaged the pump beam over the crystal length as in the z-scan model. Results for a 180 mW pulse of $\tau_{pulse} = 750\ \mu s$ and 5% duty cycle, incident on a 1 mm long, 1.84$at.$% doped Nd:YAG are shown in Fig. 5.18.

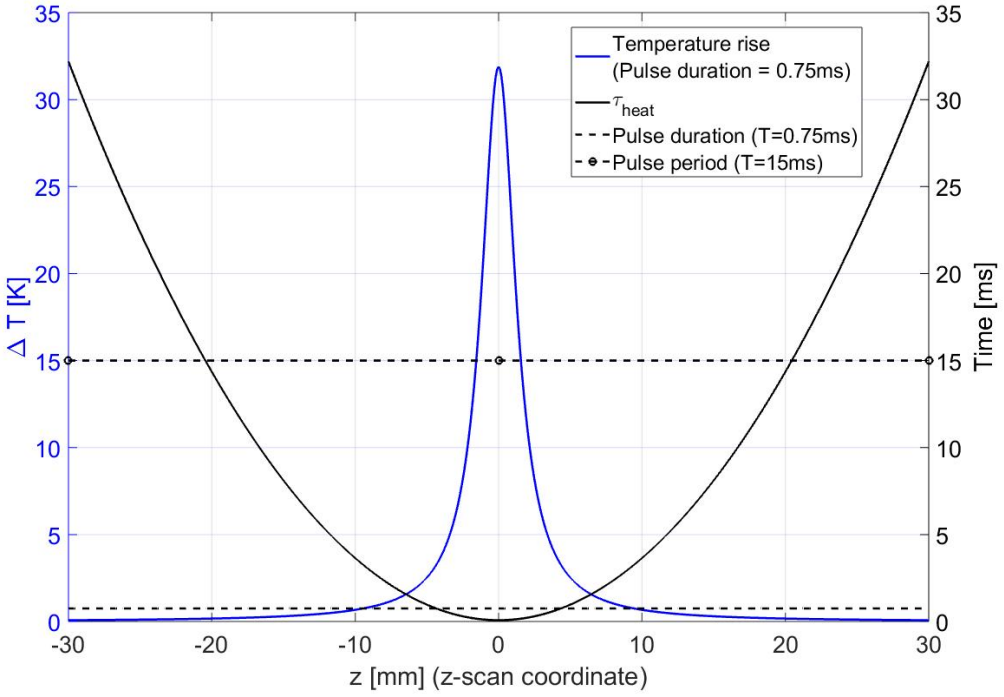

FIGURE 5.18: Left y-axis (blue): temperature rise over the scan length for a 1.84%-doped Nd:YAG crystal. Right y-axis (black): τ_{heat}, to be compared to the pulse duration and period.

This simplified model, describing the worst case scenario as not accounting for ground state bleaching, shows that in the small-signal regime, $|z| \gtrsim 10\ mm$, the assumptions of the model are easily met: even though the pulse period T_{pulse} is not consistently greater than the heat flow constant τ_{heat}, the temperature rise is negligible. However, in the high-irradiance regime, $|z| \lesssim 10\ mm$, τ_{heat} approaches τ_{pulse} as z approaches the maximum transmission position, becoming even smaller for $|z| \lesssim 5\ mm$, and reaching $\sim 0.08\ ms$ at the minimum. In this scenario, the assumptions of our model (2.7) are not fulfilled, as these calculations suggest that the localised heating in the sample is substantial.

The ETU coefficient measured in this case is lower than the trend showed by the lower doping-concentration values: this could be due to the fact that ETU has been demonstrated to decrease for elevated temperatures [1].

In fact, the rough temperature rise estimation provided by Eq. (5.5) and displayed in Fig. 5.18, suggests that the pumped region undergoes a temperature rise of $\sim 32\ K$.

With reference to Fig. 5.19, this means that, rather than the measurement being done at RT (290 K), the data point in question corresponds to a temperature of $\sim$ 322 K (blue triangle). Assuming the linear dependence of the ETU coefficent on the doping-ion concentration detailed above, we can shift the curve for the dependence of the ETU coefficient on elevated temperature reported in [1] (black solid line, and dashed solid lines for uncertainties) to get a W_{ETU} value at $\sim$ 320 K of $\sim$ 82 10^{-18} cm^3/s, consistent with our measurement. According to this scaled curve (red solid line), the estimated W_{ETU} for the 1.84at.%-doped Nd:YAG at RT is $\sim$ 91 10^{-18} cm^3/s, within uncertainty of the one expected employing our linear dependence of W_{ETU} on Nd^{3+}-concentration (red circle).

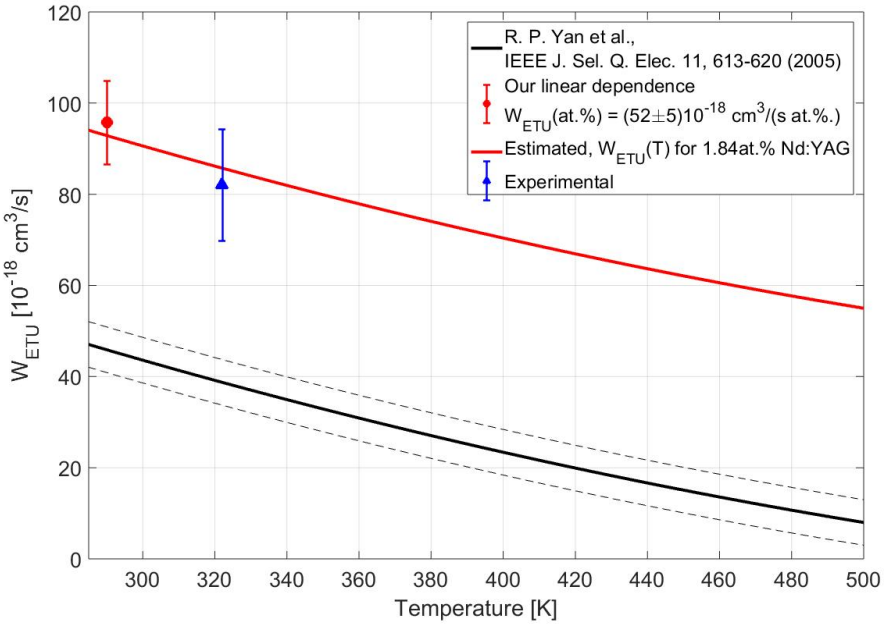

FIGURE 5.19: Black line: reported dependence $W_{ETU}(T)$ from Yan et. al [1]; red line: estimated dependence $W_{ETU}(T)$ for 1.84at.% doping; blue triangle: measured W_{ETU} for 1.84%-doped Nd:YAG accounting for the estimated temperature rise; red circle: estimated W_{ETU} for 1.84%-doped Nd:YAG at $T = 290$ K employing our measured linear dependence of W_{ETU} vs concentration.

Possible solutions to this unwanted condition are lowering the pump power so that ΔT diminishes, using a shorter pulse, focusing the beam to a larger spot size so that the τ_{heat} increases and ΔT decreases.

Herein, we have verified that the assumptions presented in Section 2.3 are met for lower concentration crystals, and hence the calculations executed above are only relevant for the specific case discussed.

Ultimately, with these measurements we have verified the consistency of the results obtained with the upgraded setup with the previous ones. As expected from existing literature [2, 8], the measured trend suggests that, in order to minimise ETU, it is preferable to employ low doping-concentration crystals. Although the measurement for

the highest concentration sample seems to have been spoiled by an excessive thermal load, considering the estimated temperature rise within the pumped region, the result is consistent with the linear trend for the other tested concentrations.

5.3.3 ETU at sub-ambient temperatures in Nd:YAG

As it is known from the literature [6, 16], the effects of ETU on laser performance are non-negligible. At RT, as outlined in Section 2.3, ETU strongly limits the power-scaling of laser operation, particularly when exploiting the low gain $9xx\ nm$ transition of Nd-doped hosts. To the best of our knowledge, there are no studies in the literature that present the ETU coefficient measurement in Nd:YAG at sub-ambient temperatures. Consequently, we were not able to quantify its effect on cryogenically-cooled Nd:YAG lasers, the main thrust of this thesis.
Driven by these motivations, we measured the ETU coefficient of two Nd:YAG samples, of concentrations 0.30at.% and 0.57at.%, in the temperature range (RT-LNT). This measurement was key to a deeper understanding of laser dynamics, particularly for the low-gain 946 nm transition, severely affected by ETU at RT, as opposed to the 1064 nm transition, for which the ETU effects are negligible, as we will discuss in Section 5.4.
We performed z-scan measurements employing the same setup represented in Fig. 5.1, with the sample tested placed in a cryostat rather than in an oven. These measurements were underpinned by the thorough characterisation of the absorption cross section of Nd:YAG, around 800 nm, and over the same range of temperatures, presented in Chapter 3.
To control the temperature the Q-drive (2s132K) acoustic pulse tube cryostat described in Section 3.2.3 was employed with the crystal mounted the same way detailed therein. Typical raw z-scan data and the respective fitted theoretical curves are shown in Fig. 5.20. The data points are color coded in red to black circles for RT to LNT, whereas the modelled curves for each respective experimental z-scan curve are dashed gray lines. The curves for which we have employed the off-peak tuning, introduced in the Methodology section 5.2, are displayed in separate subplots. In collecting these data, we have consistently employed the double-resolution feature, introduced in Section 5.2, in order to have a higher density of data points to fit the peak of the curve to. The agreement between the fit curves and the experimental data is excellent, as is the signal-to-noise ratio of the latter, thanks to suitably chosen acceptance windows for the data collection (see Methodology section 5.2). The uncertainty associated to each data point is not displayed with error bars to keep the figures as clean as possible; it is however small enough that it is slightly bigger than, if not completely contained within, the circles. The only curve that appears to be slightly noisy is the one for $T = 93\ K$, however the high density of data points, especially in the peak region, allowed a fitted curve still within the uncertainty associated to the data. Despite the data sets for this temperature being not as good as the other ones, the dispersion of the repeated measurements was

actually lower than the other cases, as the smaller error bars for the point corresponding to $T = 93\ K$ suggest, in Fig. 5.22.

The equivalent ETU coefficient characterisation over the temperature range (LNT-RT) for the 0.57at.%-doped Nd:YAG provided the data shown in Fig. 5.21. In this case, all the curves show excellent signal-to-noise ratio and their respective theoretical curves are well fitted to the data points. Again, the uncertainty associated to the single data points, i.e. standard deviation from the average of the multiple measurements executed at each z-position, is in the order of 2% of the measured value.

The results are summarised in Fig. 5.22: the ETU coefficient increases from $(21.5 \pm 2.3)\ 10^{-18}\ cm^3/s$ to $(52.6 \pm 2.5)\ 10^{-18}\ cm^3/s$ and from $(36.0 \pm 2.8)\ 10^{-18}\ cm^3/s$ to $(65.7 \pm 1.9)\ 10^{-18}\ cm^3/s$ from RT to LNT for the two concentrations investigated, respectively.

The values measured at RT are compatible within uncertainties to reported values from [2] and measurements presented in Section 5.3.2, and provide better precision thanks to the improved automation in the z-scan setup with respect to the previously reported setup. Furthermore, the trend of an increasing ETU coefficient with decreasing temperature is consistent with the equivalent measurements executed in [1] for the elevated-temperature regime.

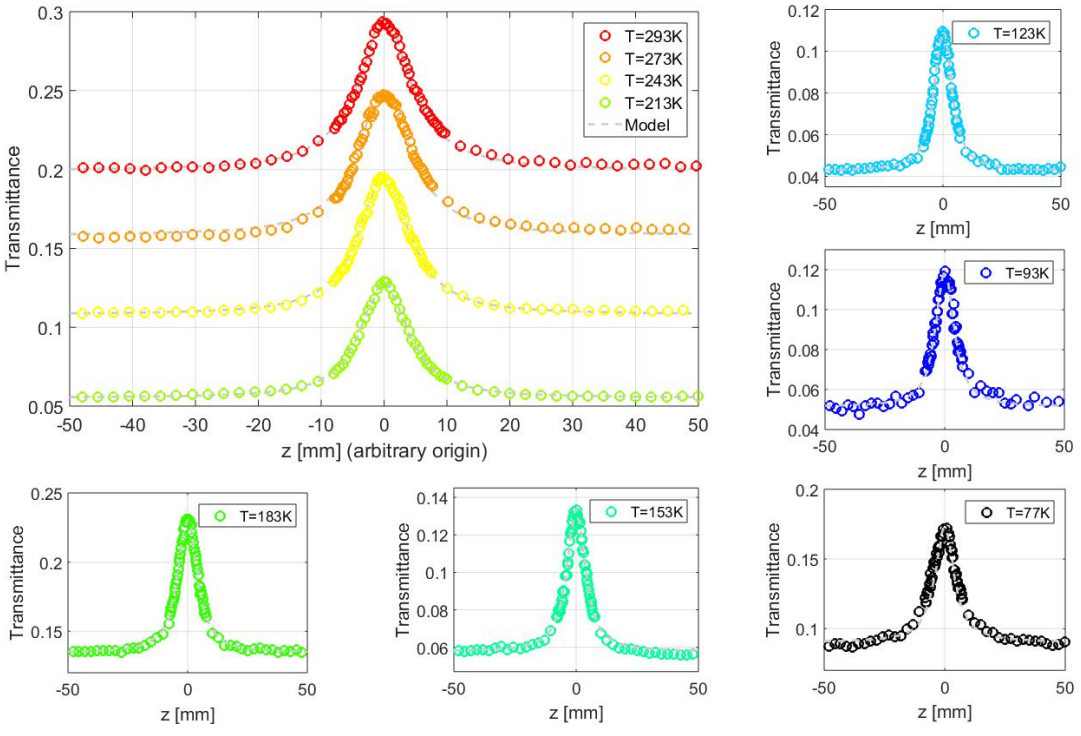

FIGURE 5.20: Z-scan transmission curves for a 0.30at.%-doped, 5.10 mm-long, Nd:YAG for temperatures from RT to LNT (red to black circles), and their respective fitted theoretical curves (dashed gray). The curves corresponding to $T = 93\ K$ and $T = 77\ K$ have been measured by tuning the pump off-peak.

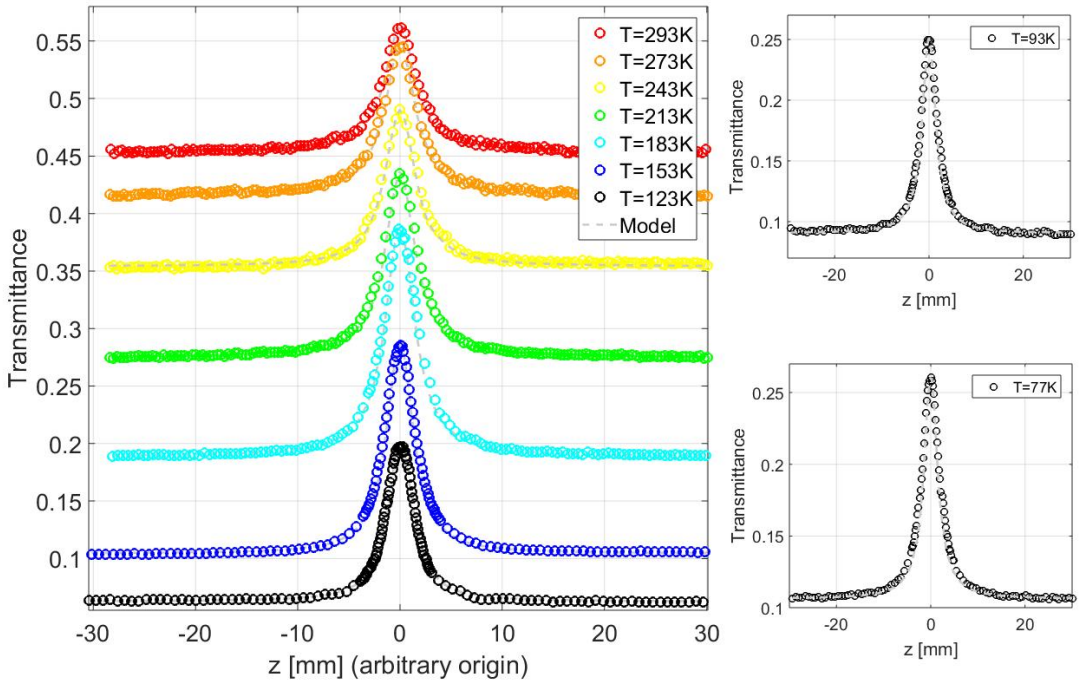

FIGURE 5.21: Z-scan transmission curves for 0.57at.%-doped Nd:YAG for temperatures from RT to LNT (coloured circles), and their respective fitted theoretical curves (dashed gray).

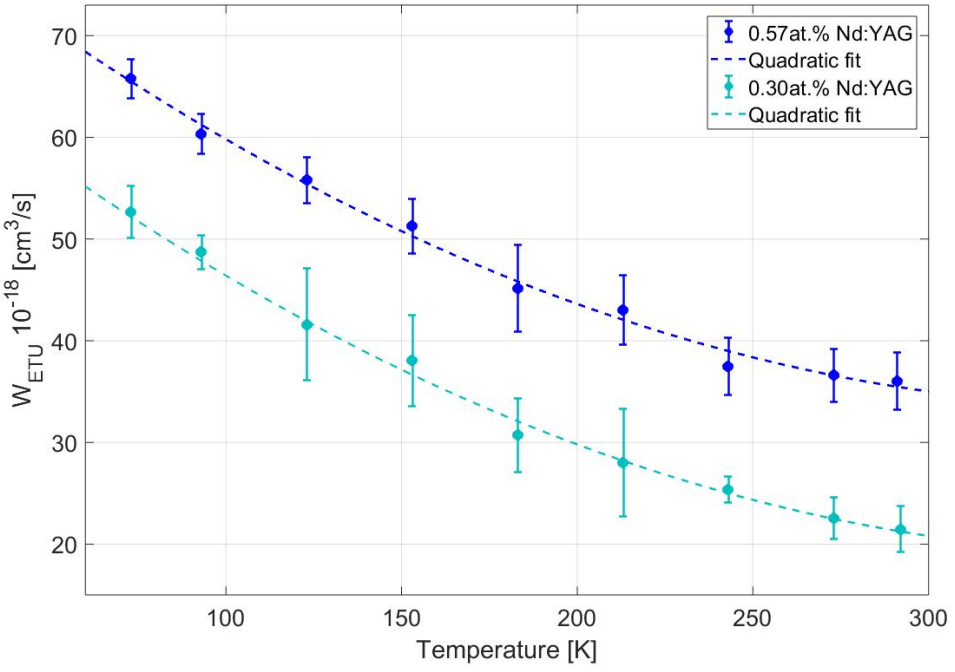

FIGURE 5.22: ETU coefficient vs sub-ambient temperatures and quadratic fits for 0.30at.% and 0.57at.% doped Nd:YAG.

Assuming that W_{ETU} has a linear dependence upon Nd^{3+}-concentration [2, 15], $m(C_{\%})$, and the temperature dependence is a function proportional to the spectral overlap integral, $O(T)$, this can be described by

$$W_{ETU}(C_{\%}, T) \propto m(C_{\%}) \cdot O(T)\ cm^3/s \tag{5.6}$$

where the overlap integral $O(T) = \int \sigma_e(\lambda, T)\sigma_{ESA}(\lambda, T)\ \mathrm{d}\lambda$ is evaluated between the emission $\sigma_e(\lambda, T)$ and $\sigma_{ESA}(\lambda, T)$ (Excited State) Absorption (ESA) cross sections of the ions involved in the energy transfer process, as described in [17].
In Nd:YAG, ETU involves transitions from the metastable state $^4F_{3/2}$ to the manifolds $^4I_{15/2}$, $^4I_{13/2}$, or $^4I_{11/2}$, and respective transitions from the same metastable level to $^4G_{5/2}$, $^4G_{7/2}$, or $^2G_{9/2}$. A detailed study on the evolution of the overlap integral $O(T)$ requires an extensive characterisation not only of the emission cross section, which can be found in [18], but also of the temperature-dependence of the ESA cross section. The latter measurements are not straightforward to execute, and although some data for the RT case can be found in the literature [19], no temperature-dependence studies have been presented for this parameter, to the best of our knowledge. An example of the spectral overlap that determines the value of $O(T)$ around 1 μm is presented in Fig. 5.23: it is appreciable that the lack of data for the ESA cross section at low temperatures doesn't allow the calculation of $O(T)$, and comparison with the experimental results.

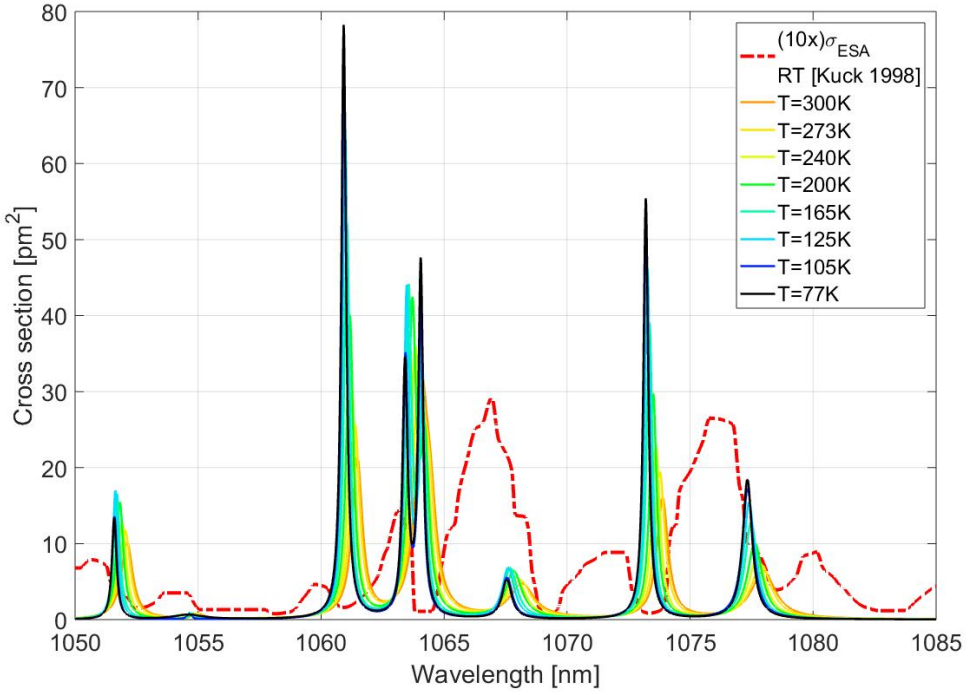

FIGURE 5.23: Spectral overlap between the emission transition $^4F_{3/2} \rightarrow {}^4I_{11/2}$ (solid lines, from [18]) and the 10x-magnified ESA transition $^4F_{3/2} \rightarrow {}^4G_{9/2}$ (red dashed line, from [19]).

In light of this discussion, we provide in Table 5.3 the best fitting parameters for a

second degree polynomial, the simplest function that fits our experimental data, for the respective concentrations. The two curves only differ from a rigid shift in the y-axis, as shown in Fig. 5.22.

Model: $(p_1 + p_2T + p_3T^2)\ cm^3/s$			
Doping [at.%]	p_1	p_2	p_3
0.30	70.6	-0.28	3.8e-4
0.57	83.6	-0.28	3.8e-4

TABLE 5.3: Nd:YAG: Coefficients for the second degree polynominal fit curves for W_{ETU} vs T in 0.30at.%- and 0.60at.%-doped samples.

The calculations executed to estimate the ratio between the intensity of the ASE and the saturation intensity, I_{ASE}/I_{sat}, for the two doping-concentrations in this cryogenic-temperature regime provided results in the order (0.7-4)%. The lower end of the range belongs to the 0.57at.%-doped, 1 *mm*-long sample, while the higher percentage corresponds to the 0.30at.%-doped, 5 *mm*-long sample, primarily due to the 5x-longer gain medium length. We report, in Fig. 5.24, key comparisons between z-scan simulations that account for the ASE, and that don't, for a z-scan executed on a 0.30at.%-doped, 5 *mm*-long Nd:YAG crystal.

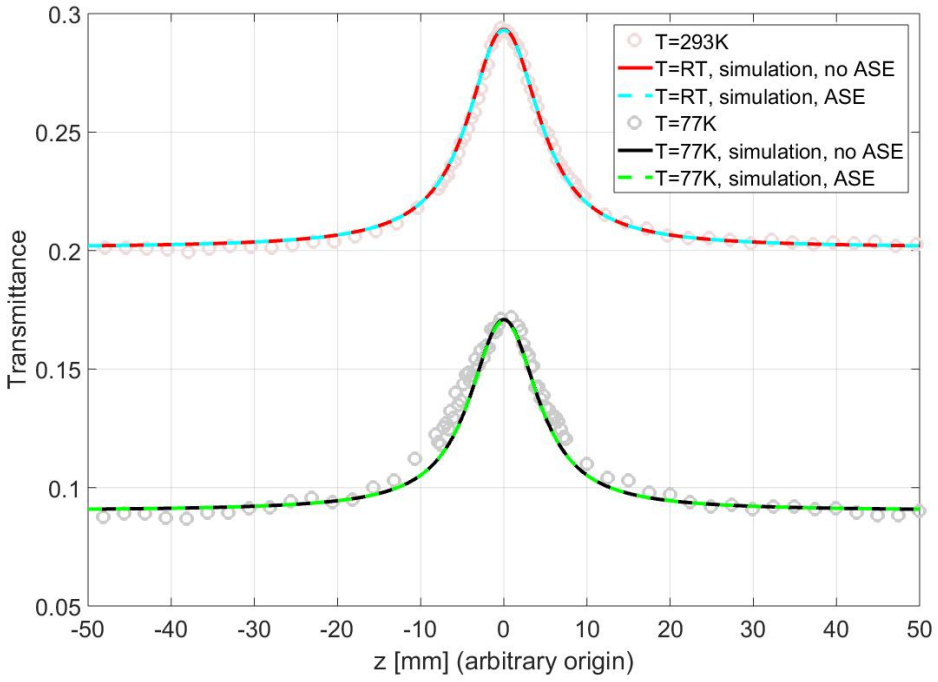

FIGURE 5.24: Z-scan experimental data (light coloured circles) and fitted transmission curves when accounting (dashed lines) and not accounting (solid lines) for ASE, for RT and LNT, for a 0.30at.%-doped, 5 *mm*-long Nd:YAG crystal.

The z-scan simulations for RT and LNT are the extremes to be analysed, as the cases for all the other temperatures spanning between these two fall within the results presented in Fig. 5.24. As one can appreciate from the plots, the simulations with and without including ASE agree well within the experimental uncertainty. We conclude, therefore, that neglecting the contribution of the ASE in depleting the upper laser level was a good assumption, confirmed by the calculations presented.
The results for the case of the 0.6at.%-doped Nd:YAG crystal are equivalent, i.e. the simulated transmission curves with and without the ASE effect are in excellent agreement, allowing for the ASE to be neglected.

5.4 Discussion: Implications of ETU on laser threshold

As we have discussed in Section 2.3, ETU, detrimental effect to laser performance, can be quantified in the form of a macro-parameter. Here, thanks to the new knowledge of the magnitude of the ETU coefficient gained through the measurements presented in the previous section, an evaluation of how ETU affects the laser performance is therefore possible. Due to the complexity of simulating laser dynamics during operation, we have chosen to quantify the effect of ETU on laser threshold, a fundamental parameter to laser performance. In order to do so, we concentrate on simple cavities, the details of which will be outlined in the relevant sections, and calculate their laser threshold with and without ETU.
In Section 2.4 we presented the factor F_q, Eq. (2.19), a Figure-of-Merit (FOM) for the laser considered, as part of the formula for the laser threshold including ETU, Eq. (2.18). Therein, we pointed out that this quantity is independent of the particular laser design considered, as it only depends on gain-material properties: the absorption and emission cross sections at the pump and laser wavelengths σ_{abs} and σ_{em}, respectively, the fluorescence lifetime τ_f, the absorption coefficient at the pump wavelength α_{abs}, and the ETU coefficient W_{ETU}. Keeping a high F_q is essential for keeping a low laser threshold, with minimial added thermal load. In the next paragraphs we will show, for the respective cases, how the aforementioned temperature-dependent gain-material properties affect F_q and what this finally means for the laser threshold and subsequent laser operation.
The general models employed for the calculation of the laser threshold are discussed in Chapter 2 and reported in [16] and [6], and, having been developed specifically for Q4L lasers, apply to both the Q4L $9xx\ nm$- and the 4L $10xx\ nm$-transitions of Nd-doped Vanadates and YAG studied here. These two transitions, besides differing in their Q4L level, or γ factor as discussed in Section 2.4, usually have quite different gain values, with the $10xx\ nm$ typically having much higher gain than the $9xx\ nm$ transition. As we demonstrate, the lower-gain $9xx\ nm$ is more affected than the $10xx\ nm$ transition by the

detrimental effects of ETU, a result that confirms the importance of characterising the ETU coefficient to gain insight on the operation of low-gain lasers.

5.4.1 ETU at elevated temperatures in Nd-doped Vanadates

The results of the measurement for the ETU coefficient of Nd:YVO_4 and Nd:$GdVO_4$ (Section 5.3.1), for two different doping concentrations each, presented in Figs. 5.13 and 5.14, showed that W_{ETU} diminishes with increasing temperature, and that it is lower for the lowest concentrations. Furthermore, this macro-parameter is one order of magnitude stronger than in Nd:YAG, in line with the generally stronger spectroscopy features of Nd-doped Vanadates. Accounting for the temperature dependence of the absorption cross section, emission cross section [5] and ETU coefficient measured, as well as fractional populations within each manifold given by the temperature-dependent Boltzmann distribution, we quantified the temperature-dependent effects of ETU. Firstly, we calculated the value of the FOM F_q defined in Eq. (2.19) for the 914 nm Q4L and 1064 nm 4L transitions of 0.5at.% and 1.0at.% doped Nd:YVO_4 in the temperature range (290-420) K. The results are presented in Fig. 5.25.

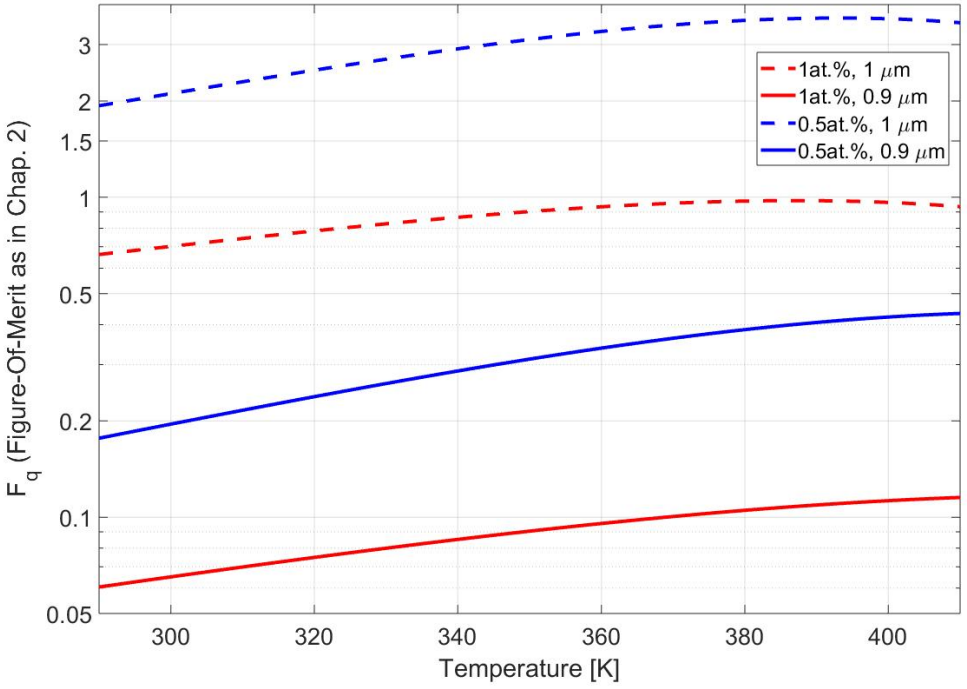

FIGURE 5.25: Figure-of-merit F_q as defined in Chapter 2 vs elevated-temperatures for the 0.9 μm and 1 μm transition of 0.5at.%- and 1.0at.%-doped Nd:YVO_4.

As expected from its higher gain, the FOM for the 1 μm- (dashed lines) is $\sim$ 10x higher than the FOM for the 0.9 μm-transition, for both the concentrations. This means, as we will see below, a lower threshold for the first transition with respect to the latter. At

the same time, the lower concentration, $0.5at.\%$ in blue lines, resulted in a higher FOM than the $1.0at.\%$ case for both the laser transitions. With all the spectroscopic parameters defining F_q being the same, this is due exclusively to the fact that W_{ETU} is lower for the lowest concentration.

Secondly, we employed the analytical formula for the incident threshold pump power P_{th} of a laser oscillator including ETU, presented in Section 2.3 and reported in [16], and applied it to a simple cavity as described in [20]. This 49 mm-long cavity, with a 54 μm cavity-mode radius and a 10% Output Coupler (OC)'s transmission, was pumped by a 808 nm fibre-coupled diode-laser. The crystal length l_r was chosen so that its product with the doping-ion concentration $C_{\%}$, $l_r \cdot C_{\%}$, was constant. E.g. 0.1 mm for $1at.\%$- and 0.2 mm for $0.5at.\%$-doped Nd:YVO_4. We compared the cases of operation on the two different laser transitions mentioned above, 1 μm and 0.9 μm. Similar results are expected for the corresponding Nd:$GdVO_4$ crystals, due to the similar results of the ETU coefficient characterisation, and other spectroscopic properties presented in Chapter 3. The results in Figs. 5.26 and 5.27 show that the threshold for the Q4L system is higher than the one for the 4L system and in this case 60 (for the 0.5at.%-) to 250 times (for the 1.0at.%-doped sample) higher. The 1064 nm transition is barely affected by the ETU process ($P_{th} \simeq 23mW$ without ETU versus $P_{th} \simeq 27mW$ with); however, the 914 nm transition is strongly affected, resulting in a more than 5x increase when considering ETU, that only slightly decreases with increasing temperature for the 1at.%-doped crystal.

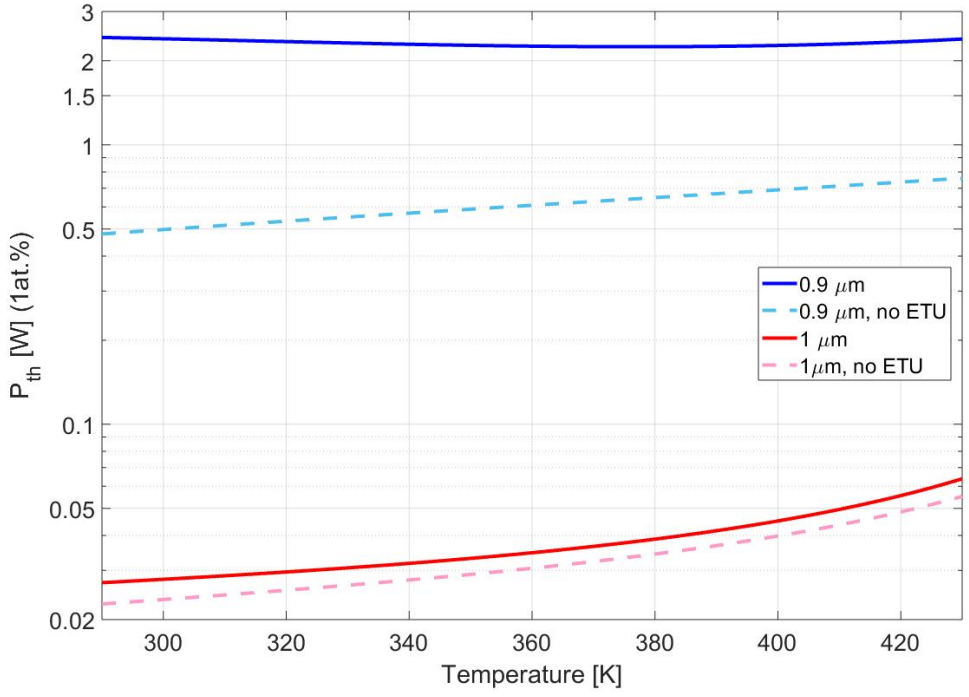

FIGURE 5.26: P_{th} vs Temperature for 0.9 μm and 1 μm 1.0at.%-doped Nd:YVO_4 laser, with and without including ETU effects.

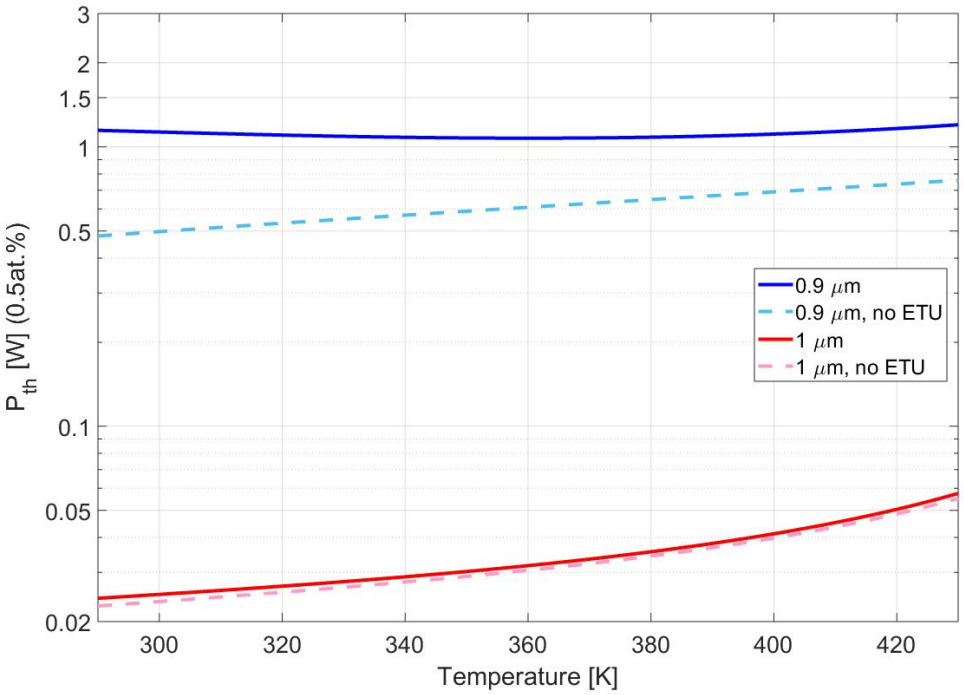

FIGURE 5.27: P_{th} vs Temperature for 0.9 μm and 1 μm 0.5at.%-doped Nd:YVO_4 laser, with and without including ETU effects.

The results for the 0.5at.% crystal are significantly better: while the 1064 nm transition is equally not significantly affected by ETU, the difference in the 914 nm transition threshold is slightly more than 2 times larger when including ETU effects. This means that, for two lasers with equivalent pump absorption and configurations, and operating on the Q4L 914 nm transition, the effect of the concentration-dependent ETU will determine a 2x increase in threshold in the laser with the higher concentration. This increase will effectively mean a 1.5 W higher thermal load in the pumped region, leading to a substantial temperature rise and thermo-optical aberrations, which will respectively decrease the gain and increase the cavity losses, i.e. worsen the efficiency and beam quality. Additionally, for Q4L operation with the vanadate hosts, the extreme gain at 1064 nm will provide a further challenge through gain depletion caused by the strong ASE. Although a preliminary analysis, this description clearly shows the challenge for Q4L Nd-vanadate system, when accounting for ETU.

5.4.2 ETU vs concentration in Nd:YAG

The results presented in Section 5.3.2 showed that the ETU coefficient increases linearly with the Nd^{3+}-concentration in Nd:YAG. Using these results, we have calculated the FOM for Nd:YAG as defined in Eq. (2.19) (Section 2.3). In this case, all the parameters defining F_q are fixed, except for W_{ETU}, the only concentration-dependent parameter. The

results of this calculation for both the 946 nm and 1064 nm transitions are displayed in Fig. 5.28.

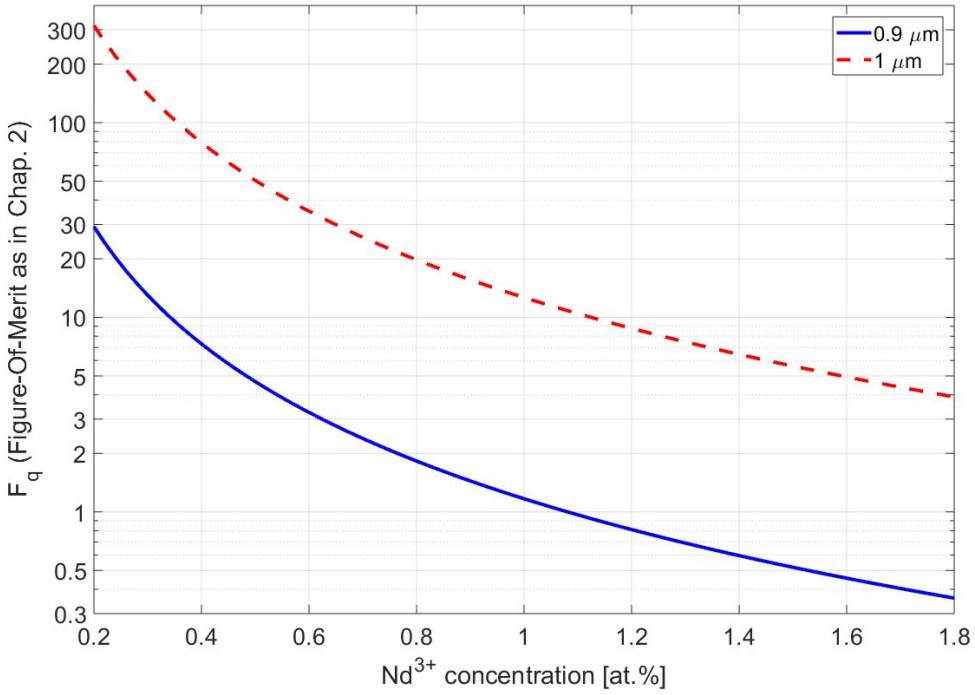

FIGURE 5.28: Figure-of-merit F_q as defined in Chapter 2 vs concentration for the 0.9 μm and 1 μm transition of NdYAG.

As for the Vanadates, and in agreement with the fact that it has a higher gain, the FOM for the 1 μm transition is $\sim$ 10x higher than the one for the 0.9 μm transition, for the lowest concentration, 0.2at.%. It presents an $\sim$ 80-fold decrease, due to the increasing W_{ETU}, over the concentration range (0.2-1.8)at.%; the curve for the 0.9 μm transition presents a similar behaviour. This calculation suggests that in order to minimise the ETU effects on laser performance, the choice of a low-concentration sample is essential. Furthermore, as will be confirmed below, the 1 μm transition seems to be less affected by ETU due to its higher gain.

To illustrate, we estimated the threshold pump power, P_{th}, dependence on the Nd^{3+}-concentration for Nd:YAG, with and without ETU. The approximations provided in [16], that led to the analytical form of Eq. (2.18), were not valid for the cases of relatively high doping-levels, therefore for the following calculations we employed the model described in [6] and Section 2.4, for both the 946 nm and 1064 nm transitions. For the calculation, the crystal lengths were chosen to be three absorption lengths, i.e. the absorbed pump power is 99% of the incident power for each value of concentration used. The cavity chosen for modeling purposes is a 50 mm-long, linear hemispheric cavity, with a ROC 200 mm, 7%-transmission OC. Both pump and cavity-mode radii are set to be 100 μm. The results are shown in Fig. 5.29.

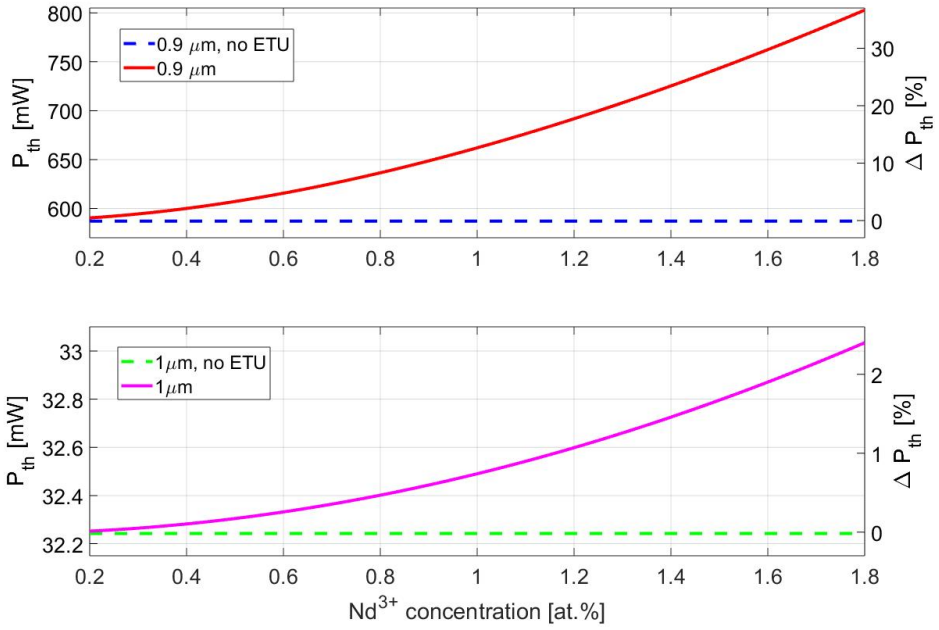

FIGURE 5.29: P_{th} vs Nd^{3+}-doping in Nd:YAG, with and without ETU. Right y-axis: percentual difference between the two.

As anticipated with the FOM calculations, and as it is also well known from the literature [2, 8], the difference in P_{th} with and without ETU increases with concentration, hence the requirement for crystals with low-doping concentrations to keep the threshold as low as possible. Furthermore, the difference in the threshold with and without ETU for the 1064 nm 4L transition is only $\sim$ 2.5% (and less than 1 mW) for the highest concentration, i.e. practically negligible, as opposed to the $\sim$ 38% (and over 200 mW) difference for the highest concentration investigated for the Q4L 946 nm transition. In the latter case, this difference means that more than one third of the threshold power becomes extra heat. These results show quantitatively how detrimental ETU is for low-gain transitions like the 946 nm of Nd:YAG, and that this effect worsens for high doping-levels. The problem is exacerbated when the power is scaled: the beam size needs to be increased, increasing the threshold and consequently, the physical amount of thermal power contributed by ETU.

5.4.3 ETU at sub-ambient temperatures in Nd:YAG

The combined results of [2, 1] and this work demonstrate that in order to minimise the detrimental effects of ETU on laser performance, employing low-concentration samples is essential, because, as it was also observed in other crystals [3, 21], the ETU coefficient increases with decreasing temperature. However, despite this trend, using the model reported in [6] (Chapter 2), which includes the effects of ETU, we determine that the laser performance is dominated by the improved spectroscopic properties at cryogenic

temperatures.
To illustrate, we have calculated the threshold pump power for a simple linear cavity for a Nd:YAG laser operating at 946 nm in function of the crystal temperature. The 170 mm-long plano-concave linear cavity comprised a flat high-reflectance (HR) mirror and a T=10%, 200mm ROC OC. The Nd:YAG crystal, coated for 946 nm operation, and positioned 50 mm from the input mirror, was in-band pumped by a 869 nm diode-laser bar providing a 350 μm beam radius. In addition, such a cavity was built and its characteristics investigates as detailed in Chapter 6. For the calculations we studied 0.3at.%- and 0.6at.%-doped Nd:YAG samples, of lengths 15 mm and 7.5 mm respectively, in order to keep the pump absorption over the two crystal lengths consistent.
As shown in Fig. 5.30, without considering the effects of ETU ($W_{ETU} = 0$), the temperature-dependent threshold pump-power reduces due to enhanced gain and lower reabsorption losses, and is the same for both doping concentrations – as one would expect from the fact that the product $C_{\%} l_r$ is a constant. When ETU is accounted however, the temperature-dependent threshold pump-power exhibits two separate curves for the two doping concentrations.
At RT the higher concentration sample would have an additional 24% heat load with respect to the threshold power without ETU, compared with only 5.5% at LNT. While for the lower concentration crystal the additional load is only 10% and 2.5% of the ETU-free threshold power, respectively. This highlights two key points: first, that despite the increasing ETU coefficient, the spectroscopic and thermo-optical enhancement dominates through the reduction in laser threshold at cryogenic temperatures; second, higher Nd-doping leads to stronger thermal loading from the ETU processes and a higher fractional thermal load, as it was known from previous results. In the cryogenic-cooling regime it is key to keep this extra heat at a minimum, due to the finite cryostats' cooling capacity, i.e. the absolute thermal power being extracted, which reduces with lowering temperatures.
Furthermore, characterising the effect of ETU on the Q4L 946 nm transition over the temperature range (RT-LNT), we calculate the temperature-dependence of the FOM F_q as defined in Chapter 2. Fig. 5.31 shows that for the 946 nm transition of in-band pumped (869 nm) Nd:YAG, this parameter increases with decreasing doping concentration and temperature. In order to estimate the FOM for the commonly used 1.1at.%-doped Nd:YAG, we have estimated an ETU curve for $\sim$1.1at.%-doping by shifting the measured 0.6at.%-doping curve by the difference between $W_{ETU}(0.6at.\%, RT)$ and $W_{ETU}(1.07at.\%, RT)$, where the second data point is reported in [2], as showed in the inset of Fig. 5.31.

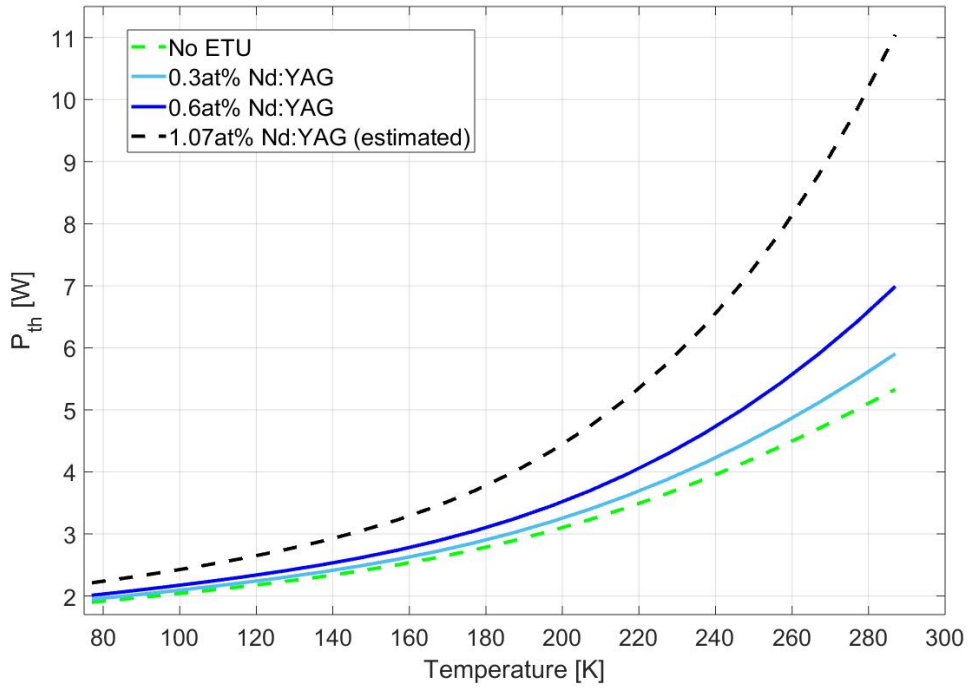

FIGURE 5.30: Calculated laser threshold vs cryo-temperatures, including and not including ETU effects, for 0.3at.%-, 0.6at.%, and 1.07at.%-doped Nd:YAG, according to [6].

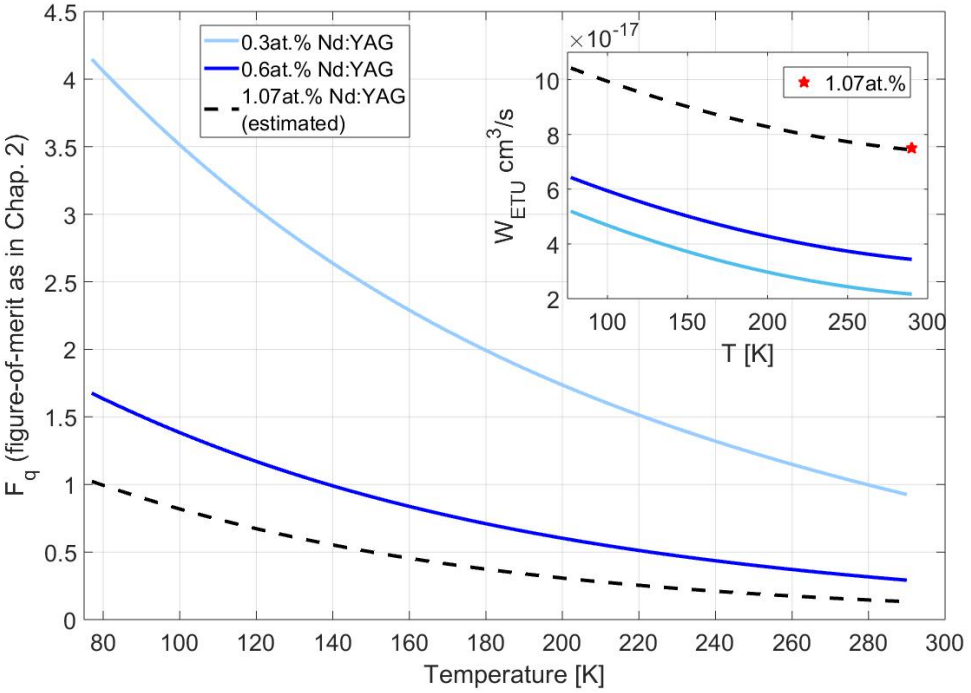

FIGURE 5.31: Figure-of-merit F_q as defined in Chapter 2 vs cryo-temperatures for 0.3at.%-, 0.6at.%-, and 1.07at.%-doped Nd:YAG.

From Eq. (2.18) it can be seen that the additional power required to reach threshold is a combination of the gain-material properties ($\sigma_{abs}, \sigma_{em}, \tau_0, \alpha_P, W_{ETU}$), through F_q, and the laser configuration at LNT, through the other terms (η_{LP}, f_1, l_r), essentially becoming additional heat. As per the calculations shown in Fig. 5.30, with the discussed configuration, this additional heat can be negligible or not, with respect to the threshold pump power estimated with no ETU: only 0.1 W for 0.3at.%-, and 0.4 W for 1.1at.%-doped Nd:YAG, with respect to $P_{th,noETU} \sim 1.9$ W, a $\sim$ 5% and $\sim$ 20% increase for the two concentrations, respectively. In the context of a reduced cooling capacity at cryogenic temperatures for compact closed-loop cryostats (like the one we employed and introduced in Section 3.2.1), the discussed non-trivial increase in thermal load may represent a significant fraction, with the temperature rise in the crystal exacerbated by a short pump absorption length and the lower thermal conductivity associated with higher doping concentrations [22].

5.5 Conclusions

In conclusion, we have developed a general procedure for measuring the ETU coefficient of crystals whose energy level dynamics are suitably described by the model detailed by the rate equations (2.7). The z-scan technique provides a robust yet simple method for performing this measurement, once the absorption cross section is fully characterised, as in Chapter 3.

We upgraded the previous z-scan setup by developing a LabView driven automation and a data processing methodology that allowed us to improve the confidence in the results. This was achieved by mitigating the pump laser instability, the main source of uncertainty, by monitoring the input and output powers simultaneously and only collecting data corresponding to pump power values within a set range. After carrying out a careful evaluation of the error propagation through the model, we came to the conclusion that the other large source of uncertainty was due to the confidence in the crystal length measurement, which we accounted for when associating an error to the ETU coefficient measurement. Finally, thanks to the automation developed, we could average over a large number of measurements, therefore pinning down the uncertainty due to statistical dispersion.

The results presented here for different neodymium-doped crystals and temperature conditions are typical for the analysed samples, however they provide a new level of understanding for the implications of the ETU dynamics on laser operation. Particularly important, is the ETU effect on the $^4F_{3/2} \rightarrow {}^4I_{9/2}$ 9xx-nm transition (914 nm for Nd:YVO_4, 912 nm for Nd:$GdVO_4$, and 946 nm for Nd:YAG), as it suffers from reabsorption losses and has lower gain than the $^4F_{3/2} \rightarrow {}^4I_{11/2}$ 10xx-nm transition (1064 nm for Nd:YVO_4 and Nd:YAG, and 1062 nm for Nd:$GdVO_4$). Utilising temperature-dependent spectroscopic parameters and the ETU coefficients measured, we illustrated their effects on the

temperature-dependent threshold pump power for simple Nd-doped lasers.
These threshold calculations for both $9xx\ nm$ and $10xx\ nm$ transitions including the measured ETU coefficients show two main facts. Firstly, that ETU becomes more detrimental in highly-doped crystals, as demonstrated in Section 5.4.2 for the RT case in Nd:YAG, and confirmed also in Section 5.4.1 for the elevated-temperatures Nd:YVO_4 and Nd:$GdVO_4$, and in Section 5.4.3 for the sub-ambient temperature case of Nd:YAG. Secondly, that ETU has a negligible effect on the $10xx\ nm$ transition, that is only a small 2.5% difference in threshold between the cases with and without ETU for the $0.60at.\%$-doped Nd:YAG sample.
The temperature regimes explored are relevant to the typical operation of Nd-doped Vanadate lasers under intense pumping conditions and/or high pump absorption, i.e. high thermal load and therefore elevated temperatures. Even more relevant, and particularly to the topic of this thesis, is the characterisation of ETU for different Nd^{3+} doping levels in Nd:YAG and in the cryogenically-cooled regime for the lower doping-concentrations. Thanks to these, we demonstrated that employing low-concentration Nd:YAG is favourable for reducing additional thermal load due to ETU. Furthermore, the results show that in the cryogenic-temperatures regime the reduction in the laser threshold of the 946 nm transition of Nd:YAG is dominated by an increased 4-level characteristic and enhanced absorption at cryogenic temperatures, while the additional thermal load associated with ETU is reduced and F_q, a figure-of-merit for the effect of ETU, is increased. Besides providing a substantial addition to the literature regarding ETU in Nd-doped Vanadates and Nd:YAG, these results pave the way for future power- and energy-scaling the cryogenically cooled 946 nm NIR laser transition, which will be presented in Chapter 6.

References

[1] R. Yan, S. J. Yoon, S. J. Beecher, and J. I. Mackenzie, "*Measuring the Elevated Temperature Dependence of Up-Conversion in Nd:YAG,*" IEEE Journal of Selected Topics in Quantum Electronics **21**, 329–336 (2015).

[2] S. J. Yoon, R. P. Yan, S. J. Beecher, and J. I. Mackenzie, "*Concentration dependence of energy transfer upconversion in Nd:YAG,*" Optical Materials Express **5**, 926–931 (2015).

[3] J. O. White and C. E. Mungan, "*Measurement of upconversion in Er:YAG via z-scan,*" Journal of the Optical Society of America B **28**, 2358–2361 (2011).

[4] Y. Sato and T. Taira, "*Comparative study on the spectroscopic properties of Nd:$GdVO_4$ and Nd:YVO_4 with hybrid process,*" IEEE Journal of Selected Topics in Quantum Electronics **11**, 613–620 (2005).

[5] Y. Sato and T. Taira, "*Temperature dependencies of stimulated emission cross section for Nd-doped solid-state laser materials,*" Optical Materials Express **2**, 1076–1087 (2012).

[6] S. Bjurshagen and R. Koch, "*Modeling of energy-transfer upconversion and thermal effects in end-pumped quasi-three-level lasers,*" Applied Optics **43**, 4753–4767 (2004).

[7] R. Yan, X. Yu, X. Li, D. Chen, and J. Yu, "*Theoretical and experimental investigation of actively Q-switched Nd:YAG 946 nm laser with considering ETU effects,*" Applied Physics B **108**, 591–596 (2012).

[8] S. Guy, C. L. Bonner, D. P. Shepherd, D. C. Hanna, A. C. Tropper, and B. Ferrand, "*High-inversion densities in Nd:YAG-upconversion and bleaching,*" IEEE Journal of Quantum Electronics **34**, 900–909 (1998).

[9] W. Lima, V. Martins, A. Monte, D. Messias, N. Dantas, M. Bell, and T. Catunda, "*Energy transfer upconversion on neodymium doped phosphate glasses investigated by Z-scan technique,*" Optical Materials **35**, 1724 – 1727 (2013).

[10] V. Ostroumov, T. Jensen, J.-P. Meyn, G. Huber, and M. A. Noginov, "*Study of luminescence concentration quenching and energy transfer upconversion in Nd-doped $LaSc_3(BO_3)_4$ and $GdVO_4$ laser crystals,*" Journal of the Optical Society of America B **15**, 1052–1060 (1998).

[11] Y. Chen, C. Liao, Y. Lan, and S. Wang, "*Determination of the Auger upconversion rate in fiber-coupled diode end-pumped Nd:YAG and Nd:YVO_4 crystals,*" Applied Physics B **70**, 487–490 (2000).

[12] Z. Wang, J. Yu, K. Xia, C. Zhou, and J. Li, "*2x2 arrayed and passively Q-switched Nd:YVO_4 laser under Dammann-arrayed pumping,*" Applied Optics **53**, 2664–2668 (2014).

[13] T. Taira, A. Mukai, Y. Nozawa, and T. Kobayashi, "*Single-mode oscillation of laser-diode-pumped Nd:YVO_4 microchip lasers*," Optics Letters **16**, 1955–1957 (1991).

[14] S. J. Yoon, "*Cryogenically-cooled neodymium-doped solid-state lasers*," Ph.D. thesis, University of Southampton (2016).

[15] L. Agazzi, K. Worhoff, and M. Pollnau, "*Energy-Transfer-Upconversion Models, Their Applicability and Breakdown in the Presence of Spectroscopically Distinct Ion Classes: A Case Study in Amorphous Al_2O_3:Er^{3+}*," The Journal of Physical Chemistry C **117**, 6759–6776 (2013).

[16] J. W. Kim, J. I. Mackenzie, and W. A. Clarkson, "*Influence of energy-transfer-upconversion on threshold pump power in quasi-three-level solid-state lasers*," Optics Express **17**, 11935–11943 (2009).

[17] M. Eichhorn, "*Quasi-three-level solid-state lasers in the near and mid infrared based on trivalent rare earth ions*," Applied Physics B **93**, 269–316 (2008).

[18] S. J. Yoon and J. I. Mackenzie, "*Implications of the temperature dependence of Nd:YAG spectroscopic values for low temperature laser operation at 946 nm*," Proc. SPIE 9135, Laser Sources and Applications II **913503** (2014).

[19] S. Kück, L. Fornasiero, E. Mix, and G. Huber, "*Excited state absorption and stimulated emission of Nd^{3+} in crystals. Part I: $Y_3Al_5O_{12}$, $YAlO_3$, and Y_2O_3*," Applied Physics B .

[20] D. C. Brown, R. Nelson, and L. Billings, "*Efficient cw end-pumped, end-cooled Nd:YVO_4 diode-pumped laser*," Applied Optics **36**, 8611–8613 (1997).

[21] S. Cante, S. J. Beecher, and J. I. Mackenzie, "*Characterising energy transfer upconversion in Nd-doped vanadates at elevated temperatures*," Optics Express **26**, 6478–6489 (2018).

[22] L. Cini and J. I. Mackenzie, "*Analytical thermal model for end-pumped solid-state lasers*," Applied Physics B **123**, 273 (2017).

Chapter 6

Power-scaling 946 *nm* cryogenically cooled Nd:YAG lasers

6.1 Introduction

In this chapter we present the power-scaling of the Quasi-four-level (Q4L) 946 *nm* transition of Nd:YAG that is aggressively cooled to cryogenic-temperatures. The spectroscopy measurements presented in Chapter 3 underpinned the subsequent ETU coefficient characterisation at cryogenic-temperatures for Nd:YAG, presented in Chapter 5. Here, we exploit these measurements to optimise the operation of this low-gain transition between the metastable ${}^4F_{3/2}$ and ground ${}^4I_{9/2}$ states of Nd:YAG.
In Chapter 1 we have also presented the similarities between the Q4L Yb^{3+} and Nd^{3+} energy levels that make the latter a potentially very efficient laser system in the cryogenic-temperature regime. Furthermore, we highlighted how the ${}^4I_{9/2} \rightarrow {}^4F_{3/2}$ transition of Nd:YAG has only a 8% QD with respect to the 9% of Yb:YAG, in addition to a more favourable sub-1 μm wavelength for frequency conversion into the DUV, and a practically classical 4L behaviour when cryogenically cooled. However, despite the improvement of the thermal and thermo-optical properties at cryogenic-temperatures, ETU, thermal effects, and aberrations are still limiting factors to the radiance and scalability of cryogenically cooled Nd:YAG lasers, as discussed in Section 6.2.3. The main contributors to the spatial phase distortion of cryogenically cooled lasers are the mechanical stress-induced birefringence, the temperature dependent strain-induced birefringence, the thermo-optic coefficient, and bulging of the crystal facets. Notwithstanding, the mechanical-stress induced birefringence due to the different contraction of the materials in the laser head can be minimized by careful design of the crystal mount, whereas the other effects could be minimised thanks to appropriate cavity designs that mitigate total phase degradation [1]. Furthermore, there are significant additional technical challenges to address, such as strong gain competition with the dominant ${}^4F_{3/2} \rightarrow {}^4I_{11/2}$

1 μm transition and a restriction in the Nd^{3+}-doping concentration due to enhanced non-radiative decay channels and heating of the host due to ETU and CR.
In this chapter, we first introduce the diode-laser pump configuration exploited for the cryogenic-cooling operation of the 946 nm Nd:YAG laser, which we will introduce successively. Lastly, we will discuss some laser-performance aspects following the model developed by Bjurshagen and Koch [2], and presented in Section 2.4.

6.2 60W 946 nm cryogenically cooled laser

6.2.1 Pump setup

We know, from previous work by our group [3], that the Nd:YAG's absorption peak around 869 nm is the strongest of the R-band, according to the nomenclature of [4], and at LNT becomes of comparable magnitude to the RT 808 nm absorption peak, making it an effective pumping wavelength. This knowledge was the impetus for the development of a novel Volume Bragg Grating (VBG)-locked diode-laser-bar source operating at 869 nm, with a spectral bandwidth of (0.20 ± 0.02) nm, matching the sharp absorption peak of Nd:YAG at LNT. We employed this source to pump a cryogenically cooled 946 nm Nd:YAG laser, leading to two high-power results, which we will present in Sections 6.2 and 6.3. Fig. 6.1 shows the evolution of the R-band absorption cross section with temperature, from [3], and the inset highlights the strongest absorption peak, around 869 nm, exploited in our work.

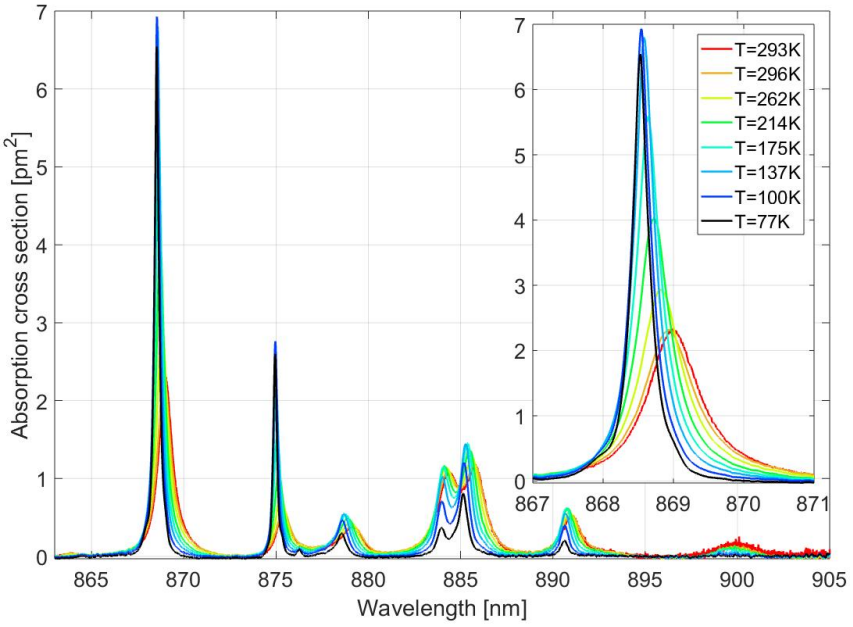

FIGURE 6.1: Nd:YAG's R-band absorption cross section for temperatures in the range (RT-LNT). Inset: zoom on the strongest peak around 869 nm.

The customised pump was developed based upon an actively-cooled 200-W diode-laser array (DLA) from DILAS, with a nominal wavelength of 873 nm. The output of the DLA was initially conditioned using a Beam Transformation System (BTS) [5] mounted by DILAS before delivering the unit. This micro-optic provided fast-axis collimation, coupled with rotation of the beams from each individual emitter in the DLA by 90^o, namely "fast" $\rightarrow$ "slow" axes (as defined by the diode-laser). Here, we define the x-coordinate as the slow-axis, and the y-coordinate as the fast-axis with reference to the DLA, respectively, while the z-axis is parallel to the direction of laser propagation. After the BTS, the beam divergence in the y-axis was nominally that of the individual emitters' slow axis, for which the collection of beamlets could be collimated with a single cylindrical lens. However, to enhance the locking efficiency, a VBG was placed immediately after the BTS. Following the VBG, cylindrical lenses were employed to manipulate and collimate the beam in the x- and y- axes separately, as shown in Fig. 6.2. A cylindrical lens, $F_y = 40\ mm$, collimated the DLA output in the y-axis; instead the x-axis was collimated by the BTS, while lenses $F_{x_1} = 75\ mm$ and $F_{x_2} = 130\ mm$ provided a 1.7x imaging telescope. A typical polarisation combining setup was employed to chop the x-axis beam in half; consequently, the beam quality for this axis was approximately halved as well.

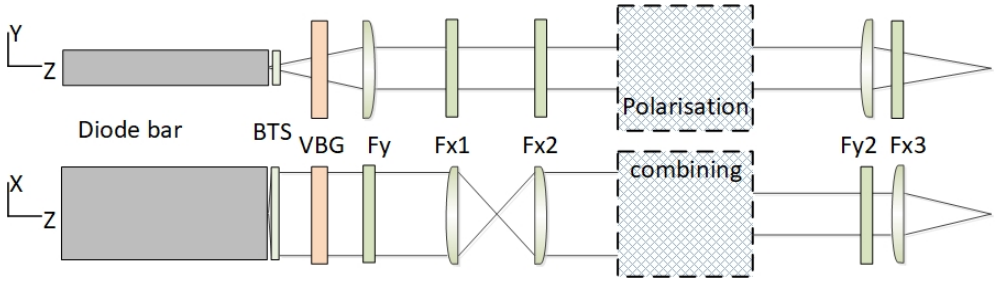

FIGURE 6.2: Layout (z-axis not in scale) of the optical components for x- and y- axes.

As a key driver in the performance of 946 nm Nd:YAG lasers is pump brightness, we characterised the DLA's beam quality at $P_{out} = 100\ W$ after the BTS, which was found to be $M_x^2 = 62 \pm 1$ and $M_y^2 = 20 \pm 1$ in the x- and y-axes respectively. The spot size and the relative beam quality in the y-axis increased substantially with drive current, as the higher-order modes of each of the broad-stripe emitters only filled out to the full width of the waveguide for pump powers $> 50\ W$. In contrast, the orthogonal fast-axis-collimated beam properties in the x-axis remained relatively constant. A VBG, with 20% reflectivity at 868.2 nm and 0.12 nm FWHM bandwidth, was mounted in an adjustable mount, positioned at $< 2\ mm$ from the BTS; its orientation was optimised in order to provide optimal locking of the DLA wavelength, monitored via the OSA. The bandwidth of the source changed from $(2.4 \pm 0.1)\ nm$ without the VBG-locking to $(0.22 \pm 0.01)\ nm$ with, whereas the beam qualities for the respective axes became $M_x^2 = 63 \pm 1$ and $M_y^2 = 22 \pm 1$.

As the photo-thermo-refractive glass has a finite absorption at the wavelength of interest,

increasing power and linear expansion of the VBG induced a temperature-dependent chirp of the central VBG-locked wavelength of 3.3 pm/W, as illustrated in Fig. 6.3. The locking wavelength at RT was designed so that the overlap between the locked wavelength and the absorption peak around 869 nm at LNT would be optimal at the maximum output power of the DLA.
The absorption efficiency was measured by monitoring the transmitted pump power through the laser crystal and cavity output coupler (OC, highly transmissive, HT, at the pump wavelength), while a second dichroic mirror (highly refletive, HR, at 946 nm and HT at 869 nm) was used to reject the 946 nm radiation. When VBG-locked, the pump absorption efficiency in the Nd:YAG crystal increased almost linearly from 20% to 95% for incident powers, measured before the cryostat's window, from 3.7 W to 58 W with a rate of 1.15%/W, associated with the pump-wavelength chirp. The absorbed power clamped at 99% for incident powers from 60 W to 120 W during lasing (see Fig. 6.4). This demonstrated the need to ensure that the small chirp in the VBG wavelength with increasing power was accounted for.

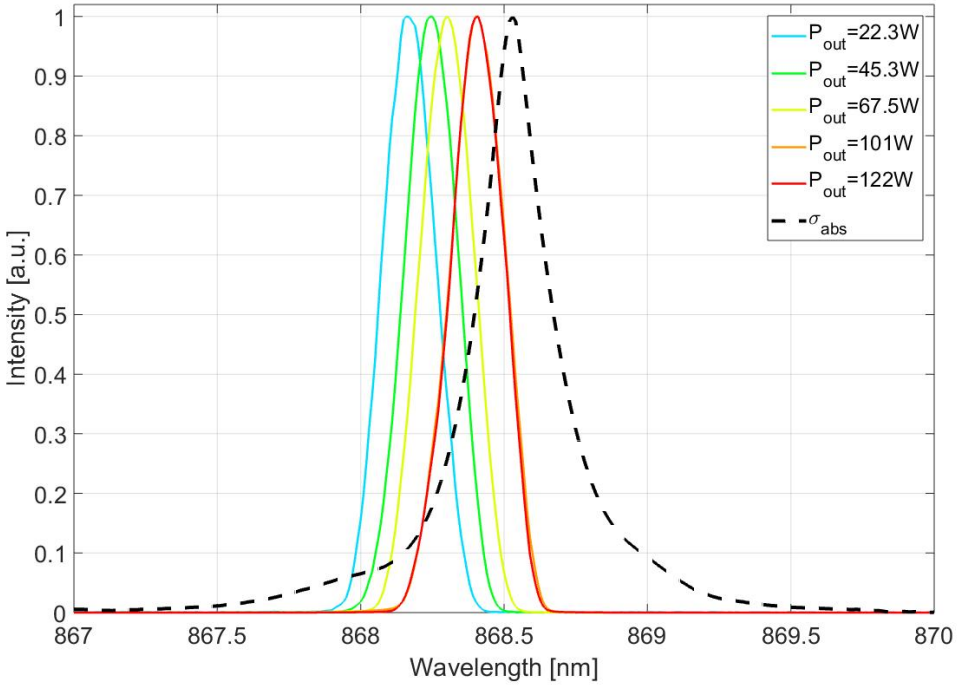

FIGURE 6.3: Central VBG-locked DLA's wavelength chirp for different output powers. Bashed black line: Nd:YAG's 869 nm normalised absorption cross section peak at LNT.

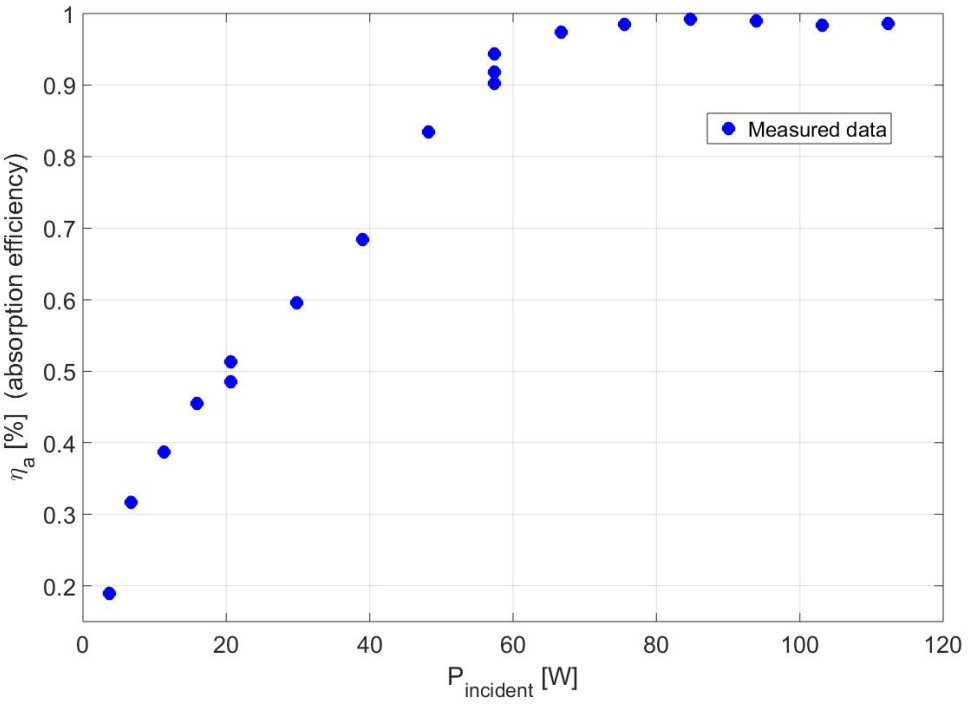

FIGURE 6.4: Absorption efficiency of the VBG-locked pump for incident powers from 4 W to 120 W during lasing.

The beam quality of the output beam was determined using a CCD camera (Spiricon BGP-USB-SP503U) positioned on a computer controlled translation stage, measuring the second moments $D_{4\sigma}$ beam caustic of the attenuated laser created by a f=250 mm focussing lens. Camera setup, data acquisition and statistical analysis were performed in conjunction with the stage control to ensure optimal measurement of the beam parameters and clean caustic measurements.

In order to reduce both the beam size and the beam quality in the x-axis, we employed a polarisation combining setup after the lens F_{x_2}, as shown in Fig. 6.5. The initial π-polarised pump beam was chopped in half by a prism mirror: one half propagated through a polarising beam splitter positioned after the prism, while the other was reflected towards two HR mirrors, angled at 45^o, such that the beam was directed on to the same polariser. Between the mirrors and polariser, a $\lambda/2$ waveplate rotated the beam polarisation by 90^o (to σ-polarisation), so that the two beams could be spatially overlapped in the centre of the beam splitter and subsequently propagate in the same direction. Comprising both polarisations, the beam had half the x-axis size whilst the divergence was unchanged. In order to minimise the new beam divergence we executed a thorough overlap alignment of the two halves in both the near and far field, which provided the best resultant beam quality.

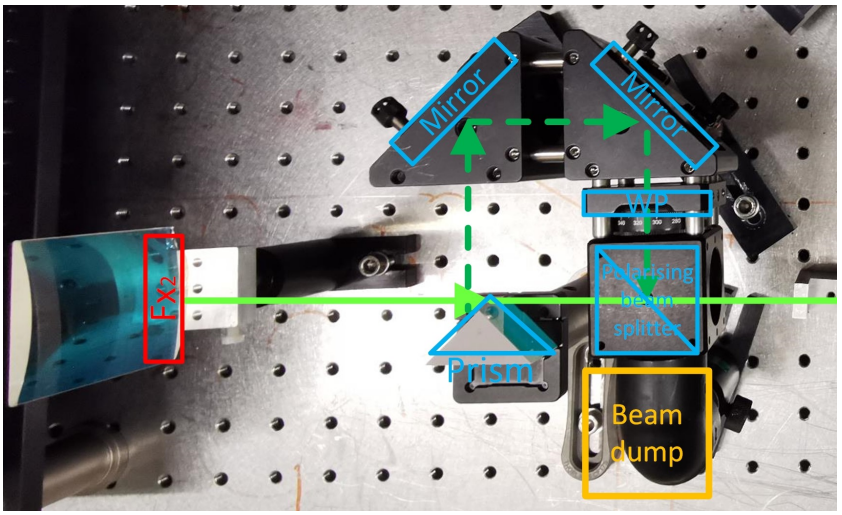

FIGURE 6.5: Polarisation combining setup, top view.

The measured beam qualities for the respective axes after the polarisation combining setup were $M_x^2 = 33 \pm 1$ and $M_y^2 = 21 \pm 1$. For the focussing of the pump light into the laser crystal we used two separate cylindrical lenses of 200 *mm* focal length for the respective x- and y-axes, (F_{y_2}, F_{x_3}) to produce an astigmatic beam waist. The final beam qualities and spot sizes, for 120 *W* of output power, were $M_x^2 = 33 \pm 1$ and $M_y^2 = 22 \pm 1$, and $w_{0_x} = 373\ \mu m$ and $w_{0_y} = 352\ \mu m$ for respectively x- and y-axes, as shown in Fig. 6.6.

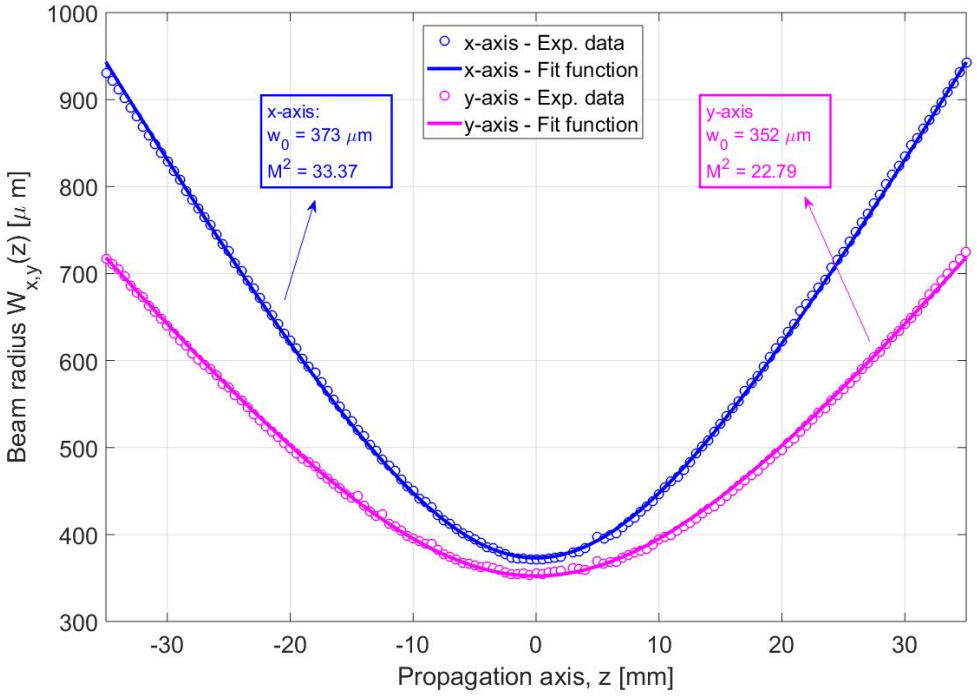

FIGURE 6.6: Beam quality and spot sizes after the focussing lenses for $P = 120\ W$.

6.2.2 Cavity configuration

A 3x3x15 mm^3, 0.3at.% Nd:YAG crystal was used for the laser experiment. The smaller facets were anti-reflection (AR) coated for the pump and laser wavelengths. Wrapped in 200 μm-thick indium foil, the crystal was clamped between two copper plates. One plate was bolted directly to the cold-head of a liquid-nitrogen dewar, the assembly providing cooling through two side faces of the crystal. A copper braid brazed to both pieces was employed to ensure a thermal link between the two copper parts; the mounting scheme is shown in Fig. 6.7. The assembly was isolated from the surrounding environment via a $\sim 10^{-7}$ $mbar$ vacuum, and the vacuum chamber was equipped with 6 mm-thick Suprasil windows that allowed optical access to the crystal while acting as sealing plates; these windows were AR-coated for the laser wavelength, and had a 98.4% and 99.9% nominal transmission at the pump and laser wavelengths, respectively. The temperature of the system was monitored by two temperature sensors positioned on the side of the cold head and on the Cu piece further from the cold head, respectively.

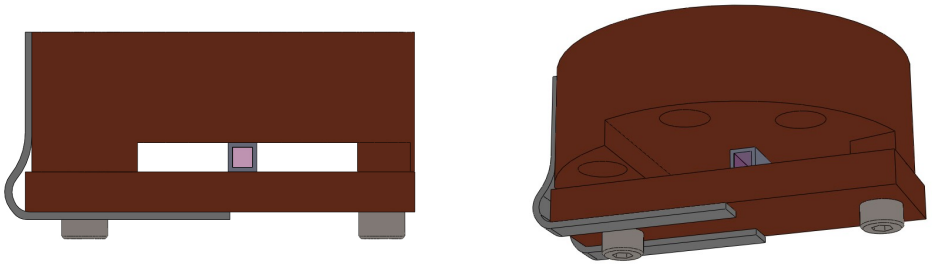

(A) (B)

FIGURE 6.7: 3x3x15 mm^3 Nd:YAG crystal wrapped in Indium foil and positioned between two Copper blocks, the largest one in contact with the cold head. The two blocks are thermally linked via a Copper braid. (A) Front view. (B) Dimetric view.

We employed a linear plano-concave 168.5 mm-long cavity, as shown in Fig. 6.8, comprising a flat input mirror, and a 200 mm radius of curvature (ROC), T=10% OC. The input mirror was positioned in close proximity to one window, resulting in a distance from mirror to crystal being 52.5 mm.

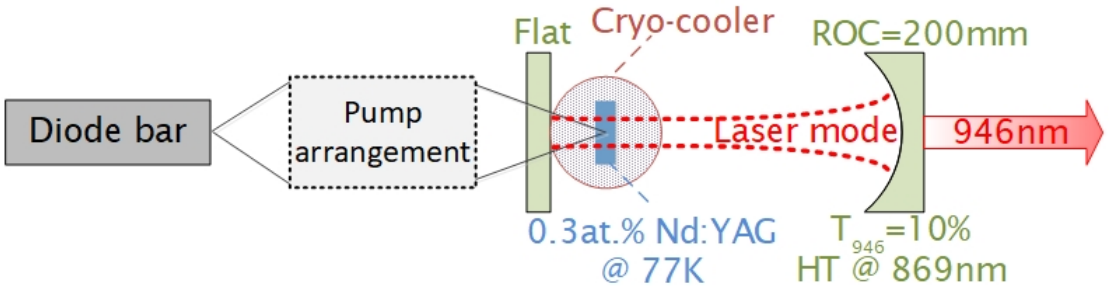

FIGURE 6.8: Linear plano-concave cavity.

This configuration provided a fundamental laser mode of $\sim 190\ \mu m$ over a thermal lens focal length range from infinity to $\sim 500\ mm$, as displayed in Fig. 6.9.

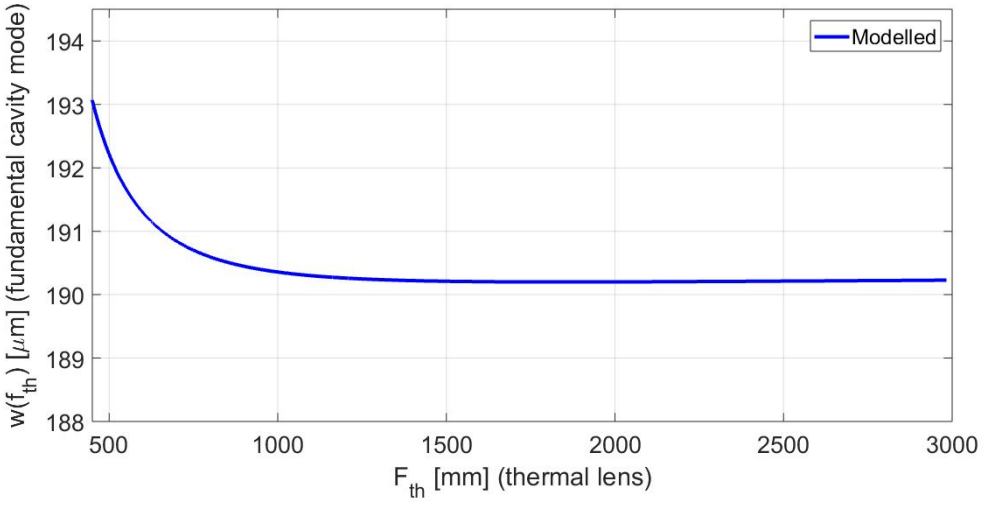

FIGURE 6.9: Fundamental laser mode radius in the crystal vs thermal lens.

6.2.3 Results and discussion

The temperature of the cold head was fixed at 77 K by the LN bath, and monitored throughout the experiment by the two temperature sensors. The emission wavelength was measured in real time by the OSA after capturing the light scattered off the thermal power-detector used to measure the output power. In fact, thanks to the known dependence of the 946 nm emission peak on the temperature [3], shown in Fig. 6.10, it was possible to estimate the average temperature of the lasing volume of ions within the crystal. Similar spectroscopic measurements to infer the local average temperature have already been employed in other works [6]. As it can be observed in Fig. 6.10, the 946 nm peak redshifts with decreasing temperature.

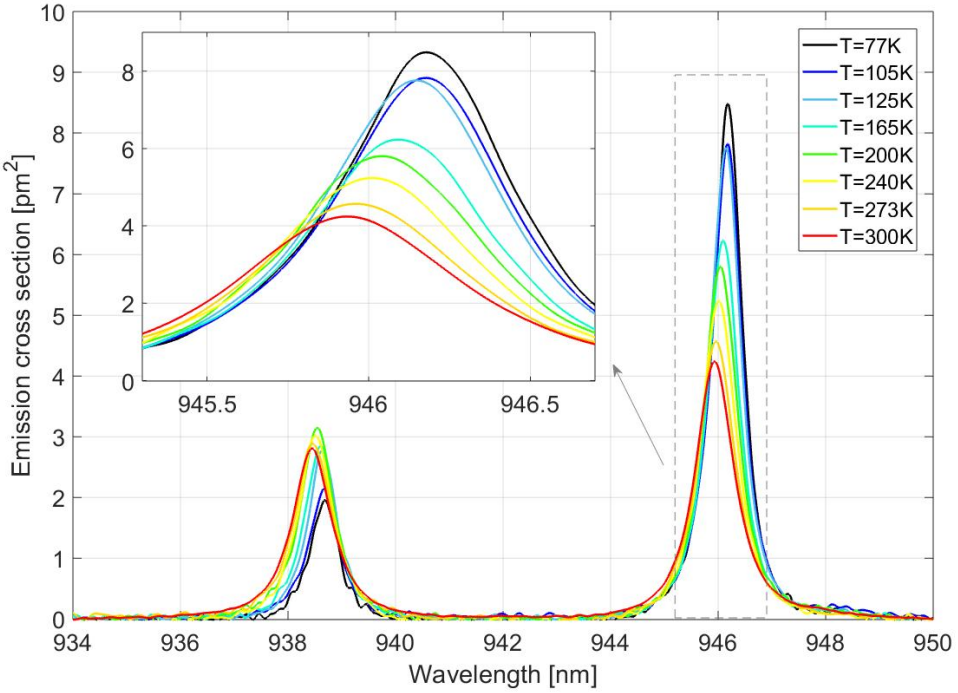

FIGURE 6.10: Emission cross section around 940 nm for several different temperatures in the range (RT-LNT) [3]. Inset: the 946 nm peak's red-shift with decreasing temperature.

The laser threshold was measured to be 2 W of absorbed pump power; at this stage the emission wavelength was (946.224 ± 0.005) nm, in line with the value at 77 K given in [3]. The slope, and optical to optical, efficiency versus absorbed pump power was measured to be 52%, with a maximum laser output power of 60 W (Fig. 6.11).
Employing the same beam profiling methodology described above, we measured the beam quality at $P_{out} = 1$ W for the respective axes to be $M_x^2 = 1.60$ and $M_y^2 = 1.08$. The significant difference between the two axes was due to the pump's beam quality being worse in the x-axis compared with the y-axis, leading to an overlap factor, $a_x = w_{P_x}/w_{L_x}$ [7], of nearly two near threshold. Furthermore, the near-threshold overlap in the y-axis, $a_y \sim 1.3$, increased to ~ 1.8 at pump powers > 50 W. In contrast, the overlap in the x-axis stayed relatively constant throughout the range of available pump output powers. The beam quality for the respective axes degraded with increasing laser power: for $P_{out} = 40$ W we measured $M_x^2 = 3.10$ and $M_y^2 = 2.32$, with modal instability affecting the precision of the measurement, as can be appreciated in Fig. 6.12. For output powers higher than 40 W the measured beam size was fluctuating significantly, and as such a stable M^2 measurement could not be achieved.

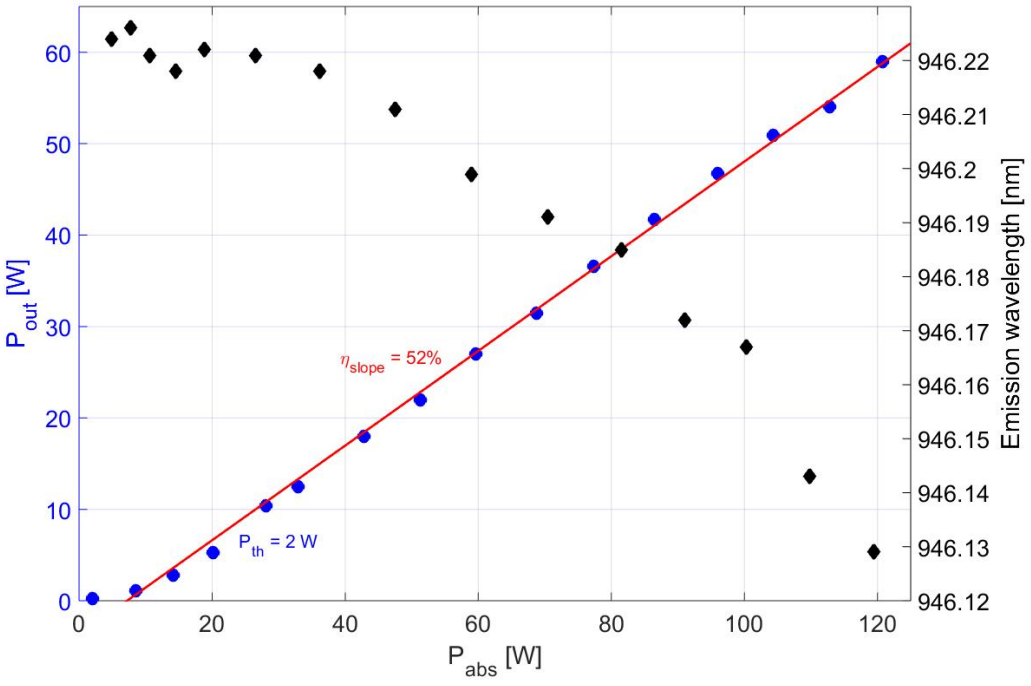

FIGURE 6.11: Right axis (black diamonds): laser emission wavelength vs absorbed pump power. Left axis (blue dots): slope efficiency vs absorbed pump power for the 60-W, 946 *nm*, cryogenically cooled Nd:YAG laser developed.

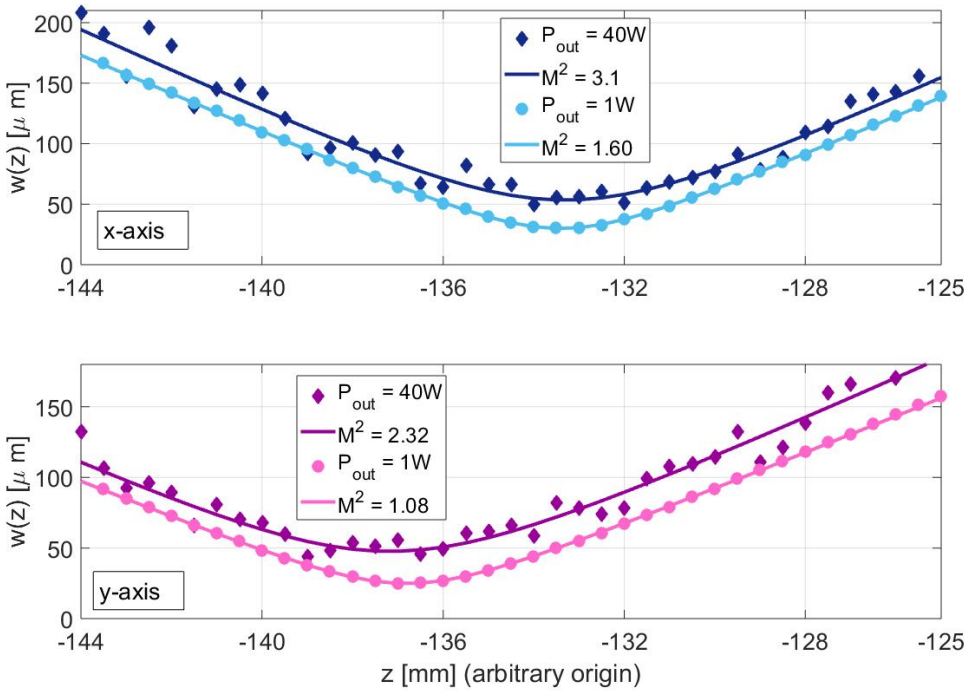

FIGURE 6.12: Measured beam qualities for the respective axes for $P_{out} = 1$ *W* (circles) and $P_{out} = 40$ *W* (diamonds).

As detailed in Chapter 2, ETU is a notorious source of additional heat that compromises the laser performance of low-gain transitions like the 946 nm in Nd:YAG, although in Section 5.4.3 we have demonstrated that the spectroscopic and thermo-optical benefits of cryogenic cooling outweigh the detrimental increase in the ETU coefficient for sub-ambient temperatures. Notwithstanding, if the thermal management is not optimal, this effect can still provide negative feedback with increased thermal loading and cavity losses, coupled with reduced gain, and eventually lead to a rollover in performance. In fact, simultaneous to the beam quality degradation, we recorded a strong blueshift in the emission wavelength, reaching $(946.129 \pm 0.005)\ nm$ when $P_{out} = 60\ W$. From this we estimated that the average local temperature rise, i.e. in the cavity-mode volume within the crystal, was $\sim 80\ K$, as suggested by Fig. 6.10. This value is substantially higher than the $\sim 20\ K$ predicted via an analytical model, which includes the temperature dependent thermal conductivity of the crystal [8]. The fact that the temperature sensors only measured an increase of a few degrees in the Copper mount and cold-head of the cryostat, suggested the existence of a large temperature gradient across the crystal-mount interface. In fact, as discussed in the aforementioned model [8], due to the temperature dependence of the crystal's thermal conductivity, if there is a significant thermal barrier at the boundary, hence temperature rise across it and therefore throughout the crystal, there is also an additional increase in temperature at the center of the crystal. Correspondingly, we estimated that the heat transfer coefficient, h, between crystal and coolant that would be associated with such a temperature rise is between $(0.25 - 0.5)\ W/K \cdot cm^2$. That is $4 - 10$ times lower than the best value reported for RT heat-sinking with a thermal grease between the crystal and a Copper mount [9]. It is evident that due to the large gradient in the thermal conductivity dependence on temperature for YAG in the cryogenic regime, the peak temperature-rise sensitivity to the magnitude of h is enhanced with comparison to operation at RT. We have therefore identified the primary cause for the detailed roll-over in power in the over-heating of the crystal, due to a non-optimal heat-sinking arrangement. In particular, as described above, the thermal barrier at the boundary, caused by an estimated lower-than-expected heat transfer coefficient, implied a significant temperature rise. This, in turn, was responsible for the decrease in the gain, and subsequent beam quality degradation, eventually leading to a power roll-over after the measured output power of 60 W.

Furthermore, the fact that the overlap factor was nearly 2 meant that the cavity supported higher-order modes, for which in modeling, it is nontrivial to allocate a proportional contribution in terms of the laser output. As the rate of ETU depends on N_2^2, its contribution to heating of the crystal is dynamic, and dependent on the number of times the laser is operating above threshold. Therefore, the induced thermal lens is highly aberrated, especially in the outer regions of the pump beam, thus leading to beam quality degradation [1, 2], as highlighted by the M^2 value obtained at higher pump powers and by the unstable laser profile near the roll-over point. Fig. 6.13 shows some screenshots of the laser beam dynamically switching from fundamental to higher-order modes; the screen

captures were executed over $\sim 10\ s$. At the same time, we observed a non-negligible signal at 1 μm which appeared to be in competition with the 946 nm laser output, though the latter was always present, the first was irregularly oscillating between zero and a value that we couldn't record this due to its instability. This seemingly dual-wavelength output was likely caused by the 946 nm signal not completely saturating the available gain, due to the strong aberrations induced by the temperature gradient and the mode competition described above. It is reasonable that the much stronger, $\sim$ 7x, transition at 1 μm would be able to reach the threshold output power and start lasing thanks to the available gain unexploited by the weaker 946 nm transition.
In order to illustrate how the almost-factor-of-2 mode match might have affected the thermal loading distribution and led to further aberrations, we employ the model developed by Bjurshagen in [2] and presented in Section 2.4. A 120 W, 869 nm pump laser is employed to pump a 15 mm-long, 0.3at.%-doped, Nd:YAG crystal at 77 K and lasing at 946 nm; all the temperature-dependent spectroscopic and thermo-optical parameters involved in the modelling are fixed on their value at 77 K. A list of the modelling parameters employed can be found in Appendix B.

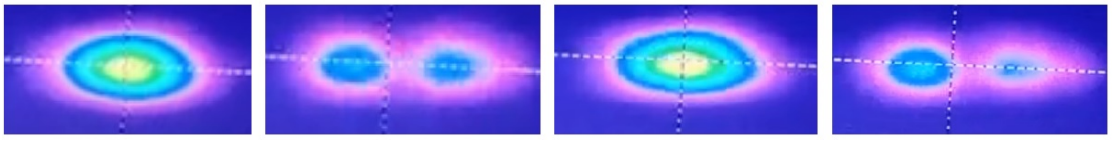

FIGURE 6.13: Captured spatial distribution of the laser mode over $\sim 10\ s$: the beam presents a high modal instability.

Due to the complexity of including a pump-power-dependent temperature distribution, this model operating at a fixed temperature of 77 K is a still informative approximation of the real, much more complex, laser dynamics taking place, and hence to be considered only as a broad view providing useful insight. Fig. 6.14 shows the spatial distribution of the pump mode, according to the measured beam radii, and fundamental laser mode, according to the modelled cavity, at the first facet of the crystal.
Since the spatial distribution of the pump mode is a key factor in the results provided by this model, employing a form that matches, or adequately approximates, the real one is paramount. The beam quality characterisation of multi-mode beams only provides information regarding the multi-mode radii and its evolution along the propagation axis, leaving the spatial distribution unknown: in order to gather the latter information, we have collected 2D-maps of the intensity profile at several z-coordinates along the propagation axis around the crystal position, and fitted the x- and y- profiles (along the (x, y) coordinate of maximum intensity) to n^{th}-order supergaussian fitting functions with the order as the relevant fitting parameter. Results showed that, although the beam caustic measurement suggested the pump mode is a highly-multimode beam, the spatial distribution at fixed z-locations around the waist is well approximated by a Gaussian distribution; therefore, for the modelled pump beam, we have employed a

2-D Gaussian distribution with different x- and y- beam radii as measured in the beam quality characterisation detailed in Section 6.2.1.

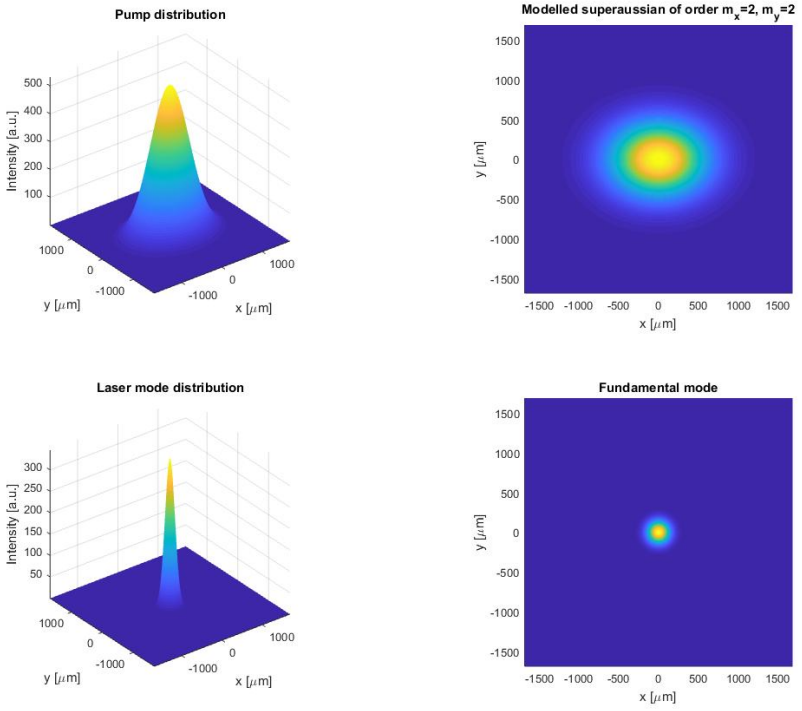

FIGURE 6.14: Spatial distribution of the pump and fundamental laser modes according to measurement and cavity modelling, respectively.

Figure 6.15 shows the spatial distribution under lasing conditions of the inversion level, including the effects of ETU as per Eq. (2.40), at the first (top plots) and second (bottom plots) facets of the crystal. The calculated population inversion, when including ETU, is reduced by this effect, which produces extra heat as we will see in the plots below. The two right-hand-side surface maps in Fig. 6.15 have a common scale to highlight the difference between the inversion levels of first and second facets. In fact, two main things are brought to light by these plots: the first is that the most of the pump power is deposited in the initial portion of the crystal, providing one order of magnitude difference between the inversion levels at the front ($\sim$ 50%) and back ($\sim$ 5%) facets of the crystal; the second is that the bigger pump mode provides a population inversion as high as 50% in the area where the gain is not saturated by the laser mode. In the latter scenario, it is likely that higher-order modes, like $TEM_{10,01,11}$, will be excited, particularly in the x-axis, resulting in a beam quality greater than 1, as experimentally observed for the x-axis even near threshold. Furthermore, experimental evidence shown in Fig. 6.13 suggest that higher-order modes (seemgly TEM_{10}) were indeed lasing in the x-axis, for the higher pump power employed, however in a dynamic competition with the fundamental mode.

Fig. 6.16 shows the fractional thermal loading distribution $\xi(\mathbf{r})$ as defined in Eq. (2.41), at the first and second facets of the crystal. As detailed in Section 2.4, in absence of ETU, i.e. with the term $F_{ETU}(\mathbf{r}) = 0$, it would be $\xi(\mathbf{r}) = \xi_0$ that, under lasing conditions, is the quantum defect between the pumping and lasing wavelengths, in this case $\sim 8\%$ which in fact corresponds to the minimum value in Fig. 6.16. The presence of ETU increases the thermal loading in the pumped regions where the gain is not saturated, i.e. the wings outside the laser mode, while reducing the population inversion. Noticeably, this results is in good agreement with the example provided by Bjurshagen in [2] in the case of a pump mode radius twice the laser mode's ($a = 2$).

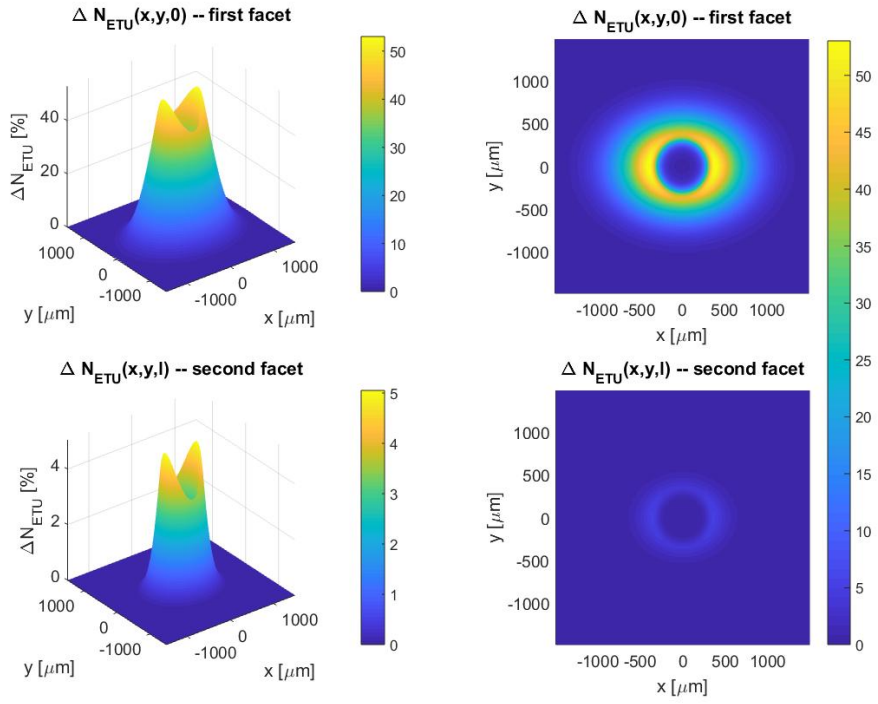

FIGURE 6.15: Spatial distribution of $\Delta N(\mathbf{r})$ at the first (top plots) and second (bottom plots) facets of the crystal.

Finally, Fig. 6.17 shows the heat-source-density distribution $Q(\mathbf{r})$ in the crystal, as defined by Eq. 2.42. By definition, this quantity has the shape of the absorbed pump radiation weighted by the thermal loading distribution. We can therefore compare the cases with and without ETU to gauge the impact that this effect has on the heat density in the crystal. The top plots of Fig. 6.17 show the case including ETU at the first and second facets of the crystal, respectively: at the first facet the heat-source-density's shape resembles the fractional thermal loading distribution $\xi(\mathbf{r})$. At this facet, in fact, $\xi(\mathbf{r})$ becomes as high as 30% in the areas outside of the fundamental laser mode, $\sim 22\%$ in excess of the quantum defect only due to ETU; as a consequence, $Q(\mathbf{r})$ at the front facet of the crystal is significantly higher in the wings of the fundamental laser mode, as opposed to the case without ETU (bottom plots of Fig. 6.17). At the second facet, instead,

$Q(\mathbf{r})$ is shaped similarly to the pump and to the case without ETU as a consequence of the low contribution given by ETU and by the low inversion level generated in that area, as showed in Fig. 6.15.

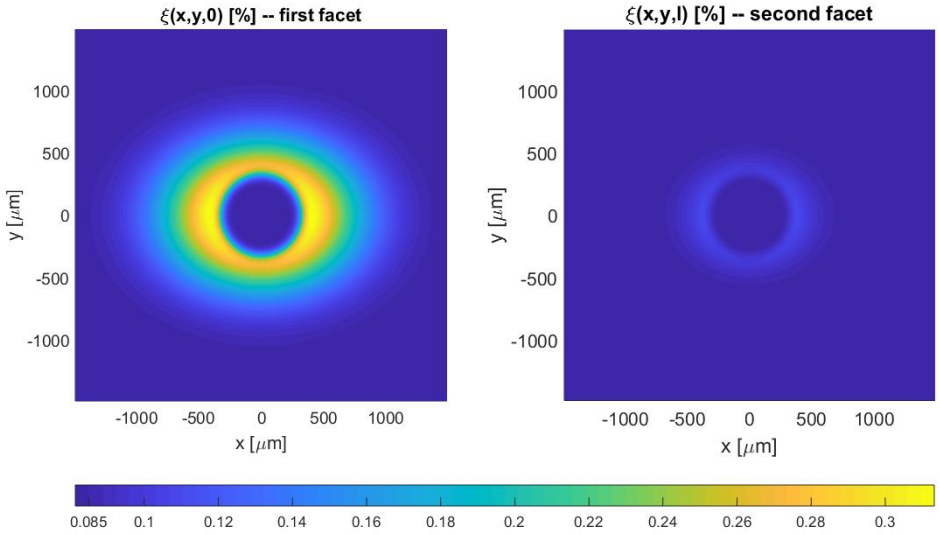

FIGURE 6.16: Fraction thermal loading distribution at the first and second facets of the crystal.

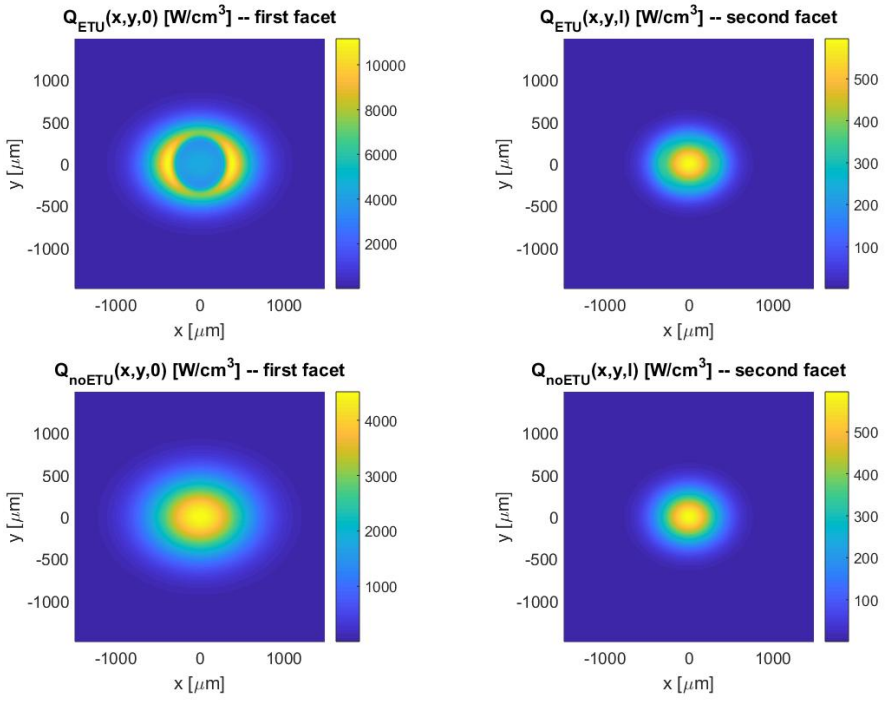

FIGURE 6.17: Heat loading distribution $Q(\mathbf{r})$, with (top plots) and without (bottom plots) accounting for ETU, at the first and second facets of the crystal.

Furthermore, the fact that at the second facet of the crystal $Q_{ETU}(\mathbf{r})$ is similar to $Q_{noETU}(\mathbf{r})$ indicates the relatively low impact that ETU has for low pump-intensity in relation to the saturation intensity, as also highlighted by Fig. 6.16, where the fractional thermal loading distribution at the second facet of the crystal is, almost uniformly, close to the quantum defect. In absence of ETU, the first facet of the crystal would experience a heat source distribution proportional to the pump distribution via the quantum defect and absorbed pump power, as detailed by Eq. 2.42. Relevant to our argument is also the relative value of these heat-source-density distributions, indicated in Fig. 6.18: in the case including ETU the maximum value reached in the ring-shaped distribution is more than 3.5-times that of the case without, indicating a substantially higher heat load in the crystal exclusively due to ETU. It is straightforward to assume that this kind of heat density distribution will exacerbate the aberrations given by the other effects listed in Section 6.1, as experimentally observed around the power roll-over point when the laser beam presented a dynamic, aberrated, profile, as shown in Fig. 6.13.

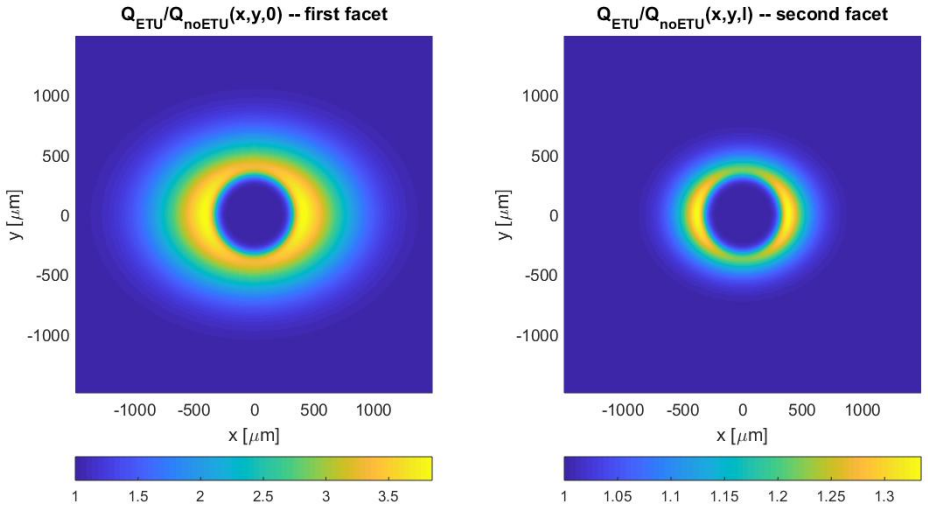

FIGURE 6.18: Ratio of the heat source distributions $Q_{ETU}(\mathbf{r})/Q_{noETU}(\mathbf{r})$ at the first and second facets of the crystal.

It is however expected that the heat-source-density distribution modelled here is mitigated by higher-order laser modes saturating the gain in the regions where there is a high population inversion, as shown in Fig. 6.15, thus reducing the fractional thermal loading distribution. Although these calculations are the results of a model that simplifies the actual laser dynamics, they still highlight the way that the $a = 2$ mode-match employed in our experiment, and the ETU effects adding to it, have contributed to the observed roll-over in laser performance.

6.3 110W 946 *nm* cryogenically cooled laser

In this section we present further power-scaling of the cryogenically cooled, in-band pumped, 946 *nm* Nd:YAG laser and implementation of a closed-cycle cryostat. In Section 6.2.3 we discussed potential causes for the output power limitation measured in the laser we developed, laying mainly in the excessive heating and aberrated thermo-optical effects in the gain medium. Here, we discuss a revised pump-laser configuration, developed in collaboration with Gholamreza Shayeganrad, aimed to reduce the ellipticity of the intensity distribution, and a new crystal mount, developed by G. Shayeganrad, employed in order to symmetrise the cooling profile and optimise the heat transfer. Finally, we apply the laser-performance model detailed in Chapter 2 for our specific case to estimate the effects that the thermal loading distribution due to ETU might have had on the laser output power and beam quality. We further propose possible improvements to increase the laser output power and beam quality.

6.3.1 Pump setup

The aim of an updated pump setup was to achieve a more symmetric, or less elliptical, pump intensity distribution in the crystal, along with a symmetric cooling, as opposed to the cooling-scheme employed previously and described in Section 6.2.2. As we have detailed in Section 6.2.1, the pump waist radii, after two 200 *mm* cylindrical lenses, were $w_{0_x} = 373\ \mu m$ and $w_{0_y} = 352\ \mu m$ for respectively x- and y-axes. Respective beam qualities of $M_x^2 = 33 \pm 1$ and $M_y^2 = 22 \pm 1$ determined an ellipticity (w_{0_x}/w_{0_y}) of the pump beam in the crystal between 1.16 and 1.04 for a pump power of 120 *W*, as shown in Fig. 6.19.
As discussed, this ellipticity coupled to an asymmetric cooling design, determined an elliptical thermal load distribution in the crystal, that ultimately led to an asymmetric laser output beam. One way of achieving a symmetric pump would have been to fibre-couple the pump light; however, requiring a careful design to maximise the coupled power, this option was left for a later development phase, due to time and raw-power considerations.
Unfortunately, while in the process of characterising the updated pump arrangement, the diode-bar failed catastrophically, which forced a complete start-over of the pump setup development and subsequent characterisation of a new, equivalent, diode-bar. Fig. 6.20 shows two microscope photos provided by the manufacturer DILAS Coherent upon inspecting the damaged diode-bar: some emitters had burned to complete destruction and this damage was possibly causing a short circuit, preventing the diode to turn on at all.

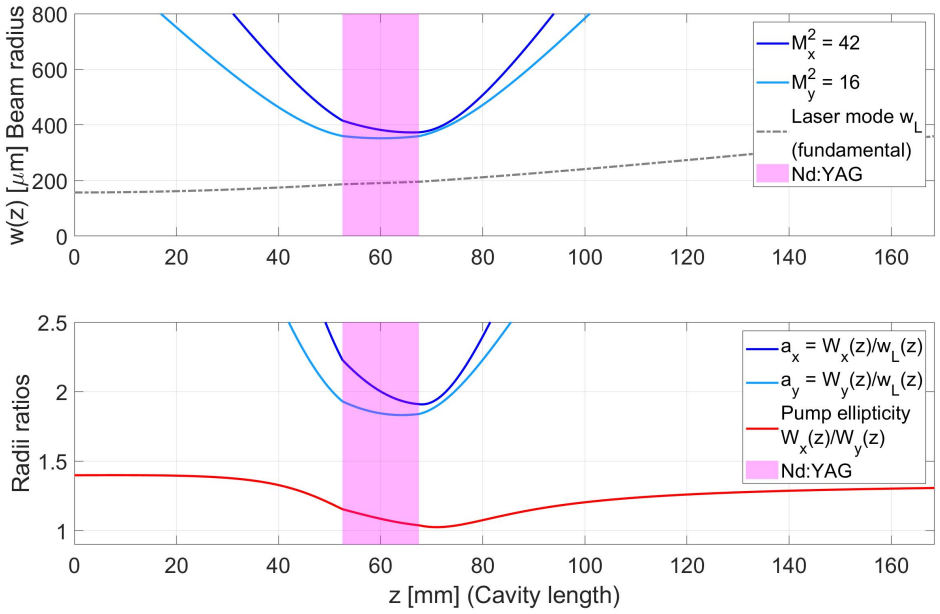

FIGURE 6.19: Top plot: Representation of the x- and y-axes' pump caustics ($P_{pump} = 120\ W$) and the fundamental laser mode according to measurement and modelling (Section 6.3.1), respectively. Bottom plot: mode match $a = W_{0_{x,y}}/w_L$ factor for the x- and y-axes (blue curves) and ellipticity (red curve) of the pump beam over the cavity length. Pink patches: Nd:YAG crystal.

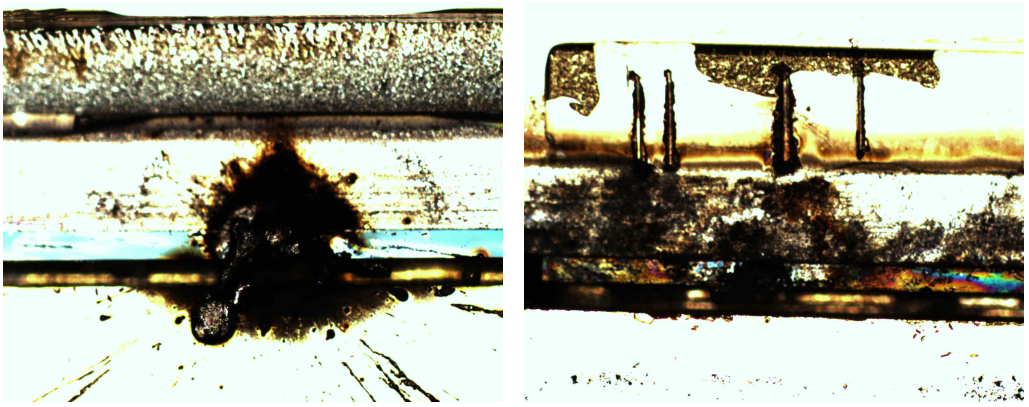

(A) (B)

FIGURE 6.20: Catastrophic damage of the DLA's emitters.

The possible cause of damage was imputed to be excessive heat in the vicinity of the emitters, although we couldn't discern the exact source of such heat. When operating near the maximum ratings, i.e. $I_{driver} \sim 200\ A$, the environment around the diode was becoming hot most likely due to both the $\sim 20\%$ feedback from the VBG and the high $\sim 180\ W$ output-power of the bar. Few measurements of the VBG's temperature, executed with a thermal camera during laser operation, had not revealed any relevant information that could have prevented the damage of the bar. In order to monitor both the VBG's and the diode-bar's housing temperature, temperature sensors were installed

on the VBG mounting's surface closest to the VBG and on the bar's housing, respectively. The new pump setup was developed similarly to the one detailed in Section 6.2.1, except for the second cylindrical lens, F_{x2}, comprised in the x-axis beam expander; a 150 mm lens was employed in the upgraded setup, instead of the $F_{x2} = 130$ mm used before. With $F_{x1} = 75$ mm, this provided a 2-fold expansion of the beam in the x-axis after the $F_y = 40$ mm y-axis collimating lens, instead of the previous 1.7. Furthermore, the two cylindrical focusing lenses, $F_{x3} = F_{y2} = 200$ mm, were positioned on translation stages in order to provide independent control of the position of the pump waists in the x- and y-axes. Measured pump caustics for the x- and y-axes at $P_{in} = 45$ W and $P_{in} = 135$ W for this configuration are shown in the top plots of Figs. 6.21 and 6.22, respectively. In these plots we have accounted for both the refraction at the air/crystal interfaces and the beam propagation through the Nd:YAG crystal (pink rectangle), though not any additional thermal-induced lensing. The z coordinate is referenced to the input cavity mirror of the linear cavity described in the next section. In order to protect the DLA from parasitic ASE/lasing at 1 μm, a dichroic mirror AR- at 869 nm and HR-coated at 1 μm mirror was positioned at a slight off-axis angle between F_{x2} and F_{y2}, as shown in Fig. 6.24.

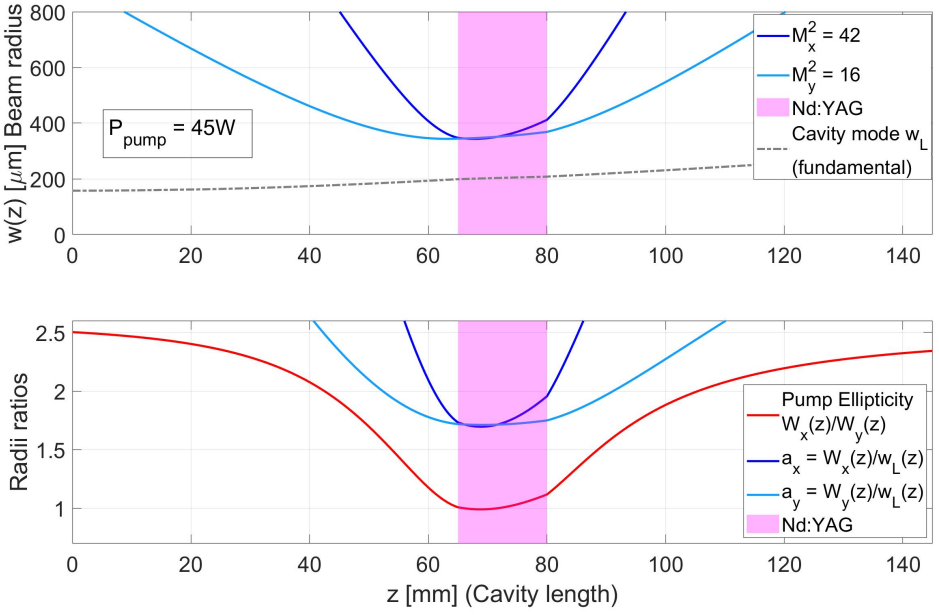

FIGURE 6.21: Top plot: Representation of the x- and y-axes' pump caustics and the fundamental laser mode according to measurement ($P_{pump} = 45$ W) and modelling, respectively. Fundamental cavity mode modelled (see Section 6.3.2) with a predicted thermal lens of 1000 mm [8]. Bottom plot: mode match $a = W_{0_{x,y}}/w_L$ factor for the x- and y-axes (blue curves) and ellipticity (red curve) of the pump beam over the cavity length. Pink patches: Nd:YAG crystal.

The new pump configuration provided an improved ellipticity parameter with respect to the previous case, particularly at the first facet of the sample, where most of the power is absorbed and the thermal load distribution presents steeper gradients than further

along the crystal length. As it can be seen from a comparison between Figs. 6.21 and 6.22, a consequence of the diode-laser array being driven further above threshold, thus increasing the higher-order mode content in each waveguide's slow axis, is that the waist position in the y-axis shifted away from the focusing lenses by $\sim 10mm$ near full operating pump power, with the ellipticity parameter changing accordingly. The values of the latter were between 1.00 and 1.03 for $P = 45\ W$, and between 0.90 and 1.00 for $P = 135\ W$, across 2/3 of the crystal, determining an improvement with respect to the previous pump configuration. The maximum available incident power was 152 W at 200 A driving current.

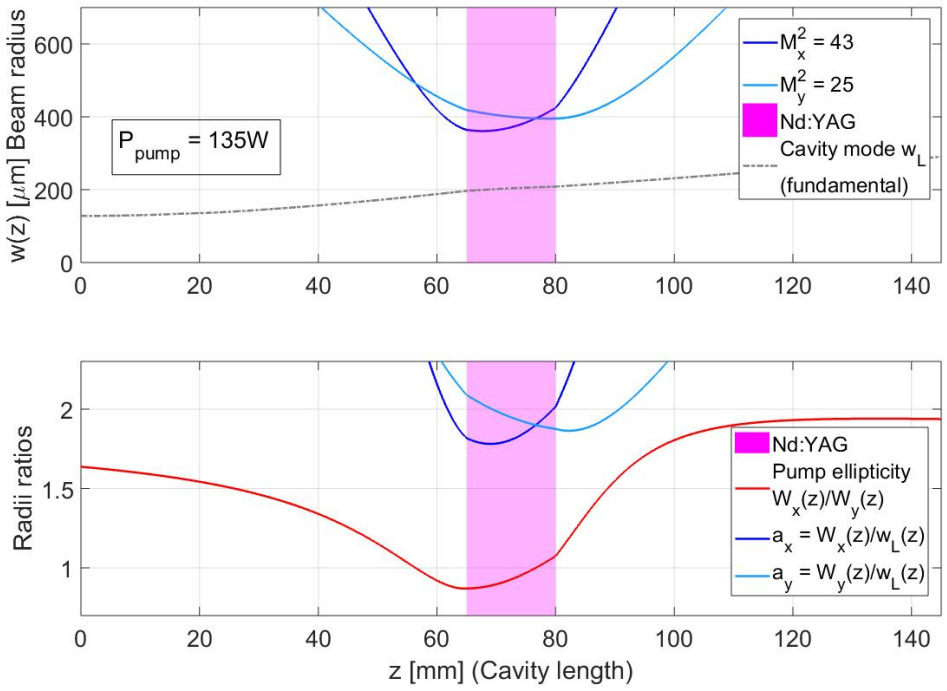

FIGURE 6.22: Top plot: Representation of the x- and y-axes' pump caustics and the fundamental laser mode according to measurement ($P_{pump} = 135\ W$) and modelling, respectively. Fundamental cavity mode modelled (see Section 6.3.2) with a predicted thermal lens of 250 mm [8]. Bottom plot: mode match $a = W_{0_{x,y}}/w_L$ factor for the x- and y-axes (blue curves) and ellipticity (red curve) of the pump beam over the cavity length. Pink patches: Nd:YAG crystal.

A challenging aspect of the pump setup was to obtain a symmetrical pump beam in the crystal for all the pump powers available: this was unattainable because, as detailed above, both the beam radius and the waist location, especially in the y-axis, were power-dependent. A solution to this challenge would be provided by coupling the pump signal into a fibre, the output of which would be symmetrical and allow the simultaneous adjustment of the x- and y- axes waists' locations with only a single spherical lens.

6.3.2 Cavity configuration

The crystal was mounted as in Fig. 6.23: a cylindrical holder made of 4 quadrants accommodated the parallelepipedal 3x3x15 mm^3, 0.3at.%-doped Nd:YAG crystal employed previously; this cylindrical assembly was held in a block bolted to the cold head of the cryostat. The careful design and material choice ensured both a good thermal contact between the crystal and the heat sink for all temperatures, especially for those lower than 150 K, and a low stress-induced depolarisation loss, as described below. At the time of writing we cannot disclose more technical details about this cooling scheme because we are evaluating the possibility of patenting it. This novel arrangement, developed in collaboration with G. Shayeganrad, provided not only cooling through all the four 3x15 mm^2 side faces of the crystal, hence a symmetric cooling profile, but also a major thermal-management improvement with respect to the previous case detailed in Section 6.2.2. The latter was key to a significantly improved efficiency and therefore higher output power of the laser developed, as depicted in the following sections. A novel aspect to the cavity developed was also that the cryostat employed was the same acoustic stirling Q-drive 2s132K described in Section 3.2.1, which, as opposed to the LN dewar exploited for the laser detailed in Section 6.2.2, allowed us to fine-tune the temperature to maximise the laser output power. Additionally, it also allowed the testing of the newly developed crystal mount over daily thermal cycles. The unit, in fact, was switched on and off on a daily basis, with cooling down times from RT to LNT in the order of 35 minutes.

(A) (B)

FIGURE 6.23: 3x3x15 mm^3 Nd:YAG crystal wrapped in Indium foil and positioned in a 4-quadrant mount. This cylindrical assembly is held in a block in contact with the cold head. (A) Front view. (B) Dimetric view.

The mechanically induced pressure due to the cooling from RT to cryogenic-temperatures can induce refractive index inhomogeneities, namely mechanical stress-induced birefringence due to photoelastic effect [10, Chapter 5]. In order to characterise this effect, depolarisation was monitored whilst cooling the crystal. A 912-nm polarised probe laser was directed through the centre of the mounted crystal positioned between two crossed

polarisers, and a depolarisation loss $< 0.3\%$ was observed over the whole temperature range. Isolation from the surrounding environment, via a $\sim 10^{-7}$ *mbar* vacuum, and optical access to the crystal were provided by the same vacuum chamber described in Section 6.2.2.

A linear cavity was employed, comprising a flat input mirror and a curved OC: both were highly transmissive at 869 *nm*, 1060 *nm* and 1320 *nm*. Two OCs with different transmittances and ROCs were tested: OC_1 with $T_1 = 10\%$ and $ROC_1 = 200$ *mm*, and OC_2 with $T_2 = 20\%$ and $ROC_2 = 1000$ *mm*. The input mirror was positioned in close proximity to the first optical window and the OC being employed was positioned after the crystal and second window, providing a cavity length of 145 *mm*. We estimated that the pump-power-dependent thermal lens value according to the analytical model developed by Cini [8] for the maximum available pump power was ~ 250 *mm*, providing average fundamental-mode radii in the crystal of 204 μm and 230 μm, for OC_1 and OC_2, respectively.

Fig. 6.24 shows the experimental setup employed for the characterisation of the laser performance. During laser operation, a water-cooled powermeter (Gentec, UP55N) (PM1) monitored the non-absorbed pump signal transmitted through the Nd:YAG crystal, the OC, and a dichroic mirror, while a second water-cooled power meter (PM2) measured the 946 *nm* laser signal, the scattered light of which was collected by a 200 $\mu m/0.22$ NA fiber, coupled to an OSA (AQ6317B), allowing us to monitor the emission spectrum. The pump wavelength was monitored similarly, although from scattering from the pump conditioning optics.

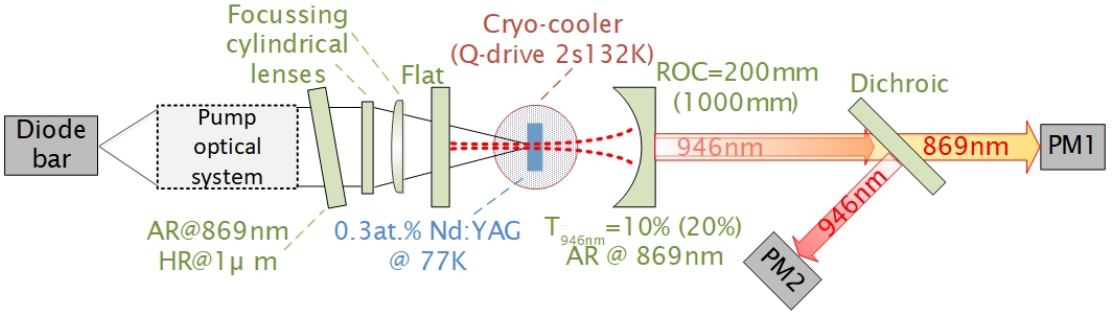

FIGURE 6.24: Experimental setup for the cryogenically cooled 946 *nm* Nd:YAG laser developed.

The right axis of Fig. 6.25 shows how the VBG-locked pump wavelength changes with power, due to the chirp discussed in Section 6.2.1; consistent with the pump setup detailed in Section 6.2.1, we observed a redshift at a rate of 3 pm/W with respect to incident pump power. Engineered to provide maximum absorption, i.e. best spectral overlap between the pump and absorption spectra, at the highest available pump power and crystal temperature of ~ 77 *K*, the chirp of the VBG-locked pump-wavelength provided a large change in pump absorption efficiency across the available pump power, as Fig. 6.25 shows. The absorption efficiency is initially low due to the non-optimal

spectral overlap with the narrow absorption band of the crystal, however it increases with pump power and saturates near 98% for powers above 100 W. Nevertheless, during the experiment with OC_2 ($T_2 = 20\%$), we speculate that the VBG temperature exceeded normal operating conditions, and the resonance wavelength moved beyond the peak absorption, at pump powers above 135 W.

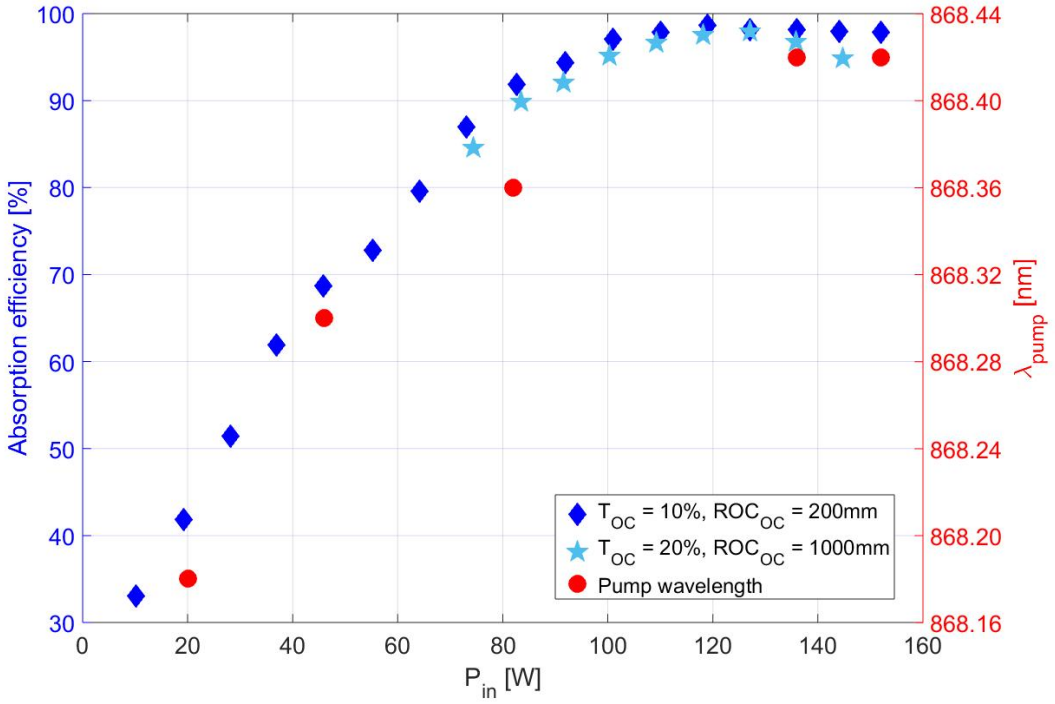

FIGURE 6.25: Left y-axis (blue): Absorption efficiency of the 0.3at.%-doped Nd:YAG crystal at 80 K, for the operating laser employing the two tested OCs. Right y-axis (red): pump wavelength variation vs pump power.

6.3.3 Results and discussion

With the crystal mounted as in Fig. 6.23 in the cryocooler Q-drive 2s132K, the operating temperature could be selected between 240 K and 77 K. The temperature that maximised the output power was observed to be $\sim$ 80 K, as measured by the internal temperature sensor of the Q-drive. When employing OC_1, the laser output power reached a maximum of 113 W, with a slope efficiency (with respect to absorbed power) of 80%. Instead with OC_2, the maximum output power was 104 W, however with an increased slope efficiency of 82%. As suggested by Fig. 6.25, the achievable maximum absorbed and, therefore, output power when using OC_2 were reduced due to warming of the VBG, which could be mitigated by controlling temperature of the VBG, a measure already in place for future laser experiments. For the cavity employing OC_1 (ROC= 200 mm), the M^2 beam quality parameter was measured at different output powers, and was found to increase from $M^2 \sim 1.3$ at 35 W to 4.9 by 105 W. Due to the ratio of pump's over

fundamental cavity mode's radius being around 2 (Fig. 6.22), it is expected that for sufficiently high pump powers higher-order modes would be supported, as discussed in more detail below.

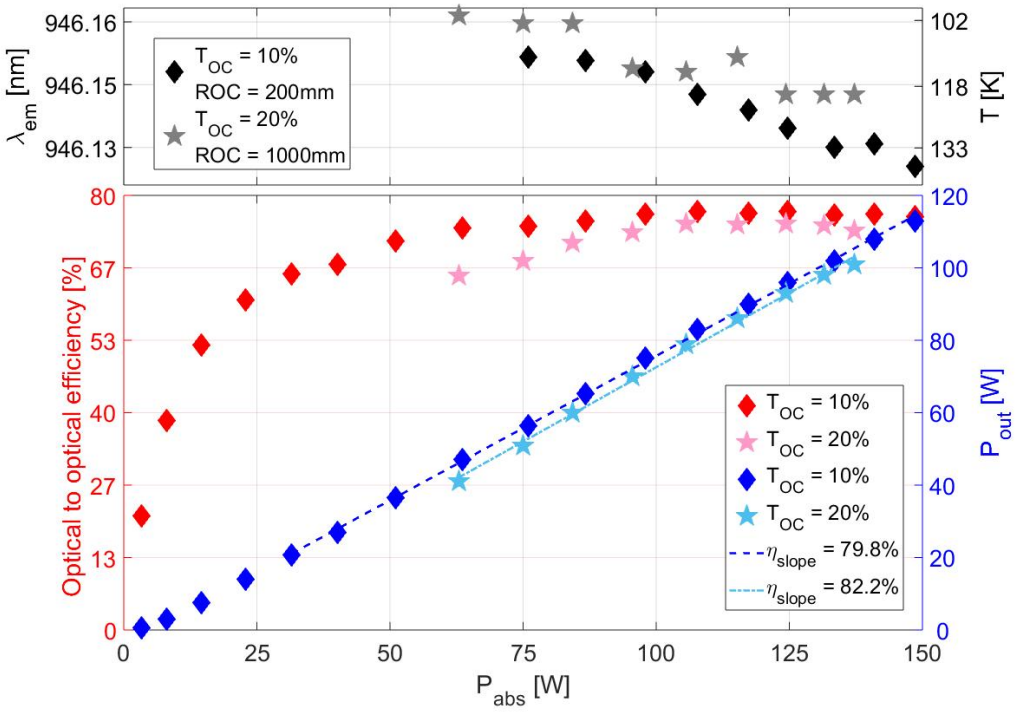

FIGURE 6.26: Top plot: measured emission wavelength (left y-axis) and estimated temperature of the emitting area of the gain medium (right y-axis). Bottom plot: optical to optical efficiency (red) and output power in function of absorbed pump power (blue) for the two OCs tested.

As in Section 6.2.3, the temperature-dependent emission wavelength was monitored with the OSA during laser operation: it was observed to operate solely at 946 nm once lasing was established and to blueshift at $\sim$ 25 pm/W (of absorbed pump power, as in Fig. 6.26), due to the peak wavelength shift in the emission cross section with temperature [11]. Noticeably, when the laser was not well aligned, parasitic amplified spontaneous emission (ASE) at 1061 nm was observed in the spectrum. This influenced the available gain for 946 nm, as observed around threshold. ASE at 1 μm is in fact another key challenge in achieving high-power 946 nm operation for Nd:YAG, even at cryogenic-temperatures. The strongest emission-peak in Nd:YAG at RT is at 1064 nm, however it, and therefore the gain, switches to 1061 nm below $\sim$ 200 K [11]; furthermore at 80 K, the latter wavelength has an effective emission cross section of 78 pm^2, compared with 8.4 pm^2 for the 946 nm transition, a nearly one order of magnitude difference. This higher gain at 1061 nm supports strong ASE if the pumping arrangements provide both a sufficiently large solid-angle and path length. For the cavity detailed above, the single-pass small-signal gain at threshold for 946 nm is only 0.28 dB and 0.54 dB for the respective output couplers, OC_1 and OC_2, (assuming a round trip loss of $L_{946} = 0.02$),

while the single-pass small-signal gain at 1061 nm would be 2.6 dB and 5 dB. Employing the same calculation of the ASE at 1 μm presented in Section 2.3, a spontaneously emitted photon at the center of the pump beam at one facet would see a solid angle defined by the pumped volume of $\Omega = A_{cr}/l_r^2 \sim 2\ 10^{-3}\ sr$ [10, Chapter 4], where A_{cr} is the pumped area at the first facet of the crystal and l_r the crystal length. This would result in the ratio between the intensity of the ASE at 1061 nm, I_{ASE}, and the saturation intensity, I_{Sat}, of $I_{ASE}/I_{Sat} = (\Omega/4)\ G_0/\sqrt{(\ln G_0)}$ [10, Chapter 4]. With G_0 the small-signal gain at 1061 nm indicated above, we have $I_{ASE}/I_{Sat} \sim 1.2 \cdot 10^{-3}$ and $I_{ASE}/I_{Sat} \sim 1.4 \cdot 10^{-3}$ for OC_1 and OC_2, respectively. I.e. I_{Sat} is 3 orders of magnitude smaller than the saturation intensity at this wavelength, thus having a negligible depletion effect on the upper laser level. However, it was observed that this influenced the available 946 nm gain around threshold, with a dramatic reduction in 1061 nm power above it. The employed optics' coatings were engineered to suppress parasitic lasing at 1061 nm, although attention to feedback into the pumped region was required as well. The input mirror provided the strongest feedback, nominally 25%, however it had little impact on the resulting ASE as it was sufficiently separated from the crystal. Furthermore, the round trip cavity loss was designed to be greater than 20 dB at 1061 nm, substantially higher than the the gain available at this wavelength, when employing the optimum output coupling for 946 nm operation. The ASE and parasitic lasing at 1061 nm were completely suppressed with optimal alignment and laser efficiency in the experiment, i.e. when 946 nm stimulated emission saturated the available gain.
Due to time restrictions it was not possible to characterise other laser output parameters such as the depolarisation loss and the thermal lens value, which would have revealed useful insight about the operation of the cavities developed.

As in Section 6.2.3, below we discuss the results obtained employing the Q4L laser performance model detailed in Section 2.4. Substantial differences with the pump and cavity arrangements exploited in Section 6.2 are the fundamental cavity mode and the pump symmetry, discussed in Sections 6.3.1 and 6.3.2, respectively. For the modelling, we have employed a pump power value of $P_{in} = 150\ W$, the maximum experimental power available, with the same 0.3at.%-doped, 15 mm-long, Nd:YAG crystal as before. Thanks to a more symmetric pump distribution, and a slightly bigger fundamental cavity mode with respect to the case detailed in Section 6.2, the population inversion distribution $\Delta N(\mathbf{r})$ at the first facet of the crystal could provide (in the case of oscillation only on the fundamental mode) a maximum inversion of $\sim 30\%$ in the pumped areas unsaturated by the laser gain, as shown in Fig. 6.27, as opposed to the 50% calculated for the previous case. As with the case of Fig. 6.15, higher-order modes are likely to have been excited due to this relatively high inversion value in the wings outside the fundamental laser mode. In fact, the output power predicted by this model, accounting exclusively for the fundamental mode lasing, is $P_{out} = 81\ W$, as opposed to the 104 W-output observed experimentally for the multi-mode laser output at 946 nm. We speculate

that the power difference between the model's prediction and the measured value is due to the higher-order modes lasing at the same time of the fundamental.
As detailed in Section 2.4, the portion of ions involved in the ETU process not only depopulates the upper laser level, i.e. decreases $\Delta N(\mathbf{r})$, but also produces excess heat in the regions where the gain is not saturated by the laser mode, quantified by the fractional thermal loading distribution $\xi(\mathbf{r})$. This parameter would equal the quantum defect, ξ_0 according to Eq. (2.41), if there were no ETU. However, in presence of ETU, $\xi(\mathbf{r})$ is a good indicator of where and by how much this process exacerbates the thermal load, because the heat-source-density distribution is calculated by weighting $\xi(\mathbf{r})$ with the pump distribution, as defined by Eq. (2.42).

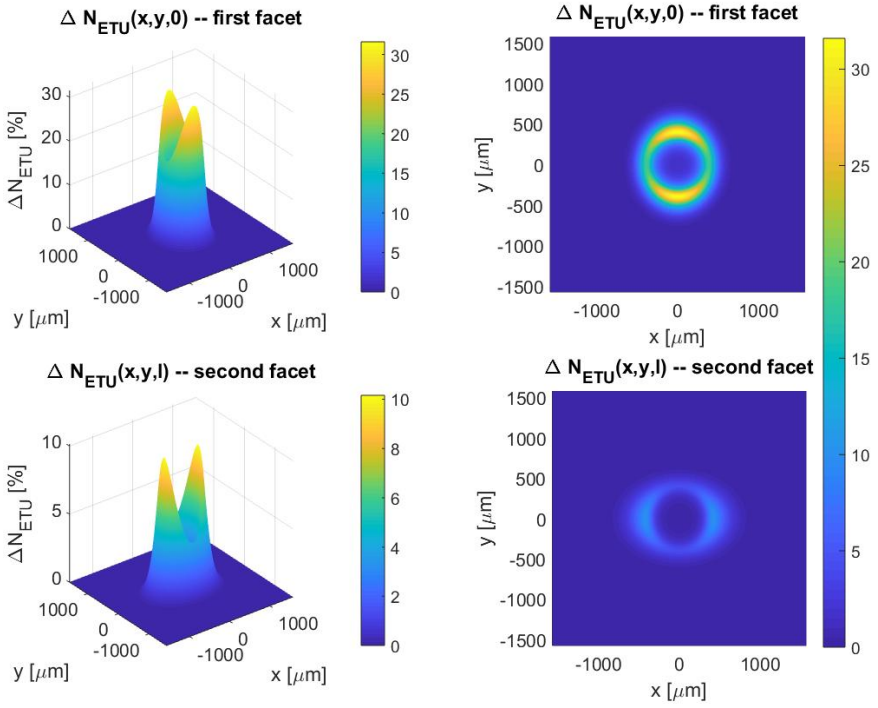

FIGURE 6.27: Spatial distribution of $\Delta N(\mathbf{r})$ at the first (top plots) and second (bottom plots) facets of the crystal.

Fig. 6.28 shows the fractional thermal loading distribution at various coordinates along the crystal length. Noticeably, the minimum is again the quantum defect ($\sim$ 8%) as expected, however the maximum of the distribution, located in the wings as in Fig. 6.16, is 21% as opposed to the $>$ 30% of Fig. 6.16, despite the higher pump power employed (150 W in this, versus 120 W in the previous case).
This significant 10% difference is due to the better symmetry of the pump profile and to the better mode-match, in this case $a_x = 1.80$ and $a_y = 2.08$ as opposed to $a_x = 2.22$ and $a_y = 1.93$ employed previously. Furthermore, as expected by the exponential decay of the pump along the crystal length, a standard form in the absence of ground state bleaching effects like in this case [2], the majority of the heat is deposited within the first

quarter of the crystal length, decaying quickly thereafter. A mitigation strategy would be to employ a longer crystal with a lower doping-ion concentration: this would, additionally, reduce the effects associated to ETU, but would also require a high-brigthness pump in order to keep its Rayleigh range comparable to the crystal length.

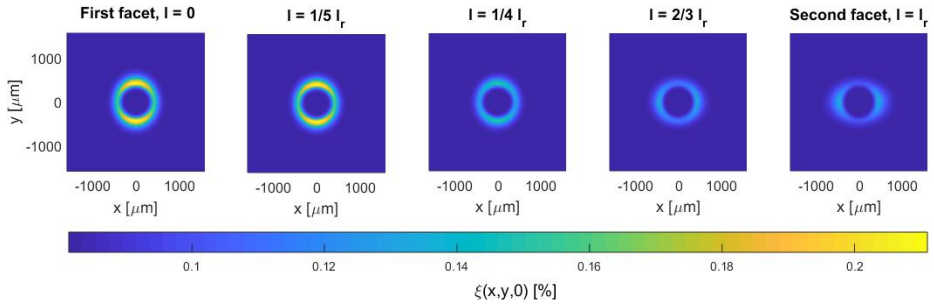

FIGURE 6.28: Fractional thermal loading distribution at several z-coordinates along the crystal length.

The heat-source-density distribution, displayed in Fig. 6.29, highlights an interesting and relevant difference with the previous case detailed in Section 6.2.3. A local maximum value reached in this case, $\sim 12\ kW/cm^3$, is larger than the one obtained in the previous case, $\sim 10\ kW/cm^3$ (Fig. 6.17), because of the higher pump power employed. However, $Q_{ETU}(\mathbf{r})$ at the first facet of the crystal, is mainly concentrated in the area corresponding to the fundamental laser mode, indicating that in this case the heat produced in the gain-saturated portion of the medium exceeds the heat produced in the wings, the contribution to which in the latter region is mainly due to ETU. Once again for the ideal case of only the fundamental mode oscillating, the ratio between $Q_{ETU}(\mathbf{r})$ and $Q_{noETU}(\mathbf{r})$ at the first facet of the crystal, shown in Fig. 6.30 reveals a maximum of ~ 2.5, as opposed to the ~ 3.9-ratio obtained in Fig. 6.18. An overall significant improvement with respect to the case examined in Section 6.2.3.

It is expected that the peak in the heat-source-density distribution will be decreased by gain saturation caused by the higher-order modes lasing, further smoothing the heat source profile illustrated so far. These simple simulations, Fig. 6.27 to Fig. 6.30, illustrate the impact of ETU and the resulting heating of the laser crystal. A much more complex model would be required to reproduce the dynamic system constituting a laser. Nevertheless, the simulation results as per the theory detailed in Section 2.4 provide a useful tool determining a specific direction to pursue for future of potential improvements. In our case, the results provided useful insight regarding the detrimental effects of ETU on the laser operation of the cryogenically cooled 946 nm Nd:YAG, as well as useful information as to why the second laser performed more efficiently than the first.

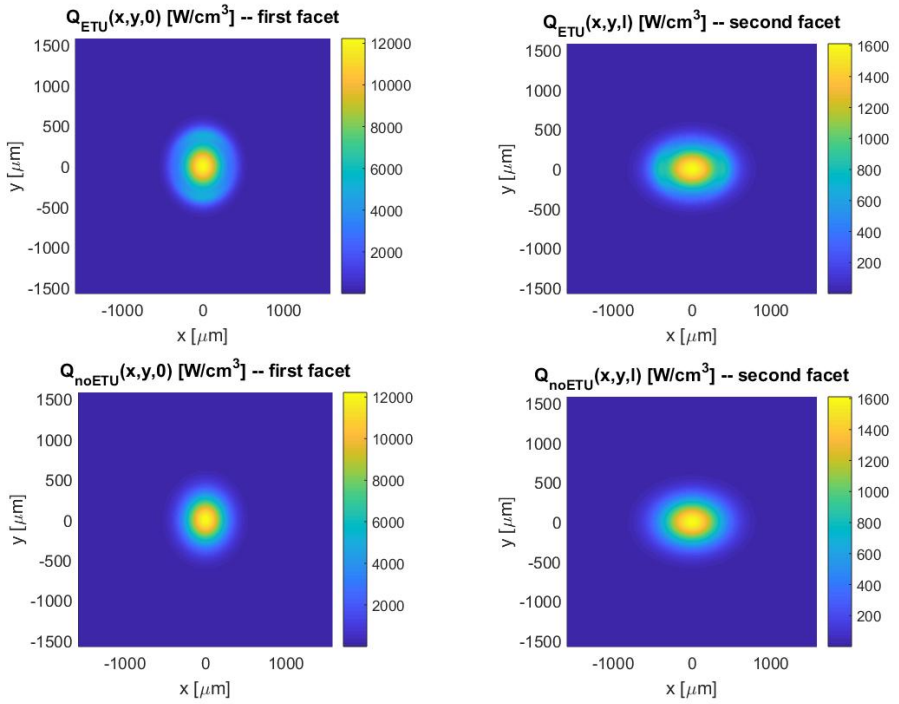

FIGURE 6.29: Heat-source-density distribution $Q(\mathbf{r})$, with (top plots) and without (bottom plots) accounting for ETU, at the first and second facets of the crystal.

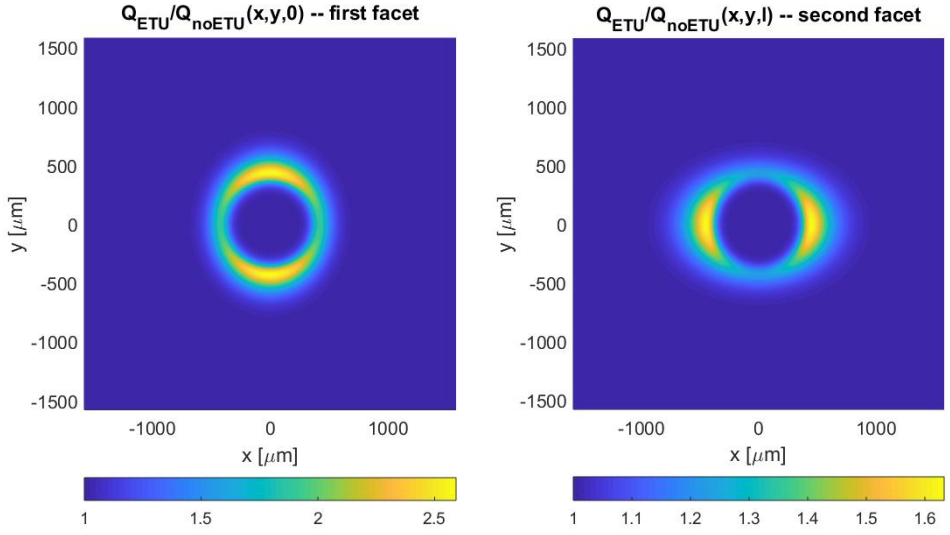

FIGURE 6.30: Ratio of the heat source distributions $Q_{ETU}(\mathbf{r})/Q_{noETU}(\mathbf{r})$ at the first and second facets of the crystal.

6.4 Conclusions

A thorough investigation of the temperature dependent R-band absorption cross section in Nd:YAG performed in [3] motivated the development of a novel VBG-locked diode-laser pump source at 869 nm. Employing this source, we achieved a 99% absorption efficiency at the maximum pump powers tested, and demonstrated the first 60-W, cryogenically cooled 946 nm Nd:YAG laser, the highest output power observed for this laser at the time of demonstration. For this laser, we observed a slope, and optical to optical, efficiency of 52%, limited by the temperature rise in the pumped volume crystal and a non-optimal overlap between pump and cavity modes. Further optimisation was not undertaken at this stage, due to the relatively poor heat extraction of the setup. We estimated an average local temperature rise in the crystal of $\sim 80\ K$ by monitoring the emission wavelength, suggesting a heat transfer coefficient in the range of (0.25-0.5) $W/K \cdot cm^2$ between the crystal and the LN coolant. This, coupled to thermally-induced optical aberrations, caused modal instabilities that resulted in degradation in beam quality for high output power and eventual termination of laser action.

While working towards the symmetrisation of the pump beam, the DLA failed catastrophically, and we were forced to start a complete re-built. A new pump setup that provided a more symmetric pump waist in the crystal with respect to the previous, was developed in collaboration with G. Shayeganrad. Furthermore, an upgraded crystal holder, developed by G. Shayeganrad, provided a symmetric cooling profile and a lower thermal resistance with respect to the one employed previously. With these arrangements, an output power for the cryogenically cooled 946 nm Nd:YAG laser above 100 W was demonstrated for the first time, with a slope efficiency of 82% with respect to absorbed power. This result was pump-power limited, though also nearing the limits of the closed-cycle cryocooler. The beam quality was measured to be 4.9 at 105 W, due to an overlap factor of pump mode over fundamental cavity mode greater than 2, allowing higher-order modes to lase, and beam degrading aberrations associated with the internal thermal gradient in the crystal.

The results provided by a theoretical model for the laser performance of Q4L lasers including ETU applied to our cases provided useful insight as to why the second laser was more efficient than the first one. In the case of the 60-W laser, the fundamental to pump mode ratio > 2 produced a significant fractional thermal loading outside the fundamental mode area reaching $\sim$ 30%, 22% in excess of the quantum defect. This distribution dominated the heat-source-density. In the upgraded setup, the better pump symmetry and mode overlap decreased the fractional thermal loading outside of the fundamental laser mode area considerably, now reaching $\sim$ 20%; in this case the heat-source-density distribution was dominated by the pump distribution, therein also decreasing the consequent thermal aberrations. In both the developed lasers a slightly better scenario than the modelled one is hypothesised due to higher-order modes lasing

above threshold (not accounted for in the model employed) and therefore saturating the gain outside the fundamental mode area, where the majority of the heat load due to ETU was located.

A mitigation strategy to the challenges aforementioned would be to fibre-couple the pump signal in order to have a symmetric pump distribution along with an easier control over the pump waists' locations through a single spherical lens. A better mode match with the pump would provide less fractional thermal load in the wings of the fundamental laser mode distribution, therein reducing the aberration in the thermal lens and improving the beam quality factor, while maintaining the excellent performance demonstrated in the experiment detailed above.

References

[1] W. A. Clarkson, "*Thermal effects and their mitigation in end-pumped solid-state lasers*," Journal of Physics D: Applied Physics **34**, 2381–2395 (2001).

[2] S. Bjurshagen and R. Koch, "*Modeling of energy-transfer upconversion and thermal effects in end-pumped quasi-three-level lasers*," Applied Optics **43**, 4753–4767 (2004).

[3] S. J. Yoon, "*Cryogenically-cooled neodymium-doped solid-state lasers*," Ph.D. thesis, University of Southampton (2016).

[4] E. H. Carlson and G. H. Dieke, "*The State of the Nd^{3+} Ion as Derived from the Absorption and Fluorescence Spectra of $NdCl_3$ and Their Zeeman Effects*," The Journal of Chemical Physics **34**, 1602–1609 (1961).

[5] R. Goering, P. Schreiber, and T. Possner, "*Micro-optical beam transformation system for high-power laser diode bars with efficient brightness conservation*," in *Proceedings, Photonics West*, vol. 3008 (SPIE, 1997).

[6] U. Demirbas, J. Thesinga, M. Kellert, F. X. Kärtner, and M. Pergament, "*Comparison of different in situ optical temperature probing techniques for cryogenic Yb:YLF*," Opt. Mater. Express **10**, 3403–3413 (2020).

[7] W. P. Risk, "*Modeling of longitudinally pumped solid-state lasers exhibiting reabsorption losses*," Journal of the Optical Society of America B **5**, 1412–1423 (1988).

[8] L. Cini and J. I. Mackenzie, "*Analytical thermal model for end-pumped solid-state lasers*," Applied Physics B **123**, 273 (2017).

[9] S. Chénais, F. Druon, S. Forget, F. Balembois, and P. Georges, "*On thermal effects in solid-state lasers: The case of ytterbium-doped materials*," Progress in Quantum Electronics **30**, 89–153 (2006).

[10] W. Koechner, *Solid-State Laser Engineering*, Springer Series in Optical Sciences (Springer, 2006).

[11] S. J. Yoon and J. I. Mackenzie, "*Implications of the temperature dependence of Nd:YAG spectroscopic values for low temperature laser operation at 946 nm*," Proc. SPIE 9135, Laser Sources and Applications II **913503** (2014).

Chapter 7

Conclusions

In this final chapter we summarise the developments achieved and detailed in the previous chapters. Finally, we give a brief overview on the future work that will follow this thesis.

7.1 Results' overview

In the first chapter of this thesis we have given an overview, including motivation for the pursuit of the power-scaling of the sub-1 μm transition in Nd-doped lasers, along with putting it into context with the current state-of-the-art. This research was motivated by numerous possible applications: LIDARs with the fundamental sub-1 μm wavelength, underwater communications and medical applications after frequency upconversion into the blue spectrum, where there exists a limited number of high-power sources available, and the possibility of fourth-harmonic-generation into the deep UV for industrial applications. The route chosen for this power-scaling is the aggressive cooling of the gain medium, exploited since early demonstrations of lasers, and known to be extremely successful for the power-scaling of Yb-doped lasers. In fact, when in-band pumped at around 869 nm, the Q4L $^4F_{3/2} \rightarrow {}^4I_{9/2}$ (946 nm) system of the Nd^{3+} impurity has equivalent characteristics to the 1 μm system of Yb^{3+}.

In Chapter 2 we have presented the theory underlying the successive experimental-work-based chapters. We introduced the Beer-Lambert law and detailed how it can be applied to small-signal absorption measurements to retrieve either the doping-ion concentration or the absorption cross section of the tested sample. These two spectroscopic parameters are key to a precise laser performance modelling.
We presented the two-rate-equation model employed for the measurement of the ETU coefficient, a macroparameter that quantifies this energy-transfer process that hinders

the laser performance and exacerbates the thermal load, effectively limiting the RT performance of ${}^4F_{3/2} \rightarrow {}^4I_{9/2}$ in a variety of hosts. Here we have presented an improved and more rigorous methodology: a steady-state solution as opposed to the time-dependent one for the rate-equation model, used in previous works from our group, which delivered a $>$ 100-fold decrease in computational times. At the same time, we have demonstrated the equivalence between the two approaches, thanks to suitably chosen experimental conditions.
Furthermore, we have introduced a simple analytical formula, reported in the literature, for the threshold pump power of Q4L lasers including ETU, comprising a figure-of-merit for ETU, which we have discussed along the experimental results obtained for the ETU coefficient measurement. Finally, we have summarised the Q4L laser performance model including ETU which we have employed later to estimate the impact that this processes had on the high-power lasers we developed.

In Chapter 3 we have presented a novel methodology to measure with high accuracy the doping-ion concentration of laser crystals, which was exploited to measure the effective doping-level of several Nd-doped samples. This procedure, applicable to potentially any laser crystal with known absorption cross section spectrum, is useful to either test the doping-concentration of new samples from vendors, or measure it where traceability records have been lost. Moreover, we have detailed the methodology and results for the thorough characterisation of the ground absorption cross section into the ${}^2H_{9/2} + {}^4F_{5/2}$ energy levels for Nd-doped Vanadates (YVO_4 and $GdVO_4$) in the elevated temperatures regime (RT-450) K, and for Nd:YAG in the sub-ambient temperature range (RT-LNT). We found that the absorption cross section in Nd-doped Vanadates decreases with increasing temperatures, while it increases with decreasing temperatures in Nd:YAG, presenting a $\sim$ 6-fold increase for the dominant peak around 808 nm. These results, besides providing a better precision with respect to previously published data, underpinned the subsequent measruements of the ETU coefficient for the same crystals in the respective temperatures regimes.

In Chapter 5 we have introduced the automated z-scan technique employed to measure the ETU coefficient of Nd-doped Vanadates at elevanted temperatures, Nd:YAG at cryogenic temperatures, and to probe the dependence of this macro-parameter on doping-ion concentration in Nd:YAG. We have thoroughly discussed the error analysis and the way we exploited the developed automation to minimise the uncertainty associated to the measurement. We found that the ETU coefficient, linearly dependent on doping-ion concentration in Nd:YAG as already reported in the literature, decreases with increasing temperatures in Nd-doped Vanadates and increases with decreasing temperatures in Nd:YAG. We have estimated that the influence of ETU on the strongest four level 1 μm transition of Nd:YAG and Nd-doped Vanadates is negligible, whereas it is of critical

importance when operating on the low-gain Q4L 0.9 μm transition for the same crystals. In order to mitigate these effects, low-doping cocentrations should be employed. Furthermore, we have calculated that although the ETU coefficient for Nd:YAG increases with decreasing temperatures, the spectroscopic and thermo-optical enhancements provided by cryogenic-cooling dominate the laser performance of the 946 nm Q4L transition.

In Chapter 6 we have detailed the development of a novel VBG-locked at 869 nm diode-laser array pump laser. We have employed this pump for the demonstration of two in-band pumped cryogenically cooled 946 nm Nd:YAG lasers, the first producing a 60-W output with a 52% slope and optical-to-optical efficiency, and the second producing a $>$ 100-W output with a 82% slope and 74% optical-to-optical efficiency. In both cases, the VBG-locked pump, engineered to match the sharp 77 K absorption peak at 869 nm for the maximum available pump power, provided a (95-99)% absorption efficiency.
The 60-W laser appeared to be limited by non-optimal thermal management: we estimated a $\sim$ 80 K temperature rise in the lasing region of the crystal by monitoring the temperature-dependent emission wavelength, a much higher value with respect to the one predicted using an analytical thermal model. The laser action was eventually terminated due to a roll-over in power and a significant degradation in beam quality, with an evident dynamic mode competition coupled to thermal aberrations. By employing the laser performance model introduced previously, we estimated that the factor-of-2 bigger pump with respect to the fundamental laser mode caused both an extra heat load mainly due to ETU in the wings of the fundamental mode distribution, and a significant population inversion that might have caused higher-order modes to operate as well.
For the $>$ 100-W lasers, a closed-cycle cryo-cooler was employed instead of the liquid Nitrogen dewar used in the previous 60-W laser experiment. The laser output, limited by pump power, presented a much higher efficiency, which we have associated to two factors: the upgraded crystal mounting developed by G. Shayeganrad, and the symmetrisation of the pump distribution coupled to a better mode-match. In fact, the results of the Q4L modelling applied to this case highlighted, that although still present, a lower heat load due to ETU outside of the fundamental laser mode area thanks to a pump-to-laser-mode ratio $<$ 2. It is likely, however, that higher-order modes were operating, in light of the measured M^2 of $\sim$ 5 at high output powers.
A non-trivial challenge to address was the gain competition with the 10x stronger 1 μm transition (at LNT). Due to its high gain, even the small feedback provided by the optical coatings would excite this transition if the gain wasn't completely saturated by the 0.9 μm transition. It was observed that with optimal alignment of the cavity, i.e. maximising the gain saturated by the 0.9 μm, the 1 μm ASE could be mitigated and laser action at this wavelength completely prevented.

7.2 Future work

In this work we have demonstrated the power-scaling of the Q4L 946 nm cryogenically cooled Nd:YAG laser with results that currently stand as the state-of-the-art demonstration for the output power of this laser. Our priority is to improve the beam quality, whilst maintaining the excellent performance demonstrated. As we have discussed in the previous chapters, the degradation in the measured M^2 factor was due to the pump's distribution being bigger than the fundamental laser mode's in the crystal, hence exciting higher-order modes and inducing further thermal aberrations due to the significant heat load in the wings of the fundamental mode. A mitigation strategy would be to design the laser so that the mode-match factor is around 1, providing no significant population inversion outside the fundamental laser mode. Furthermore, given the two different $M^2_{x,y}$ factors for the pump beam, we could not achieve a symmetric pump beam over the entire crystal length. To remove this limitation, it would be appropriate to fibre-couple the pump beam: this would provide a much easier and straightforward way of conditioning the beam through spherical lenses instead of cylindrical ones. Although, there would be the challenge of maximising the coupling efficiency between DLA and delivery fibre. We have demonstrated, with the Q4L laser performance modelling, that the majority of the pump is deposited within the first half of the crystal, causing a high thermal load in a relatively small volume, despite the small quantum defect provided by in-band pumping. With the aim of further reducing the thermal load, we will consider employing even longer crystals with a lower doping-level, although this would introduce restrictions on the pump's brightness. Additionally, further technical challenges need to be addressed in order to optimise the setup handling and operation: the temperature tuning of the VBG, requiring and adequate VBG-cooling implementation, could be beneficial to control the locked wavelength with respect to the peak absorption of the cryogeniccaly cooled gain medium and thus maximising the absorption efficiency, even when operating at very high powers.

In the motivations driving this research we have listed the advantage of sub-1 μm high-power lasers frequency upconverted into the blue around 470 nm and deep-ultraviolet (DUV) around 240 nm, shorter wavelengths with respect to the popular frequency upconversion of 1 μm lasers into the green around 530 nm and DUV around 270 nm. Through fourth-harmonic generation of the 946 nm transition, indeed, there would be a chance to develop potentially comparable sources to the possibly harmful Excimer lasers. In order to reach these advanced stages of laser development, we are planning to firstly demonstrate a pulsed cryogenically-cooled 946 nm Nd:YAG laser employing the cavity-dumping technique, suitable for ns-long pulses and repetition rates in the hundreds-of-kHz. These lasers would underpin MOPA configurations for future energy-scaling architectures.

In conclusion, in this work we have developed novel measurements methodologies potentially applicable to any laser crystal, and presented record results that stand as the state-of-the-art for the power-scaling of the cryogenically cooled 946 *nm* Nd:YAG laser.

Appendix A

General Fitting Procedure

A.1 Overview

In presence of a physical phenomenon and relative experimental data, the experimental scientist is usually equipped with formulas that describe the data: a model. A model describes a formal relation between an independent variable x and the dependent variable y. The form of the dependence will be of the kind

$$y = f(x, p) \tag{A.1}$$

with f a generic function, and p the set of parameters that, appropriately chosen, best describe the data. The aim of a fitting procedure is to determine these parameters, for which we employ the minimisation of the χ^2. The quantity χ^2 of an experimental data set is defined as the weighted sum of the squared residual of each data point. To illustrate, we give relevant definitions below.
Once the form of the model provided by Eq. (A.1) is established, and an educated guess for the parameters p made, the theoretical value y_{th} corresponding to the experimental x-value is calculated as

$$y_{th} = f(x, p) \tag{A.2}$$

The comparison between Eq. (A.2) and the experimentally measured value y_{ex} provides information about the match between theory and experiment. Given a set of n experimental data points, a residual for the i-th point is defined as

$$RES_i = y_{ex,i} - y_{th,i} = y_{ex,i} - f(x_i, p) \tag{A.3}$$

The value of a residual as defined in Eq. (A.3) depends on both the model chosen and the parameters; as the model is fixed, the parameters p are the only quantity that can vary. Thus a residual so defined is a function of the set of fitting parameters p: $RES_i = RES_i(p)$. The χ^2, besides strongly depending on the residuals, also takes

into account the statistical value of each data point, i.e. the error associated to the measurement y_i, Δy_i. By definition

$$\chi^2(p) = \sum_{i=1}^{n} \frac{RES_i^2(p)}{(\Delta y_i)^2} = \sum_{i=1}^{n} \left[\frac{1}{(\Delta y_i)^2} (y_{ex,i} - f(x_i, p))^2 \right] \tag{A.4}$$

Eq. (A.4), depending on the parameters p, is the quantity to be minimised. Therefore, the set of parameters that minimises Eq. (A.4) provides the best fitting parameters sought.

A.2 Procedure

The minimisation of Eq. (A.4) means that for each parameter p_j we want

$$\frac{\partial \chi^2}{\partial p_j} = \frac{\partial}{\partial p_j} \left(\sum_{i=1}^{n} \left[\frac{1}{(\Delta y_i)^2} (y_{ex,i} - f(x_i, p))^2 \right] \right) = 0 \tag{A.5}$$

Mathematically, problem (A.5) can be very complex, especially when (A.2) does not depend linearly on the parameters p. However, the algorithms used for this minimisation are very well and efficiently implemented in most calculus softwares.
©MatLab, our data analysis software of choice, supplies a a number of efficient built-in routines aimed particularly to the search of the minimum of functions defined as the sum of squares, like $\chi^2(p)$. The one used in our fitting procedure is `lsqnonlin`. This function solves problems of the form

$$\min_p \| G(p, x) \|^2 = \min_p \sum_{i=1}^{n} g_i(p, x)^2 \tag{A.6}$$

where $G(p, x)$ is the user-defined array

$$G(p, x) = \begin{bmatrix} g_1(p, x) \\ g_2(p, x) \\ \vdots \\ g_n(p, x) \end{bmatrix} \tag{A.7}$$

However, if we define $G(p, x)$ as

$$G(p, x) = \begin{bmatrix} g(p, x_1) \\ g(p, x_2) \\ \vdots \\ g(p, x_n) \end{bmatrix} = \begin{bmatrix} RES_1/\Delta y_1 \\ RES_2/\Delta y_2 \\ \vdots \\ RES_n/\Delta y_n \end{bmatrix} \tag{A.8}$$

then `lsqnonlin` returns the minimum

$$\min_p \{g(p,x_1)^2 + g(p,x_2)^2 + \cdots + g(p,x_n)^2\} = \min_p \left\{ \sum_{i=1}^{n} \frac{RES_i^2(p)}{(\Delta y_i)^2} \right\} = \min_p \{\chi^2(p)\} \tag{A.9}$$

which is exactly the minimisation of χ^2 defined in Eq. (A.4).

In order to execute the fitting procedure, the user needs to

- Define the theoretical model function $f(x,p)$, which depends on the independent variable x and on the set of parameters p;
- make an educated guess of the parameters p, which will be the starting point for the iterative procedure that MatLab performs, varying the parameters while minimising the χ^2;
- write a MatLab function that includes
  - the function $f(x,p)$ itself,
  - the derivative of f with respect to each parameter $\frac{\partial f(x,p)}{\partial p_i}$;
- define a function as detailed in Eq. (A.8);
- use `lsqnonlin` to minimise the function defined above.

At the end of this procedure, the returned values are the best fitting parameters sought initially.
Furthermore, this methodology can be generalised to work not only with analytical models of the form $f(x,p)$, but also with generic, numerical functions $F_{bb}(x,p)$ where bb stands for 'black box'. In fact, a MatLab function is defined by code lines that manipulate the inputs, and return the outputs: a black box. Thanks to its extensive features, the built-in `lsqnonlin` can be set to work without the explicit form of the derivatives of $F_{bb}(x,p)$ with respect to the parameters, in general cases where calculating them is not possible. This option extends the computational time, however ultimately providing excellent results. In this thesis work, we have employed this procedure for both analytical functions and 'black box' functions. The latter being the MatLab function that calculates the transmitted power through a crystal by numerically solving the system of equations (2.7) and with W_{ETU} the only fitting parameter, as detailed in Chapter 5. In this particular case, $F_{bb} = F_{bb}(z, W_{ETU}) = P_{out}(z, W_{ETU})$, with z being the z-scan coordinate and W_{ETU} the fitting parameter to find.

A.3 An application

As discussed in the previous section, we have employed the procedure detailed above in a number of measurements throughout this thesis, one of them being the measurement of the beam quality factor, M^2. To illustrate, we report, as an example, the analytical function used for this characterisation, highlighting the role of the fitting parameters with respect to the experimental conditions.
The second moment beam radii $w(z)$, also referred to as "beam size", of a beam with waist w_0 and known wavelength λ, depends on the coordinate z as

$$w(z) = w_0\sqrt{1 + \frac{z^2(M^2)^2\lambda^2}{\pi^2 w_0^4}} \tag{A.10}$$

where the location of the waist w_0 is assumed to be $z = 0$. When this is not the case, it is necessary to shift z by the appropriate amount given by z_0, the waist position with respect to an arbitrary coordinate system. Eqn. (A.10) becomes

$$w(z) = w_0\sqrt{1 + \frac{(z - z_0)^2(M^2)^2\lambda^2}{\pi^2 w_0^4}} \tag{A.11}$$

Referring to the setup in Fig. 5.1, we positioned a wedge after the focusing lens L_3, redirecting $\sim 4\%$ of the beam into a CCD beam profiling camera (Spiricon BGP-USB-SP503U). The camera's software could reveal the beam and measure its second moment beam radii $w(z)$ on both axes (x- and y-axis, with z the direction of propagation). The automated data collection consisted in moving the translation stage and registering the rail position z with respect of an arbitrary origin and the beam size at each step of the scan. An example of raw data is shown in Fig. A.1.
We employed z_0, w_0 and M^2 as fitting parameters for the analytical function defined in Eq. (A.11). In this case

$$f(x, p) = w(z, (z_0, w_0, M^2)) \tag{A.12}$$

y_{ex} was the set of experimentally measured beam sizes w_{ex}, and Δy the uncertainty provided by the CCD camera software, Δw. The quantity to minimise, χ^2, in this case had the form

$$\chi^2(z_0, w_0, M^2) = \sum_{i=1}^{n} \frac{RES_i^2(z_0, w_0, M^2)}{(\Delta w_i)^2} = \sum_{i=1}^{n} \left[\frac{1}{(\Delta w_i)^2}(w_{ex,i} - w(z_i, (z_0, w_0, M^2)))^2\right] \tag{A.13}$$

By using the procedure depicted above we obtained a set of best fitting parameters that, substituted in (A.11), provided the results shown in Fig. A.2: a very good match between model and experimental data. In fact, the 'best' match, according to how we have developed this procedure.

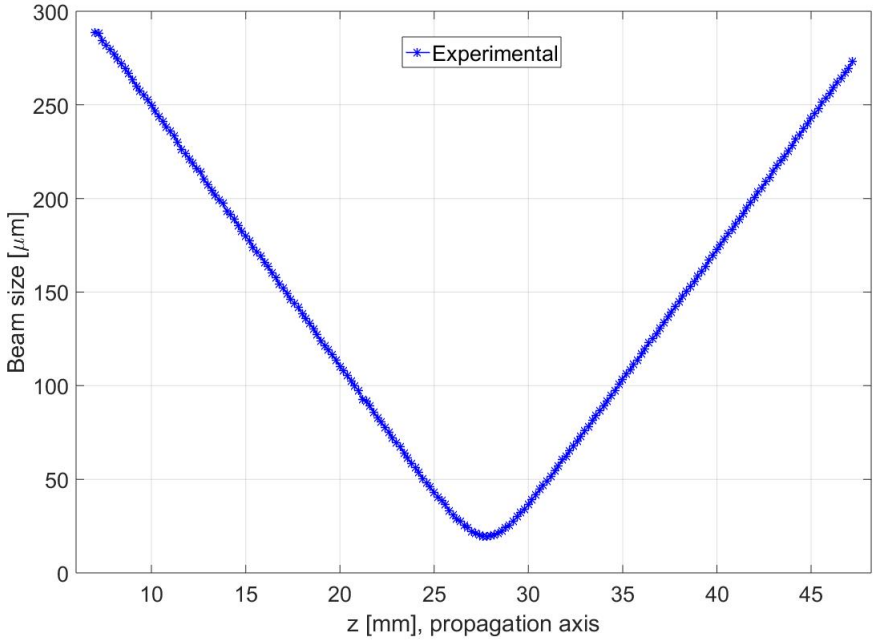

FIGURE A.1: Example of raw data for a M^2 measurement.

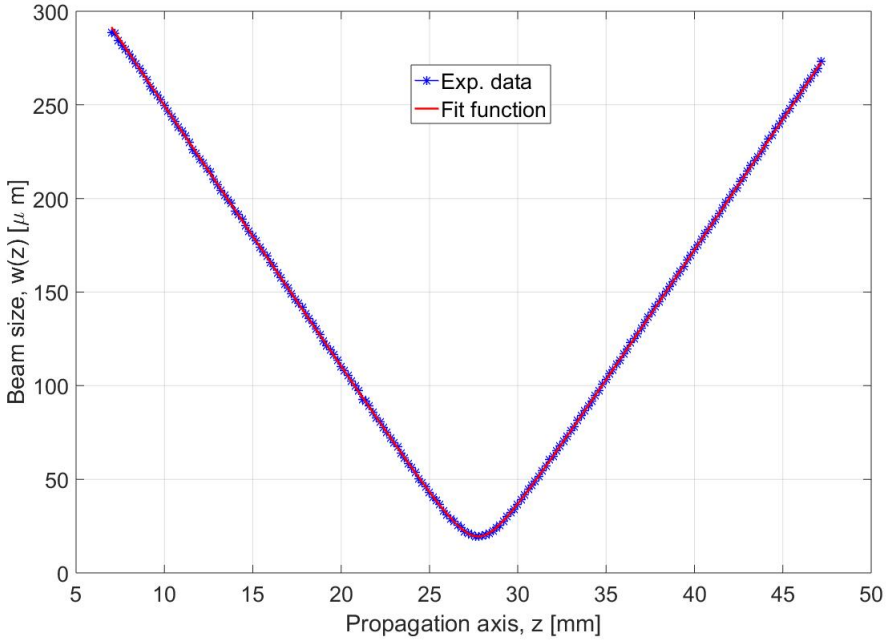

FIGURE A.2: Example of raw data vs best fit curve for a M^2 measurement.

In conclusion, we have developed a simple but successful method to find the best fitting parameters to any model – even nonlinear, or non-analytical – provided that the form of the physical law describing the experimental conditions is known.

Appendix B

Laser performance model parameters

In this appendix we report a list of the parameters employed for the modelling of the laser performance for the Q4L transition of the cryogenically-cooled 946 nm Nd:YAG laser. As detailed in Section 6.2.3, all the temperature-dependent parameters are fixed at their value at 77 K.

- $T_c = 77$; [K] Temperature of the crystal
- $f_2 = 0.8281$; Fractional population in the upper laser level at 77 K according to Boltzmann distribution
- $f_1 = 1.067\ 10^{-7}$; Fractional population in the lower laser level at 77 K according to Boltzmann distribution
- $\sigma = 8.4\ 10^{-20}/f2$; [$cm^2$] Transition cross section from R_1 to Z_5
- $\sigma_{abs} = 0.5 \cdot 6.5\ 10^{-20}$; [$cm^2$] Effective absorption cross section at the pump wavelength
- $W_{ETU} = 5.3\ 10^{-17}$; [cm^3/s] ETU coefficient at 77 K for 0.3at.%-doped Nd:YAG

Appendix C

Publications list

This thesis work was based on the following peer-reviewed journal publications and conference papers.

C.1 Peer-reviewed journals

- S. Cante, S. Beecher, and J. I. Mackenzie, "*Characterising energy transfer upconversion in Nd-doped Vanadates at elevated temperatures*," Optics Express **26**(6), 6478-6489 (2018).
- S. Cante, S. Valle, S. J. Yoon, and J. I. Mackenzie "*60-W 946-nm cryogenically-cooled Nd:YAG laser*," Applied Physics B **125**, 135 (2019).
- S. Cante and J. I. Mackenzie, "*Energy transfer upconversion in Nd:YAG at cryogenic temperatures*," Optical Materials Express **10**(9), 2019-2029 (2020).
- G. Shayeganrad, S. Cante, J. P. Mosquera, W. O. S. Bailey, and J. I. Mackenzie, "*Highly efficient 110-W closed-cycle cryogenically cooled Nd:YAG laser operating at 946 nm*," Optics Letters **45**(19), 5368-5371 (2020).

C.2 Conference papers

- S. Cante, S. Beecher, and J. I. Mackenzie, "*Characterising energy transfer upconversion in Nd:YVO_4 at elevated temperatures*," in *Laser Congress 2017 (ASSL, LAC)*, OSA Technical Digest (online) (Optical Society of America, 2017), paper JM5A.9.
- S. Cante, and J. I. Mackenzie "*60-W cryogenically-cooled Nd:YAG 946 nm laser*," in *OSA International Siegman School of Lasers*, Sweden. 28 Jul - 04 Aug 2018.

- S. Cante, S. Valle, and J. I. Mackenzie "*60-W cryogenically-cooled Nd:YAG 946nm laser*," in *8th EPS-QEOD Europhoton Conference*, Spain. 02 - 07 Sep 2018.
- S. Cante, and J. I. Mackenzie "*Spectroscopic characterisation of Yb:LiLuF$_4$ between (63-293)K*," in *Laser Congress 2019 (ASSL, LAC, LSC)*, OSA Technical Digest (Optical Society of America, 2019), paper JM5A.4.
- G. Shayeganrad, S. Cante, J. P. Mosquera, W. O. S. Bailey, and J. I. Mackenzie, "*113-W cryogenically-cooled 946-nm Nd:YAG laser*," in *OSA Advanced Photonics Congress (AP) 2020 (IPR, NP, NOMA, Networks, PVLED, PSC, SPPCom, SOF)*, OSA Technical Digest (Optical Society of America, 2020), paper ITh2B.3.
- G. Shayeganrad, S. Cante, J. P. Mosquera, W. O. S. Bailey, and J. I. Mackenzie, "*Highly efficient cryogenically cooled 110-W 946-nm Nd:YAG laser*," in *9TH EPS-QEOD Europhoton Virtual Conference*. 30 Aug - 04 Sep 2020.

Final remarks

The Awkward Yeti, Heart and Brain having an exchange of opinions at the end of thesis writing.